GFZ

Helmholtz Centre Potsdam

Helmholtz Centre Potsdam
GFZ German Research Centre for Geosciences

Sabrina Herrmann

Capacity of imaging spectroscopy for the characterisation of REO, REE bearing minerals & primary REE-deposits

Scientific Technical Report STR19/08

www.gfz-potsdam.de

HELMHOLTZ
RESEARCH FOR GRAND CHALLENGES

Recommended citation:

Herrmann, S. (2015): Capacity of imaging spectroscopy for the characterisation of REO, REE bearing minerals & primary REE-deposits, Master Thesis at the University of Potsdam, (Scientific Technical Report STR ; 19/08), Potsdam: GFZ German Research Centre for Geosciences.
DOI: http://doi.org/10.2312/GFZ.b103-19089

Imprint

HELMHOLTZ CENTRE POTSDAM
GFZ GERMAN RESEARCH CENTRE FOR GEOSCIENCES

Telegrafenberg
D-14473 Potsdam

Published in Potsdam, Germany
April 2019

ISSN 2190-7110

DOI: http://doi.org/10.2312/GFZ.b103-19089
URN: urn:nbn:de:kobv:b103-19089

This work is published in the GFZ series Scientific Technical Report (STR) and electronically available at GFZ website www.gfz-potsdam.de

Sabrina Herrmann

Capacity of imaging spectroscopy for the characterisation of REO, REE bearing minerals & primary REE-deposits

Scientific Technical Report STR19/08

Capacity of Imaging Spectroscopy for the Characterisation of REO, REE Bearing Minerals & Primary REE-Deposits

by

Sabrina Herrmann

A thesis
presented to the University of Potsdam
in fullfillment of the
thesis requirements of the degree
Master of Science
in
Geoscience

1^{st} Supervisor
Dipl. Geol. Nina Boesche (GFZ Potsdam)
2^{nd} Supervisor
apl. Prof. Dr. Uwe Altenberger (University of Potsdam)

Potsdam, March 2015

Abstract

The spectral characteristics of Rare Earth Elements (REEs) have been poorly researched although the economic interest in these elements is increasing. This study investigates the detection of REEs using remote sensing data. For this purpose the spectral response of each individual REE has been studied with four spectrometers (*HySpex (VNIR-1600, SWIR-320m-e), ASD Field Spec 3, Perkin Elmer LAMBDA 950, FTIR Spectrum GX*) using a spectral range of 350 to 16000 nm to incorporate different techniques. The relationship between the spectral response and the REE concentration as well as the influence of other materials on the detection of REEs was examined using mixtures of calcium carbonate (the main component of REE ore rocks) and iron (III) oxide (hematite). Finally, characteristic absorption bands have been employed on an EO-1 Hyperion satellite image, covering the REE Mountain Pass mine in California and a HySpex image of a rock sample from Norway (soevite) to evaluate their potential use as REE detectors.

The results show that the REEs lanthanum, neodymium, samarium, europium, terbium, dysprosium, holmium, erbium, thulium and ytterbium cause several and differing absorption features in the visible near-infrared (VNIR) and shortwave-infrared (SWIR) region. However, in wavelength ranges between 2500 and 16000 nm no absorption bands distinctive of REEs appeared. In most cases, the concentration of REEs and the absorption depth show a logarithmic relationship for different absorption features.

The mixtures of neodymium and iron (III) oxide show that in presence of hematite the absorption features of neodymium are superimposed by those features caused by iron (III) oxide. In comparison to hematite, calcium carbonate has had no influence on the detection of neodymium in the VNIR.

The application of characteristic absorption bands on the satellite image shows that the REE signal causes only, if any, very small absorption bands in the spectrum at higher REE concentrations. In the rock sample, however, REEs related absorption bands are detectable and can be seen clearly in the spectrum with a neodymium concentration of around 0.14%.

This study shows that imaging spectroscopy serves as a helpful tool for the characterization and detection of REE concentrations in the laboratory and field environment. The detection of REEs via satellite images is limited by the low intensity of the absorption features, despite the high REEs concentration. Nevertheless, the detection of REEs by means of remote sensing is a non-invasive method that saves both money and time for sample preparation, underlining its economic value.

STR 19/08. GFZ German Research Centre for Geosciences
DOI: 10.2312/GFZ.b103-19089

Kurzfassung

Das spektrale Verhalten der Seltenen Erden (SEE) wurde, trotz des wachsenden wirtschaftlichen Interesses, bislang wenig erforscht. Diese Arbeit beschäftigt sich mit der Identifizierung von SEE mithilfe von Fernerkundungsdaten. Dazu wurde eine ausführliche spektrale Analyse der SEE, mithilfe von vier Spektrometern durchgeführt (*HySpex (VNIR-1600, SWIR-320m-e), ASD Field Spec 3, Perkin Elmer LAMBDA 950, FTIR Spectrum GX*). Diese decken einen Wellenlängenbereich von 350 bis 16000 nm ab und benutzen unterschiedliche Messtechniken zur Identifizierung spektraler Merkmale. Zusätzlich wurde die Korrelation zwischen den spektralen Merkmalen und der SEE Konzentration, sowie die Einflüsse durch andere Materialien auf die Detektion der SEE, untersucht. Dazu wurden Mischungen mit Calciumcarbonat und Eisen (III)-oxid (Hämatit) angefertigt und spektroskopisch gemessen. Für die Analyse der Detektion von SEE mithilfe von Satellitendaten wurde zusätzlich ein Satellitenbild des EO-1 Hyperion, welche die Mountain Pass Mine in Kalifornien (USA) abdeckt, und eine HySpex Aufnahme einer SEE haltigen Gesteinsprobe (Sövite) aus Norwegen hinzugezogen.

Die Ergebnisse zeigen, dass die SEE Lanthan, Neodym, Samarium, Europium, Terbium, Dysprosium, Holmium, Erbium, Thulium und Ytterbium spezifische und unterschiedliche Spektralmerkmale im Wellenlängenbereich des sichtbaren und nahem Infrarot (VNIR) und des kurzwelligen Infrarot (SWIR) aufweisen. Für den Bereich zwischen 2500 und 16000 nm wurde kein elementspezifisches Spektralmerkmal bestimmt. Die Analyse zwischen der Absorptionstiefe und der SEE Konzentration anhand der Mischungen zeigte überwiegend einen logarithmischen Zusammenhang. Anhand der angefertigten Mischungen wurde nachgewiesen, dass die Signale von Neodym im Spektrum durch den störenden Einfluss von Hämatit überlagert werden. Im Vergleich mit der Calciumcarbonatmischung zeigt sich, dass Hämatit einen deutlich größeren Einfluss auf die Detektion von Neodym besitzt. Weiterhin zeigt die Anwendung der identifizierten Spektralmerkmale in Satellitenaufnahmen, dass die Detektion von SEE begrenzt ist, aufgrund des schwachen SEE Signals. Die Gesteinsprobe aus Norwegen verursachte im aufgenommenen Spektrum mit dem HySpex deutliche Spektralmerkmale von Neodym. Die Konzentration von Neodym im Sövite betrug ca. 0.14%.

Die Arbeit zeigt, dass die Fernerkundung und die abbildende Spektroskopie ein großes Potential zur Analyse von SEE im Labor und Feld besitzen. Die spektrale Klassifizierung von SEE mittels Satellitenaufnahmen ist, trotz höherer Konzentrationen, wegen des geringen SEE Signals limitiert. Dennoch ist die spektrale Klassifizierung der SEE mittels fernerkundlicher Analyseverfahren eine schnelle und nicht invasive Methode. Sie spart Geld und Zeit und ist ohne jegliche Probenpräparation eine besonders interessante Methode für die Wirtschaft.

STR 19/08. GFZ German Research Centre for Geosciences
DOI: 10.2312/GFZ.b103-19089

List of Figures

STR 19/08. GFZ German Research Centre for Geosciences
DOI: 10.2312/GFZ.b103-19089

STR 19/08. GFZ German Research Centre for Geosciences
DOI: 10.2312/GFZ.b103-19089

STR 19/08. GFZ German Research Centre for Geosciences
DOI: 10.2312/GFZ.b103-19089

STR 19/08. GFZ German Research Centre for Geosciences
DOI: 10.2312/GFZ.b103-19089

List of Tables

STR 19/08. GFZ German Research Centre for Geosciences
DOI: 10.2312/GFZ.b103-19089

Contents

STR 19/08. GFZ German Research Centre for Geosciences
DOI: 10.2312/GFZ.b103-19089

STR 19/08. GFZ German Research Centre for Geosciences
DOI: 10.2312/GFZ.b103-19089

1 Introduction

Rare Earth Elements (REEs) are becoming increasingly important for the global industry. They are used for many applications of economic significance. The exploration of resources builds the basis for the motivation of gathering information about these elements. As a consequence, the provision of data about REE deposits needs a methodology, which provides data reliability and validity. Geologists have been using remote sensing data to collect information about an object and use reflectance spectroscopy for material characterization [42]. Technological progress and hence the worldwide availability of high resolution hyperspectral satellite and airborne digital data make it possible to acquire detailed information about an object in a very simple and effective way [42]. The method of interpreting digital images is also used by the exploration and mining industry where exploration geologists use this tool to investigate the prospect of natural resources [42].

Nevertheless, using remote sensing data to detect rare earth deposits is not a very common technique. The comparatively low concentration of REEs in the Earth's crust and the underexplored spectral characteristics of these elements render this method less than conclusive. However, the special interest in REEs by the global economy requires new and innovative techniques to find deposits of these elements. The basis for remote sensing is spectroscopy. It is necessary to understand the interaction between electromagnetic radiation and REEs in order to be able to use the spectral information of satellite images or digital data.

Rowan et al. [29] provide results of the distribution of REEs in carbonatites with spectral reflectance measurements. The spectral results for the carbonatites show absorption bands caused by REEs at wavelength positions of around 580, 740 and 800 nm and achieves that these elements are detectable using reflectance measurements [29]. The results of Rowan et al. [29] show that spectral reflectance measurements can be applied for the detection and determination of REEs in rock samples.

The spectral characteristic of REEs and their relationship to the concentration of REEs were analyzed by Dai et al. [23]. The paper presents the results of using reflectance spectroscopy to estimate the concentration of dissolved REEs in aqueous media [23]. The study of Dai et al. shows that the intensities of the diagnostic absorption bands of REEs increase with higher concentration of total REEs [23].

Turner et al. [13] investigated the spectral responses of REEs in the minerals bastnaesite, parisite and synchysite. Most of the observed spectral features could be related to neodymium, praseodymium, samarium and europium [13].

However, the spectral responses of individual REEs have not been determined. The aim of this

STR 19/08. GFZ German Research Centre for Geosciences
DOI: 10.2312/GFZ.b103-19089

study is to analyze and determine spectral characteristics of REEs and to answer the question whether spectroscopy and remote sensing, respectively, can be used as an alternative method to prospect rare earth ores. The determination of the spectral signatures of REEs is the basis for further investigations in this field. REEs naturally occur with a very low concentration (see table 2.1). Thus, the spectral responses (especially absorption depth and position) caused by different REEs concentrations must be well understood to make a reliable statement about the detection of REEs with remote sensing data.

It is also important to analyze whether the spectral absorption bands of REEs can be detected with a lower spectral and spatial resolution of a hyperspectral satellite image (compared to laboratory devices). In addition it is important to observe that information from satellite images or from field measurements contain spectral responses of not only one material. It is necessary to investigate, which characteristic absorption bands of REEs can be used for the detection of REEs and at which position a spectral overlapping with other materials occur. This study will reveal new ways for the detection of REEs deposits and improve exploration techniques. Currently, mainly geochemical and geophysical methods are common for the exploration of new deposits. These involve high costs and higher efforts because several field samples have to be collected and shipped to international laboratories for the geochemical analysis. As a result, remote sensing techniques have great potential for the detection of REEs in a simple and fast way and can be used to map large surface areas.

STR 19/08. GFZ German Research Centre for Geosciences
DOI: 10.2312/GFZ.b103-19089

2 Remote Sensing as a Tool for Mineral and Rock Characterization

2.1 Rare Earth Elements – Characteristics and Primary Deposits

2.1.1 Chemical and Physical Properties

REEs are members of the group IIIB in the periodic table and represent the 14 elements from lanthanum to lutetium, with atomic numbers of 57 to 71 [21]. REEs are subdivided into Light Rare Earth Elements (LREEs), including the elements from lanthanum to samarium with lower atomic numbers and masses, and Heavy Rare Earth Elements (HREEs), including the elements from europium to lutetium, with higher atomic numbers and masses [33]. Together, the elements from cerium to lutetium are called lanthanides [21].
The name REEs is related to the fact that they only rarely occur with high concentrations and mostly as trace elements in many minerals [33]. Moreover, the continental crust is enriched in REEs and the abundance is not as low as for gold and mercury (see Table. 2.1) [3]. The REE cerium is the most abundant element with a crustal abundance of around 63 parts per million (ppm) while thulium with around 0.30 ppm is the REE with the lowest abundance [39]. The upper crust is enriched, with about 10 to 25% REEs content [39]. In the lower crust REEs with lower atomic masses (LREE) will be more abundant than REEs with higher atomic masses (HREE) [3]. Hence, most REEs are rarely found in sufficient abundance and the concentration is not always high enough for economical extraction.
REEs are strongly electropositive and they form ionic bonds (selected chemical properties can be seen in table 2.2) [34]. The regular oxidation state in nearly all natural mineral species is 3+. Only neodymium, samarium, europium, thulium and ytterbium exist also at 2+. Cerium as well as praseodymium, terbium and dysprosium may exists at oxidation state 4+ (but only Ce 4+ occur in nature) [33, 34]. The different oxidation states depend on the temperature, pressure, composition, and redox conditions of the chemical system [3].
All REEs have the same outer-electron configuration ($5p6s^2$) and differ only in the progressive filling of the 4f sub-shell with an electron with increasing atomic number (see table 2.2) [21]. Generally, chemical interactions are only influenced by the outer shells [3]. The fact that the 4f electrons in the inner-shell remain well shielded and the outer-shell remains the same for all REEs explains the chemical similarity of REEs [21].

STR 19/08. GFZ German Research Centre for Geosciences
DOI: 10.2312/GFZ.b103-19089

Table 2.1: Crustal Abundance (upper continental crust) of the REEs, yttrium, niobium and tantalum in ppm. For comparision also the crustal abundance of gold and mercury are shown here (modified after [39]). Condie (1993): averages of surface exposures. Taylor and McLennan (1985,1995): estimates from sedimentary and loess data. Rudnick and Gao (2014): Values for Y,La-Tb,Er,Yb,Lu: Averages of all values of table 2 in [39] (excluding Wedepohl (1995) value or Taylor and McLennan (1985) value for Au). Value for Dy,Ho,Tm: Value interpolated from REE pattern. Values for Nb, Ta: Average of all surface exposure data in table 2 in [39] (minus Shaw et al. (1976) values) plus data from sediments and loess (Plank and Langmuir, 1998; Barth et al., 2000; McLennan, 2001b; Teng et al., 2004). For more details see [39].

Element (Symbol)	**Condie**	**Taylor and McLennan**	**Rudnick and Gao**
	(1993)	(1985, 1995)	(2014)
Yttrium (Y)	24	22	21
Niobium (Nb)	9.8	12	12
Lanthanum (La)	28.4	30	31
Cerium (Ce)	57.5	64	63
Praseodymium (Pr)	-	7.1	7.1
Neodymium (Nd)	25.6	26	27
Samarium (Sm)	4.59	4.5	4.7
Europium (Eu)	1.05	0.88	1.0
Gadolinium (Gd)	4.21	3.8	4.0
Terbium (Tb)	0.66	0.64	0.7
Dysprosium (Dy)	-	3.5	3.9
Holmium (Ho)	-	0.8	0.83
Erbium (Er)	-	2.3	2.3
Thulium (Th)	-	0.33	0.30
Ytterbium (Yb)	1.91	2.2	2.0
Lutetium (Lu)	0.32	0.32	0.31
Tantalum (Ta)	0.79	1.0	0.9
Gold (Au)	-	1.8	1.5
Mercury (Hg)	-	-	0.05

The progressive filling of the 4f sub-shell with electrons and the increasing atomic number is accompanied with a decreasing ionic radius [21, 3]. This is due to the fact that the electrons get closer to the nucleus and reduce the size of the 4f sub-shell, which is caused by the effective nuclear charge acting on each 4f electron [21].

The chemical similarity of REEs is responsible for the difficulties in distinguishing these elements and the reason why they can substitute each other in crystal structures [34]. The element yttrium has a strong chemical similarity to HREEs because it has the same ionic radius as dysprosium and holmium [21]. Hence, in nature yttrium occurs mostly with REEs, which is why these elements are often grouped together [21]. Scandium is also considered as a part of the REEs group but is not included in this study. Tantalum and niobium have also an almost identical ionic radius as REEs and are considered as transition elements. They often occur together with REEs in pegmatites and carbonatites (see chapter 2.1.3.2) [21, 34]. They belong with REEs to the High-Field-Strength Elements (HFSE) [24]. Selected chemical properties for yttrium, niobium and tantalum are shown also in table 2.2.

STR 19/08. GFZ German Research Centre for Geosciences
DOI: 10.2312/GFZ.b103-19089

However, the physical behavior of each REE is different and not influenced by their chemical resemblance [45]. REEs occur as metallic elements not naturally [47]. They are forming oxides when they are exposed to air, except the element promethium which does not have a stable isotope and cannot be found in nature [47]. In appearance REEs are iron-grayish to silvery metals that tarnish and are relatively soft and malleable. They have a high melting and boiling point that increases across the REE series from cerium to lutetium [8]. Most REE compounds are strongly paramagnetic and characterized by catalytic, chemical, electrical, and optical properties, which make them useful for a wide range of applications (see chapter 2.1.2) [47, 45].

STR 19/08. GFZ German Research Centre for Geosciences
DOI: 10.2312/GFZ.b103-19089

Table 2.2: Selected geochemical properties of the REEs, yttrium, niobium and tantalum;[1]:[32],[2][11].

Property	**Yttrium**	**Niobium**	**Lanthan**	**Cerium**	**Praseodymium**	**Neodymium**
Atomic number[1]	39	41	57	58	59	60
Electronic configuration[1]	$[Kr]4d^15s^2$	$[Kr]4d^35s^2$	$[Xe]5d^16s^2$	$[Xe]4f^15d^16s^1$	$[Xe]4f^36s^2$	$[Xe]4f^{13}6s^2$
Oxidation states[2]	+3	(+3)	+3	+3,+4	+3,+4	+2,+3,+4
Atomic weight[1]	88.90585(2)	92.90638(2)	138.90550(2)	140.11600(1)	140.90765(2)	144.24000(3)
Atomic radius (in the metall) [pm][2]	180	146	187	182	182	181
Ionic radius M^{3+} [pm][2]	-	-	103	101	99	98
Melting point $[C^\circ]$[1]	1530	2468	920	798	931	1021
Boiling point $[C^\circ]$[1]	3264	4758	3420	3433	3520	3074
Density $[(25C^\circ)\ g/cm^3]$[1]	4.500	8.570	6.170	6.770	6.773	7.007
Property	**Promethium**	**Samarium**	**Europium**	**Gadolinium**	**Terbium**	**Dysprosium**
Atomic number[1]	61	62	63	64	65	66
Electronic configuration[1]	$[Xe]4f^56s^2$	$[Xe]4f^66s^2$	$[Xe]4f^76s^2$	$[Xe]4f^75d^16s^2$	$[Xe]4f^96s^2$	$[Xe]4f^{10}6s^2$
Oxidation states[2]	+3	+2,+3	+2,+3	+3	+3,+4	+3,+4
Atomic weight[1]	-	150.36000(3)	151.96400(1)	157.25000(3)	158.92534(2)	162.50000(3)
Atomic radius (in the metall) [pm][2]	181	180	204	179	178	177
Ionic radius M^{3+} [pm][2]	97	96	95	94	92	91
Melting point $[C^\circ]$[1]	1042	1074	822	1313	1365	1412
Boiling point $[C^\circ]$[1]	(3000)	1794	1429	3273	3230	2567
Density $[(25C^\circ)\ g/cm^3]$[1]	-	7.520	5.234	7.900	8.229	8.550
Property	**Holmium**	**Erbium**	**Thulium**	**Ytterbium**	**Lutetium**	**Tantalum**
Atomic number[1]	67	68	69	70	71	73
Outer electron configuration[1]	$[Xe]4f^{11}6s^2$	$[Xe]4f^{12}6s^2$	$[Xe]4f^{13}6s^2$	$[Xe]4f^{14}6s^2$	$[Xe]4f^{14}5d^16s^2$	$4f^{13}6s^2$
Oxidation States[2]	+3	+3	+2,+3	+2,+3	+3	(-1,+1,+2,+3,+4),+5
Atomic weight[1]	164.93032(2)	167.26000(3)	168.93421(2)	173.04000(3)	174.96700(1)	180.94790(1)
Atomic radius (in the metall) [pm][2]	176	175	174	193	174	146
Ionic radius[2] M^{3+} [pm]	90	89	88	87	86	-
Melting point $[C^\circ]$[1]	1474	1529	1545	819	1663	2980
Boiling point $[C^\circ]$[1]	2700	2868	1950	1196	3402	5534
Density $[(25C^\circ)\ g/cm^3]$[1]	8.795	9.066	9.321	6.965	9.840	16.650

STR 19/08. GFZ German Research Centre for Geosciences
DOI: 10.2312/GFZ.b103-19089

2.1.2 Applications

Scientific research about REEs is beneficiary to the industry since REEs are used in many important applications. Most important functional uses of REEs are in the following fields: magnets, metallurgy, battery alloys, ceramics, polishing, glass, phosphors and as catalysts [47]. Magnets are a major application for samarium and neodymium [47]. Neodymium-based magnets (contain also dysprosium) have better magnetic properties than samarium-cobalt magnets and are mainly used in applications where cost is not crucial [47]. However, neodymium-based magnets have a lower temperature and corrosion susceptibility [47]. Magnetic refrigeration uses gadolinium-based solids, which heats up or cools down, depending on the presence of a strong magnetic field [47]. This principle has its greatest prospect in cryongenic applications [47].
Another major application field of REEs is metallurgy [47]. REEs are used for alloys, especially as mischmetals, which improve the physical and rolling properties of iron and steel [47]. Lanthanum and cerium are used in galvanizing zinc alloys and improve the fluidity, wettability, and eliminate intergranular corrosion [47]. Further, in combination with nickel and cobalt alloys, selected REEs can improve the durability of and the consolidation with the underlying metal [47]. In aluminum alloys, cerium is required for corrosion resistance. Other REEs, like erbium in a titanium alloy, improve the ductility of the metal [47]. Yttrium and other REEs are used for magnesium alloys, which have their functional use in aircraft engines, space rockets and satellites [47].
Another field of application includes the use of REEs in ceramics [47]. Cerium and yttrium are used to increase the density and heat resistance of the sinter [47]. Cerium eliminates weakening voids, while yttrium has high thermal-insulation properties and protects for example hot parts in jet engines [47].
Further, yttrium is also used for electronic devices to convert energy from one form to another [47]. Gadolinium and lanthanum are also used in this application field in combination with gallium and zirconium titanate [47]. An example for energy converters is phosphor, which converts electricity to luminescence and also lanthanum, which is used in window glass to switch between transparent and opaque. [47].
Another application of REEs takes place in the petroleum and auto industries [47]. Cerium, neodymium, and lutetium are used as catalysts in petroleum refining and increase the yield of gasoline [47]. Cerium and lanthanum is also used as a catalytic converter in automobiles to alter hydrocarbons, carbon monoxide and nitrous oxides in the engine exhausts to water, carbon dioxide and nitrogen [47].
The optics industry is a large application field for REEs where almost all REEs are used in glasses, lasers, fiber optics, phosphors and fluorescent lights [47]. Praseodymium is being applied for lenses and tinted-glass filters for vacuum-deposited antireflective coating and selective light absorption [47].
The colors of the television and computer screens are made by many REEs, including europium, yttrium, terbium and cerium [47]. To convert X-rays into visible light (in health care), terbium, thulium and europium are used to reduce the radiation exposure [47]. Also used in this

STR 19/08. GFZ German Research Centre for Geosciences
DOI: 10.2312/GFZ.b103-19089

application field is holmium, which is needed for glass coloring and ytterbium, which is being applied in various laser applications [47].
Tantalum and niobium also have a diverse range of applications [7]. Niobium's main use is in the production of ferro-niobium, which is needed for high-strength low-alloy steels [7]. It is also used to produce niobium alloys, niobium chemicals and other niobium metals [7]. The largest end-use of tantalum is in the production of capacitor-grade powder and in the manufacture of tantalum metal products [7]. It is applied in the metallurgical production of grade powders and is also used to manufacture tantalum chemicals [7].

2.1.3 Mineralogy and Geology

2.1.3.1 REE Minerals

All REEs are lithophile elements and occur predominantly together in geologic deposits, where they mostly concentrate in silicates, oxides, carbonates and phosphates [33, 3].
Mostly they are hosted by rock-forming minerals or, if the concentration of REEs is higher, they can form their own minerals [34].
Rare earth minerals can be classified into groups, according to the contained rare earths. The Ce-group contains predominantly lanthanides from lanthanum to europium [33]. The Y-group is composed of lanthanides from gadolinium to lutetium and yttrium [33]. Often the mineral contains REEs of both groups [3]. Around 150 to 200 minerals are defined as rare earth minerals (REE minerals), which means the essential constituents are REEs but only very few have been identified to be of economic importance [3, 8]. Major and economically significant mineral ores are bastnasite ($CeFCO_3$), monazite $(Ce, Th, Y)PO_4$ and xenotime (YPO_4) wherein more than 95% of the REEs are concentrated [47, 34]. Bastnasite is a fluorocarbonate mineral that occurs in many pegmatites, carbonatites and granites [47]. It contains 70% rare earth oxides (REOs) and primarily LREE, like cerium, lanthanum and neodymium [47, 34]. Monazite, a rare earth thorium phosphate, contains about 70% REOs, mainly LREEs [47]. It constitutes only in rarely ore-forming bodies and the most recoverable monazite is found in placers [47]. It also originates in granites and carbonatites and is often a byproduct of titanium mining where the radioactive thorium requires particular care during the beneficiation process [47]. Xenotime is an yttrium phosphate that is characterized by HREEs [47]. It contains about 67% REOs and originates in igneous and metamorphic rocks [47].

2.1.3.2 REE Deposits - Carbonatites and Pegmatites as Host Rocks for REEs

Rare earths occur in all three major rock types (sedimentary, igneous and metamorphic) and can be found in hard rock deposits or in placer sands [47]. Hard rock deposits are of primary origin and hence associated with igneous rocks and hydrothermal processes [47, 8]. Placer deposits are of secondary origin and are concentrated by sedimentary processes and weathering [3, 47]. The most important primary REE deposits are found in Mountain Pass, California/USA

STR 19/08. GFZ German Research Centre for Geosciences
DOI: 10.2312/GFZ.b103-19089

and in Bayan Obo iron ore deposit/P. R. China [8]. Both are ore carbonatite-related where high concentrations of LREEs occur in rocks with essentially fresh igneous minerals and textures [24]. The carbonate complex in the Mountain Pass is a major bastnasite operation, which is the greatest rare earth deposit (related to carbonatites) in the world at the time being [25, 45]. Bayan Obo (inner Mongolia) is the largest mining site in China and a polymetallic REE-Fe-Nb deposit [45]. The primary product at Bayan Obo is iron, REEs and Nb are only by-products [45]. Bastnasite and monazite are the main REE minerals at Bayan Obo. They comprise about 26% La_2O_3, 50% Ce_2O_3, 5% Pr_2O_3, 16% Nd_2O_2, 1% Sm_2O_3 of the extractions, the remaining REE represents less than 1% each. Since the most important REE deposits are found in alkaline igneous rocks (like carbonatites and pegmatites), this study focuses on these both deposit types.

Carbonatites are rare igneous rocks and compromise more than 50% of primary carbonate minerals (mixtures of calcite, dolomite and siderite) [24]. They originate from carbon dioxide-rich and silica-poor deep-seated magmas, which intruded the earth's crust and solidified [47]. Many of them occur as cylindrical, composite, pipe-like or as irregular lenticular bodies [24, 25]. They are the primary global source rock for a wide variety of metals and minerals, including Rare Earths (mostly LREE), niobium and tantalum [25, 18]. REEs in carbonatites are hosted in different minerals such as bastnasite and monazite [24].

During the crystallization of carbonatites REEs incorporate at low levels of rock formation into the rock-forming minerals apatite and calcite [34, 3]. Calcite is partially replaced by other minerals during later cooling and releases REEs [34]. The minerals bastnasite, parisite, synchysite, and monazite crystallize from the fluids during this stage [3, 34].

The development of REE deposits is also associated with hydrothermal solutions [47]. Hot underground water, which carries REEs, interacts with crustal material and causes a replacement mineralization within the carbonatites [47]. Since REE minerals develop in the late stages of carbonatite emplacement, it is difficult to determine whether the minerals precipitate from carbonatite magma or from hydrothermal fluids [3]. REE-bearing minerals from the Mountain Pass in California are produced by primary crystallization (bastnasite and parisite) [33]. According to Jones [3] this is the only known example for this kind of production. Moreover, Jones [3] also concludes that the redistribution by fluids after the precipitation of REE minerals through fractional crystallization of carbonatite magmas is clearly effective [3].

Pegmatites are also a hard-rock source of REEs and are formed by the crystallization of larger masses of associated plutonic rock [9]. When the magma cools, crystals form, which are enriched into HREEs while the liquid residue is enriched into LREEs and crystallizes afterwards (because of their large ionic radii) [47]. Hence, pegmatites are extremely coarse-grained igneous or metamorphic rocks that are final residual melts rich in silica, alumina, water, halogens, alkalis and lithophile elements like REEs, niobium and tantalum [25]. The pegmatites form mostly dikes or lenses and vary from a few meters to hundreds of meters in the longest dimension [25]. Pegmatite refers to granite-pegmatites, since they are genetically associated [9].

STR 19/08. GFZ German Research Centre for Geosciences
DOI: 10.2312/GFZ.b103-19089

2.2 The Origin of the Spectra of Rare Earths

The next section briefly describes the fundamental principles for the detection of REEs with the technique of remote sensing.

2.2.1 Interaction Between Electromagnetic Radiation with Matter, Atoms, Molecules, and the Atmosphere

Every time radiation strikes an object or a material, it interacts with the surface, which is fundamental to remote sensing. These interactions are absorption, transmission, emission and reflection, which depend on the target properties as well as on the radiation and thus the wavelength [40]. The relationship between these three energy interactions is shown in Formula 2.1, where E_I = incident energy, E_R = reflected energy, E_A = absorbed energy and E_T = transmitted energy as functions of the wavelength λ [44].

$$E_I(\lambda) = E_R(\lambda) + E_A(\lambda) + E_T(\lambda) \tag{2.1}$$

The reflection of energy from a surface is a function of the surface roughness and can be described in two different ways [44]. First, the object's surface is flat and has a mirror-like plane which reflects the radiation specular and the angle of reflection equals the angle of incidence [38, 40]. Second, the object's surface is rough and reflects in a multitude of directions, which is the so-called scattering or non-specular reflection [40, 44]. If the reflection acts uniformly in all directions it is called a Lambertian reflector [44]. These types of reflection are extremes and most of the rare earths has reflection characteristics somewhere in-between. The intensity of reflected electromagnetic radiation depends on the geometry manner and it is necessary to consider both the viewing and the illuminating geometry [48, 40]. Variable relief, shading and angle effects are influencing the incident radiation received by the remote sensor [40].
As described above, the reflection mechanism, which occurs on all surfaces, can be really complex because of the numerous small non-parallel plane surfaces, which result in multitudes of reflection patterns as well as diffraction [40]. The amount of energy, which is reflected by an object in different wavelengths, is called the spectral reflectance, which provides information about the spectral characteristics of an object [44].
Yet, it is not only the reflection, which scatters, the electromagnetic radiation, which is transmitted into the medium, becomes additionally scattered (volume and surface scattering, depending whether the material is inhomogeneous or homogeneous) and contributes to the total reflected signal received by the sensor [40]. The penetration depth is often related to a matter property, called complex dielectric constant [40]. If the dielectric constant of an object is lower, the radiation penetrates to greater depths [40]. With a higher dielectric constant, the penetration depth is shallower and the electromagnetic radiation will be more scattered at the surface [40].

STR 19/08. GFZ German Research Centre for Geosciences
DOI: 10.2312/GFZ.b103-19089

The electromagnetic radiation absorbed by the object is also influencing the reflection factor (Formula 2.1) and is the result of atomic-molecular processes.
The amount of absorbed electromagnetic radiation is given by the Beer-Lambert law, which describes the relationship between the absorbance and the concentration of the absorbing material, which reduces the intensity of radiation (Formula 2.2 where I = light intensity, I_0 = light of incident intensity, γ_a=absorption coefficient, z = distance) [48]. It is the basis for quantitative interpretation of remote sensing data.

$$I = I_0 \cdot e^{-\gamma_a \cdot z} \tag{2.2}$$

This law includes the optical path length, which is directly dependent on the particle size and its scattering properties. Further, it influences the degree of reflection and the intensity of the absorption bands, meaning, smaller particles create more scattering surfaces, which causes a higher reflection of the material, thus a higher intensity of the absorption bands. In this study, the spectral characteristic of rare earth powder and solid REE minerals are measured.
Atoms and molecules can absorb or emit energy from interactions with electromagnetic radiation, which transports energy in discrete packages (photons) [48]. By absorbing or emitting a photon a molecule can jump from one energy level to another [38]. Quantum-mechanics describe that atoms and molecules can only exist in specific quantum-states and hence absorb or emit the energy only in these discrete energy packages (certain amount of energy) for the transition from one energy level to another [36]. A molecule possesses energies in the following different forms: vibrational, rotational, and electronic energy [40]. Every energy type needs a different amount of energy for the transition between the levels. The energy processes correspond to different parts of the electromagnetic spectrum [40].
The electronic energy form predominantly occurs in the visible-near infrared (VNIR) part, while vibrational energy states normally take place in the thermal infrared (TIR) and short wave infrared (SWIR) regions of the spectrum (see Figure 2.1) [40]. The rotation energy state is not considered here, as this process is restricted on gas molecules and the materials of interest in this study are provided in solid form [40]. Rowan [29] assumes that REE absorption bands occur due to electronic processes. This would involve that the recorded spectra should only show absorption bands in the VNIR part and no characteristic absorption features should be caused by REEs in the thermal and short wave infrared regions of the spectrum.
Electromagnetic radiation interacts with the atmosphere on its way from the source to the reflected surface and on its way back [40]. The constituents of the atmosphere, like gases (nitrogen, oxygen, carbon dioxide and other gases), solid and liquid particulates (aerosols, water droplets, ice crystals), have effects on the electromagnetic radiation and cause wavelength dependent absorptions as well as scattering and transmission [10]. The influence of the atmospheric effects depends on the travel-distance through the atmosphere (path length) and the wavelength [10].

STR 19/08. GFZ German Research Centre for Geosciences
DOI: 10.2312/GFZ.b103-19089

The atmospheric scattering is commonly described by the Raleigh scattering, which is inversely proportional to the fourth power of the wavelength, resulting in the fact that shorter wavelengths are scattered more than longer wavelength [40]. This type of scattering is caused by atmospheric molecules and tiny particles [44]. Appropriate filters can minimize or eliminate this effect by the collection of longer wavelengths [40, 44].
Another scattering mechanism is called Mie scattering, which occurs when larger particles (atmospheric particle diameter essentially equals the wavelengths of the radiation being sensed) like water vapor and dust are present in the atmosphere [44]. Compared to Raleigh scattering Mie scattering scatters longer wavelengths more than shorter wavelengths, and takes mostly place in slightly overcast atmospheric conditions (in the lower altitudes of the atmosphere) [40].
Besides these scattering types described above, nonselective scattering occurs when the particles are much larger than the incident radiation [44]. It is not wavelength dependent and scatters all visible (VIS) and near to mid-IR wavelengths about equally (e.g. fog and clouds appear white) [44].
Atmospheric absorption is caused by water vapor, carbon dioxide and ozone (caused by vibrational and rotational transitions) [44]. They tend to absorb electromagnetic energy, which results in loss of energy [44]. Those spectral regions where the atmosphere is particularly transmissive for radiation and where absorption occurs are called "atmospheric windows" [40, 44]. Figure 2.2 shows the major atmospheric windows in relation to the energy sources [44]. For every remote sensing task the absence or presence of atmospheric windows has to be considered.

2.2.2 Spectral Signature: The Importance of the Spectral Characterization of REEs

The spectral reflectance of an object or material as a function of wavelength will be varying in different regions of the electromagnetic spectrum. The ability to measure these interactions allows the identification of any given material. Further, any object or material has its own response value for a given wavelength, which is called the spectral signature [38]. This makes it possible to classify various kinds of materials by measuring these differences as a function of wavelength and intensity.
It is important to understand the interaction of the electromagnetic radiation with the surface and the factors, which influence the spectral response. Besides of the chemical composition of the material, the scattering processes on solid material and thus the physical structure of the material also have a great influence on the spectral character [38].
Spectral information recorded by a sensor depends not only on the properties of the material, but also on many influencing factors from the surroundings and the sensor itself, e.g., the intensity and the wavelength of the radiant energy or the angle of incidence [48]. It is necessary to know the spectral signature and the behavior of the spectral response and the influencing factors of other materials present in order to be able to detect and distinguish different materials. A collection of spectra of pure materials is given by spectral libraries, which form the basis for any spectral interpretation. Developing a comprehensive spectral library containing spectra

STR 19/08. GFZ German Research Centre for Geosciences
DOI: 10.2312/GFZ.b103-19089

that take into account the recording circumstances is not only impossible but also unnecessary. Instead it is important to measure the material of interest under well-known conditions and understand its spectral behavior.

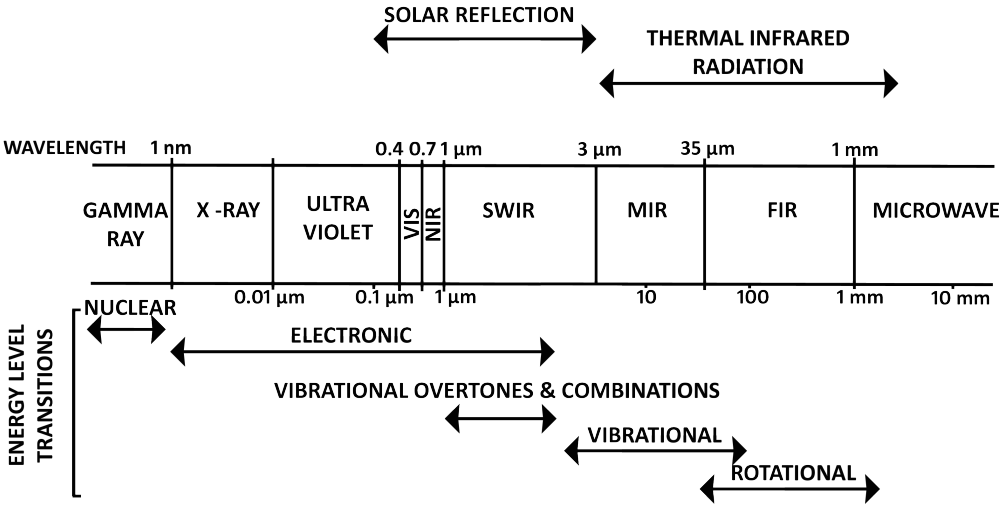

Figure 2.1: Diagram shows the different types of energy levels concerning their appearance in different regions of the electromagnetic spectrum [40].

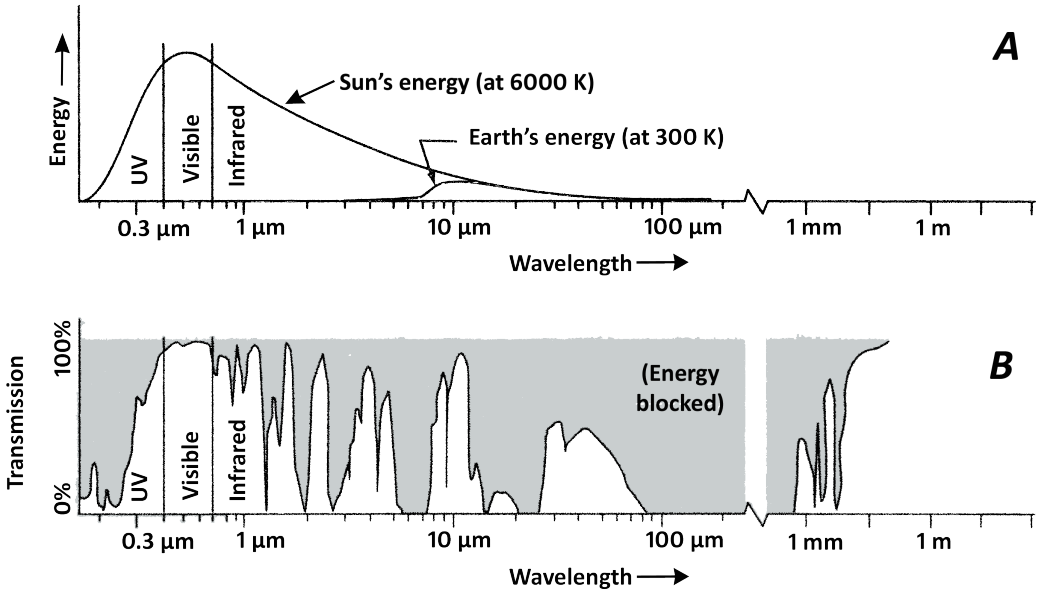

Figure 2.2: (A) Available energy for remote sensing, **(B)** atmospheric transmittance for the radiation (modified after [44]).

STR 19/08. GFZ German Research Centre for Geosciences
DOI: 10.2312/GFZ.b103-19089

2.3 Remote Sensing - Data Collection

Remote sensing uses laboratory, field, airborne and spacecraft spectrometers to provide a continuous spectral curve of an object and to identify and map materials. In this section, the spectral devices, which were provided by the *GFZ Potsdam* and satellite data are described briefly.

2.3.1 HySpex (VNIR-1600, SWIR-320m-e)

The *HySpex* is an imaging spectrometer, consisting of two hyperspectral cameras (*HySpex VNIR 1600 and HySpex SWIR 320m-e*, for technical details see table 2.3) from *NEO (Norsk Elektro Optikk AS)*. This hyperspectral imaging system generates an image where every pixel contains a continuous spectrum, forming a data cube that can be used to characterize materials and objects. Together the cameras measure a full radiance spectrum for each pixel with a spectral range of 400 to 2500 nm. The *HySpex VNIR 1600* camera provides 160 bands and measures with a spectral sampling of 3.7 nm, while the *HySpex SWIR 320m-e* camera measures with 256 Bands and a spectral sampling of 6.25 nm [4].
The device's design and the principal components are shown in Figure 2.3. The following information is taken from the *HySpex* Imaging Spectrometer User's Manual of *Norsk Elektro Optikk AS* [4].

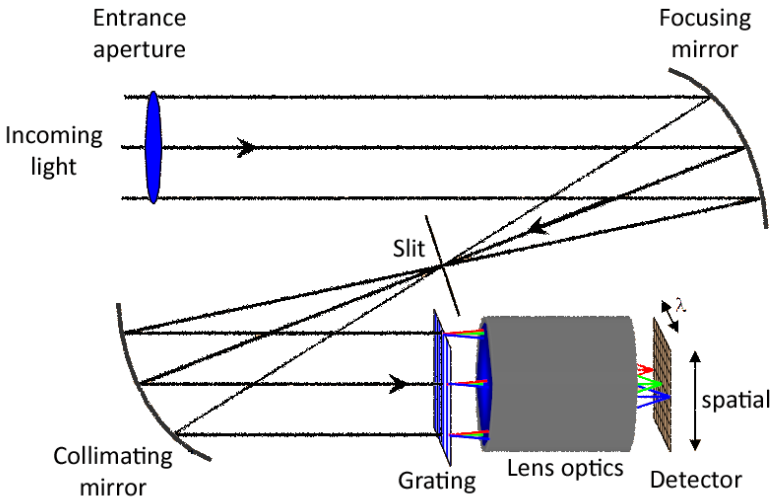

Figure 2.3: Schematic diagram of the *HySpex* (modified after [4])

Two aspherical mirrors are focusing and collimating the incoming light to reduce the stray light and avoid spherical and chromatic aberrations. A slit between these mirrors ensures that only light is passing from „a narrow line in the scene“ by defining a row [4]. A transmission grating, which is polarization independent, is used to distribute the different wavelengths of the collimated light. Before the light is focused on the detector array, the point speed function

STR 19/08. GFZ German Research Centre for Geosciences
DOI: 10.2312/GFZ.b103-19089

across the field of view and the spectral range is optimized (minimization and equalization) by a lens optic system. The detector array projects the spectral and spatial information in two directions, where every column on the array has a spectrum. As a consequence, only one line at a time is detected and a scanning part is needed to get a spatial two-dimensional image (push-broom scanning). For the push-broom scanning the sensor is arranged nadir-looking to the object plane, whereas the scan line is perpendicular. There are three different ways to scan a scene. The first scanning method is using a rotation stage, which rotates the cameras; the second one operates by cameras on a linear translation, and the third by moving the scene on a linear translation stage with a static camera system. Such a scanning method can only be achieved because the camera movement and the camera frame rate are adjusted to each other. An important aspect is the real time calibration, which allows the user to work with the resulting image immediately.

Table 2.3: Technical details of the *HySpex (VNIR-1600, SWIR-320m-e)* spectroradiometer [4].

Camera	**VNIR-1600**	**SWIR-320m-e**
Detector	Si CCD	HgCdTe
Spectral range	0.4 - 1.0 μm	1.0 - 2.5 μm
Spatial pixels	1600	320
Field of view	17°	14°
Spectral sampling interval	3.7 nm	6.25 nm
Number of bands	160	256

2.3.2 ASD Field Spec 3

The *Analytical Spectral Device (ASD) Field Spec 3* is a portable spectroradiometer that can be used for spectral measurements in the laboratory as well as in the open field. It measures the interaction between the sample or soil and the radiation of a lamp or the sun and covers the full spectral range of VNIR and SWIR (350 to 2500 nm).
All the following information of the *ASD Field Spec 3* concerning the structure and functionality are from the website of the company *Analytical Spectral Devices, Inc.* [14] and the FieldSpecPro, User's Guide [15].
The *ASD Field Spec 3* spectroradiometer consists of a portable, resistant case and a cable which protects the fibre optic bundle and collects the light. With a field of view of 25° the fibre optic can be modified with a fibre pistol (for better handling) or a contact probe which has an integrated light source and is used for contact measurements. The field of view changes with the distance to the object (see Figure 2.4 and formula 2.3 (Near Field, less than 1 meter) where D = effective diameter of foreoptic lens, A = foreoptic's angular (FOV), X = distance to viewed surface, Y = diameter of FOV).
The signal of radiation, which interacts with the material to be investigated, is transferred through the fibre optic and projected onto a holographic diffraction grating inside the instrument. The three detectors of the *ASD Field Spec 3* separate the wavelength components to convert

STR 19/08. GFZ German Research Centre for Geosciences
DOI: 10.2312/GFZ.b103-19089

the incident photons into electrons and digitize the converted voltage by a 16-bit converter. The spectral range of the VNIR (350 to 1000 nm) is detected by a silicon photodiode while the remaining spectral range of the SWIR and NIR (1000 to 1800 nm, 1800 to 2500 nm) is detected by two Indium-Gallium-Arsenide (InGaAs) photodiodes. The diode detectors transform the information of the incoming radiation into an electrical signal independent from each other (for technical details see table 2.4).
Connected to a computer, the detected spectral data is seen immediately and the user is able to control the measurements with the supplied software *RS*^{3}.

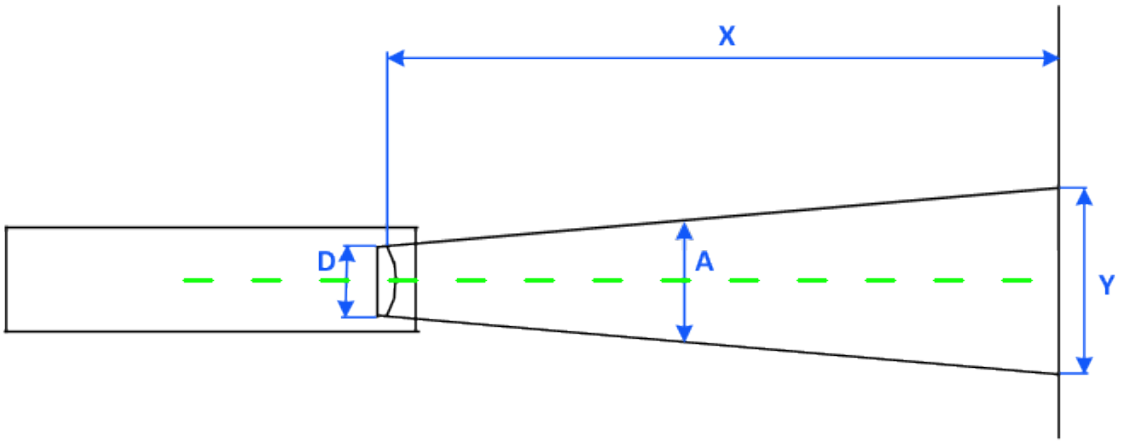

Figure 2.4: Schematic diagram shows the relationship of the FOV and the distance to the viewed surface (modified after [15]).

$$Y = D + 2 \cdot X \cdot tan(\frac{A}{2}) \tag{2.3}$$

Table 2.4: Technical details of the *ASD Field Spec 3* [14].

Parameter	Setting
Spectral range	350 - 2500 nm
Scanning time	100 ms
Bands	2151
Spectral resolution	3 nm @ 700 nm
	10 nm @ 1400/2100 nm
Sampling intervall	1.4 nm @ 350 - 1050 nm
	2 nm @ 1000- 2500 nm
Wavelength accuracy	0.5 nm

2.3.3 Perkin Elmer LAMBDA 950

The *Perkin Elmer LAMBDA 950* is an spectrophotometer which uses integrating spheres to measure reflectance or transmittance of any solid or liquid sample. The *Perkin Elmer LAMBDA 950* is able to measure a spectrum within a wavelength range of 175 - 3300 nm [17].

STR 19/08. GFZ German Research Centre for Geosciences
DOI: 10.2312/GFZ.b103-19089

The basic components of the *Perkin Elmer LAMBDA 950* and the device's design are shown in Figure 2.5. All the following information on the *Perkin Elmer LAMBDA 950* are from the *Perkin Elmer LAMBDA 950* hardware guide [17].

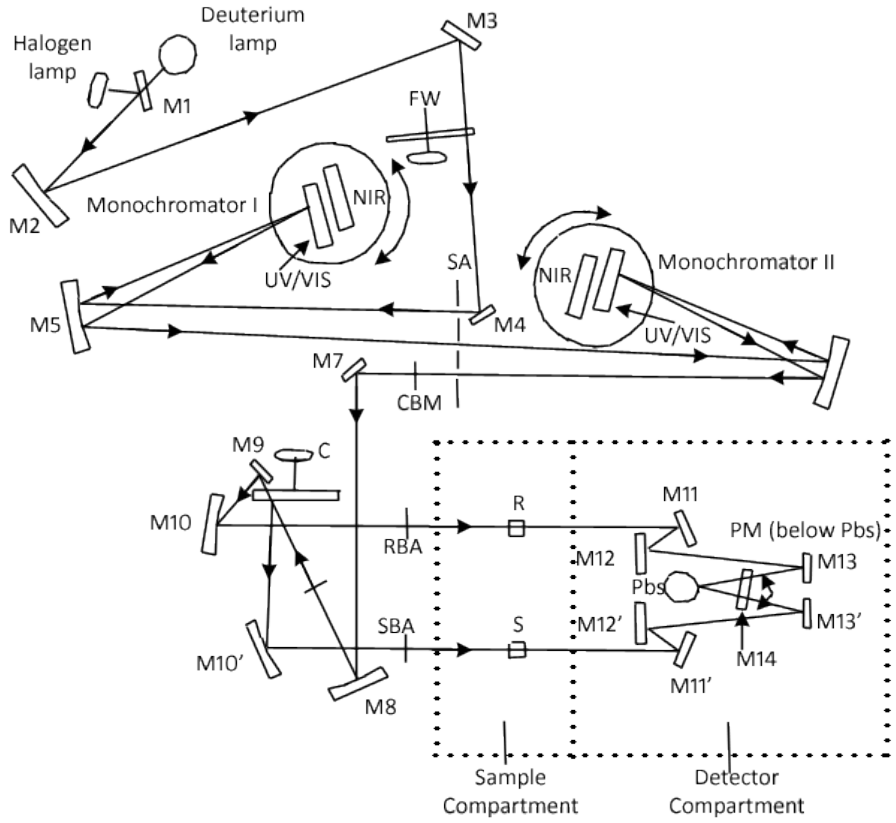

Figure 2.5: Schematic diagram of the *Perkin Elmer LAMBDA 950 Lambda 950*[17]

The radiation source within this optical system is a deuterium lamp and a halogen lamp, the deuterium lamp is used for the ultraviolet (UV) range and the halogen lamp is used for the measurements in the near infrared (NIR) and VIS spectral range. The source change occurs automatically by moving mirrors which block or strike the radiation from the source during the slewing of the monochromator. The radiation emitted from the lamps is transferred to the entrance of monochromator I via several mirrors, a slit, an optical filter and a filter wheel which prefilters the radiation. When the radiation reaches the entrance slit, it is collimated and reflected to the UV/VIS grating or the NIR grating of monochromator I which depends on the current wavelength range. The grating disperses the incident light and produces a spectrum by selecting a part of it and leading this segment over a mirror to the exit slit. The restricted spectrum segment is transferred over the mirrors to the monochromator II where the same procedure takes place.

By passing the two monochromators the radiation exhibits a high spectral purity with low stray radiation content. This radiation beam is reflected over several mirrors to a chopper assembly that has three different segments (a window segment, a mirror segment and a dark segment) which can be chosen over the rotation of the chopper. The window segment creates the

STR 19/08. GFZ German Research Centre for Geosciences
DOI: 10.2312/GFZ.b103-19089

reference beam while the mirror segment forms the sample beam. By choosing a dark segment the detector receives no signal and gets the permission to create the dark signal. Again the radiation passes several mirrors and reaches the detector by passing the sample- and detector compartment. Depending on the investigated spectral range a photomultiplier (PMT) (UV/VIS range) or a lead sulphide (PbS) (NIR range) detector is used to measure the direct and diffusive reflection (or exclusively the diffusive reflection) via an integrating sphere (spectralon-coated; for more technical details see table 2.5).

Table 2.5: Technical details of the *Perkin Elmer LAMBDA 950* [17].

Parameter	**Setting**
Wavelength range	175 - 3300 nm
Source	Tungsten-halogen and Deuterium lamp
UV/VIS resolution	$\leq$ 0.05 nm
NIR resolution	$\leq$ 0.02 nm
Wavelength accuracy	+/- 0.08 nm UV/NIR
	+/- 0.30 nm NIR
Standard deviation	$\leq$ 0.005 nm (10 measurements UV/VIS)
Standard deviation	$\leq$ 0.020 nm (10 measurements NIR)

2.3.4 FTIR Spectrum GX

The samples investigated here were also analyzed with a Fourier Transformation Infrared (FTIR) spectrometer from the company *Perkin Elmer* (model: *Spectrum GX*). It uses the technique of a Michelson-Interferometer combined with a Directional-Hemispheric-Reflection (DHR) integrating sphere from the company *Labsphere*. The basic idea of this spectrometer is to create an interferogram based on two beams which interfere with each other [6]. The spectral range is from 1 to 25 μm (10000-400 cm^{-1}).

The heart of this spectrometer is a Michelson interferometer where the basic components are a radiation source, a beamsplitter, a fixed and a moving mirror and a detector (see Figure 2.6) [27].

The radiation source is a tungston halogen lamp for the NIR (750 to 1400 nm) and a wire spool for the mid- and long-wavelength infrared (3000 to 15000 nm). The beam of radiation from the source is divided into two partial beams by the beamsplitter [6]. 50 % of the incident radiation is reflected on the fixed mirror while 50% is transmitted to the movable mirror [35]. Reflected from the mirrors, the two beams are turned back to the beamsplitter where they recombine and are brought to interfere [35]. Again, the two beams are partially reflected and partially transmitted where the part returning to the source gets lost and is rarely of interest for spectrometry [20]. Only the beam which travels perpendicular to the input beam is detected and measured by the *FTIR* spectrometer [6]. The moving mirror changes the optical path difference between the interfered beams [20]. If the two beams travel the same distance before reaching the detector, they are in phase and interfere constructively, reinforcing each other (energy maximum) [20]. On the other hand, if the two beams are out of phase they interfere

STR 19/08. GFZ German Research Centre for Geosciences
DOI: 10.2312/GFZ.b103-19089

destructively (energy minimum) [6]. The changing interference amplitude from the moving mirror reaches the sample and is reflected to the detector where it results in an interferogram [27]. This interferogram contains all the spectral information, which reaches the detector over the recorded signal as a function of the change by the optical path length [27]. The produced interferogram is transformed into a spectrum by the fourier transformation pair equation [6]. The *FTIR Spectrum GX* spectrometer of the GFZ is modified by an integration sphere which is gold-coated and has a sample compartment hole at the bottom of the sphere. The interference beam is directed through the top of the sphere directly on the sample on the bottom. The detector is placed at the side of the sphere and measures the whole diffuse reflection of the sample. For further technical details of the *FTIR Spectrum GX* spectrometer and the integration sphere see table 2.6.

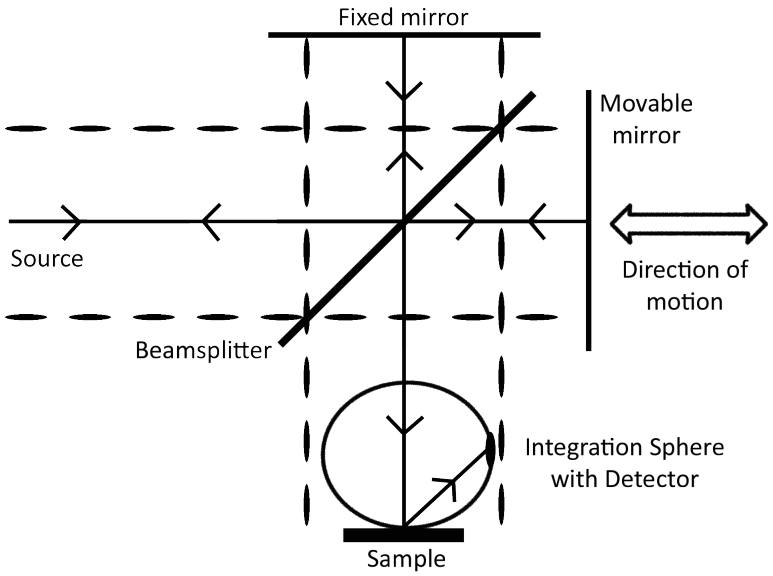

Figure 2.6: Schematic diagram of the used *FTIR Spectrum GX* spectrometer with a Michelson Interferometer and the Integration Sphere (modified after [35])

STR 19/08. GFZ German Research Centre for Geosciences
DOI: 10.2312/GFZ.b103-19089

Table 2.6: Details of the *FTIR Spectrum GX* spectrometer.

Perkin Elmer	**FTIR Spectrum GX**
Technique	Michelson interferometer with beamsplitter
Range	1-25 μm (10000-400 cm^{-1})
Method	transmission and reflection
Energy sources	NIR: Tungston Halogen lamp
	MWID and LWIR: wire spool
Resolution	2-640 nm (0.2-64 cm^{-1})
Measurement speed	0.05-5.0 cm/s
HeNeLaser	wavenumber or wavelength calibration
Integration sphere	
Diameter	10.20 cm, gold-coated
Spectral range	1-25 μm
Method	diffusive reflection
Geometry	directional-hemispheric-reflection (DHR)
Detector	MCT cooled with liquid nitrogen
Sample compartment	2.5 cm in diameter
Range	integration over 1.5 cm in diameter

2.3.5 Satellite Data from EnMAP, EO-1 Hyperion and HyMap

Remote sensing uses satellite data to extract information about an object or area. The Environmental Mapping and Analysis Program (*EnMAP*) will be the first German hyperspectral satellite mission, which will monitor Earth's environmental processes and changes, starting in the year of 2018 [16]. Using hyperspectral imaging technologies *EnMAP* will operate with a spatial resolution of 30 m x 30 m and a broad spectral range of 420 to 1000 nm (VNIR, number of bands: 89) and 900 to 2450 nm (SWIR, number of bands: 155) [16]. Besides Geological applications, *EnMAP* is also suitable to monitor land use/land cover changes, land degradation, natural hazards and mineral deposits. [16].

EO-1 Hyperion is a high resolution hyperspectral imager, which senses Earth's surface with a 30 m x 30 m resolution and covers a spectral range from 400 to 2500 nm (two spectrometers, VNIR and SWIR) with 220 spectral bands [30]. The EO-1 satellite started on November 21, 2000 and is part of NASA's New Millennium Program [30]. Major application of the sensor *Hyperion* is to gather information about the land cover/land use, mineral resources, coastal processes, and atmospheric processes [30].

The *HyMap* (Hyperspectral Mapper) sensor has been developed in Australia (by HyVista) and operates commercially around the world [43]. With up to 128 spectral bands *HyMap* covers the spectral wavelength region of 440 to 2500 nm[43]. The major application of *HyMap* is the

STR 19/08. GFZ German Research Centre for Geosciences
DOI: 10.2312/GFZ.b103-19089

geological mapping and mineral exploration as well as the monitoring of soil and vegetation changes [43].

2.4 Chemical Analysis

2.4.1 XRF-Thermo Niton XL3t

A handheld energy dispersive X-ray fluorescence (XRF) analyzer (*Thermo Scientific Niton XL3t*) identifies and analyses the amount present of the elemental composition of any material. It is a non-destructive method and based on the principle that atoms emit secondary x-ray photons when irradiated with X-rays [5]. All the following information concerning the principle function of an XRF device is from [5].
The function of a handheld-XRF and how x-ray fluorescence works is shown in Figure 2.7. Technical properties of the handheld-XRF *Thermo Scientific Niton XL3t* are listed in table 2.7. Each element has a specific wavelength and energy of X-ray emission. The atoms of a material are excited by high energy primary X-ray photons, which are emitted from an X-ray tube or radioisotope. When radiation strikes the material, electrons from the inner shell are knocked out. Subsequently, electrons from outer shells move into the vacant space and fill the inner shell. During this process, the electron emits a fluorescence radiation (secondary X-ray), which is characteristic for a particular material. The intensity of the fluorescent radiation is used to calculate the concentration of each element and is recorded by the detector in counts per seconds.

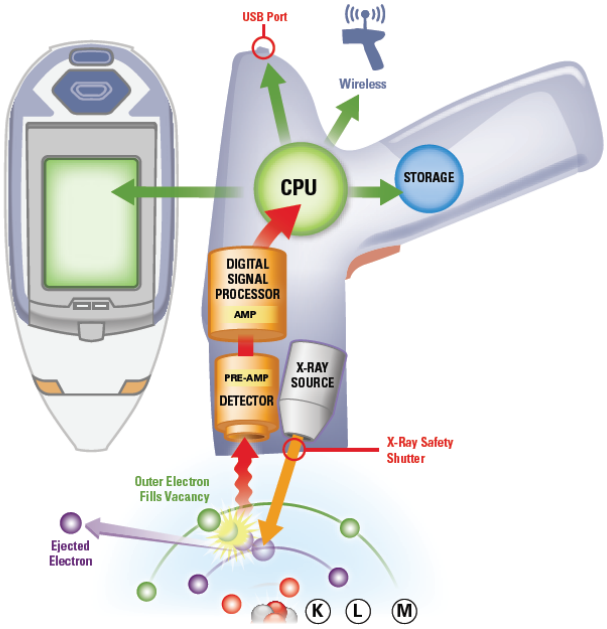

Figure 2.7: Schematic diagram of the *Thermo Scientific Niton XL3t* handheld-XRF device and the way how X-ray fluorescence works [41].

STR 19/08. GFZ German Research Centre for Geosciences
DOI: 10.2312/GFZ.b103-19089

Table 2.7: Technical details of the handheld-XRF *Thermo Scientific Niton XL3t* [2].

Parameter	**Setting**
Tube	Ag anode (6-50 kV, 0-200 μm max)
Detector	geometrically optimized large area drift detector (GOLDD)
	Propietary detector with 180,000 throughout cps
	Resolution: $<$185 eV @ 60,000 cps @ 4μ sec shaping time
Standard analytical range	Up to 30 elements from Mg to U (varies by application)
Mode (varies by application)	alloy modes: metal alloy, electronics alloy, precious metals
	Bulk Modes: soil, mining, test all^{TM}
Accessories	integrated CCD camera for locating and storing images

STR 19/08. GFZ German Research Centre for Geosciences
DOI: 10.2312/GFZ.b103-19089

3 Material and Practices

3.1 Sample Collection

For this study, 16 REO powders, 14 REE minerals and 19 self-created mixtures of the REO powders were spectroscopically examined.
The REO powders were produced by *Alfa Aesar*, a company from the *Johnson Matthey Group* that produces and supplies research chemicals for scientific purposes [1]. The *REacton* (Rare Earth Metals and Compounds) series offer a number of rare earth products with certificates of analysis [1].
The REE minerals were ordered by the mail-order trade *Gunnar Färber Minerals*, which sells REE minerals from all over the world [31].
The mixtures were made with calcium carbonate powder and iron (III) oxide powder, which were provided by *Rudolf Naumann (GFZ, Section 4.2: Inorganic and Isotope Geochemistry)*. The calcium carbonate (product number: 31208) was produced by the *Riedel-de Haen AG* (today the company is called *Honeywell Specialty Chemicals Seelze*), which supplies inorganic fine- and other specific chemicals [22]. The company *Laborchemie Apolda GmbH* provided the iron (III) oxide powder (EOR 1113 Typ N 201), it also produces special chemicals as well as pharmaceutical agents [28].
The REO powders were mixed with calcium carbonate powder of different concentration ranges to determine at which percentage REO absorption bands would be visible and how these absorption bands change with an increasing REO concentration. Up to 12 mixtures were made and weighed on a micro scale for each REO, depending on how much REO powder was available. Since REEs occur naturally at a very low concentration, the following ranges of concentrations in percent were made, focusing mainly on the lower values: 0.1%, 0.5%, 1%, 2%, 5%, 10%, 20%, 30%, 50%, 70%, 80% and 95%. Further, two basic mixtures of the REO neodymium and calcium carbonate were made (Nd 0.1% and Nd 0.5%) and mixed with iron (III) oxide also in different ranges of concentration (0.1%, 0.5%, 1%, 2%, 5% and 10%) to investigate the influence of iron(III) oxide on the detection of REE because the largest known REE resource is the iron deposit at Bayan Obo and it is a very common element in the Earth's crust. The full sample collection is seen in Table 3.1 and 3.2.The values of the certificates of analysis for the REOs and the exact values of the concentrations for every mixture are listed in the Appendix (see Table A.1 and B.1).

STR 19/08. GFZ German Research Centre for Geosciences
DOI: 10.2312/GFZ.b103-19089

Table 3.1: Sample list of the analysed REOs and the self-created mixtures.

REO, wt(g)	Formula	Manufacturer
Yttrium, 25 g	Y_2O_3	Aldrich Chemistry
Lanthanum, 100g	La_2O_3	Alfa Aesar, REacton
Cerium, 25g	CeO_2	Alfa Aesar, REacton
Neodymium, 25g	Nd_2O_3	Alfa Aesar, REacton
Samarium, 25g	Sm_2O_3	Alfa Aesar, REacton
Europium, 5g	Eu_2O_3	Alfa Aesar, REacton
Gadolinium, 10g	Gd_2O_3	Alfa Aesar, REacton
Terbium, 5g	Tb_4O_7	Alfa Aesar, REacton
Dysprosium, 10g	Dy_2O_3	Alfa Aesar, REacton
Holmium, 10g	Ho_2O_3	Alfa Aesar, REacton
Erbium, 25g	Er_2O_3	Alfa Aesar, REacton
Thulium, 2g	Tm_2O_3	Alfa Aesar, REacton
Ytterbium, 25g	Yb_2O_3	Alfa Aesar, REacton
Lutetium, 2*1g	Lu_2O_3	Alfa Aesar, REacton
Niobium, 100g	Nb_2O_5	Alfa Aesar, REacton
Tantalum, 10g	Ta_2O_3	Alfa Aesar, REacton

Mixtures (numbers)	Mixing components
Yttrium(12x)	Calciumcarbonat
Lanthanum(12x)	Calciumcarbonat
Cerium(12x)	Calciumcarbonat
Neodymium (12x)	Calciumcarbonat
Neodymium (2x6)	Calciumcarbonat, Ironoxide
Neodymium (12x)	Ironoxide
Samarium (12x)	Calciumcarbonat
Europium(12x)	Calciumcarbonat
Gadolinium(12x)	Calciumcarbonat
Terbium(11x)	Calciumcarbonat
Dysprosium(12x)	Calciumcarbonat
Holmium (12x)	Calciumcarbonat
Erbium (12x)	Calciumcarbonat
Thulium(8x)	Calciumcarbonat
Ytterbium(12x)	Calciumcarbonat
Lutetium(8x)	Calciumcarbonat
Niobium(12x)	Calciumcarbonat
Tantalum(12x)	Calciumcarbonat

STR 19/08. GFZ German Research Centre for Geosciences
DOI: 10.2312/GFZ.b103-19089

Table 3.2: Sample list of the investigated REE minerals with their formula [12] and the collection locality (mineral name and locality [31]).

Rare Earth Mineral	Formula	Mineral size	Collection Locality
Baropyrochlore, Fluorapatite	$(Ba,Sr)(Nb,Ti)_2(O,OH)_7$	0.5 x 0.2 cm	Mina Boa Vista, Catalao, Goias/Brazil
Bastnaesite (Ce)	$Ce[F\|CO_3]$	3 x 1.3 cm	Zagi Mountain, Warzal Dam,
			Pechawar, North-West Frontier Prov./Pakistan
Gadolinit (Y), Synchysite (Y), Fluorite	$Y_2Fe^{2+}Be_2O_2(SiO_4)_2$	1.1 x 0.7 cm	White Cloud Pegmatite, South Platte,
			Jefferson Co., Colorade/USA
Monazite (Sm) incl. Monazite (Nd)	$SmPO_4$,	0.2 x 0.2 cm	Svodovyi, Grubependity Lake, Maldynyrd Range,
	$(Nd,Ce,La)(P,Si)O_4$		Prepolar Ural, Komi Republic, Russia
Parisite (Nd) incl. Parisite (Ce)	$Ca(Nd,Ce,La)_2(CO_3)_3F_2$	2.6 x 1.6 cm	Mountain Pass Mine, Ivanpah Mts.,
	$Ca(Ce,La)_2(CO_3)_3F_2$		San Bernardino Co., California/USA
Polycrase (Y)	$(Y,Ca,Ce,U,Th)(Ti,Nb,Ta)_2O_6$	0.5 x 0.1 cm	Puoutevare Pegmatite, Tjalmejaure Lake,
			Jokkmokk Lappland/Northern Sweden
Synchysite (Y)	$CaY(CO_3)_2F$	1.5 x 2.5 cm	White Cloud Pegmatite, South Platte,
			Jefferson Co., Colorade/USA
Xenotime (Y) (a)	YPO_4	0.7 x 0.3 cm	Novo Horizonte, Ibitiara, Bahia/Brazil
Xenotime (Y) (b)	YPO_4	1.2 x 0.4 cm	Novo Horizonte, Ibitiara, Bahia/Brazil

REE associated Mineral	Formula	Mineral size	Collection Locality
Aegirine, "Acmite"	$NaFe^{3+}[Si_2O_6]$	4.5 x 2.5 cm	Rundemyr, Øvre Eiker, Buskerud, Norway/TYP
Fluorapatite, Albite	$Ca_5(PO_4)_3F$,	1.2 x 0.5 cm	Golconda Mine, Governador Valadares,
	$NaAlSi_3O_8$		Doce Valley, Minas Gerais/Brazil
Fluorite	CaF_2	1 x 0.7 cm	Arbegona, Shashemanne,
Ilmenite	$Fe^{2+}TiO_3$	2.5 x 1.5 cm	Mogok, Sagaing District, Mandalay/Myanmar
Zircon	$ZrSiO_4$	2 x 3 cm	Peixe alkaline complex, Monteirópolis,
			Jaú do Tocantins, Tocantis/Brazil

3.2 Spectral and Chemical Measurement

The sample collection was examined with four different spectrometers, covering various spectral ranges and recording the spectrum with different techniques (REE minerals were also analyzed with the XRF *Thermo Scientific Niton XL3t*). Thus it is possible to determine a spectral signature for every sample, independent of sensor characteristics. All used instruments, the laboratory work, and the pre- and post-processing steps needed to compare all recorded spectra are described in this section.

3.2.1 Pre-processing

HySpex (VNIR-1600, SWIR-320m-e) - Determination of Influencing Factors

It is important to recognize the influencing factors during the measurements with the *HySpex* because they can change the results of the spectral information. Relating to repeatable measurement it is also necessary to detect the influences on the resulting spectra, to ensure the frequency stability of the measurement and also to know the level of influence and, if necessary, to eliminate it by subtracting the value of influence. For this reason, test measurements were carried out where one influencing factor was changed while all the other were kept constant.

The following factors, regarding their level of influence on the results, were investigated: cellular rubber (black) as underpacking material, registration marks, reference panel, regarding to the position, to the sample and sensor, and the factor of reflectance, the light source, regarding to its angle and position to the sample, as well as the light stability and the influence of the integration time, which can be set for the VNIR and the SWIR.

To determine the influence of the black cellular rubber and the registration marks, a measurement of each material was performed to record the spectrum for the different materials.

To convert the calculated radiance data into reflectance data, a reference panel is needed where the factor of reflection is known. Panels with different factors of reflection (5%, 50% and 95%) were placed at three different positions, regarding to the position of the sample and the sensor, during the measurements.

The lamp was also placed at three positions, regarding to the sample and sensor, and the angle of the light source was also changed and the spectra of one and the same sample were recorded. Further, after the lamp was turned on, the spectrum of the sample was measured in certain time intervals to detect any influence on the spectrum.

The influence of different integration times were determined during different measurements of the same sample, with different integration times for the VNIR and SWIR.

The results of these test measurements and the resulting conclusions are described in the next paragraph.

STR 19/08. GFZ German Research Centre for Geosciences
DOI: 10.2312/GFZ.b103-19089

HySpex (VNIR-1600, SWIR-320m-e) - Results of the Measurement Concerning the Influencing Factors

Even though the cellular rubber reflects, absorbs and transmits, there are only very low absorption bands. No high influences were expected in the spectral range of 350 to 2500 nm, thus it could be used for these measurements.

Registration marks, which are necessary for the geometrical correction of the data, consist of paper and thus show a characteristic spectrum, which has an influence on the spectrum of the sample. Therefore, the sample was always placed at a higher altitude as the registration marks, minimizing the spectral influence.

Concerning the position of the panel and the resulted reflectance of the spectra no direct control factor could be identified. Nevertheless, the panel was measured prior to the sample to avoid any direct reflectance of the panel during the recording of the sample. The factor of reflectance influences the saturation, thus e.g. the choice of the reflectance panel with a factor under 95 % is important for dark materials. Because rare earth powders have a high reflectance for all measurements, a reflectance panel with a factor of 95% was used. The panel was placed on a stack of cellular rubber material to avoid the falling of any reflected light from the sample onto the panel. The influence of the panel is greater if it is placed near the sample that is the reason, why the panel was placed as far as possible from the sample.

The light source was set up next to the translation stage with an angle of vision of 45 ° to the moving direction of the translation stage, because with this angle the radiance values are the highest. The position of the lamp was at a distance to the *HySpex* to avoid overheating of the sensors. It is also important that the lamp can heat up. The test measurements showed that the resulted radiance values were constant only after two hours.

Higher integration times lead to more spectral information, because more photons can reach the detector. But if the integration time is too high, saturation is reached and if it is set too low spectral information gets lost. The test measurements indicated that for the rare earth powder the best integration time for VNIR is between 30 000 and 31 000 and for SWIR between 4000 and 5000 (SWIR is much more sensitive compared to VNIR). With these values the signal to noise ratio is minimized and no saturation is reached. To compare the resulting spectra, the integration time has also been kept constant during all measurements.

The *HySpex* laboratory has black-painted walls and doors as well as black curtains, which reduces any possible reflections; objects that could not be removed during the measurements, e.g. translation stage, computer, table ect., were assumed as constant during all measurements.

3.2.2 Laboratory Work

HySpex (VNIR-1600, SWIR-320m-e)

In the laboratory the translation stage was used to scan the samples with a static camera system (see Figure 3.1). The two *HySpex* cameras where mounted, shoulder on shoulder, on a tripod to scan the moving sample scene from above, perpendicular to the translation stage. Again, the light source was set up next to the translation stage with an angle of vision of 45°

STR 19/08. GFZ German Research Centre for Geosciences
DOI: 10.2312/GFZ.b103-19089

to the moving direction of the translation stage. The moving translation stage table is covered with cellular rubber, because this material does not have any significant absorption bands or high reflection values in a spectral range of 350 to 2500 nm. For the geometrical correction at least three registration marks where placed within the sample scene. Furthermore, to convert the radiance values into reflectance values, a reference panel was also located in the sample scene.

The two *HySpex* cameras were connected to a computer working station, where it was possible to work with the provided software *HySpex Ground* and *HySpex Rad*. The settings of the measurement are shown for the two *HySpex* cameras in Table 3.3.

First, the number of frames to record and how often one frame had to be recorded before averaging had to be specified. The correct scanning mode (translation- or rotation stage), the lenses (30 cm or 1 m) and the CCD equalization filter (on) also had to be adjusted. The filter equalizes the wavelength dependent sensitivity. It attenuates the central wavelengths, allows higher integration times and signals at the edges (without saturating the central wavelength) [4].

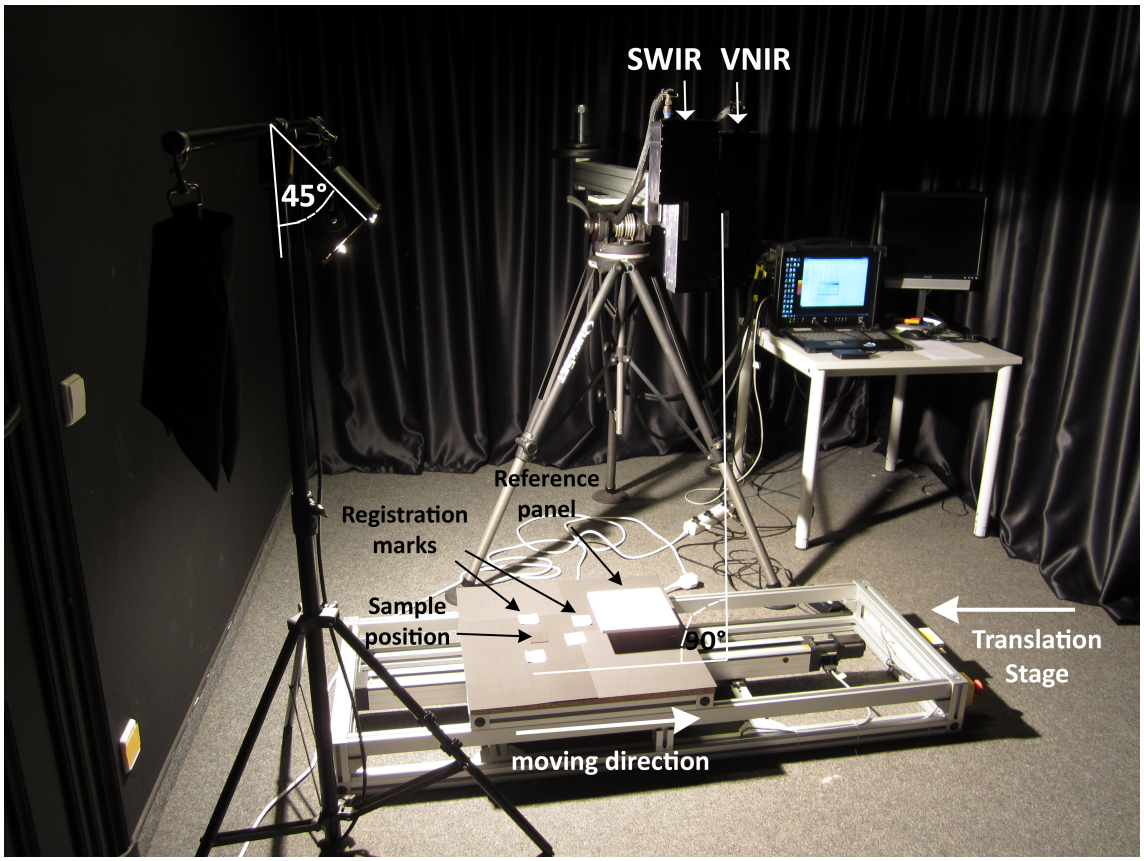

Figure 3.1: Laboratory setup for all *HySpex* measurements.

The REE powder was filled into a petri dish made of 100% quartz glass, which has not any known significant absorption bands and high reflection values in the wavelength from 350 to 2500 nm. Every sample was measured separately to avoid spectral influences from the different samples and also the petri dish was wrapped in cellular rubber to avoid transmittance spectra.

STR 19/08. GFZ German Research Centre for Geosciences
DOI: 10.2312/GFZ.b103-19089

Table 3.3: Settings used for the *HySpex*.

Parameter	**Setting**	
Lamp arrangement	45°	
Distance, sample to sensor	1 m	
FOV/Lens	1 m	
Sensor arrangement	head to head, eq on	
Lightsource	2 x 1000 W	
1.Record options:		
frames of records	variable	
Number of frames	16	
2.Scanning mode:		
Translation stage	on	
Speed multiplication	1	
3.Apperture options		
Lens	1m	
CCD eq filter	on	
4.Camera	**VNIR(1600px)**	**SWIR(320px)**
Frames:	variable	variable
Integration time [μs]:	30 000	5000
Frameperiod [μs]:	31 000	123506

Because one measurement takes up to 30 minutes (depending on the settings), the 12 mixtures of one REO were measured together. Also the mixtures were measured in plastic retainers with all sides covered by cellular rubber to avoid transmittance spectra and minimize the influences of the plastic material.

ASD Field Spec 3

The *ASD Field Spec 3* measurements were carried out in a darkened room where most of the furniture and the walls were painted black to minimize reflection. Before the real measurement started, a few adjustments had to be made and the detectors had to be optimized. The sample count for the dark current, white reference and the spectrum had to be defined, the bare fibre had to be selected to record raw digital numbers (for settings, see Table 3.4).

Following that, the optimization had to be conducted to record the dark current and the white reference. The dark current is characterized by the amount of electrical current within the detector in absence of external photons [15]. For the calculations of the reflectance values of the sample it is necessary to measure the white reference panel under the same conditions. The software considers all of these influencing factors and calculates the produced spectra within the recorded information.

The contact probe (Halogen bulb, 6.5 W, Spot size 10 mm) was used as an accessory to record

STR 19/08. GFZ German Research Centre for Geosciences
DOI: 10.2312/GFZ.b103-19089

the spectra from the REOs and the REE minerals. Although the contact probe is actually used for direct contact measurements, in this case it was necessary to avoid any contact to the rare earth powder to prevent a contamination of the contact probe, which would falsify the measurement result. To keep the distance constant, the contact probe was placed in a holder with a distance set to 3 to 4 cm between the surface of the sample and the contact probe.
To avoid the falling of incoming light from the computer display on the sample a cardboard box was used, which was covered inside with cellular rubber. The REO powder was filled into a quartz glass, which has not any known significant absorption bands and high reflection values in the wavelength from 350 to 2500 nm. Every recorded spectrum represents 200 sample counts with an integration time of 68 ms.

Table 3.4: Settings used for the *ASD Field Spec 3*.

Parameter	**Setting**
Instrument number	1643
Calibration Number	2
Calibration files	abs164032.ref
Wavelength Start	350 nm
Wavelength Step	1
Sample Count	200
File Data Typ	Refl.
Integrationtime	68 ms
Number of bits	16
Programm Version	6.00
File Version	1.00

SWIR	**Gain**	**Offset**
1	110	2073
2	184	2141

Spectra	**Minimum**	**Maximum**
x	350	2500
y	0	1.25

Perkin Elmer LAMBDA 950

To operate the *Perkin Elmer Lambda 950* the program *UV Winlab* is used to set up the method and parameters before starting the measurement (for settings, see Table 3.5). With the program it is possible to optimize the measurement by starting the alignment mode and checking whether the measuring surface is correct. If that isn't the case, is has to be corrected by adjusting the mirrors.
When starting the measurement, the system will perform a baseline correction where all samples have to be removed from the compartments. In the detector compartment two white reference panels are placed in two sample holders where the direct and diffuse reflections are measured.

STR 19/08. GFZ German Research Centre for Geosciences
DOI: 10.2312/GFZ.b103-19089

After the baseline correction the real measurement starts. Each sample has to be placed in the sample holder where the direct and diffuse reflection is measured. Since the powder cannot lay mounted in a retainer, it has to be filled into a quartz glass-cuvette which is cleaned after each measurement with ethanol.

Table 3.5: Settings used for the *Perkin Elmer LAMBDA 950* spectrometer.

Parameter	**Setting**	
Deuterium- and Tungston Lamp	on	
Lamp Change	319.2 nm	
Wavelength Range	175 to 2500 nm	
Data Interval	1 nm	
Ordinate Mode	%R	
Scan Speed	283.8 nm/min	
Number of Cycles	1	
Cyclespeed	as fast as possible	
Monochromator	860.8 nm	
CBM	100 %	fixed
CBD	on	
Attenuators	100%	100%
Slit	**Settings**	
PMT	fixed	4.0
Pbs	servo	2.0
Detector (Settings)	**Gain**	**Response**
PMT	Auto	0.2
Pbs	2.0	0.2

FTIR Spectrum GX

The detector of the integrating sphere is cooled with liquid nitrogen, thus the first preparation step for the measurements with this spectrometer is to fill the liquid nitrogen into the provided cylinder. The second step is to calibrate the device with the integrated software spectrum and to measure a reference standard to check the state of the instrument. If everything is correct, the current energy of the beam should be controlled over a reference plate to make sure the detector is cooled and ready for the measurements. Before each sample measurement the background radiation was recorded to identify and eliminate sources of error. The sample (powder or mineral) was placed in a petri dish which was wrapped in aluminum foil, knowing that the aluminum foil has not any significant absorption bands and high reflection values in the infrared spectral range. The sample was mounted from underneath the integration sphere, making it possible to measure the surface of the sample. Table 3.6 shows the settings selected for the measurements.

STR 19/08. GFZ German Research Centre for Geosciences
DOI: 10.2312/GFZ.b103-19089

Table 3.6: Settings used for the *FTIR Spectrum GX* spectrometer.

Parameter	Setting
Range	7800 - 580 cm^{-1}
Number of Scans	1064
Resolution	4.0 cm^{-1}
Interval	1.0 cm^{-1}
Units	%R
H_2O/CO_2	On

XRF-Thermo Niton XL3t

For the XRF *Thermo Scientific Niton XL3t* analysis no sample preparation was needed as the handheld XRF device can measure solid, powder and liquid samples. With a portable test stand and a lead shielded case, which is placed on top of the holder, the mineral samples were placed separately in the shielded case to measure the element composition. With the help of an integrated camera the measuring surface can be selected easily. The mining and exploration mode was used and for each measurement a balance value is given. Besides that the handheld XRF *Thermo Scientific Niton XL3t* is not calibrated for the detection of REEs (factory-adjusted), the "Balance" value indicates the number of elements that could not be detected. The result of this analysis helps to understand and interpret the resulted spectra of the minerals.

3.2.3 Post-processing

HySpex (VNIR-1600, SWIR-320m-e)

For the radiometric calibration of the images the software *HySpex Rad* was used, which enables the conversion of the data format raw.hyspex (raw DN data) to rad.img (radiometrically calibrated data). During this step, the number of photoelectrons collected by the sensor is converted to radiance values. Converted into 32-bit BSQ-files, no scaling factor is needed and also no loss of numerical precision is caused.

The radiometric calibrated *HySpex* images were converted from radiance data to reflectance data by an IDL script from *Dr. Christian Rogass (GFZ, Sektion 1.4: Remote Sensing)* in the following steps:

1. The camera produces two pictures, the script resizes the VNIR data parameters and uses resampling to produce one picture with the whole spectral information.
2. The script creates a region of interest (ROI) of the white reference panel, which were recorded for each measurement, to calculate the reflectance value by normalization of the radiance values.
3. The registration marks, which were also recorded for each measurement, were used as ground control points to arrange the two pictures exactly on top of each other and create for each pixel a spectrum with a spectral range from the VNIR to the SWIR.

STR 19/08. GFZ German Research Centre for Geosciences
DOI: 10.2312/GFZ.b103-19089

4. The script corrects the created detector jump.

The result is one *HySpex* image, which contains the whole recorded spectral information from both images as reflectance data. To extract a representative spectrum it was necessary to create a ROI for each *HySpex* image. This ROI contained mostly 500 to 800 pixel of the recorded rare earth powder and was placed as a polygon in the middle of the powder, avoiding effects of light and shadow of the plastic box. The extracted spectra were averaged to one spectrum by using the median statistic method, which neglects outlier spectra (using a provided IDL script by *Nina Boesche, GFZ, Section 1.4: Remote Sensing*).

ASD Field Spec 3

The *ASD Field Spec 3* saves the produced spectra in an .asd format, which contains only the relative reflectance data of the recorded spectra. To compare these spectra with spectra from other devices it is necessary to convert the .asd file into a .ref format. This can be done by the software *ViewSpec Pro*, which converts the relative reflectance into absolute reflectance by multiplying it with the known reflectance of the white reference panel.
Another post processing step is to correct the created detector jump. The spectra of each detector are adjusted to one another by subtracting the differences between the three levels of the spectra (using a provided IDL script by *Nina Boesche, GFZ, Section 1.4: Remote Sensing*).

Perkin Elmer LAMBDA 950

The *Perkin Elmer LAMBDA 950* saves all measured spectra in an ASCII-format, which is compatible with *ENVI* or other programs where spectra can be viewed, thus no conversion is needed.
Since the powder was measured in a quartz-cuvette, the recorded data had to be corrected by the transmittance spectrum of the quartz-cuvette. The transmittance spectrum of the quartz-cuvette had to be measured as well as every powder measured by the *Perkin Elmer LAMBDA 950* had to be divided by this transmittance spectrum.
Also, the detector jump in the spectra, had to be corrected by using the same principle as in the *ASD Field Spec 3* processing. Therefore, the existing method from the *ASD Field Spec 3* was adapted.

FTIR Spectrum GX

The produced data of the *FTIR Spectrum GX* spectrometer are given in wave number (cm^{-1}), which is typical for the IR-Spectroscopy. Hence, it had to be converted into the unit nanometer for further comparison, using the following relationship showed with the formula 3.1 (The script for this conversion was created and provided by *Dr. Karl Segl, GFZ, Section 1.4: Remote Sensing*).

STR 19/08. GFZ German Research Centre for Geosciences
DOI: 10.2312/GFZ.b103-19089

$$\tilde{\nu} = \frac{1}{\lambda[cm]} = \frac{1 * 10^7}{\lambda[nm]} \tag{3.1}$$

Besides, the recorded data was restricted to a wavelength range of 1600 – 16000 nm because of the noise of the sensor.

XRF-Thermo Niton XL3t
The result of the measurements is stored in a common table format and thus no further post-processing steps are needed.

3.3 Spectral and Chemical Analysis

The spectral results for **REO powder** from the four spectrometers (*HySpex (VNIR-1600, SWIR-320m-e), ASD Field Spec 3, Perkin Elmer LAMBDA 950, FTIR Spectrum GX*) were analyzed and compared. The most diagnostic absorption bands with their shoulders and maxima were marked for each REO. They were additionally analyzed for the minimum concentration levels at which these characteristic absorption features were detectable. Also a visual interpretation of the functional relationship with an increasing concentration of REOs was made. To accomplish this analysis the absorption depth was calculated for the different concentration of REOs for several absorption features (using a provided IDL script by *Nina Boesche, GFZ, Section 1.4: Remote Sensing*).
The spectra of the **REE minerals** from the four spectrometers (*HySpex(VNIR-1600, SWIR-320m-e), ASD Field Spec 3, Perkin Elmer LAMBDA 950, FTIR Spectrum GX*) were also analyzed and compared, based on characteristic absorption features. For this analysis the chemical results from the XRF *Thermo Scientific Niton XL3t* measurement were used to understand the spectral results and compared to the typical chemical composition.
For the determination of materials that have an influence on the detection of REEs, the neodymium mixtures with calcium carbonate and hematite were compared and also the absorptions depths of the basic mixtures 1 and 2 were visually analyzed to get more detailed information on the influence of iron (III) oxide on the detection of REEs.
In order to determine which absorption features of REEs can be used for the detection in the field, it is necessary to compare these features to the absorption bands of water, vegetation and carbonatite associated minerals.
Another approach was the spectral resampling of the results of the *Perkin Elmer LAMBDA 950* on the satellites *EnMap*, *EO-1 Hyperion* and *HyMap*. The resampled spectra were compared to the original spectra to determine the absorption features, which can still be detected with a lower spectral resolution of a satellite image.
Further, an *EO-1 Hyperion* scene covering the Mountain Pass rare earth mine in California was used to detect REE related absorption bands under satellite image conditions (e.g. atmospheric superimposition, lower SNR). For this reason, a median spectrum was extracted from the scene

STR 19/08. GFZ German Research Centre for Geosciences
DOI: 10.2312/GFZ.b103-19089

by using a ROI (using a provided IDL script by *Nina Boesche, GFZ, Sektion 1.4: Remote Sensing*). This ROI covers the middle area of the Mountain Pass mine, avoiding shadow effects. The carbonatite complex of the Mountain Pass consists mostly of LREEs [29], hence, the spectrum was compared to the spectra of lanthanum, cerium, neodymium, samarium, europium and gadolinium to determine whether any REEs can be recorded in the *EO-1 Hyperion* image. Additionally, an analysis on a field sample from the Fen carbonatite complex in Norway was conducted. The rock sample is a calcite carbonatite (soevite), which was sampled from a stone pit (N 59.165665; E 9.17643). It was measured with the *HySpex* and the XRF *Thermo Scientific Niton XL3t* to detect REE related absorption bands and the REE composition. Finally, the extracted spectrum (calculated median from a ROI, using a provided IDL script by *Nina Boesche, GFZ, Sektion 1.4: Remote Sensing*) was compared to the spectrum of the self-made mixture, which contains 0.11% neodymium and 99.89% calcium carbonate. The sampling and measurement has been conducted by Nicole Köllner (topic of her diploma thesis: *Verwitterungsprofile des Fen-Karbonatit-Komplexes (Telemark, Norwegen)*). Exact values from the inductively coupled plasma optical emission spectrometry (ICP-OES) and a description of the rock sample are discussed in the master thesis of Caroline Müller (topic of her master thesis: *Mineralogical investigations of weathering crust of the Fen-Carbonatite-Complex, South Norway*).

STR 19/08. GFZ German Research Centre for Geosciences
DOI: 10.2312/GFZ.b103-19089

4 Results

4.1 Spectral Characteristic Absorption Features of REEs and their Correlation to Concentration

Lanthanum

The REO lanthanum causes only one sharp, intense absorption band at 1419 nm in the VNIR and SWIR region (Fig. C.1). This diagnostic absorption band becomes smaller with decreasing concentration of lanthanum(Fig. C.3). Lanthanum can be detected in the spectrum with a concentration of 0.1% and higher.
Besides this diagnostic absorption band in the VNIR and SWIR region, lanthanum shows two absorption bands in the thermal infrared wavelength region at 2767 and 6675/7204 (doublet) nm (Fig. C.2). Figure C.4 shows a logarithmic correlation between the absorption depths of the feature at 1419 nm and the concentration of lanthanum. At lower concentrations of under 5% the curve increases quickly and reaches between 5% and 10% at a steady rate. At 80% the curve levels out and reaches a saturation point.

Cerium

The REO cerium causes two very low, wide absorption bands with maxima at 1435 nm and 1927 nm (Fig C.5). The shoulders can be detected at 1298 and 1679 nm for the 1435 nm feature and at 1679 and 2136 nm for the 1927 nm feature. The spectral results of the mixtures show that both features are only detectable with a concentration of cerium at around 30% and higher(Fig. C.7). Furthermore, only a low variance between the absorption depths of the different cerium contents is detectable.
The recorded spectra in the TIR region indicate three absorption bands at 2906, 6112 and 9416 nm (Fig. C.6). The shoulders for the first features appear at 2173 nm and 4189 nm. The shoulders for the 6112 feature occur at 5330 and 7627 nm. The left shoulder of the 9416 feature superimposes on the right shoulder of the 6112 nm feature, at 7627 nm. The right shoulder is detectable at 10604 nm.
The relationship between the concentration of cerium and the absorption depth of the features at 1435 and 1927 nm are shown in Figure C.8. With decreasing cerium concentration, the intensities for both absorption features decrease. The absorption depth at 1435 nm shows

STR 19/08. GFZ German Research Centre for Geosciences
DOI: 10.2312/GFZ.b103-19089

high fluctuations if the concentration of cerium is under 10%. Between 10% and 95% the trend between the absorption depth and the concentration of cerium reflects a linear correlation. However, the second feature at 1927 nm appears to have a more logarithmic correlation between the concentration in cerium and the absorption depth. The rate of change in absorption depth is clearly low, until cerium reaches a concentration of 30%. However, between a concentration of 30% and 70% cerium, the absorption depths show a higher increase as with a concentration of under 30% cerium. Finally, the data show a flat section and indicate a saturation point when the concentration of cerium is around 70%.

Neodymium

The REO neodymium has several absorption features between 400 and 1000 nm (Fig. C.9). In the spectrum from the *ASD Field Spec 3* and the *Perkin Elmer LAMBDA 950* the main absorption bands appear with local minima at 438, 470/484 (doublet), 521/537 (doublet), 600, 694, 751, 823 and 895 nm. Besides these features, in the 1000 to 1851 wavelength region two absorption features with maxima at 1421 and 1606 nm occur. The difference compared to other REEs is that neodymium shows a shift of maxima wavelength position in the spectrum of the *HySpex*. Here, the main absorption bands appear at 429/436 (doublet), 469/476 (doublet), 516/523 (doublet), 578, 683, 745, 800/807 (doublet) and 869 nm. The absorption features between 1000 and 1851 nm occur in the spectrum of the *HySpex* at the same wavelength position as in the spectrum of the *ASD Field Spec 3* and the *Perkin Elmer LAMBDA 950*. In the next sections the absorption feature position of both spectra (from *HySpex* and from *ASD Field Spec 3*/*Perkin Elmer LAMBDA 950*) were used for the detection of neodymium.
Both features can only be seen clearly above a REO content of 1 to 2% (Fig. C.11). The spectrum with a REO content of 0.1% shows absorption at 523, 538, 578, 600, 751, 800, 807, 823 and 869 nm, which become more pronounced and sharper with an increase in the concentration of neodymium.
In the thermal infrared wavelength region the most intense absorption features are between 1851 and 4061 nm and 5470 and 8285 nm (Fig. C.10). The maximum absorption appears at 2772 and 6635/7183 nm. Furthermore, between 4384 and 5470 nm two maxima occur at 4819 and 5197 nm.
Figure C.12 shows the correlation between the absorption depth and the concentration of neodymium. All curves indicate a steep increase in the absorption depth if the concentration of neodymium is under 10%. Between concentrations of 10 to 50% the increase of absorption depth is less pronounced especially in comparison with a neodymium concentration of under 10%. When the concentration reaches 50% the absorption depth decreases slightly with increasing neodymium concentration.

STR 19/08. GFZ German Research Centre for Geosciences
DOI: 10.2312/GFZ.b103-19089

Samarium

In the VNIR and SWIR regions samarium shows several sharp absorption features with maxima at 367/381 (doublet), 410, 446, 469/482 (doublet), 533, 568, 954, 1091, 1251, 1402 and 1567 (Fig. C.13). One wide absorption feature at 1966 is detectable. All shoulders of these characteristic bands are marked (dashed line) in Figure C.13.
These absorption features of samarium are detectable by all used spectrometers. Furthermore, the mixtures show a deepening of diagnostic absorption bands with increasing samarium concentration (Fig. C.15). These spectral reflectance features can already be detected if the concentration of samarium is about 0.5% while a concentration of 0.1 % does not cause any characteristic, REO samarium related absorption features.
The *FTIR Spectrum GX* spectrometer detected three wide features in the TIR region, showing smaller and more pronounced absorptions with mostly more than one main absorption (Fig. C.14). The maxima are located at 2770 nm, 6697/7194 (doublet) nm as well as at 8818/9337 (doublet) nm. The shoulders of these features are marked (dashed line) in Figure C.14.
The relationship between the absorption depth of the absorption bands at 480, 1091, 1567 and 1969 nm are shown in Figure C.16. At this point a logarithmic trend line of the curves is clearly detectable. At lower concentrations (less than 5%) the absorption depths increases rapidly. Furthermore, at concentrations of 80% the curves level out. These results indicate a saturation point where the absorption depth increases only slowly with increasing concentrations of samarium.

Europium

Europium causes several sharp and wide absorption features in the VNIR and SWIR regions with maxima at 395, 467, 535, 581/593 (doublet), 1425, 1787, 1842, 1999, 2081 and 2184 nm (see Fig. C.17). All spectrometers detected these features of europium, which are marked with their maximum peaks (solid line) and shoulders (dashed line) in Figure C.17. The results of the mixtures with lower concentrations of europium show that the diagnostic absorption features become smaller and only the characteristic absorption features at 395, 467, 535, 1842, 1999 and 2184 nm can be clearly detected at a total concentration of europium around 1% and higher (see Fig. C.19). Less than 1% causes no significant or detectable absorption bands.
In the TIR region europium causes several diagnostic absorption features between 2279 and 9569 nm (see Fig. C.18). Between 2279 and 8326 nm two main intense absorption features with a maximum at 2924 nm and 6622/7168 (doublet) nm are detected by the *FTIR Spectrum GX* spectrometer. In addition, two wide absorption bands can be detected at a wavelength of 8764 and 9337 nm. The shoulders for these absorptions are marked (dashed line) in Figure C.18.
At lower concentrations (under 2%) the rise in absorption depth is steeper than at higher concentrations between 2 and 70% (see Fig. C.20), at concentrations of 70% europium a saturation point is reached where the absorption depth rises only slightly with an increasing

STR 19/08. GFZ German Research Centre for Geosciences
DOI: 10.2312/GFZ.b103-19089

concentration of europium. Altogether, the relationship between the concentrations of the REO europium and the absorption depth is not clearly a logarithmic correlation; it appears to be rather linear.

Gadolinium

The VNIR/SWIR wavelength region shows two very low and wide absorption bands, one between 1360 and 1863 nm and one between 1863 and 2137 nm (see Fig. C.21). The maximum absorption appears at 1423 nm for the first range and at 1944 nm for the second range. Both main absorptions become wider with an increase in the concentration of gadolinium, but they become deeper at concentration values of 30% and higher (see Fig. C.23).
In addition, the thermal infrared spectrum shows two wide features between 2475 and 8183 nm. The first feature (with shoulders at 2475 and 4512 nm) reaches a maximum at 2903 nm. The second feature indicates two absorption bands, which appear at 6675 and 7204 nm. All shoulders (dashed line) and maxima (solid line) of these features are marked in Figure C.22.
Figure C.24 shows the result of the correlation between the concentration of gadolinium and the absorption depth. The two features at 1423 and 1944 nm indicate no clear trend with fluctuations at lower concentrations of gadolinium (0.1 to 30%). With a concentration of 30% gadolinium the absorption bands become diagnostic and the curve shows a clear increase of the absorption depth with increasing concentrations of gadolinium.

Terbium

Terbium is characterized by two absorption features at 1806 and 2212 nm in the VNIR and SWIR region (see Fig. C.25). The shoulders of the feature at 1806 nm appear at 1625 and 2081 nm and can be detected by all used spectrometers. The second absorption feature at 2212 with shoulders at 2081 and 2452 nm is also detected by all instruments. Furthermore, terbium causes a lower reflection in the VNIR wavelength region. In the results of the mixtures this energy loss increases with an increase in the concentration of terbium (see Fig. C.27). With a terbium content of 5 % the two main absorption features at 1806 and 1625 nm are detectable. The *FTIR Spectrum GX* spectrum also shows two features, one with a maximum peak at 2926 nm and shoulders at 2452 and 5293 nm, and one that indicates a doublet band with maximum peaks at 6591 and 7153 nm and two shoulders at 5293 and 8051 nm (see Fig. C.26).
Figure C.28 shows the correlation between the concentration of terbium and the absorption depth. Once again, a logarithmic trend line of the curves is clearly detectable. The increase at lower concentrations between 0.1 and 10% terbium is higher than at concentrations between 10 and 70% terbium. At around 70% the curve levels out and the absorption depth decreases with an increasing of concentration.

STR 19/08. GFZ German Research Centre for Geosciences
DOI: 10.2312/GFZ.b103-19089

Dysprosium

Dysprosium causes several absorption bands in the VNIR and SWIR region (see Fig. C.29). The most intense absorption band is centered near 1261 nm. Weaker absorptions appear in the spectra at 385, 424 and 454 nm. In addition, more characteristic absorption bands are shown at wavelengths of 744, 800 and 887 nm as well as between 1465 and 2127 nm at 1681 nm. The most intense absorption band (1261 nm) can already be seen with a REO content of 0.1% and higher (see Fig. C.31). With a dysprosium concentration of 0.5% the absorption feature near 800, 887 1066 nm, and the several absorption bands between 1465 and 2127 nm can be seen clearly in the spectrum. Further, with the increase in the concentration of dysprosium, these diagnostic bands become more pronounced and sharper.
Diagnostic absorption features in the thermal infrared spectrum appear between 2127 and 3889 nm with a maximum peak at 2849 nm and between 5330 and 8143 nm with maximum peaks at 6662 and 7204 nm (doublet) (see Fig. C.30).
Figure C.32 shows the correlation between the concentration of dysprosium and the absorption depth for the four features at 454, 800, 1261, and 1681 nm. Concentrations between 0.1 and 2% cause a quick increase in the absorption depth. With a further increase in the concentration of dysprosium the absorption depth rises linear until the concentration of dysprosium reaches 70%. After this point, saturation is reached and the increase of the absorption depth with an increase in the concentration is smaller as with concentrations at under 70%.

Holmium

The reflectance spectra for the REO holmium show several intense, sharp absorptions both in the VNIR and in the SWIR region (see Fig. C.33). In the 350 to 1000 nm wavelength region the most intense absorption appears at 449 nm. Two absorptions appear centered near 387, 420 nm and 538 and 647 nm. Two more absorptions, but smaller and wider, occur near 756 and 886 nm. In the 1000 to 2500 nm region holmium causes two absorption features with maxima near 1135 and 1933 nm. Shoulders for all absorption features are marked in Fig. C.33. With a REO content of 0.1 % and higher the absorption bands at 449, 463, 538, 647, and 1933 nm can be detected (see Fig. C.35). All other intense features are observed in the spectrum with an REO content of 0.5 % and higher. Additionally, with the increase in the REO holmium all absorption bands become more pronounced.
In the spectrum for the TIR region two wide absorptions appear close to 2935 and 6635/7137 nm (see Fig. C.34). The shoulders for these absorptions are detected at 2193 and 4340 nm for the feature at 2935 nm and at 5714 and 7930 nm for the doublet feature at 6635/7137 nm.
The absorption depth of the diagnostic absorption features at 449, 647, 1135, and 1933 nm were calculated for different concentrations. The results are shown in Figure C.36. All four curves indicate a steep increase between concentration of 0.1 and 2%. Reaching a concentration of 2%, the curve decreases and reaches a steady rate of at 20%. Altogether, the four curves clearly describe a logarithmic correlation between the absorption depth and the concentration.

STR 19/08. GFZ German Research Centre for Geosciences
DOI: 10.2312/GFZ.b103-19089

Erbium

The spectra of the REO erbium show several diagnostic absorption features between 350 and 1088 nm, which are intense and sharp (see Fig. C.37). Most intense absorption bands appear at 380, 523, 654, 800, and 976 nm. Further, the 1000 to 2138 nm wavelength region shows two main absorption features. One appears as a wide but also intense feature with shoulders near 1172 and 1718 nm and two maximum peaks at 1475 and 1535 nm. The second feature is a very low and wide absorption band between 1718 and 2138 nm with a maximum at 1946 nm. Further absorptions appear at 409, 454, and 491 nm. All absorption features with maxima (solid line) and shoulders (dashed line) are marked in Figure C.37.
In the spectra of the mixtures absorption bands at the wavelength 380, 491, 523, 654, 800, 976, and 1535 nm are shown clearly with an REO content between 0.1 and 0.5% (see Fig. C.39). All absorption features become diagnostic and sharper with the increase in the concentration of erbium.
Characteristic absorption bands within the TIR region appear with a maximum near 2914 and 6620/7158 (doublet) nm (see Fig. C.38). The shoulders for these absorptions are detected near 2160, 4452, 5720 and 7874 nm, respectively.
The depths of the absorption features at 523, 800, 1535 and 1946 nm at different concentrations of the REO erbium are calculated and shown in Figure C.40. At concentrations between 0.1 and 2 % the absorption depth increases quickly and then reaches a steady rate with a smaller slope as in the beginning.

Thulium

Thulium causes several sharp and intense absorption bands for the VNIR and SWIR region (see Fig. C.41). In the 350 to 900 nm region the spectra show four absorption features centered near 360, 465/476 (doublet), 685, and 796 nm. In the 900 to 2500 region the sensor observes two intense and very wide absorptions with maxima near 1204 and 1633 nm. The maxima (solid line) and shoulders (dashed line) of these absorption features are marked in Figure C.41. The absorptions at 465, 685, 796, 1204, and 1633 can clearly be detected with a REO content of 0.1% and higher (see Fig. C.43). Furthermore, all absorption bands become more pronounced and sharper with an increase of the REO content.
The spectrum of the TIR region shows two absorption features between 2137 and 7949 nm (see Fig. C.42). The maximum absorption is detected for the first feature at 2918 nm and for the second feature at 6570/7102 (doublet) nm. The shoulders (dashed line) for these absorptions are marked in Figure C.42.
Figure C.44 shows the correlation between the concentration of thulium and the absorption depth. Between 0.1% and 2% the absorption depth increases quickly with an increase in the concentration of thulium. When a concentration of 2% is reached, the absorption depth increases with a steady rate until a concentration of 30%.

STR 19/08. GFZ German Research Centre for Geosciences
DOI: 10.2312/GFZ.b103-19089

Ytterbium

Ytterbium causes three absorption features in the VNIR and SWIR region (see Fig. C.45). The first absorption band is very intense and sharp with three maximum peaks around 903, 947, and 976 nm. A second and third feature appears with an absorption maximum around 1415 and 1932 nm, which is very wide and less intense compared to the feature between 770 and 1128 nm.
The spectrum with an REO content of 0.1% can only be observed at the absorption band around 976 nm (see Fig. C.47). The other absorption bands can be detected with a REO content of 0.5% and higher. With an increase in the REO content the feature at 976 nm becomes diagnostic. The smaller absorptions around 1415 and 1932 nm are only visible with an ytterbium content of 5 to 10% and higher. These features become more pronounced with an increase in the concentration of the REO ytterbium.
The spectrum of the TIR region shows two major absorptions between 2158 and 8019 nm (see Fig. C.46). The maximum peaks appear at 2916 nm for the first absorption band and at 6600/7132 (doublet) nm for the second.
The correlation between the concentration of ytterbium and the absorption depth for the features at 947 and 1951 nm are shown in Figure C.48. The curve for the 947 nm feature indicates a quick increase of absorption depth between concentrations of 0.1 and 5% ytterbium. Between the concentration of 5 and 95% the absorption depth increases steadily with an increasing concentration of ytterbium, showing a logarithmic trend. The curve for the feature at 1951 nm indicates a linear trend with a very low rate of increase.

Lutetium

Figure C.49 shows the reflectance spectra for the REO lutetium. Lutetium causes two wide, but shallow absorption bands, centered near 1413 and 1927 nm. The shoulders appear for the first feature at 1201 and 1560 nm and for the second feature at 1560 and 2138 nm. Both absorptions are detectable with an REO content of around 5 to 10% or higher (see Fig. C.51). For REO content less than 5 to 10 % no absorptions are detectable. With an increasing concentration of lutetium these two absorption bands become more pronounced.
In the thermal infrared spectrum two major absorptions are observed between 2137 and 7968 nm (see Fig. C.50). The maxima for these features appear at 2900 and 6570/7147 (doublet) nm, respectively. The shoulders (dashed line) and maxima (solid line) are marked in Figure C.50.
The correlation between the concentration of lutetium and the absorption depth show very high fluctuations for the feature at 1413 nm. Mostly a linear correlation for both features (1413 and 1927 nm) are shown by the curves (see Fig. C.52).

STR 19/08. GFZ German Research Centre for Geosciences
DOI: 10.2312/GFZ.b103-19089

Yttrium

Yttrium has two absorption features in the VNIR and SWIR region (see Fig. C.53). The first feature has a maximum at 1423 nm with shoulders at 1249 and 1719 nm. The second feature has its maximum peak at 1938 nm and shoulders at 1719 and 2137 nm. These features appear in the spectra of the mixtures when the concentration of yttrium reaches around 50% (Fig. C.55). With an increase in the concentration of yttrium these absorption features become more pronounced.
The results of the *FTIR Spectrum GX* spectrometer also indicates two absorption features, one with a maximum at 2926 nm, a second with as a doublet at 6591/7153 nm (see Fig. C.54). The shoulders of the 2926 nm feature are observed at 2173 and 5330 nm, for the doublet feature at 5676 and 8019 nm.
The calculated absorption depths for the features at 1423 nm show a linear correlation with the concentration of yttrium (see Fig. C.56). The data for the feature at 1938 nm show a high fluctuation, while the data for the feature at 1423 increase only slightly with an increasing concentration of yttrium.

Niobium

The spectrum of niobium in the VNIR and SWIR is characterized by two very small, wide absorptions between 1715 to 2143 nm and 2143 to 2375 nm. (see Fig. C.57). The maxima of these absorption bands are at 1924 and 2243 nm. The visual analysis of the results from the mixture leads to no significant change in the absorption depth with an increase of the concentration (see Fig. C.59).
The thermal infrared spectrum for niobium shows two absorption features (see Fig. C.58). The first is located at 2910 nm, shoulders at 2313 and 4103 nm. The second absorption shows very wide features between 4482 and 6313 nm with two main peaks at 5216 and 6142 nm.
The visual analysis of the mixture shows no trend of the absorption depth with the concentration, while the calculation for the correlation of the spectral responses and the concentration of niobium show a linear trend (see Fig. C.60). At lower concentrations, between 0.1 and 5%, there are fluctuations in the data, but with an increase of the concentration of Niobium the absorption depth increases as well, even if very subtly.

Tantalum

The spectra for tantalum show two small, wide absorption features in the VNIR and SWIR region (see Fig. C.61). The maximum absorptions appear near 1447 and 1927 nm. The shoulders for the feature at 1447 can be detected at 1276 and 1702 nm, while the shoulders for the feature at 1927 are located at 1843 and 2341 nm. These absorption bands become smaller with a decrease in the REO content (see Fig. C.63). With a concentration of around 20% both

STR 19/08. GFZ German Research Centre for Geosciences
DOI: 10.2312/GFZ.b103-19089

absorptions can be detected in the spectrum.
In the TIR region tantalum causes two absorption features between 2300 and 7429 nm (see Fig. C.62). The first is centered with the maximum near 3085 nm. The maximum absorption for the second feature appears near 6097/6988 (doublet) nm.
The analysis for the correlation between the concentration of the REO tantalum and the absorption depths at 1447 and 1927 nm are shown in Figure C.64. Both features show a similar trend: With a decrease of concentration of tantalum the depths of the two absorption features decrease. A linear correlation between the depth and the concentration is indicated by the analysis.

STR 19/08. GFZ German Research Centre for Geosciences
DOI: 10.2312/GFZ.b103-19089

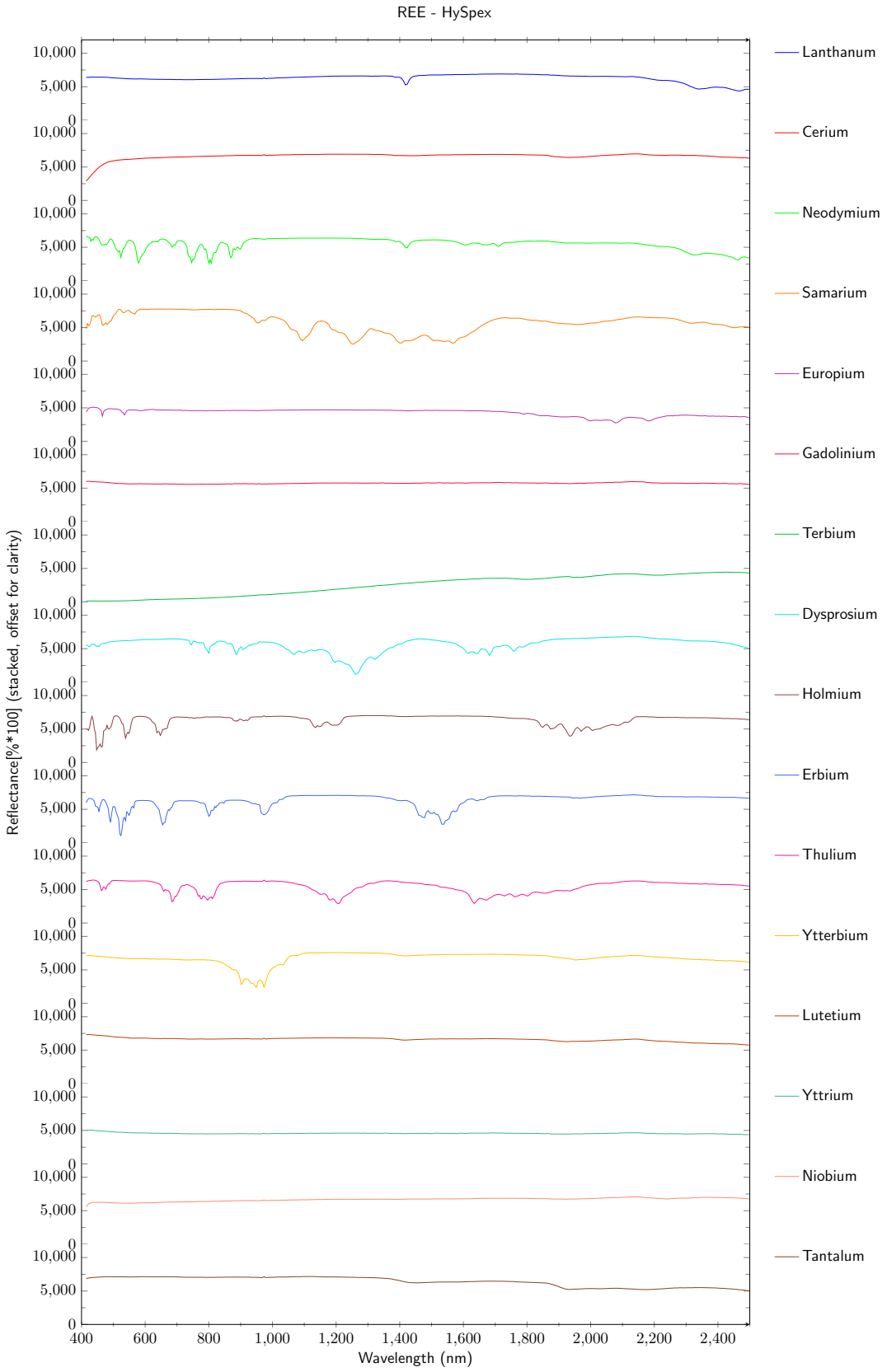

Figure 4.1: Reflectance spectra for all REO for the VNIR, SWIR region. Results are from the measurements with the *HySpex (VNIR-1600, SWIR-320m-e)*.

STR 19/08. GFZ German Research Centre for Geosciences
DOI: 10.2312/GFZ.b103-19089

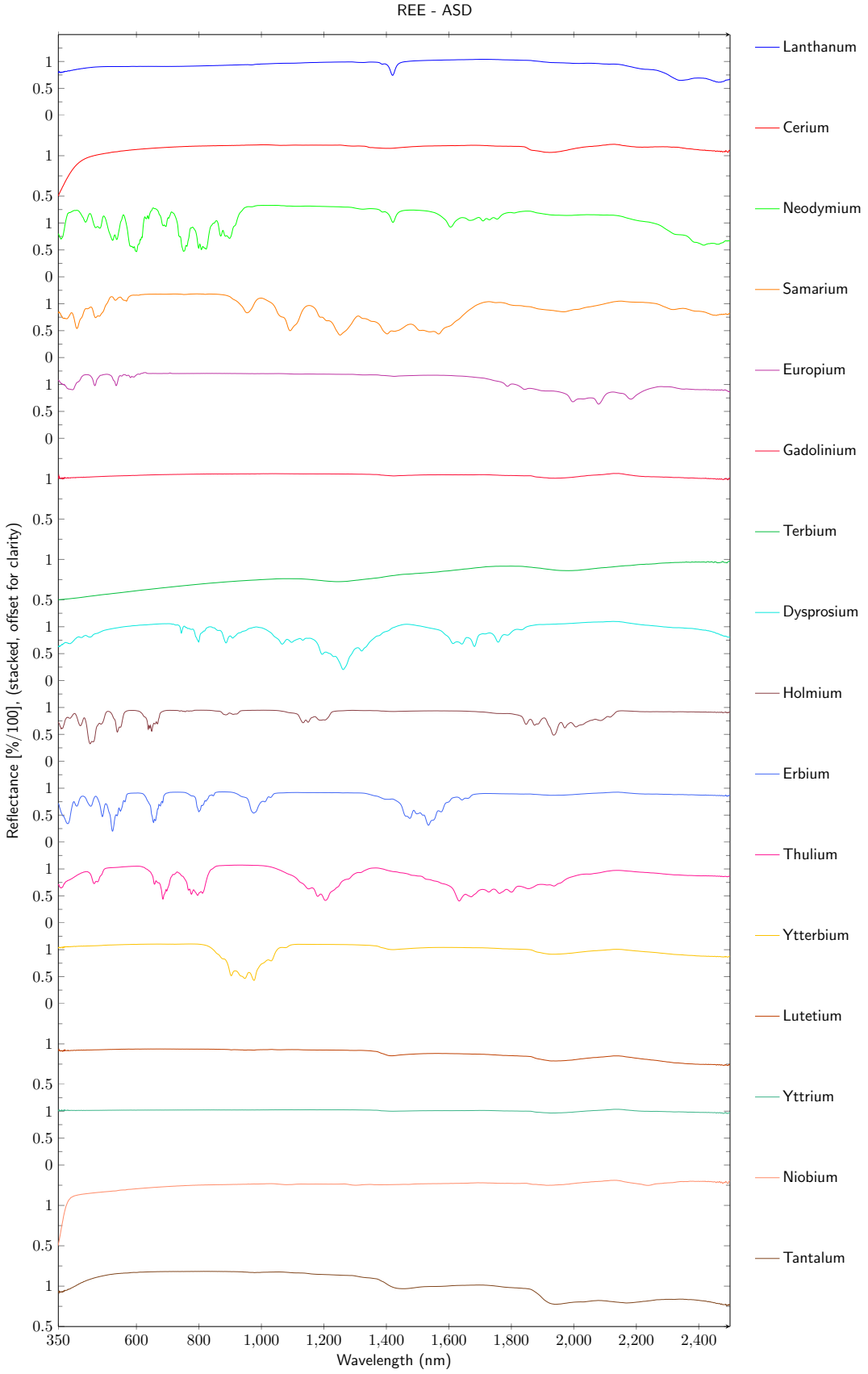

Figure 4.2: Reflectance spectra for all the REO for the VNIR, SWIR region. Results are from the measurements with the *ASD Field Spec 3*.

STR 19/08. GFZ German Research Centre for Geosciences
DOI: 10.2312/GFZ.b103-19089

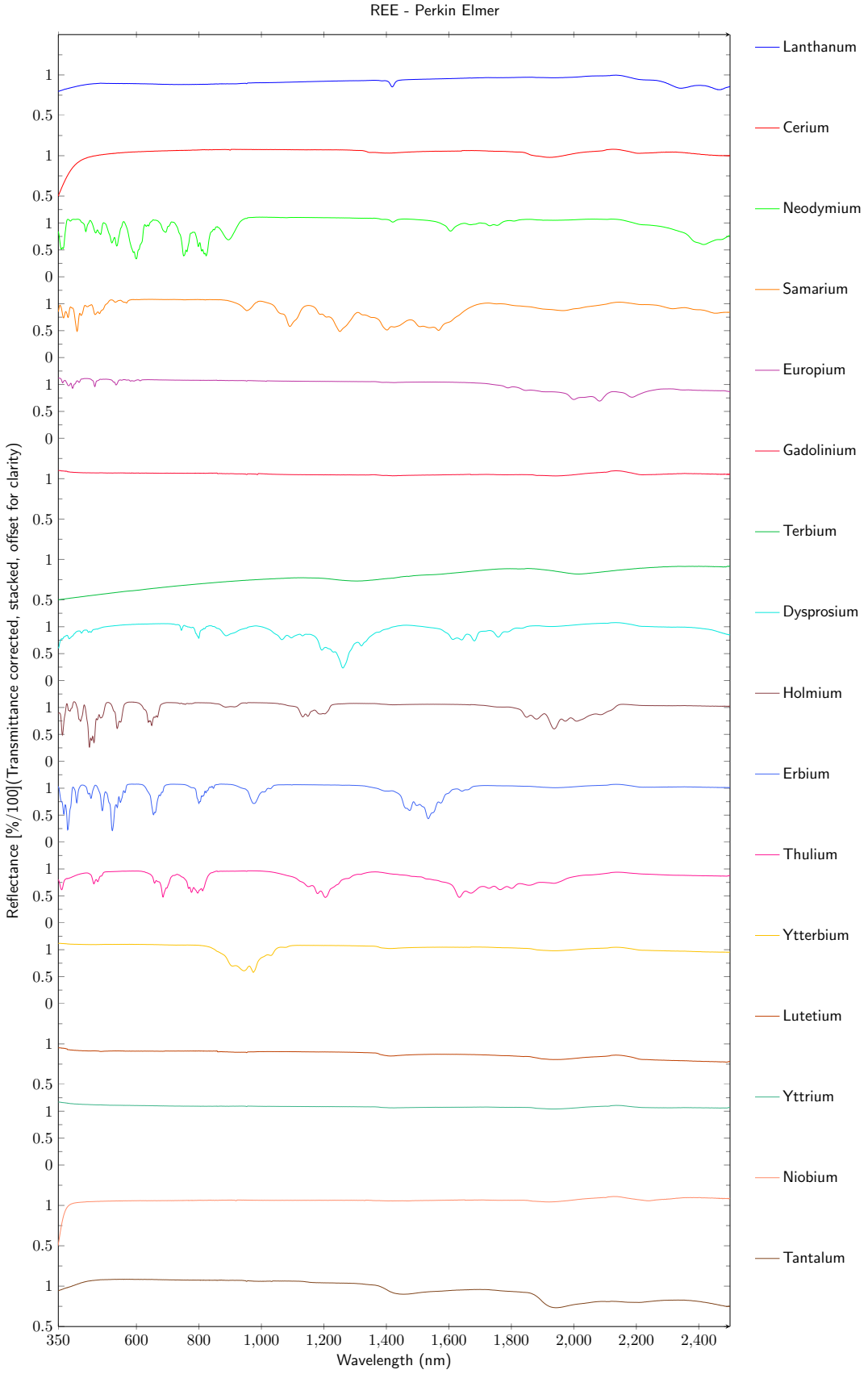

Figure 4.3: Reflectance spectra for all the REO for the VNIR, SWIR region. Results are from the measurements with the *Perkin Elmer LAMBDA 950*.

STR 19/08. GFZ German Research Centre for Geosciences
DOI: 10.2312/GFZ.b103-19089

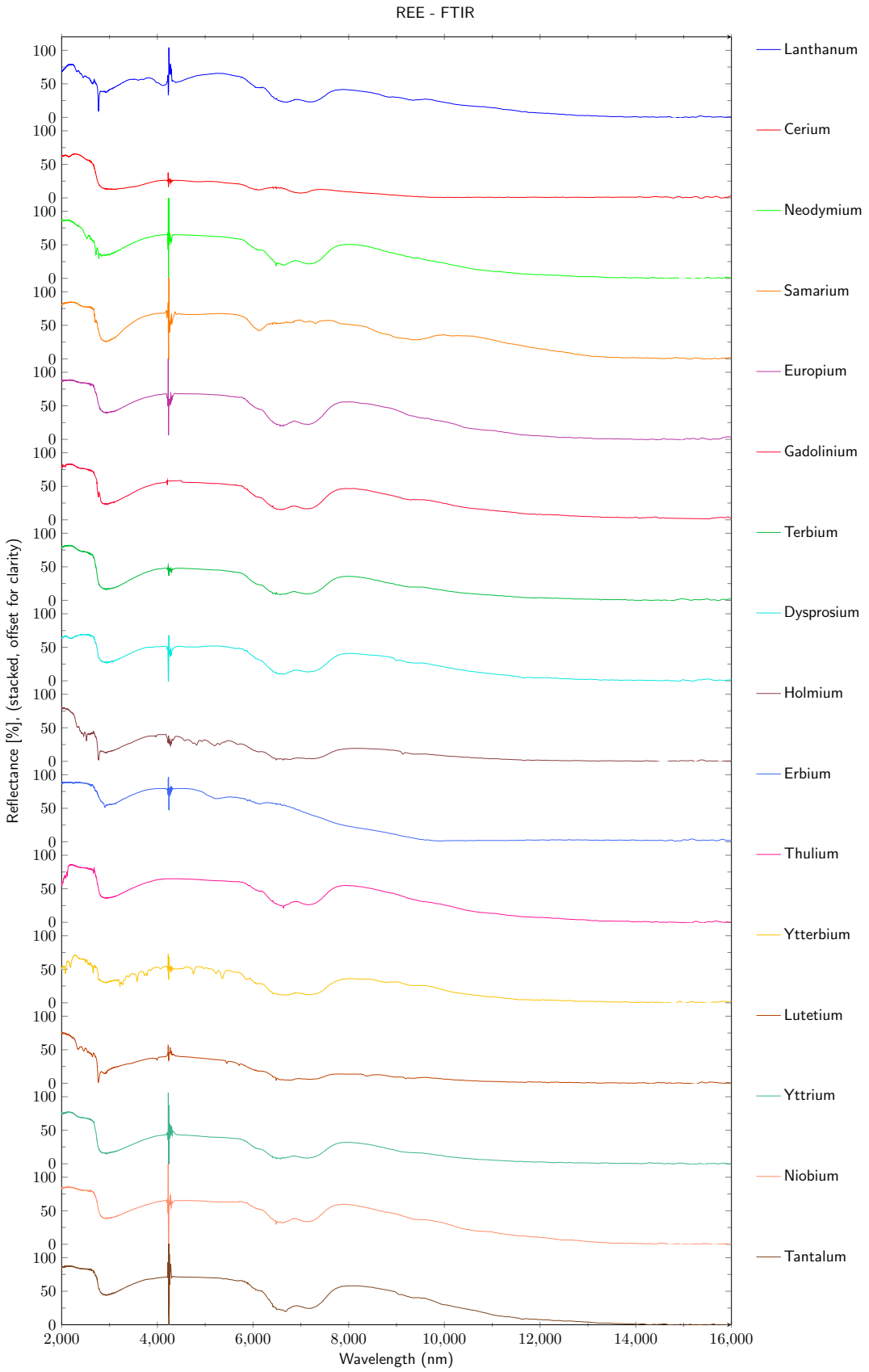

Figure 4.4: Reflectance spectra for all the REO for the VNIR, SWIR region. Results are from the measurements with the *FTIR Spectrum GX*.

STR 19/08. GFZ German Research Centre for Geosciences
DOI: 10.2312/GFZ.b103-19089

4.2 Spectral Characteristics of REE Bearing Minerals

4.2.1 REE Minerals

Bariopyrochlore (Fluorapatite)

The mineral bariopyrochlore (with fluorapatite) causes several absorption bands centered around 491, 677, 973, 1424, 1949, and 2258/2292 (doublet) nm (see Fig. D.65). These absorption features are mostly very wide and appear in all spectra with a low intensity. The wavelength position of the maximum and the shoulders for each absorption band is shown in Figure D.65. In the TIR region one absorption band is caused by the mineral bariopyrochlore near 2993 nm (Fig. D.66).
Niobium (around 48.68%), oxygen (around 29.81%) and barium (around 11.99%) are the main components of the mineral bariopyrochlore [12]. The XRF *Thermo Scientific Niton XL3t* measures that around 76% are not detectable. This could be attributable to a no fully contact between the measuring window and the sample. Hence only a very low barium content of 1.7 % and a niobium content of around 6 % are measured (further XRF results are shown in Table E.1).

Bastnasite

Bastnasite shows a very characteristic spectrum with several single and doublet absorption bands (see Fig. D.67). Doublet absorption bands appear with a maximum around 522, 625, 676, 866, 1096, and 2313 nm. Single absorption bands are caused at wavelength positions of 579, 740, 798, 952, 1253, 1541, and 1970 nm. All absorption features are intense and sharp, except an absorption feature with a maximum around 1541 nm, which appears very intense but also as a very wide absorption feature.
In the TIR region the mineral bastnasite causes absorption maxima near 2941, 6281, 7980, 9009, and 11325 nm (see Fig. D.68).
The XRF *Thermo Scientific Niton XL3t* measurement shows that 76.76% are not detectable and it analyses the highest value of around 9.39% as cerium, which is with around 63.94% [12] the main component of bastnasite. Further, the XRF *Thermo Scientific Niton XL3t* measures a neodymium- and lanthanum content with around 4.16% and 4.4%. Traces of yttrium with 0.6%, silicon with 1% and praseodymium with around 1% are also determined by the XRF device.

Gadolinite (Synchysite, Fluorite)

Gadolinite is a very black mineral and shows no characteristic absorption features measured by the *Perkin Elmer LAMBDA 950* (see Fig. D.69). The spectrum that is measured with the *ASD Field Spec 3* shows several characteristic absorptions, which cannot be caused by

STR 19/08. GFZ German Research Centre for Geosciences
DOI: 10.2312/GFZ.b103-19089

gadolinium. The *ASD Field Spec 3* spectrum shows mostly the absorption features caused by the mineral synchysite, which is associated around the mineral gadolinite in this sample. The measured spectrum from the *HySpex* can also not be used for a determination of characteristic absorption features for gadolinite because of its high signal to noise ratio.
The results of the *FTIR Spectrum GX* spectrometer show a spectrum which is characterized by four main absorption features (see Fig. D.70). The maxima of these features are centered near 2874, 6297/7610 (doublet) and 8628 nm.
The XRF device determined around 51.36 % as not detectable. The mineral gadolinite contains mainly yttrium (38.01%), silicon (12.01%), and iron (11.94%) [12]. The XRF *Thermo Scientific Niton XL3t* determines an yttrium content of 2.3% and other REO elements like neodymium (4.7%), cerium (7.2%), and lanthanum (2%). Silicon has a content of 14.94% and iron is detected with around 3%.

Monazite

The diameter of the monazite in the sample was about 2 mm, which is responsible for the very different spectra measured by the three spectrometers (*ASD Field Spec 3, Perkin Elmer LAMBDA 950, HySpex (VNIR-1600, SWIR-320m-e)*; see Fig. D.71). The results of the measurements cannot be used to determine significant characteristic absorption features of the mineral monazite. It is questionable whether the measured spectrum of the *FTIR Spectrum GX* spectrometer is reliable and represents the mineral monazite. However, the spectra show no characteristic absorption features between 2000 to 16000 nm (see Fig. D.72).

Parisite

Parisite shows a characteristic spectrum with several absorption features between 350 and 2500 nm (see Fig. D.73). The main absorption bands are centered near 580, 741, 799, 872, 1450/1590 (doublet), 1947, and 2345 nm. The main components of the mineral parisite are neodymium (23.39%), lanthanum (20.02%), cerium (10.10%), calcium (7.22%), and fluorine (6.85%). The XRF device analyzed (46.15% not detectable), a calcium content of around 15.29%, cerium (7.7%), lanthanum (5.5%) and neodymium (1.7%) can also be detected.

Polycrase

The spectral results of the mineral polycrase show no characteristic absorption bands that are caused by the mineral polycrase (see Fig. D.75). The small absorptions in the spectra of the *Perkin Elmer LAMBDA 950* and the *ASD Field Spec 3* are caused by the surrounding (bright) material. The black crystals of polycrase are 0.5 x 0.3 cm in size and too small for any spectral characterization. The surrounding material highly influences the spectral response of the mineral polycrase.

STR 19/08. GFZ German Research Centre for Geosciences
DOI: 10.2312/GFZ.b103-19089

In the TIR region the sample caused absorption maxima around 2924, 7462, 8628, and 9451 nm (see Fig. D.76). The mineral polycrase mainly contains oxygen (25.74%), titanium (15.41%), niobium (14.95%), tantalum (14.56%), and yttrium (11.92%) [12]. The value of not detectable parts of the XRF *Thermo Scientific Niton XL3t* measurement was around 70.58% (see Table E.2). The residue was determined as silicon (9.8%), phosphorus (5.6%), titanium (2.5%), aluminum (2.2%), niobium (1.8%), iron (1.7%), and yttrium (1.5%).

Synchysite

Synchysite causes four absorption features between the wavelength position of 350 and 1000 nm (see Fig. D.77). These features are centered near 578, 738, 793/800 (doublet), and 865 nm. Between 1000 and 2500 nm synchysite also causes several absorption bands with maxima near 1093, 1249, 1399, 1716, 1951, and 2318 nm.
The spectrum of the *FTIR Spectrum GX* spectrometer indicates maximum absorption bands near 2962, 3976, 6207/7347 (doublet), 8628, and 9074 nm (see Fig. D.78).
The main components of the mineral synchysite are oxygen (35.82%), yttrium (33.17%), and calcium (14.95%) [12]. The elements silicon (with around 22.0%), calcium (8.6%), and yttrium (1.1%) were analyzed by the XRF device (not detectable: 57.74%; see Table E.2).

Xenotime a and Xenotime b

There were two samples available for the mineral xenotime, which were differenciate into xenotime a and xenotime b. The spectrum of the mineral xenotime shows several characteristic absorption features in the VNIR and SWIR region (see Fig. D.79 and D.80). The most diagnostic absorptions are located near 454/487 (doublet), 523/542 (doublet), 651, 760, 811, 913, 1105, 1279/1309 (doublet), 1412, 1507/1525 (doublet), 1723, 2005, 2210/2260/2312 (triplet), and 2466 nm.
Xenotime causes three main absorption features in the TIR region (see Fig. D.81 and D.82) The main components of this mineral are yttrium (48.35%), oxygen (34.80%), and phosphorus (16.83%) [12]. The XRF device measures an yttrium content of 5.95% and a phosphor value of around 27.92% (not detectable: 36.96%; see Table E.2). For sample b an yttrium value of around 9.54% and a phosphorus content of 33.66% were measured (not detectable: 19.84%). Also the elements zirconium (sample a: 9.17%, sample b: 14.07%), silicon (sample a:7.54%, sample b: 8.0627%), and thorium (sample a: 1.09%, sample b:1.53%) were determined.

STR 19/08. GFZ German Research Centre for Geosciences
DOI: 10.2312/GFZ.b103-19089

4.2.2 REE Associated Minerals

Aegirine (Acmite)

The spectra of the measurements for the mineral aegirine show that this mineral decreases the albedo (see Fig. D.83). In fact, aegirine causes a lower reflectance that can be described as a very wide absorption. The reflectance decreases at around 548 nm, reaching the minimum at around 1219 nm, and increases until a wavelength of 2353 nm.
In the TIR region aegirine causes three absorption features with maxima centered near 2969, 9107, and 9708 nm (see Fig. D.84). The main components of aegirine are oxygen (41.56%), iron (24.18%), and silicon (24.32%) [12]. The XRF *Thermo Scientific Niton XL3t* detects a concentration of iron and silicon of around 20.26% and 22.8%, respectively. Around 51.55% could not be detected (see Table E.3).

Fluorapatite (Albite)

The spectral results for the mineral fluorapatite (associated with albite) show several absorption bands with maxima near 683, 1411, 1291, 2192, and 2355 nm (see Fig. D.85). However, these are not caused by the mineral fluorapatite, but rather by the mineral albite. Moreover, it appears that the fluoarapatite crystals are too small to get a spectral response (1.2 x 0.5 cm in size) and the spectral response of fluorapatite is overlapped by the much larger albite crystals. The *Perkin Elmer LAMBDA 950* shows different spectra compared to the results of the *ASD Field Spec 3* and the *HySpex*, because the sample was too fragile to chuck the whole sample in the holder of the *Perkin Elmer LAMBDA 950* spectrometer. The measured spectrum of the *Perkin Elmer LAMBDA 950* is from a single piece, which was about 1 cm in size. In the TIR region this sample causes two main absorption features with maxima near 2989 and 9199 nm (see Fig. D.86).
The main components of the mineral apatite are calcium (39.74%), phosphorus (18.43%), oxygen (38.07%), and fluorine (3.77%) [12]. The mineral albite contains mostly silicon (31.50%), oxygen (48.66%), aluminum (10.77%), sodium (8.30%), and calcium (0.76%) [12]. The results of the XRF *Thermo Scientific Niton XL3t* measurements indicate a calcium content of around 12.77%, 10.47% silicon, 7.95% phosphorus, 4.3% aluminum, and 3.29% potassium (see Table E.3). Around 60.39% are not detectable.

Fluorite

The spectral results of the mineral fluorite show absorption features near 523, 902, 1147, and 1933 nm (see Fig. D.87). The shoulders and their maxima are marked in Figure D.87.
The result of the measurement with the *FTIR Spectrum GX* spectrometer shows three main absorption bands in the TIR region near 2980, 4699, and 6067 nm (see Fig. D.88). The main components of the mineral fluorite are calcium (51.33%) and fluorine (48.67%) [12]. The XRF

STR 19/08. GFZ German Research Centre for Geosciences
DOI: 10.2312/GFZ.b103-19089

results indicate that this sample consists of around 56.94% calcium (see Table E.3). However, around 41% of the sample could not be analyzed.

Ilmenite

The spectra of the mineral ilmenite show two very wide absorption bands between 350 and 2150 nm (see Fig. D.89). The maximum of the first absorption feature appears at around 620 nm, while the maximum of the second absorption feature is around 1450 nm in the spectrum measured by the *Perkin Elmer LAMBDA 950* spectrometer and around 1576 nm in the spectra of the *HySpex* and the *ASD Field Spec 3*.
In the TIR region ilmenite causes two absorption bands with maxima around 3063 and 11337 nm (see Fig. D.90). The main components of ilmenite are iron (36.81%), oxygen (31.63%), and titanium (31.56%) [12]. The XRF *Thermo Scientific Niton XL3t* measured an iron content of 0.6% and a titanium content of around 41.65% (46.45% are not detectable; see Table E.3). Traces of magnesium (6.4%), aluminum (2.5%), and silicon (1.0%) are also detected by the XRF device.

Zircon

The mineral zircon causes a very wide absorption feature between 350 and 800 nm (see Fig. D.91). The maximum is centered in all spectra at different wavelength positions and cannot be determined clearly. The spectrum of zircon is also characterized by an intense absorption feature near 1115 nm. Zircon causes doublet absorption bands at 1327/1346 nm and at 1476/1503 nm, which appear with a lower intensity. At a wavelength position of 1662, 2068, 2185, and 2296 nm absorption bands can be identified.
In the TIR region three main absorptions can be detected (see Fig. D.92). The maxima are located at a wavelength position of around 3040, 8771, and 9532 nm. Zircon consists of zirconium (43.14%), oxygen (33.63%), silicon (14,76%), hafnium (4.69%), and is associated with REEs like lanthanum, cerium, praseodymium, neodymium and samarium (4,69%) [12]. The results of the XRF *Thermo Scientific Niton XL3t* show that this sample consists of around 52.75% zirconium and 12.60% silicon (see Table E.3). Around 33.79% of the sample could not be measured; the measured amount for each REE is mostly under 0.1%.

STR 19/08. GFZ German Research Centre for Geosciences
DOI: 10.2312/GFZ.b103-19089

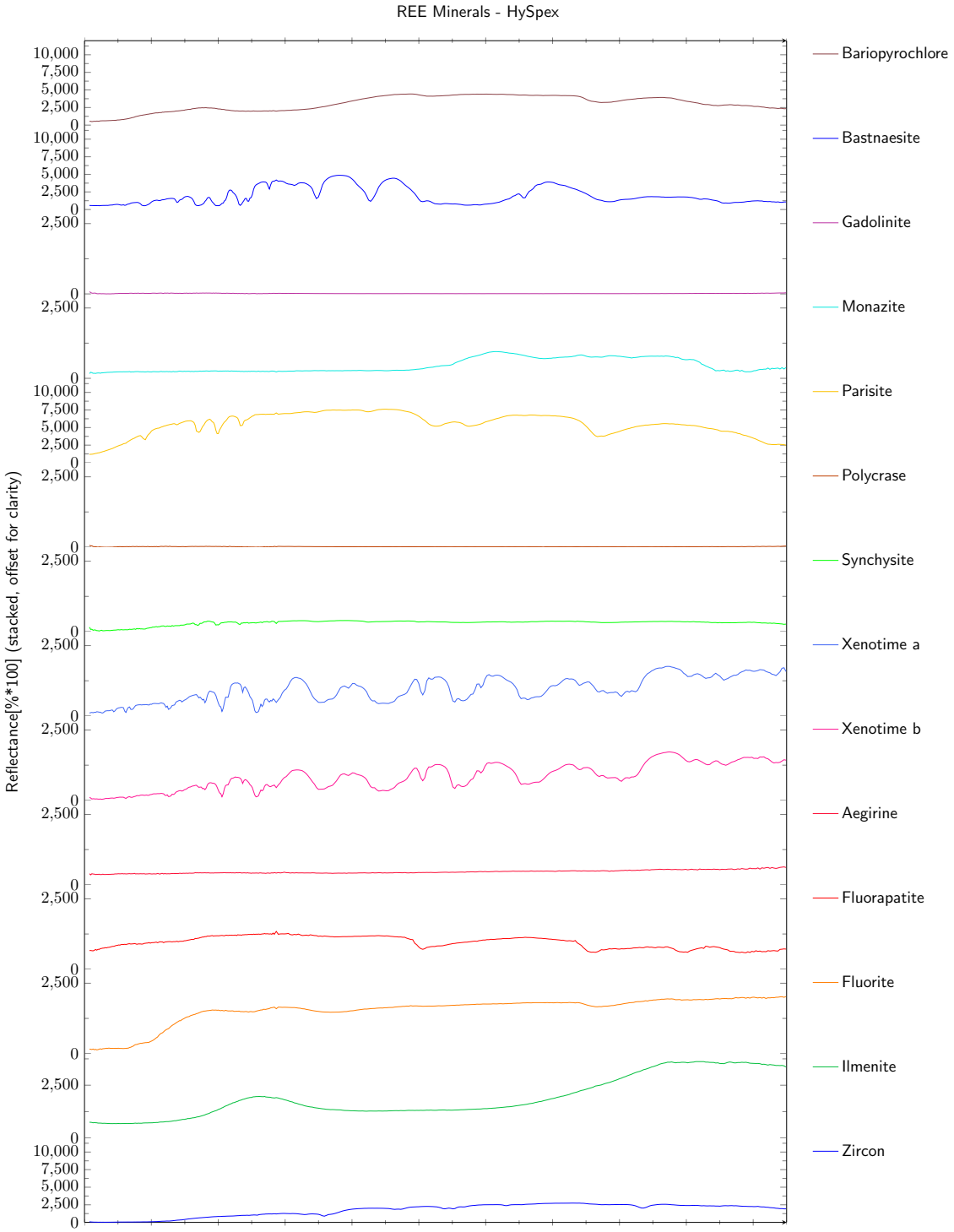

Figure 4.5: Reflectance spectra for all the REO minerals for the VNIR, SWIR region. Results are from the measurements with the *HySpex (VNIR-1600, SWIR-320m-e)*.

STR 19/08. GFZ German Research Centre for Geosciences
DOI: 10.2312/GFZ.b103-19089

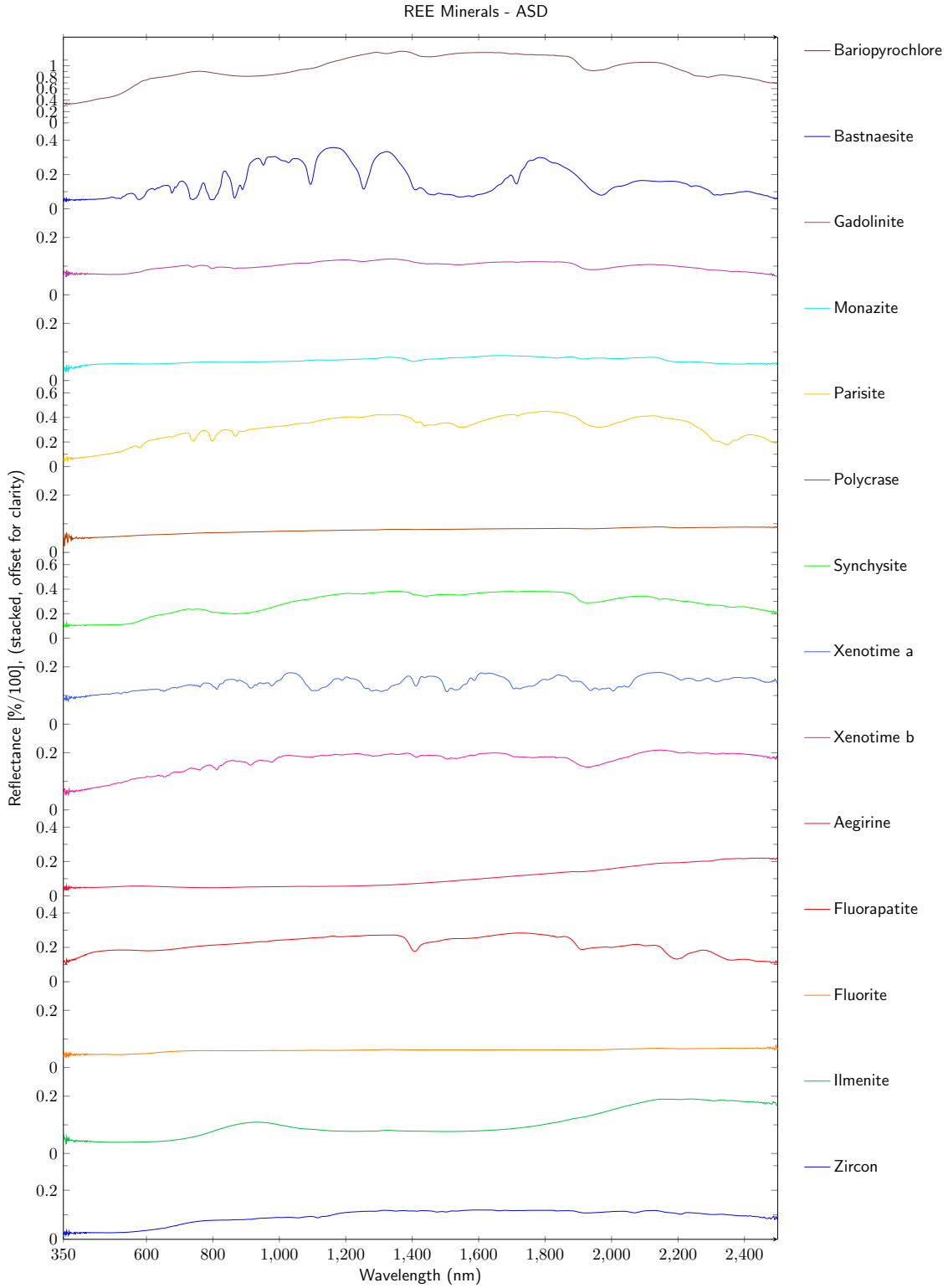

Figure 4.6: Reflectance spectra for all the REE minerals for the VNIR, SWIR region. Results are from the measurements with the *ASD Field Spec 3*.

STR 19/08. GFZ German Research Centre for Geosciences
DOI: 10.2312/GFZ.b103-19089

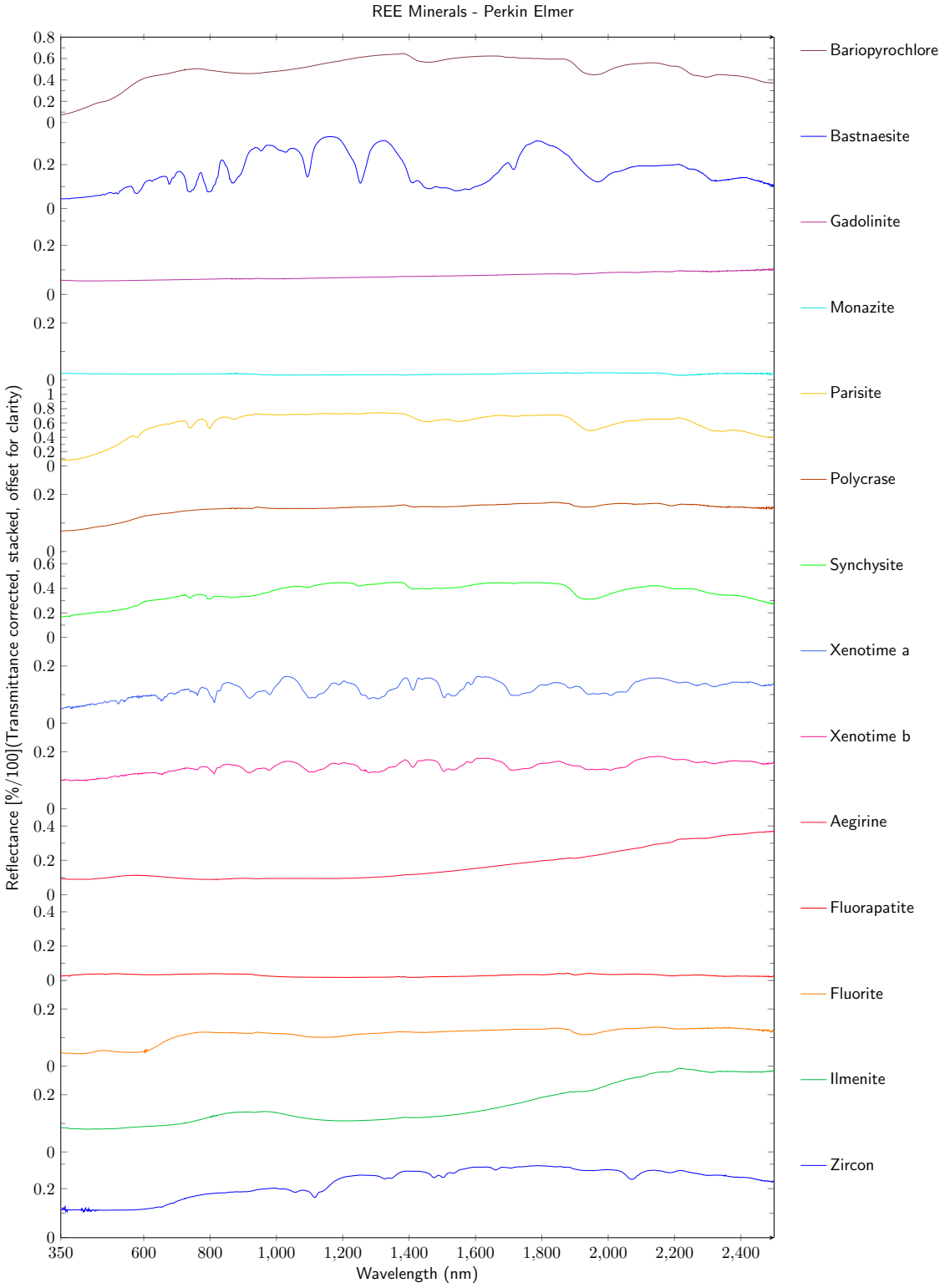

Figure 4.7: Reflectance spectra for all the REE minerals for the VNIR, SWIR region. Results are from the measurements with the *Perkin Elmer LAMBDA 950*.

STR 19/08. GFZ German Research Centre for Geosciences
DOI: 10.2312/GFZ.b103-19089

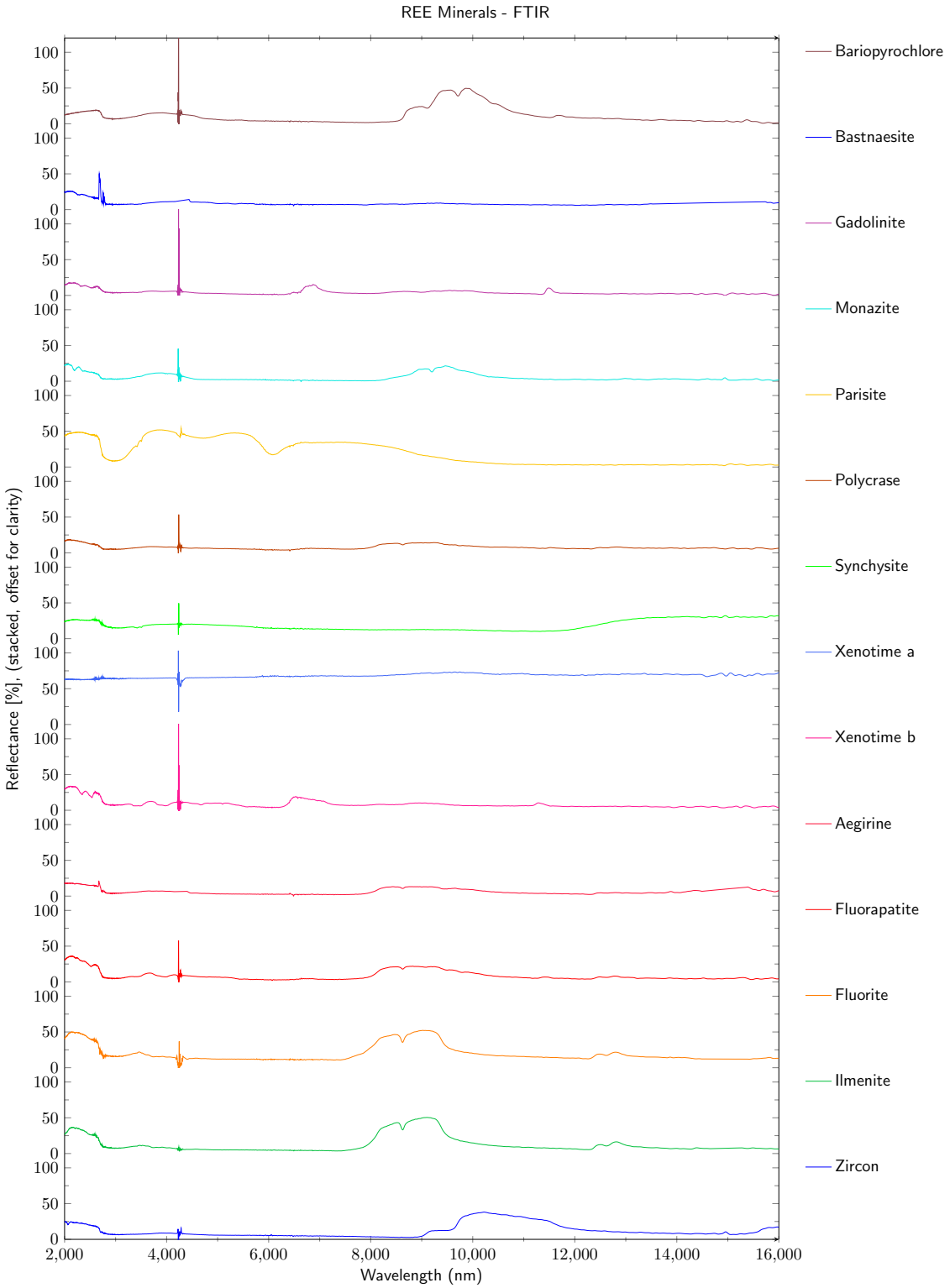

Figure 4.8: Reflectance spectra for all the REE minerals for the VNIR, SWIR region. Results are from the measurements with the *FTIR Spectrum GX*.

STR 19/08. GFZ German Research Centre for Geosciences
DOI: 10.2312/GFZ.b103-19089

4.3 Detection of Neodymium with Presence of Iron (III) Oxide

The results for the mixture of neodymium with calcium carbonate show that neodymium already causes absorptions in the spectrum with a concentration of about 0.1% (see Fig. C.11). Compared to the mixture of neodymium with hematite the spectrum with a 0.1% concentration of neodymium and 0.90% hematite only shows three very broad absorptions and can be assigned to hematite (see Fig. 4.9). The first low absorptions associated with neodymium appear at 752 and 823 nm with a concentration of around 5% neodymium. At a concentration of 30% of neodymium all characteristic features for neodymium appear in the spectrum but are mainly not strongly pronounced. These absorptions become sharper and more intense with an increase of the concentration of neodymium. Comparing both spectra (from the calcium carbonate and hematite mixtures) with a neodymium content of 95% it can clearly be seen that the absorption depths in the hematite mixture is significantly lower for several features.
This fact can also be observed for the two basic mixtures of neodymium and calcium carbonate with hematite. With a concentration of 0.1% neodymium (basic mixture 1) there are only very small absorptions observable at 538, 600, 751, and 823 nm if the concentration of hematite is less than 2% (see Fig. 4.10). Above around 2% hematite no characteristic absorptions caused by the REO neodymium can be detected. For the basic mixture with a concentration of 0.5% neodymium (basic mixture 2) these characteristic absorptions are also observable (4.11). Further, the features are more intense and also appear if the concentration of hematite is around 2%. These absorption bands become smaller with an increase of the concentration of hematite and are almost undetectable or appear too small in the spectrum for any detection if the hematite reaches a concentration of around 10%.

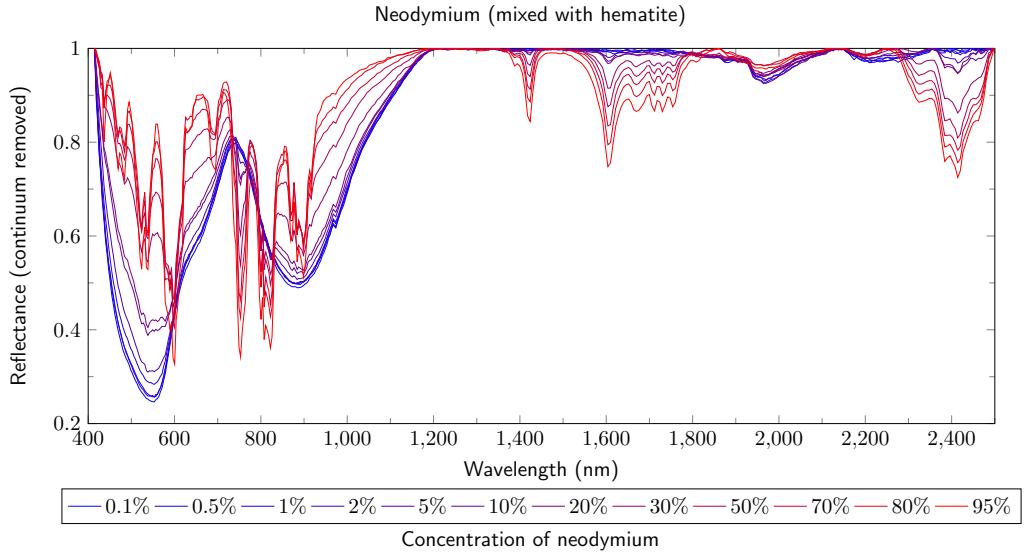

Figure 4.9: Reflectance spectra for the REO neodymium with hematite for the VNIR and SWIR region. The figure shows the results from the measurement of the *HySpex (VNIR-1600, SWIR-320m-e)*. The spectra of all samples are colored from high (red) to low (blue) according to the concentration of neodymium.

STR 19/08. GFZ German Research Centre for Geosciences
DOI: 10.2312/GFZ.b103-19089

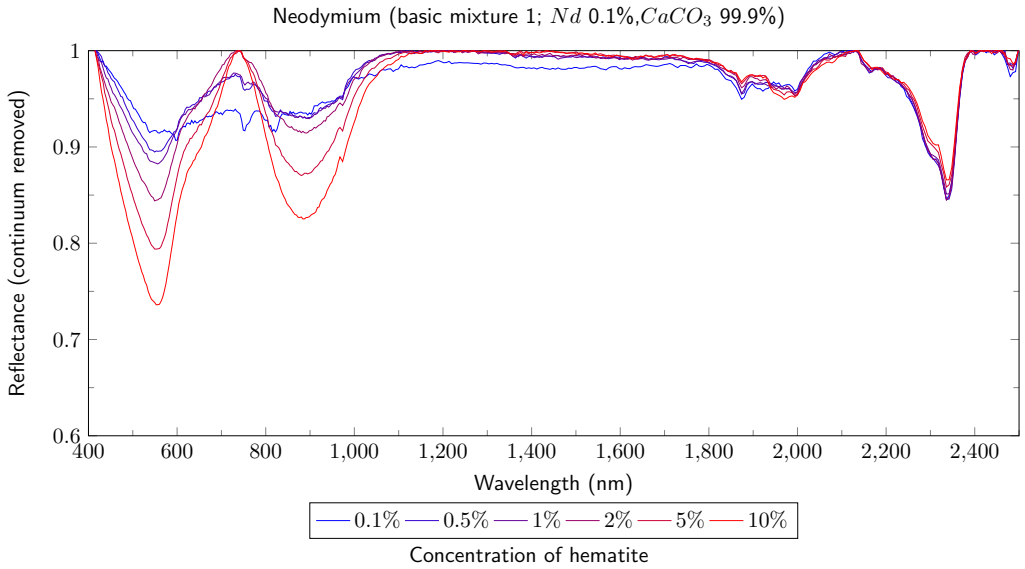

Figure 4.10: Reflectance spectra for the REO neodymium (basic mixture 1; Nd 0.1%,$CaCO_3$ 99.9%) with hematite for the VNIR and SWIR region. The figure shows the results from the measurement of the *HySpex (VNIR-1600, SWIR-320m-e)*. The spectra of all samples are colored from high (red) to low (blue) according to the concentration of hematite.

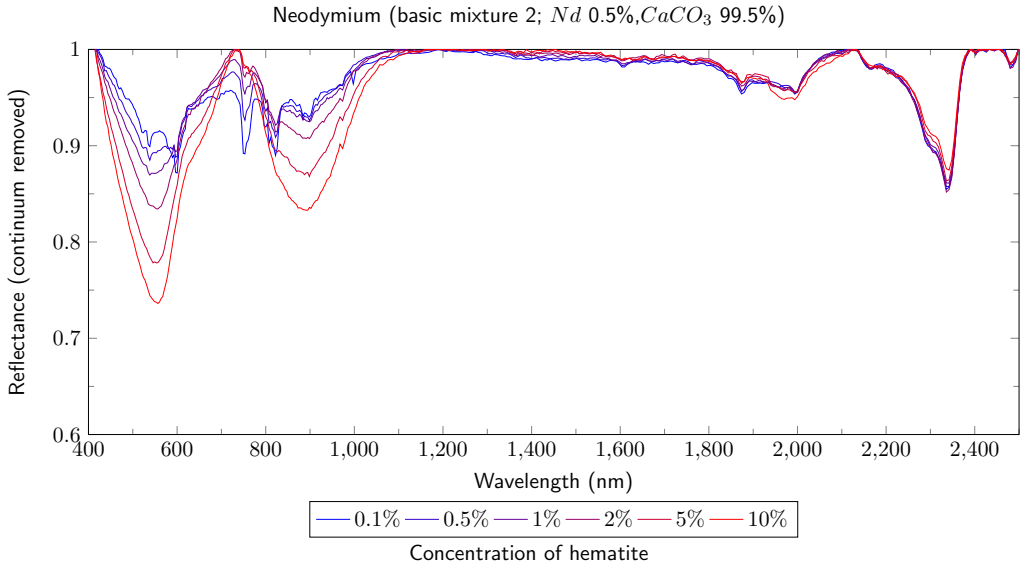

Figure 4.11: Reflectance spectra for the REO Neodymium (basic mixture 2; Nd 0.1%,$CaCO_3$ 99.5%) with hematite for the VNIR and SWIR region. The figure shows the results from the measurement of the *HySpex (VNIR-1600, SWIR-320m-e)*. The spectra of all samples are colored from high (red) to low (blue) according to the concentration of hematite.

STR 19/08. GFZ German Research Centre for Geosciences
DOI: 10.2312/GFZ.b103-19089

4.4 Approach on Different Scales

4.4.1 Detection of REEs in the Field

Once the characteristics of the REE in the laboratory are determined, the characteristic absorption features of each REE is now compared to the absorption features of water, vegetation and carbonatite associated minerals.
Molecular water causes two bands at 1400 and 1900 nm in the near-infrared region [37][29]. Hence, the REEs cerium, gadolinium, lutetium, yttrium, and tantalum only show characteristic absorption features with a very low intensity with an REE content of 100% at 1400, and 1900 nm, thus it is difficult to detect these REEs. Even lanthanum, that appears to cause a more intensive absorption feature at 1400 nm, will overlap with the molecular water absorption band at this position. The absorption feature that is caused by chlorophyll appears between 450 and 670 nm (Vegetation Red Edge)[44]. Here, chlorophyll strongly absorbs energy and thus other spectral responses are suppressed [44]. Within this spectral range characteristic absorption features by the REEs neodymium, holmium, erbium, and thulium occur. However, these REEs also cause absorption at different positions. Hence, if vegetation causes a red edge within the spectra they can be detected by the other characteristic absorption features.
REE minerals are highly enriched in carbonatites and alkaline rocks, which are both igneous rocks. The main constituents of these igneous rocks are quartz, feldspar, mica (biotite and muscovite), olivine, and hornblende [46].
Quartz and feldspar appear to have no significant absorption bands in the near-infrared region [19]. The absorption band of biotite and muscovite appears around 2300 and 2400 nm [19]. No absorption band caused by REEs is located at that position.
The mineral hornblende also causes absorption bands at 2300 and 2400 nm, while the mineral olivine appears to have absorption bands at 2100 and 2300 nm [19]. Hence, there are no bands at this wavelength positions that are caused by REEs, because there is no spectral overlapping. Europium is the only REE that causes a minor absorption band at 2100 nm.
Further, terbium and niobium have a low absorption band at 2200 nm. Hence, the presence of hornblende and olivine could cause an spectral overlapping in these wavelength position. Hematite and calcite are also important rock forming minerals. At 500 and 800 hematite causes very intensive and broad absorptions [19]. At least one characteristic absorption band of the REEs neodymium, samarium, europium, dysprosium holmium, erbium, and thulium are located in these wavelength positions. Samarium, dysprosium, holmium, erbium, and thulium also cause absorption bands between 900 and 1300 nm. Hence, with a presence of hematite it should still be possible to detect these REEs.
Calcite causes a characteristic absorption band at 2100 and 2300 nm that can influence the detection of europium. None of the other REEs show a significant absorption band in this wavelength region.

STR 19/08. GFZ German Research Centre for Geosciences
DOI: 10.2312/GFZ.b103-19089

4.4.2 Detection of REEs in Rock Samples

The results of the *HySpex* measurements from the soevite show absorption bands at 738, 800, 967, 1081, 1429, 1933, 2156, and 2336 nm (see Fig. 4.12). The XRF device measures the following REE values for the rock sample: neodymium 0.14%, praseodymium 0.07%, cerium 0.08%, lanthanum 0.0576%, and yttrium 0.01%. Since the spectral characteristic of praseodymium is unknown and cerium, lanthanum and yttrium show only absorption bands near 1400 and 1900 nm, where water causes absorption bands, only the spectrum (mixture) of 0.11% neodymium and 99.89% calcium carbonate is compared to the soevite spectrum. Figure **??** shows, which absorption bands in the spectrum of the rock sample are caused by neodymium. The first absorption band at 578 nm can almost not be detected in the rock sample compared to the other absorption features at 738, 800, and 967 nm. These three absorption bands can be clearly detected in the rock sample with a concentration of neodymium at around 0.14%.

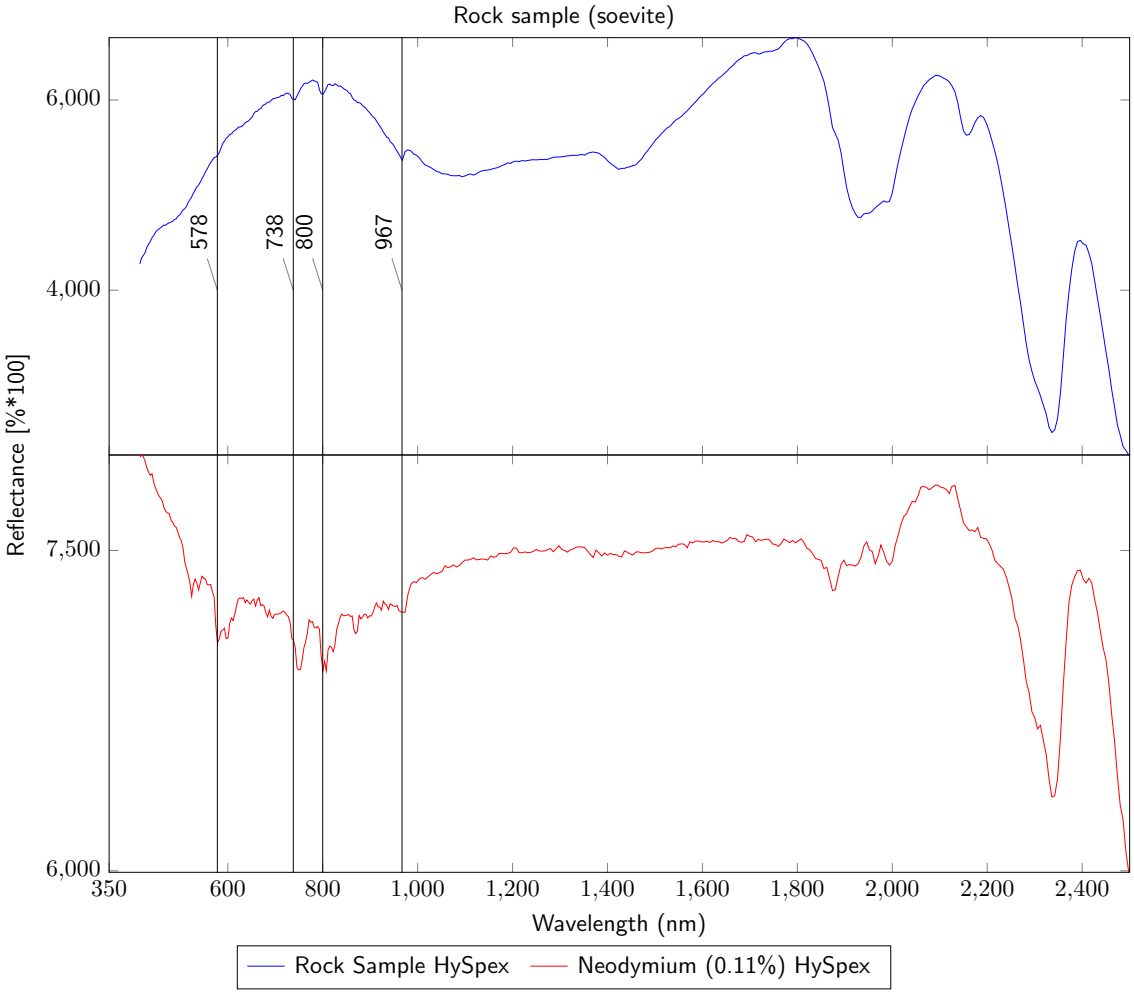

Figure 4.12: The Figure shows the reflectance spectra of the rock sample and neodymium with a concentration of 0.11%. Both spectra show the results from the measurement of the *HySpex (VNIR-1600, SWIR-320m-e)*. Compared maxima (solid lines) are marked.

STR 19/08. GFZ German Research Centre for Geosciences
DOI: 10.2312/GFZ.b103-19089

4.4.3 Spectral Resampling on EnMap, EO-1 Hyperion and HyMap

The absorption band at 1400 nm in the spectrum of lanthanum can be detected in all resampled spectra. Further, the spectral resampling of the REEs cerium, gadolinium, terbium, lutetium, yttrium, niobium and, tantalum show no influence of the absorption bands, due to the fact that these elements have no intense, but rather low and broad absorptions bands. The spectral resampling shows that these elements would be detected with a lower spectral resolution (e.g. *HyMap*) as good as with a higher spectral resolution (e.g. *EnMap*).

Neodymium

With a spectral resolution of the *Hyperion* the doublet feature at 359/366 nm appears as one absorption band with a maximum near 365 nm. The two doublet absorption bands near 469/485 and 521/537 nm can also be detected with a spectral resolution of *EnMap* but appear as one absorption band centered near 477/538 (*Hyperion*) and 482/527 nm (*HyMap*) with a lower spectral resolution (such as *Hyperion* and *HyMap*). The spectral results of the spectral resampling show that the absorption bands of neodymium near 438 and 600 nm are also detectable with lower spectral resolutions. The maxima shift to 440/597 (*EnMap*), 436/599 (*Hyperion*) and 604 nm (*HyMap*), respectively. Moreover, the absorption bands between 650 and 1000 nm can also be found in the spectra after the spectral resampling. Maxima shift appear for almost all spectral resolutions and shift up to 8 nm from the maxima position in the *Perkin Elmer LAMBDA 950* spectra. The absorption bands between 1000 and 2000 nm occur in all resampled spectra, except the doublet at 1731/1756 nm appears as one low, broad absorption band. With a concentration of 0.1% neodymium following absorption features can be detected: in the spectrum of *EnMap* the features at 469/485 (doublet), 521/537 (doublet), 597, 691, 755, 823, 895, and 1382 nm are detectable. The spectrum of *Hyperion* shows with a concentration of 0.1% neodymium absorption features at: 365, 477, 538, 599, 691, 755, 823, 894 and 1386 nm. The resampled spectrum of *HyMap* indicates absorption bands at wavelength positions of 482, 527, 604,695, 755, 815, 895, and 1405 nm.

Samarium

The spectral resampling of samarium shows that the absorption band at 444 nm is seen in all spectra after the spectral resampling. The doublet at 469/482 nm appears in the resampled spectra as one absorption band with maxima at 469 (*EnMap*), 467 (*Hyperion*), and 482 nm (*HyMap*). The low absorption features at 533 and 568 nm occur weaker with a decrease in the spectral resolution; hence, they are only clearly seen in the *EnMap* spectrum. The absorption bands of samarium between 800 and 2500 nm appear in all resampled spectra. The maxima at 954, 1091, 1251, 1402, 1567, and 1966 nm can be detected, while doublet or triplet bands cannot be resolved separately anymore with a decrease in the spectral resolution. In the resampled spectra of the *Hyperion* the absorption feature at 410 can be found, while the

STR 19/08. GFZ German Research Centre for Geosciences
DOI: 10.2312/GFZ.b103-19089

doublet at 367/381 nm became one absorption band with a maximum around 365 nm. With a concentration of 0.1% samarium the absorption features around 1094, 1251, 1394, and 1568 are shown in all resampled spectra (*EnMap*, *Hyperion*, *HyMap*).

Europium

The absorption feature of europium at around 395 nm became one, broad absorption with a spectral resolution of the *Hyperion*. The absorption bands with a maxima near 467 and 535 nm became smaller with a decrease in the spectral resolution and the maxima shifts to 469/533 (*EnMap*), 467/538 (*Hyperion*), 466/527 nm (*HyMap*). The several small absorption bands between 560 and 629 nm are clearly detectable with a higher spectral resolution, while with a decreasing spectral resolution these features are getting too small for detection. Around 1422 nm very low and wide absorption bands appear in all resampled spectra. The broad absorption features with several bands near 1787, 1842, 1999, 2081, and 2184 nm can be detected also after the spectral resampling, except that the absorption band around 1842 nm cannot be found with a spectral resolution with the *HyMap* and only the maxima of the 1999 features shift to 2009 nm in the *Hyperion* resampled spectrum. Following absorption bands can be detected with a concentration of 0.1% samarium: 469 and 2098 nm.

Dysprosium

The absorption bands of dysprosium around 385 and 424 nm can also be detected with a spectral resolution of the *Hyperion* while the doublet absorption near 447/455 nm appear as one broad absorption in all resampled spectra. The spectral results show that the absorption features of dysprosium near 744 and 799 can also be recorded with a lower spectral resolution of the *HyMap*. However, the maxima of these absorption bands shifts to 748/800 (*EnMap*), 742/793 (*Hyperion*) and 740/800 nm (*HyMap*). The broad absorption bands near 887 nm are also detectable with lower spectral resolutions of the *EnMap*, *Hyperion* or *HyMap*. Moreover, the very intense, broad absorption of dysprosium between 983 and 1465 can be detected after the spectral resampling. The doublet absorption band around 1613/1614 nm appears in the resampled spectra as one broad absorption with no clearly maximum. The two absorption bands centered near 1681 and 1758 nm can also be detected if the spectral resolution is low (e.g. *HyMap*). With a concentration of 0.1% dysprosium the absorption bands around 800, 1068, 1263 and 1679 nm can be detected.

Holmium

The results of the spectral resampling of holmium indicate that the absorption features near 363, 386 and 421 nm appear as one absorption band in the spectral resampling of *Hyperion*. The three absorption features with maxima at 449, 538, and 649 also appear in the spectral

STR 19/08. GFZ German Research Centre for Geosciences
DOI: 10.2312/GFZ.b103-19089

resampling in each case as one absorption feature, except the *EnMap* resampling of the absorptions band near 449 nm. The maxima for the absorption band near 449 nm shift to 457 (*Hyperion*) and 451 nm (*HyMap*). The maxima for the absorption band with a maximum near 538 nm also shift after the spectral resampling on *HyMap* to 543 nm. The absorption feature near 886 nm and also the absorption band at 1189 nm do not change after the spectral resampling, while the absorption feature near 1132 nm became one absorption band for all resampled spectra. The characteristic absorption of holmium between 1602 and 2154 nm can also be identified in the spectra that were resampled on *EnMap* and *Hyperion*. The resampled spectrum on *HyMap* for this feature shows one absorption band with a maximum near 1953 nm. Absorption features around 450 (*EnMap* appears as doublet), 538, 645, and 1144 nm appear in the spectra with a concentration of 0.1% holmium.

Erbium

The doublet bands around 368/380 and 446/455 nm appear in the resampled spectrum as one absorption band with maxima at 375 nm (for the 368/380 nm feature at the resampled spectra of *Hyperion*) and 455 (*EnMap*), 457 (*Hyperion*) and 451 (*HyMap*) nm (for the feature at 446/455). The maximum of the absorption band at 409 nm shifts to 406 nm after the resampling on *Hyperion*. The absorption bands around 491 and 523 nm occur after the spectral resampling on *HyMap* only as one wide absorption feature with a maximum around 527 nm, while in the resampled spectra of the *EnMap* and the *Hyperion* both absorption features can be detected. The three absorption features around 654, 800 and 976 nm appear after the spectral resampling in all spectra. Further, the absorption feature with maxima near 1475 and 1535 nm can also be identified in all resampled spectra. With a concentration of 0.1% erbium absorption features around 493 (except in the *HyMap* spectrum), 523, 658, 800, 977, 1476, and 1537 nm are shown in the resampled spectra.

Thulium

For the REE thulium the doublet band around 465/476 nm can be detected after the spectral resampling as one absorption feature with maxima around 464 (*EnMap*), 467 (*Hyperion*), and 466 (*HyMap*) nm. Further, the two wide absorption features between 607 and 865 nm occur in all resampled spectra only as one absorption with maxima at 685 (*EnMap*), 691 (*Hyperion*) and 695 (*HyMap*) for the feature around 685 nm and at 793 (*EnMap*), 800 (*Hyperion*) and 793 (*HyMap*) nm for the feature near 796 nm. Also the two absorption features in the SWIR region, which show maxima around 1204 and 1633 nm can be detected with a spectral resolution of *EnMap*, *Hyperion* and *HyMap*. However, both features appear mostly as an absorption feature with one wide absorption band. Absorption features around 464, 685, 800, 1203, 1634, and 1762 nm can be detected with a concentration of 0.1% thulium in all resampled spectra.

STR 19/08. GFZ German Research Centre for Geosciences
DOI: 10.2312/GFZ.b103-19089

Ytterbium

The characteristic triplet absorption feature at 974/947/903 nm appears after the resampling in all spectra, except the lower absorption at 903 that cannot be clearly seen with a spectral resolution of the *HyMap*. The absorption band around 976 nm can be detected with a concentration of 0.1% ytterbium in all resampled spectra.

STR 19/08. GFZ German Research Centre for Geosciences
DOI: 10.2312/GFZ.b103-19089

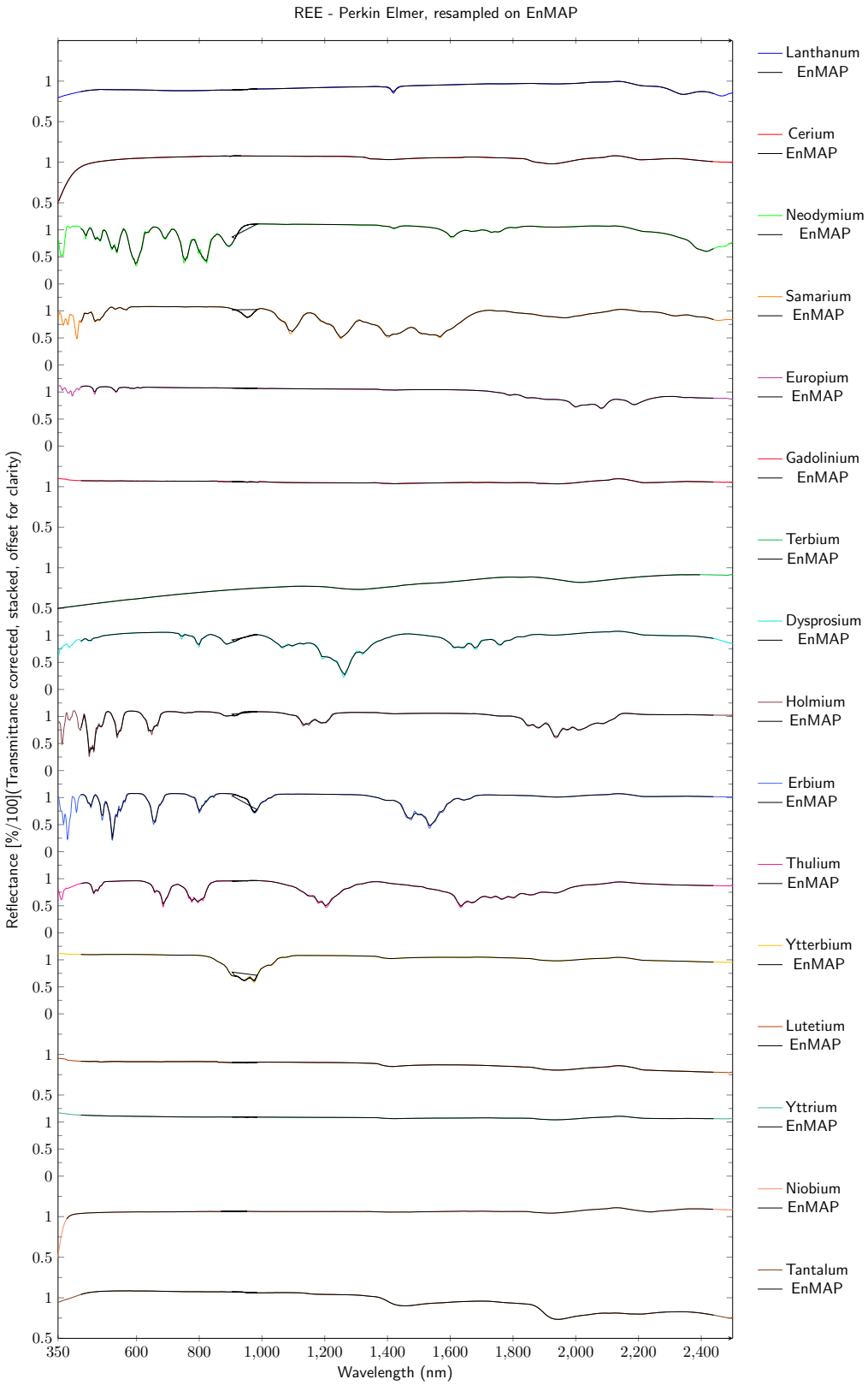

Figure 4.13: Reflectance spectra for all the REO for the VNIR, SWIR region after the spectral resampling to *EnMap*. For the spectral resampling the results of the *Perkin Elmer LAMBDA 950* were used.

STR 19/08. GFZ German Research Centre for Geosciences
DOI: 10.2312/GFZ.b103-19089

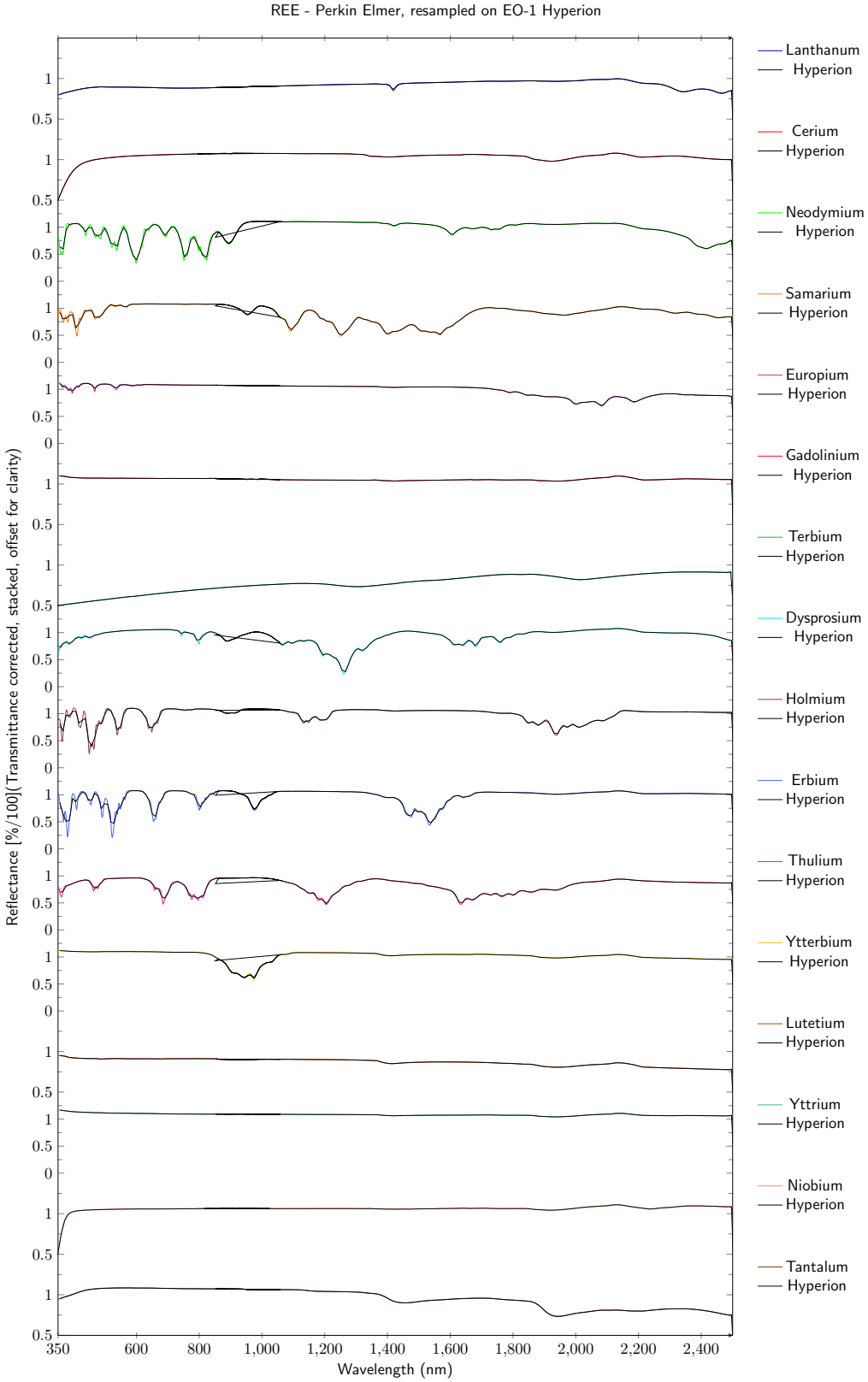

Figure 4.14: Reflectance spectra for all the REO for the VNIR, SWIR region after the spectral resampling to *EO-1 Hyperion*. For the spectral resampling the results of the *Perkin Elmer LAMBDA 950* were used.

STR 19/08. GFZ German Research Centre for Geosciences
DOI: 10.2312/GFZ.b103-19089

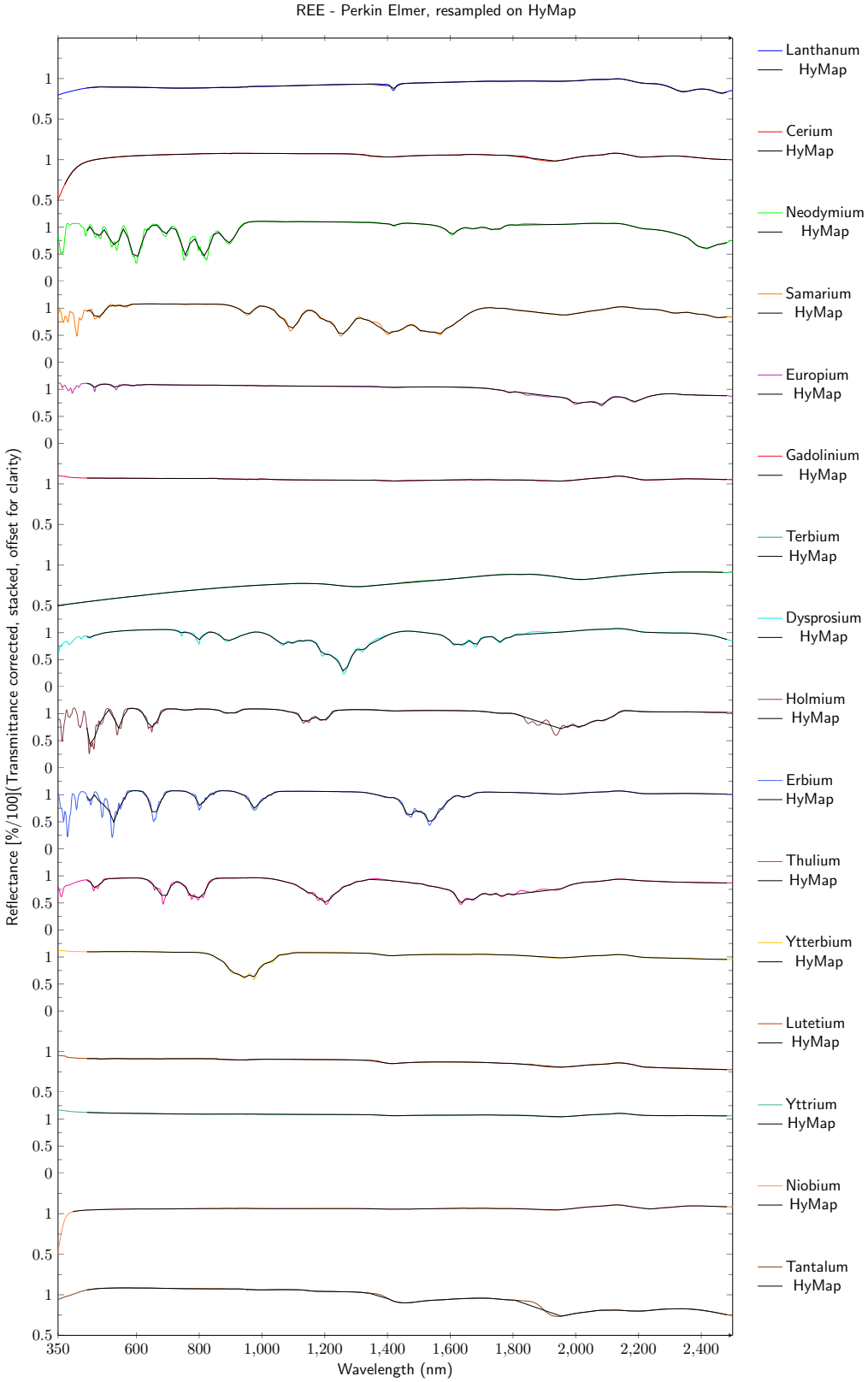

Figure 4.15: Reflectance spectra for all the REO for the VNIR, SWIR region after the spectral resampling to *HyMap*. For the spectral resampling the results of the *Perkin Elmer LAMBDA 950* were used.

STR 19/08. GFZ German Research Centre for Geosciences
DOI: 10.2312/GFZ.b103-19089

4.4.4 Finding REEs in the Mountain Pass Mine

The spectrum of the Mountain Pass mine is a median of the spectra extracted from the *Hyperion* image with a ROI (contains 74 pixels). The spectrum shows several absorption bands between 400 and 1500 nm (see Fig. F.94). The maxima of these absorptions appear at 630, 660, 711, 823, 932, 1033, 1124, 1194, 1255, and 1467 nm, marked with their shoulders in Figure F.94. Between 1400 and 2400 nm absorption bands are centered near 1568/1598 (doublet), 1659, 2002, 2042, 2113, 2193, 2294, 2314, and 2345 nm.
The REEs lanthanum, cerium, and gadolinium show absorption features around 1400 and 1900 nm, which cannot be used for comparison, since water causes very intense absorption features at this wavelength position.
Figure 4.16 shows the spectrum of the Mountain Pass mine in comparison to the neodymium spectrum with a content of 0.11% neodymium and to the samarium spectrum with a content of 0.56% samarium.

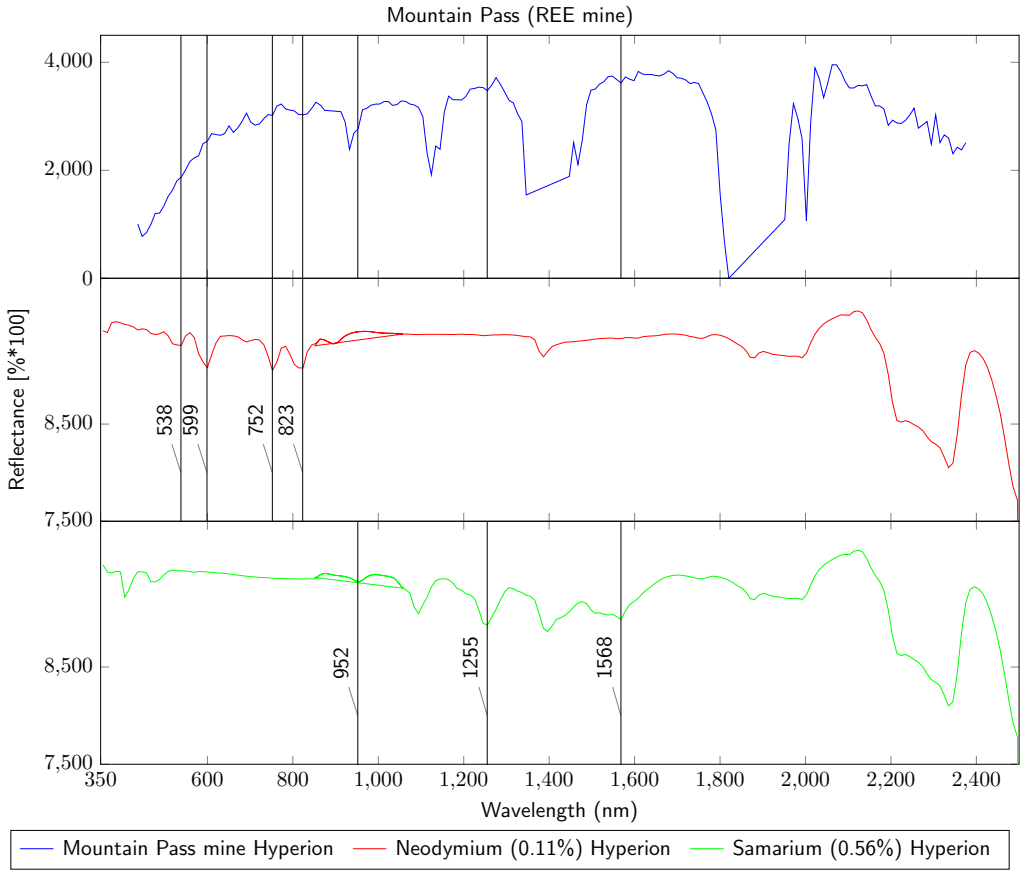

Figure 4.16: The Figure shows the reflectance spectra of the Mountain Pass mine and the REOs neodymium (0.11%) and samarium (0.56%)(resampled on *Hyperion*). Compared maxima (solid lines) are marked.

Both spectra are resampled on the *Hyperion*. Four absorption bands between 400 and 900 nm at 538, 599, 752 and 823 nm appear to be related mainly to the REO neodymium, which

STR 19/08. GFZ German Research Centre for Geosciences
DOI: 10.2312/GFZ.b103-19089

already shows absorption bands at low concentrations in this wavelength region. Three small absorption bands that occur between 900 and 1600 nm at 952, 1255 and 1568 nm in the Mountain Pass mine spectrum can be attributed to the REO samarium, which only causes absorption features in the spectrum with a concentration of 0.56% and higher. The absorption bands observed for neodymium and samarium in the spectrum of the Mountain Pass mine have only a very low intensity.

STR 19/08. GFZ German Research Centre for Geosciences
DOI: 10.2312/GFZ.b103-19089

5 Discussion

5.1 Can Reflectance Spectroscopy Be Used for the Detection of REEs?

In this study pure REO powders and self-made mixtures of REO with calcium carbonate in different concentrations were analyzed using reflectance spectroscopy.
The spectral results show that lanthanum, neodymium, samarium, europium, terbium, dysprosium, holmium, erbium, thulium, and ytterbium show at least one significant absorption band and most of them have several absorption features in the VNIR and SWIR region. It was also observed that for these REEs (except europium) a logarithmic correlation between the absorption depths and the concentration of these individual rare earths can be determined. The mixtures show that the absorption features of these REEs increase with an increasing REEs content. The results demonstrate that these REEs cause an individual spectrum, which makes it possible to directly detect them separately in the spectrum. Except for neodymium (this is discussed in an extra section), all three spectrometer show the same results for each individual REE.
For the other REEs cerium, gadolinium, lutetium, yttrium, and tantalum two main absorptions at around 1400 and 1900 nm were detected. Niobium also causes two main absorption bands at 1900 and 2200 nm. Here, instead of a logarithmic correlation between the absorption depths and the concentration of this individual rare earth a linear relationship occurs. Moreover, the calculated curves of the absorption depth for these REEs mainly show high fluctuations with increasing concentrations. The visual interpretation of the spectral results of the mixtures indicates no clear difference in the absorption depth with increasing concentrations. Compared to REEs where a more logarithmic trend could be observed, the absorption features around 1400 and 1900 show a clear difference. They are mostly of a low depth and wide compared to other diagnostic absorption features e.g., neodymium, samarium or even lanthanum that also cause an absorption depth around 1400 nm.
The most important fact is that for gadolinium, lutetium, yttrium, niobium and tantalum no clear increase of the absorption depth with an increasing concentration of the individual REE can be observed. This leads to the assumption that these absorption depths might rather be caused by water than by the REEs. However, it is difficult to validate this observation as two small absorption bands are caused by $CaCO_3$ around 1900 nm. The absorption band at around 2200 nm that can be observed by the measurements of niobium can also not be determined by

STR 19/08. GFZ German Research Centre for Geosciences
DOI: 10.2312/GFZ.b103-19089

the mixtures, because calcium carbonate causes a large absorption band around 2300 nm.
However, the results of this study show that the technique of using spectral reflectance for the characterization of REEs provides a robust basis for the development of new REE detection methodologies, since the individual elements lanthanum, neodymium, samarium, europium, terbium, dysprosium, holmium, erbium, thulium, and ytterbium show diagnostic absorption bands and, as a consequence, are identifiable.
Besides lanthanum, samarium and terbium, all these elements show several absorption bands that can be detected with a concentration of around 0.1% REO. With a concentration lower than 0.1% it is not possible to mix both components homogenously. This result represents an important aspect for the detection of REEs with reflectance spectroscopy, since these elements occur naturally at very low concentrations. Dai [23] also analyzed different concentrations of dissolved REEs in aqueous media with reflectance spectroscopy. The concentration of REEs in the solutions was very low (0.03-2.3%), but the spectral absorption features were detectable in the VNIR and NIR wavelength region [23].
This study also shows that with an increasing concentration of REO the absorption features become more pronounced. Dai [23] observed that the intensities of the absorption features decrease with the descending of the REE concentration, but he calculated a linear correlation between both. Based on this study the relationship between the absorption depth and the concentration of REEs can be described and estimated with rather a logarithmic than a linear correlation, at least for the absorption features of lanthanum, neodymium, samarium, terbium, dysprosium, holmium, erbium, thulium, and ytterbium. The calculated curves for the correlation of the absorption depth with the concentration of REEs show between 0.1 and 2% also a very steep slope, until they reach 2 to 5 % were the slope rate decreases significantly. This could explain the difference between the correlation results of Dais [23] and this study. Moreover, the curves of lanthanum, neodymium, samarium, europium, terbium, and dysprosium reaches a saturation point between 50 and 70% and even decreases in that range for certain REEs.
All the previously described spectral behaviors are related to the VNIR and SWIR region between 350 and 2500 nm. Figure 4.4 shows the overview of the spectral results for all REEs. All REEs show two absorption features around 2900 nm and 6600/7100 (doublet) nm. Some of the REEs also show very small absorptions between 8000 and 9000 nm. However, these absorption features are not caused by any REE. Because the absorption bands here are also attributable to water, which absorbs absorption features in the infrared region at around 2900 and 6000 nm [26]. No REE shows diagnostic absorption features in a higher wavelength than 2500 nm. The results of this study support the assumption of Rowan [29] that the absorption bands of REEs are related to electronic field transitions, which do not occur in the TIR. Hence, for the detection of REEs the wavelength region after 2500 nm cannot be used. However, this cannot be said with certainty. This topic is further discussed in the next section together with the neodymium wavelength shift.

STR 19/08. GFZ German Research Centre for Geosciences
DOI: 10.2312/GFZ.b103-19089

5.2 The Neodymium Problem

Neodymium is the only REE where the spectral results of all three spectrometers do not agree. The results of the *ASD Field Spec 3* and *Perkin Elmer LAMBDA 950* show different absorption feature positions for the measured neodymium powder as the results from the *HySpex*. The number of absorption bands and the pattern of the spectral absorptions feature are the same for all spectrometers. A device failure on the measuring day can be rejected, since the mixtures show the same problem and the measurements of the powder and the mixtures do not took place on the same day (same measurement conditions on both days). The probability of an error on both days is very low, since this problem occurs only for neodymium. The spectral results of the neodymium mixtures measured by the *Perkin Elmer LAMBDA 950* show the same absorption band positions as for the powder with 100% neodymium content. The same behavior is detected by the *HySpex*, where the spectral results of the mixtures agree with the spectral results of the 100% neodymium powder. An error during a post processing step of the *HySpex* data can also be excluded, since the raw and radiance data were examined and show the same spectral pattern as the reflectance spectra. The minerals bastnasite and parisite contain both detectable neodymium content. Several absorption bands can be regarded to be caused by neodymium. The absorption band position of the maxima appears rather at the absorption band positions of neodymium detected by the *HySpex* (100% sample). Yet, the spectral results for the minerals bastnasite and parisite agree for all three spectrometers. The absorption bands show no differences in the wavelength position. Further, the rock sample also contains a detectable concentration of neodymium and the absorption bands, which are caused by neodymium, appear at the same wavelength position as for the minerals and the powder with a concentration of 100% neodymium measured with the *HySpex*. The absorption bands, which are contributed to neodymium in the satellite image of *EO-1 Hyperion* occur rather at the wavelength position of neodymium measured by the *ASD Field Spec 3* and *Perkin Elmer LAMBDA 950*. At this time there is no explanation for the shift of the wavelength position for neodymium in the different spectra. This problem occurs only in the measurements for the REE neodymium, no other REE shows any difference in the spectral results by the *HySpex*, *ASD Field Spec 3* and *Perkin Elmer LAMBDA 950*. It is known that viewing geometries and lighting conditions influence the reflectance of materials. At the first place it was assumed that this problem is caused by such an influence, but that does not explain why it only occurs for neodymium. However, the spectral results of the minerals for all spectrometers agree, which rejects the possibility of any influences of the reflectance by the viewing geometry or lighting conditions during the measurement with the *HySpex*. I assume that the absorption bands of neodymium are not only based on electronic transitions but also on vibrations. The absorption bands of the REO neodymium are probably caused by the oxide. The wavelength shift in the minerals may therefore be the result of the inhomogeneity of the mineral. Meaning that neodymium occurs in the mineral probably in different phases and the combination of the vibrations by different oxides of different elements lead probably to the shift of the maxima absorption in the spectrum. To be sure, the samples would have to be chemically analyzed to

STR 19/08. GFZ German Research Centre for Geosciences
DOI: 10.2312/GFZ.b103-19089

determine the exact composition. Turner et al. [13] observed that carbonate related spectral responses depended on the crystallographic sites and as a consequence distinct absorption bands of the same element shifts within different minerals. Nevertheless, this does not explain why the neodymium powder, measured with different spectrometers, causes the wavelength shifts. On the other hand, it implies that the assumption that the absorption bands of REEs are caused only by electronic field transitions should be reconsidered. To answer this question, further investigations, by for example determining the spectral response of pure REEs, are necessary.

5.3 The Influence of Other Materials on the Detection of REEs

The spectral results of the investigation of the detection of neodymium in presence of iron (III) oxide demonstrates, how important the understanding of the interactions between the different materials and how strong the influence of the REE signal collected by the sensor is.
The variability of different material influences on the neodymium signal is shown by two identical mixtures, at which neodymium is firstly mixed with calcium carbonate and secondly with hematite. The result demonstrates that hematite has a much higher influence on the received signal from neodymium than calcium carbonate. In the mixtures with hematite a neodymium signal can be detected if neodymium reaches a value of 30% and higher. This is a significant difference compared to mixtures with calcium carbonate where the signal of neodymium can be already detected with a concentration of 0.1% neodymium. The measurements of the basic mixtures 1 and 2 indicate how difficult the detection of neodymium in the presence of iron (III) oxide is. Both mixtures contain a low concentration of neodymium values, but they are values that are representative for natural occurrences. From these results it can be concluded that if the concentration of iron (III) oxide is around 2 to 5% and the neodymium content is around 0.5% and lower, the detection of neodymium is not possible. All diagnostic absorption features of neodymium will be suppressed or superimposed, respectively, by the wide and very intense absorption bands of hematite in the VNIR region. In nature hematite can occur together with neodymium at much higher values than 2%. These results demonstrate that in the eventual presence of hematite, an accurate evaluation of the neodymium concentration (by using the absorption depth) exceeds the possibilities by spectral reflectance measurements. Rowan et al. [29] also come to this conclusion in their studies where they detect that limonite causes ferric absorption bands, which may mask other absorption features.

STR 19/08. GFZ German Research Centre for Geosciences
DOI: 10.2312/GFZ.b103-19089

5.4 The Detection of REEs in Mineral Ores

The economically important minerals bastnasite and xenotime show many characteristic absorption features in the VNIR and SWIR region. The absorption features of bastnasite near 522, 579, 676, 740, 798, and 866 nm are probably caused by neodymium. This is supported by the mixture measurements of neodymium, which show, given a neodymium content of around 5%, absorption bands near 523, 578, 683, 745, 800, and 869 nm. Lanthanum could cause and widen the very broad absorption band of water with a maximum near 1541 nm, since lanthanum is characterized by an absorption band near 1419 nm. The major component of the mineral xenotime is yttrium and other HREE. Yttrium has no significant absorption features in this wavelength regions, the diagnostic absorptions in the spectrum of xenotime cannot be caused by the REE by considering the all determined absorption features in this study. However, the characteristic spectrum of the xenotime makes it possible to detect this mineral with reflectance spectroscopy, given the opportunity to find yttrium. The mineral monazite is also economically important, but a characteristic spectrum could not be measured during this study because of the inadequate sample size. However, the mineral monazite should cause a very characteristic spectrum, since the main REEs of this mineral are samarium and neodymium, both showing several diagnostic absorption bands in the VNIR and SWIR region.
Parisite also causes diagnostic absorption bands. The mineral contains the REEs cerium, lanthanum and neodymium. The maximum absorption bands appear at wavelength positions of 580, 741, 799, and 872 nm, probably caused by the REE neodymium. Lanthanum and cerium could be responsible for the absorption bands around 1450 and 1947 nm or at least intensify the absorption (caused probably by water) at this position.
The REE mineral bariopyrochlore shows a characteristic spectra, which are not caused by any REEs, since niobium (component of bariopyrochlore) have no diagnostic absorption features.
Synchysite shows also a characteristic spectrum. The absorption features near 600, 738, 793, 800 and 865 nm are probably caused by neodymium, which is according to the XRF device with a concentration of 0.53% constituent of the sample.
The spectral results of the REE minerals gadolinite and polycrase cannot be evaluated, because of the mineral size (in the case of polycrase) and the high signal to noise ratio (in the case of gadolinite). The spectral response of both minerals is also influenced by the surrounding material, which prevents a spectral characterization.
Aegirine and ilmenite are REE associated minerals. The spectra of both minerals show a lower reflectance in the VNIR and SWIR region and contain different amounts of iron. The detection of REEs in presence of both minerals will probably be difficult as a consequence of the suppression of REE signals by the spectral response of iron.
In conclusion it can be noted that the minerals which contain REEs with diagnostic spectra show several absorption features, which are caused by these elements.

STR 19/08. GFZ German Research Centre for Geosciences
DOI: 10.2312/GFZ.b103-19089

5.5 Theory Versus Approach

The spectral results were applied on different scales. It was investigated whether the characteristic absorption features of REEs can be detected with a lower spectral resolution, because satellites have a smaller number of spectral bands. The spectral resampling on the satellites *EnMAP*, *EO-1 Hyperion* and *HyMap* show that doublet or triplet features appear as one feature with a lower number of spectral bands. Often the maxima of the resampled features shift up to a few nanometers and the intensities are smaller as without the spectral resampling. The spectrally resampled data were based on laboratory reflectance data und here most absorption features of the REEs could be detected. Satellite images are influenced by the atmosphere, topography, and calibration that change the signal received by the sensor [37]. In the Mountain Pass mine the REE concentration is about 5%. Nevertheless, the satellite image of the *Hyperion* shows only very low absorption bands caused by REEs. Though some absorption features in the spectra of the Mountain Pass mine are related to neodymium and samarium, but this assumption cannot be proved. Even if the received signal is caused by REEs, the main reason for the signal degradation are probably the atmospheric influences through scattering and absorption and the characteristics of the sensor *Hyperion*. In summary, it is possible to detect an REE signal by satellite images, but is limited by different factors. Because of a combination of the very low REE concentration in nature and the influences of surrounding materials, atmospheric processes and the characteristics of the sensor the collected signal cannot be clearly associated to REEs. With a better SNR and a higher spectral resolution (e.g. *EnMap*) it is probably possible to detect a more characteristic REE signal. However, the absorption depth in the spectrum from a satellite image does not implicate the real REE concentration.
Another approach was the investigation of REE detection in a rock sample (soevite) from Norway with the *HySpex*. The results demonstrate that it is possible to detect neodymium in that rock sample. This implicates that despite the very low concentration of REEs in nature it is possible to receive an REE signal by the sensor. This was also confirmed by Rowan [29] et al. where absorption features in carbonatites related to neodymium with concentrations of 0.03% neodymium were already detected.

STR 19/08. GFZ German Research Centre for Geosciences
DOI: 10.2312/GFZ.b103-19089

6 Conclusion and Outlook

This study has set out to answer the question whether spectroscopy can be used as a tool for the characterization and hence detection of REEs, taking into account several influencing factors by the environment and sensor characteristics. The results of this study can be summarized by the following statements:

- The REEs lanthanum, neodymium, samarium, europium, terbium, dysprosium, holmium, erbium, thulium, and ytterbium show different absorption bands in the VNIR and SWIR region, even if the concentration of the REE is around 0.1% (except lanthanum and samarium).
- With an increasing concentration of REO the absorption feature of these REEs become more pronounced.
- The REEs cerium, gadolinium, lutetium, yttrium, and tantalum cause two main absorptions at around 1400 and 1900 nm, which are probably caused by water. Niobium also causes two main absorption bands at 1900 and 2200 nm, that would be superimposed by water absorptions.
- No REE causes diagnostic absorption features in higher wavelength than 2500 nm.
- Hematite has a much higher influence on the received signal from neodymium than calcium carbonate.
- The two wide and very intense absorption bands of hematite in the VNIR region suppress or superimpose all diagnostic absorption features of neodymium in this region if the hematite concentration is about 2%.
- Bastnasite and xenotime show several characteristic absorption features in the VNIR and SWIR region.
- REEs can be detected in the spectrum of the Mountain Pass mine in California, but the absorption depth does not implicate the real REE concentration.
- With lower spectral resolutions (e.g. *EnMap*, *Hyperion* and *HyMap*) several diagnostic absorption bands are detectable. Doublet or triplet features appear as one absorption feature with decreasing spectral resolution and the maxima may shift by a few nm.
- In the rock sample from Norway, REE related absorption bands can be detected.

STR 19/08. GFZ German Research Centre for Geosciences
DOI: 10.2312/GFZ.b103-19089

These results have several implications for the use of remote sensing for the detection of REEs. This study demonstrates that REEs cause diagnostic absorption features in the VNIR and SWIR wavelength region, even if the concentration of the REE is very low. The technique of using reflectance spectroscopy for the detection of REEs can be affirmed. Portable spectrometers can be used in fieldwork as a fast and simple method to determine REE contents and make it possible to find REEs without laboratory work. However, it should be kept in mind that the results of the measurements can be affected or totally masked by the surrounding material, meaning that a concentration calculated by the absorption depth does not represent the true value of the REE content. Also the collected REE signal by a satellite sensor should be questioned. Mostly, the low concentration of REEs in nature makes it difficult to detect these elements in any satellite image. However, there are still questions remaining unanswered. More research should be conducted concerning the mineralogy and petrogenesis of rare earth elements to understand the spectral response of these elements. Therefore, pure REEs should be spectroscopically analyzed. This would answer the question whether the absorption bands in the spectrum are caused by electronic field transitions by the REEs or vibrations by the oxides. Such a study would contribute to a better understanding of the spectral response by the different REE minerals in nature. In this study it was also established that with an iron (III) oxide concentration of around 2%, the REE signal is superimposed by the iron (III) oxide signal. In a future study rock samples with a known iron (III) oxide and REE content needed to be measured by different spectrometers to define exactly how this material influences the detection of an REE signal. In the diploma thesis of Nicole Köllner different rock samples are chemically analyzed to answer the question whether the REE concentration measured at the thin rock crust correlates to the REE concentration within the rock. This study helps to understand the detection of REE in the field and also the REE transport in soils.

STR 19/08. GFZ German Research Centre for Geosciences
DOI: 10.2312/GFZ.b103-19089

Bibliography

[1] Alfa Aesar. *A Johnson Matthey Company*. 12.12.2014 16:34. URL: https://www.alfa.com/de/gh100w.pgm.

[2] Thermo Scientific Niton XL3t GOLDD+ XRF Analyzer. *Product Specifications*. 8.03.2015 10:09. URL: http://www.thermoscientific.com/content/dam/tfs/ATG/CAD/CAD%20Documents/Product%20Manuals%20&%20Specifications/Elemental%20Analysis/XRF/D00828~.pdf.

[3] Jones A.P., Wall F., and Williams C.T. *Rare Earth Minerals: Chemistry, Origin and Ore Deposits*. Chapman & Hall, Mineralogical Society Series, 1996.

[4] Norsk Elektro Optikk AS. *HySpex: Imaging Spectrometer, User's Manual*.

[5] Beckhoff B. et al. *Handbook of Practical X-Ray Fluorescence Analysis*. Springer, 2006.

[6] Stuart B.H. *Infrared Spectroscopy: Fundamentals and Applications*. John Wiley & Sons, 2008.

[7] Natural Environment research council British Geological Survey. *Niobium-Tantalum*. 8.03.2015 10:11. URL: https://www.bgs.ac.uk/downloads/start.cfm?id=2033.

[8] Natural Environment research council British Geological Survey. *Rare Earth Elements*. 8.03.2015 20:10. URL: https://www.bgs.ac.uk/downloads/start.cfm?id=1638.

[9] Klein C. and Hurlbut C.S. *Manual of Mineralogy*. John Wiley & Sons, 1993.

[10] Pease C.B. *Satellite Imaging Instruments: Principles, Technologies and Operational Systems*. John Wiley & Sons, 1994.

[11] Mortimer C.E. and Müller U. *Chemie, Das Basiswissen der Chemie*. Thieme, 2001.

[12] Barthelmy D. *Mineralogy Database*. 8.03.2015 10:12. URL: http://webmineral.com/.

[13] Turner D., Rovard B., and Groat L. "Rare Earth Element Ore Grade Estimation of Mineralized Drill Core From Hyperspectral Imaging Spectroscopy". In: *IGARSS* (2014).

[14] Analytical Spectral Devices. *FieldSpec Portable Spectroradiometer*. 8.03.2015 10:15. URL: http://www.asdi.com/products/fieldspec-spectroradiometers.

[15] Analytical Spectral Devices. *FieldSpec Pro Manual (User's Guide)*. 8.03.2015 10:16. URL: http://support.asdi.com/Document/Viewer.aspx?id=19.

[16] Earth Observation Center EOC of DLR. *EnMAP Hyperspectral Imager*. 13.03.2015 10:07. URL: http://www.enmap.org/.

STR 19/08. GFZ German Research Centre for Geosciences
DOI: 10.2312/GFZ.b103-19089

[17] Perkin Elmer. *UV-VIS Spectroscopy: Lambda 650/850/950 Hardware Guide*. 8.03.2015 10:04. URL: https://www2.ul.ie/pdf/234493239.pdf.

[18] Neukirchen F. and Ries G. *Die Welt der Rohstoffe-Lagerstätten, Förderung und wirtschaftliche Aspekte*. Springer Verlag, 2014.

[19] Hunt G.R. and Salisbury J.W. "Visible and Near-Infrared Spectra of Minerals and Rocks: I Silicate Minerals". In: *Modern Geology* 1 (1970).

[20] Günzler H. and Gremlich H.U. *IR Spectroscopy: An Introduction*. WILEY-VCH Verlag, 2002.

[21] Stosch H.G. *Geochemie der Seltenen Erden*. 8.03.2015 10:10. URL: http://institut-seltene-erden.org/wp-content/uploads/2012/03/uni-koeln-geochemie-der-seltenen-erden.pdf.

[22] Honeywell. *Specialty Chemicals Seelze*. 12.12.2014 15:10. URL: http://www.riedeldehaen.de/.

[23] Dai J. et al. "Quantitative Estimation of Concentrations of Dissolved Rare Earth Elements Using Reflectance Spectroscopy". In: *Journal of Applied Remote Sensing* 7 (2013).

[24] Ridley J. *Ore Deposits-Geology*. Cambridge, University Press, 2013.

[25] Guilbert J.M. and Park C.F. *The Geology of Ore Deposits*. W.H. Freeman and Company/New York, 1986.

[26] Salisbury J.W., Walter L.S., and D. Aria. "Mid-Infrared Spectra of Igneous Rocks". In: *Geological Survey* (1974).

[27] Avila L. and Schiering D. *Infrared Spectroscopy: Basic Techniques and Experiments*. Perkin Elmer, 1993.

[28] Laborchemie. *Apolda*. 13.01.20.15 20:13. URL: http://www.laborchemie.de/.

[29] Rowan L.C., Kingston M.J., and Crowley J.K. "Spectral Reflectance of Carbonatites and Related Alkalic Igneous Rocks-Selected Samples from Four North American Localities". In: *Economic Geology* 81 (1986).

[30] Folkman M. et al. "EO-1/Hyperion Hyperspectral Imager Design, Development, Characterization and Calibration". In: *Hyperspectral Remote Sensing of the Land and Atmosphere* (2001).

[31] Gunnar Färber Mineral's. *Minerals From All Over the World*. 14.12.2014 13:28. URL: http://www.seltene-mineralien.de/.

[32] Greenwood N.N. and Earnshaw A. *Chemistry of the Elements*. Butterworth-Heinemann, Elsevier, 2002.

[33] Henderson P. *Rare Earth Element Geochemistry*. Elsevier Science B.V., 1986.

[34] Möller P., Cerný P., and Saupé F. *Lanthanides, Tantalum and Niobium*. Springer Verlag, 1989.

STR 19/08. GFZ German Research Centre for Geosciences
DOI: 10.2312/GFZ.b103-19089

[35] Griffiths P. R. and Haseth J.A. *Fourier Transform Infrared Spectrometry*. John Wiley & Sons, 1986.

[36] Tipler P.A. and Mosca G. *Physik für Wissenschaftler und Ingenieure*. Spektrum, 2009.

[37] Schowengerdt R.A. *Remote Sensing - Models and Methods of Image Processing*. Elsevier, 2007.

[38] Vincent R.K. *Fundamentals of Geological and Environmental Remote Sensing*. Prentice Hall, 1997.

[39] Rudnick R.L. and Gao S. "Composition of the Continental Crust". In: *Elsevier* (2014).

[40] Gupta R.P. *Remote Sensing Geology*. Springer Verlag, 1991.

[41] Thermo Scientific. *Mining and Exploration*. 8.03.2015 10:08. URL: `http://www.niton.com/docs/literature/Mining_Brochure.pdf?sfvrsn=2`.

[42] Haldar S.K. *Mineral Exploration-Principles and Applications*. Elsevier, 2013.

[43] Clocks T. et al. "The HyMap Airborne Hyperspectral Sensor: the System, Calibration and Performance". In: *EARSEL Workshop on Imaging Spectroscopy* (1998).

[44] Lillesand T.M., Kiefer R.W., and Chipman J.W. *Remote Sensing and Image Interpretation*. John Wiles & Sons, 2008.

[45] Zepf V. *Rare Earth Elements, A New Approach to the Nexus of Supply, Demand of Use:Exemplified along the Use of Neodymium in Permant Magnets*. Springer, 2013.

[46] Schuhmann W. *Der große BLV Steine- und Mineralienführer*. BLV Buchverlag, 2013.

[47] Jackson W.D. and Grey C. "Rare-Earth Oxides". In: *U.S. Geological Survey circular; 930-N* (1993).

[48] Rees W.G. *Physical Principles of Remote Sensing*. Cambridge University Press, 2013.

STR 19/08. GFZ German Research Centre for Geosciences
DOI: 10.2312/GFZ.b103-19089

Acknowledgements

I would like to express my thanks to all of the people who contributed to the successful completion of my master thesis at the University of Potsdam and GFZ Potsdam.
First and foremost I offer my sincerest gratitude to my supervisor, Nina Boesche, who supported me throughout my thesis with her patient guidance, encouragement and advice, while also allowing me to work in my own way. Without her knowledge and effort this master thesis would not have been completed or written.
Professor Uwe Altenberger has offered much advice and I am grateful for his help and encouragement during my research.
I would also like to thank all the members of staff at the GFZ Potsdam, especially Dr. Christian Rogass and Christian Mielke, who helped me with broad knowledge and discussions to improve my thesis.
Finally, I would like to acknowledge my friends for their moral support and motivation. They supported me in so many ways and drive me to give my best. My special thanks go here to Anne Papenfuß for the endless hours that we have spent together in the library and in the laboratory. She always patiently answered all my questions and showed much encouragement during ups and downs in my research. Last but not least I would like to express my deep gratitude to my family for their financial support, unending encouragement throughout my life and their faith in me.

STR 19/08. GFZ German Research Centre for Geosciences
DOI: 10.2312/GFZ.b103-19089

Appendix A - REO, Certificate of Analysis

Table A.1: The Table shows the certificate of analysis for the REOs, which were supplied by *Alfa Aesar*.

Lanthanum (III) oxide, REacton	**Product Number: 11272**	**Lot Number: B08X015**
La_2O_3: 99.9996 %	TREO: 99.24 %	Loss on ignition: -
CeO_2/TREO	0.32 ppm	
Pr_6O_{11}/TREO	0.27 ppm	
Nd_2O_3/TREO	0.44 ppm	
Sm_2O_3/TREO	0.97 ppm	
Y_2O_3/TREO	1 ppm	
Fe_2O_3	2 ppm	
CaO	$<$ 10 ppm	
SiO_2	22 ppm	
CuO	$<$ 2 ppm	
NiO	1 ppm	
PbO	1.1 ppm	
Cl	33 ppm	
D10	5.826 μm	
D50	10.7811μm	
D90	18.802 μm	

Cerium (IV) oxide, REacton	**Stock Number: 11327**	**Lot Number: L07S057**
CeO_2: 99.99 %	TREO: 99.26 %	Loss on ignition: 0.73 %
La_2O_3/TREO	0.005 %	
Pr_6O_{11}/TREO	0.001 %	
Nd_2O_3/TREO	0.001 %	
Sm_2O_3/TREO	0.001 %	
Y_2O_3	0.001 %	
Fe_2O_3	0.0009 %	
CaO	0.0050 %	
SiO_2	0.0024 %	
Cl^-	0.005 %	

STR 19/08. GFZ German Research Centre for Geosciences
DOI: 10.2312/GFZ.b103-19089

Neodymium (III) oxide, REacton	**Stock Number: 11250**	**Lot Number: C02W029**
Nd_2O_3: 99.99 % min	TREO: - %	Loss on ignition: - %
Na 1 ppm	Fe 4 ppm	Tb 2 ppm
Mg 2 ppm	Ni 0.2 ppm	Dy 1 ppm
Al 10 ppm	Cu <0.1 ppm	Ho <0.2 ppm
Si 20 ppm	Zn 0.6 ppm	Er <0.2 ppm
K 1 ppm	Y 2 ppm	Tm <0.2 ppm
Ca 4 ppm	La 4 ppm	Yb <0.2 ppm
Sc <0.1 ppm	Ce 4 ppm	Lu <0.2 ppm
Ti <0.1 ppm	Pr 5 ppm	Pb <0.2 ppm
V <0.1 ppm	Sm 2 ppm	Bi <0.1 ppm
Cr <0.1 ppm	Eu <0.4 ppm	Th <0.2 ppm
Mn 0.3 ppm	Gd 10 ppm	U <0.1 ppm

Samarium (III) oxide, REacton	**Product Number: 11229**	**Lot Number: 61200836**
Sm_2O_3: $>$ 99.98 %	TREO: $>$ 98.5 %	Loss on ignition: 1.35 %
Remaining RE-Oxide total	0.02 %	
Fe_2O_3	13 ppm	
NiO	$<$ 1 ppm %	
Co_3O_4	$<$ 1 ppm	
Cr_2O_3	$<$ 1 ppm	

Europium (III) oxide, REacton	**Product Number: 11299**	**Lot Number: A16Z001**
Eu_2O_3: 99.99 %	TREO: 99.62 %	Loss on ignition: 0.18 %
CeO_2	$<$ 2 ppm	
Pr_6O_{11}	$<$ 2 ppm	
Dy_2O_3	$<$ 2 ppm	
La_2O_3	$<$ 2 ppm	
Nd_2O_3	$<$ 2 ppm	
Sm_2O_3	$<$ 2 ppm	
Gd_2O_3	$<$ 2 ppm	
Tb_4O_7	$<$ 2 ppm	
Ho_2O_3	$<$ 2 ppm	
Er_2O_3	$<$ 2 ppm	
Tm_2O_3	$<$ 2 ppm	
Yb_2O_3	$<$ 2 ppm	
Lu_2O_3	$<$ 2 ppm	
Y_2O_3	$<$ 2 ppm	
Ca	5 ppm	
CuO	$<$ 1 ppm	

STR 19/08. GFZ German Research Centre for Geosciences
DOI: 10.2312/GFZ.b103-19089

NiO	$<$ 1 ppm
PbO	$<$ 1 ppm
Fe_2O_3	$<$ 2 ppm
ZnO	$<$ 5 ppm
SiO_2	23 ppm
Cl	$<$ 77 ppm
Al_2O_3	$<$ 10 ppm
D50	3.28 μm

Gadolinium (III) oxide, REacton	**Product Number: 11290**	**Lot Number: A13W016**
Gd_2O_3: $>$ 99.97 wt%	TREO: $>$ 99.52 wt%	Loss on ignition: 0.40 wt%
Remaining RE-Oxide total	$<$ 0.1 %	
Eu_2O_3/REO	0.0008 %	
Dy_2O_3/REO	0.0004 %	
Y_2O_3/REO	0.0003 %	
Tb_4O_7/REO	0.0004 %	
Sm_2O_3/REO	0.0003 %	
Fe_2O_3	0.0002 %	
Ca	0.0015 %	
NiO	0.0001 %	
CuO	0.0001 %	
SiO_2	0.0015 %	
MnO	0.0001 %	
CoO	0.0001 %	
Cr_2O_3	0.0001 %	

Terbium (III,IV) oxide, REacton	**Stock Number: 11208**	**Lot Number: J24Q019**
Tb_4O_7: 99.99 % min	TREO: - %	Loss on ignition: - %
Li $<$ 1 ppm	Fe 3 ppm	Eu $<$ 1 ppm
Na 2 ppm	Co $<$ 1 ppm	Gd 8 ppm
Mg $<$ 1 ppm	Ni $<$ 1 ppm	Dy 1 ppm
Al $<$ 1 ppm	Zn $<$ 1 ppm	Er 2 ppm
Si 20 ppm	Y 2 ppm	Tm $<$0.2 ppm
P $<$ 1 ppm	Sr $<$ 1 ppm	Tm 0.5 ppm
S 5 ppm	Y 3 ppm	Yb 20 ppm
K $<$ 1 ppm	Ba $<$ 1 ppm	Lu 1 ppm
Ca 10 ppm	La 1 ppm	Hg $<$ 1 ppm
Ti $<$ 1 ppm	Ce $<$ 1 ppm	Pb $<$ 1 ppm
V $<$ 1 ppm	Pr $<$ 1 ppm	Bi $<$ 1 ppm
Cr $<$ 1 ppm	Nd $<$ 1 ppm	Th $<$ 0.2 ppm
Mn $<$ 1 ppm	Sm 4 ppm	U $<$ 0.3 ppm

STR 19/08. GFZ German Research Centre for Geosciences
DOI: 10.2312/GFZ.b103-19089

Dysprosium (III) oxide, REacton	**Product Number: 11319**	**Lot Number: 61300733**
Dy_2O_3: 99.91 %	TREO: 99.5 %	Loss on ignition: 0.49 %
Remaining RE-Oxide total	$<$ 0.09 %	
Fe_2O_3	41 ppm	
Co_3O_4	$<$ 1 ppm	
NiO	$<$ 1 ppm	
CuO	$<$ 1 ppm	

Holmium (III) oxide, REacton	**Product Number: 11280**	**Lot Number: J11X030**
Ho_2O_3: $>$ 99.9 %	TREO: $>$ 99 %	Loss on ignition: 1 %
Er_2O_3	0.005 %	
Dy_2O_3	$<$ 0.001 %	
Yb_2O_3	0.001 %	
Y_2O_3	0.002 %	
Fe_2O_3	0.001 %	
CaO	0.006 %	
SiO_2	0.0025 %	

Erbium (III) oxide, REacton	**Product Number: 11310**	**Lot Number: 61000356**
Er_2O_3: $>$99.9 %	TREO: 99.8 %	Loss on ignition: 0.13 %
Remaining RE-Oxide total	$<$ 0.1 %	
Fe_2O_3	$<$ 5 ppm	
V_2O_5	$<$ 2 ppm	
TiO_2	$<$ 2 ppm	
Co_3O_4	$<$ 2 ppm	
NiO	$<$ 2 ppm	
Particle size d50	$<$ 9.59 μm	

Thulium (III) oxide, REacton	**Stock Number: 11198**	**Lot Number: F25S060**
Tm_2O_3: 99.99 % min	TREO: - %	Loss on ignition: - %
Si 20 ppm	Zn $<$ 2 ppm	Dy $<$ 10 ppm
Ca $<$ 5 ppm	Y $<$ 10 ppm	Ho $<$ 50 ppm
Sc $<$ 1 ppm	La $<$ 10 ppm	Er $<$ 200 ppm
Ti $<$ 5 ppm	Ce $<$ 10 ppm	Yb $<$ 100 ppm
V $<$ 5 ppm	Pr $<$ 10 ppm	Lu $<$ 100 ppm
Cr $<$ 5 ppm	Nd $<$ 10 ppm	Hg $<$ 1 ppm
Mn $<$ 5 ppm	Sm $<$ 10 ppm	Pb $<$ 1 ppm
Fe $<$ 10 ppm	Eu $<$ 10 ppm	Bi $<$ 1 ppm
Ni $<$ 5 ppm	Gd $<$ 50 ppm	Th $<$ 1 ppm

STR 19/08. GFZ German Research Centre for Geosciences
DOI: 10.2312/GFZ.b103-19089

Cu $<$ 5 ppm	Tb $<$ 10 ppm	U $<$ 1 ppm

Ytterbium (III) oxide, REacton	**Product Number: 11191**	**Lot Number: 61201069**
Yb_2O_3: $>$ 99.99 %	TREO: 99.2 %	Loss on ignition: 0.7 %
Remaining RE-Oxide total	$<$ 0.01 %	
Fe_2O_3	$<$ 2 ppm %	
CaO	29 ppm	
Co_3O_4	$<$ 2 ppm	
NiO	$<$ 2 ppm	
PSD (Microtrac Y100-SRA)	$d_{50}5.38\mu m$	

Lutetium (III) oxide, REacton	**Product Number: 11255**	**Lot Number: G14X082**
Lu_2O_3: 99.97 % min	TREO: 99.00 % min	Loss on ignition: 1 % max
Fe_2O_3	0.0003 %	
SiO_2	0.0028 %	
CaO	0.0078 %	
Er_2O_3	0.0040 % max	
Tm_2O_3	0.0020 % max	
Yb_2O_3	0.020 % max	
Y_2O_3	0.0020 % max	

STR 19/08. GFZ German Research Centre for Geosciences
DOI: 10.2312/GFZ.b103-19089

Appendix B - REO Mixture, Values of the Weighted Portion

Table B.1: The Table shows the values of the weighted portion of the REO mixtures for each REO, including the additional mixutres of neodymium with hematite and both basic mixtures 1 and 2.

Rare Earth Mixture	REO in g	REO in %	$CaCO_3$ in g	$\sum$ in g
Lanthanum	0.0015	0.15	1.0098	1.0073
	0.0046	0.46	1.0081	1.0127
	0.0112	1.12	0.9966	1.0078
	0.0200	2.00	0.9942	1.0142
	0.0503	5.03	0.9667	1.0130
	0.1028	10.28	0.9139	1.0167
	0.1997	19.97	0.8139	1.0136
	0.2940	29.40	0.7169	1.0109
	0.5074	50.74	0.518	1.0362
	0.6900	69.00	0.3225	1.0125
	0.8208	82.08	0.1896	1.0104
	0.9451	94.51	0.0644	1.0095
Cerium	0.0013	0.13	1.001	1.0021
	0.0048	0.48	0.998	1.0028
	0.0110	1.10	0.9913	1.0023
	0.0267	2.67	0.9733	1.0000
	0.0511	5.11	0.9595	1.0106
	0.1010	10.10	0.9043	1.0053
	0.2093	20.93	0.7941	1.0034
	0.3050	30.50	0.7018	1.0068
	0.5051	50.51	0.4972	1.0023
	0.7023	70.23	0.3213	1.0254
	0.8378	83.78	0.19	1.0278
	0.9567	95.67	0.0453	1.0050
Neodymium	0.0011	0.11	1.0019	1.0030
(Calciumcarbonat)	0.0054	0.54	0.9953	1.0007
	0.0118	1.18	0.9977	1.0095

STR 19/08. GFZ German Research Centre for Geosciences
DOI: 10.2312/GFZ.b103-19089

Rare Earth Mixture	**REO in g**	**REO in %**	$CaCO_3$ **in g**	$\sum$ **in g**
	0.0203	2.03	0.9798	1.0001
	0.0503	5.03	0.9564	1.0067
	0.1088	10.88	0.8962	1.0050
	0.2017	20.17	0.8002	1.0019
	0.3010	30.10	0.7064	1.0074
	0.5025	50.25	0.5073	1.0098
	0.7055	70.55	0.298	1.0035
	0.8028	80.28	0.2004	1.0032
	0.9558	95.58	0.0464	1.0022
Neodymium	0.0024	0.24	1.0012	1.0036
(Hematite)	0.0058	0.58	0.9992	1.0050
	0.0103	1.03	0.9959	1.0062
	0.0216	2.16	0.1239	1.1455
	0.0586	5.86	0.9499	1.0085
	0.1044	10.44	0.9024	1.0068
	0.2045	20.45	0.7969	1.0014
	0.3122	31.22	0.6922	1.0044
	0.5076	50.76	0.4953	1.0029
	0.7063	70.63	0.3036	1.0099
	0.8190	81.90	0.1816	1.0006
	0.9460	94.60	0.0565	1.0029
Neodymium	**hematite in g**	**hematite in %**	$Nd + CaCO_3$ **in g**	$\sum$ **in g**
Basic mixture 1	0.0012	0.12	0.9994	1.0006
$(Nd0.1\%, CaCO_3 99.9\%)$	0.0058	0.58	1.0057	1.0115
	0.0107	1.07	0.9906	1.0013
	0.0208	2.08	0.9819	1.0027
	0.0523	5.23	0.9492	1.0015
	0.1037	10.37	0.9006	1.0043
Basic mixture 2	0.0011	0.11	0.9993	1.0004
$(Nd0.5\%, CaCO_3 99.5\%)$	0.0057	0.57	0.9974	1.0031
	0.0122	1.22	0.989	1.0012
	0.0222	2.22	0.988	1.0102
	0.0501	5.01	0.9517	1.0018
	0.1009	10.09	0.9048	1.0057
Rare Earth Mixture	**REO in g**	**REO in %**	$CaCO_3$ **in g**	$\sum$ **in g**
Samarium	0.0011	0.11	1.001	1.0021
	0.0056	0.56	0.997	1.0026
	0.0122	1.22	0.9898	1.0020
	0.0243	2.43	0.9796	1.0039

STR 19/08. GFZ German Research Centre for Geosciences
DOI: 10.2312/GFZ.b103-19089

Rare Earth Mixture	REO in g	REO in %	$CaCO_3$ in g	$\sum$ in g
	0.0522	5.22	0.9509	1.0031
	0.1002	10.02	0.9086	1.0088
	0.2025	20.25	0.8094	1.0119
	0.3016	30.16	0.7026	1.0043
	0.5042	50.42	0.5006	1.0078
	0.7015	70.15	0.3005	1.0022
	0.8001	80.01	0.2093	1.0094
	0.9514	95.14	0.0516	1.0003
Europium	0.0016	0.16	1.0025	1.0041
	0.0065	0.65	0.9941	1.0006
	0.0110	1.10	1.0121	1.0231
	0.0218	2.18	0.9822	1.0040
	0.0507	5.07	0.9501	1.0008
	0.1031	10.31	0.9055	1.0086
	0.2011	20.11	0.8108	1.0119
	0.3019	30.19	0.6992	1.0011
	0.5025	50.25	0.5017	1.0042
	0.7007	70.07	0.3229	1.0236
	0.8025	80.25	0.199	1.0015
	0.9524	95.24	0.476	1.0000
Gadolinium	0.0012	0.12	1.0251	1.0263
	0.0057	0.57	1.0057	1.0114
	0.0137	1.37	1.0078	1.0215
	0.0208	2.08	0.9804	1.0012
	0.0549	5.49	0.9523	1.0072
	0.1008	10.08	0.9054	1.0062
	0.2272	22.72	0.8286	1.0958
	0.3004	30.04	0.79	1.0004
	0.5043	50.43	0.5017	1.0060
	0.7008	70.08	0.3176	1.0184
	0.8142	81.42	0.1972	1.0114
	0.9484	94.84	0.0596	1.0080
Terbium	0.0009	0.09	1.0157	1.0166
	0.0068	0.68	1.0183	1.0251
	0.0136	1.36	1.0176	1.0312
	0.0197	1.97	1.0616	1.0818
	0.0514	5.14	0.949	1.0004
	0.1155	11.55	0.8905	1.0060
	0.2275	22.75	0.777	1.0054
	0.3086	30.86	0.6936	1.0022

STR 19/08. GFZ German Research Centre for Geosciences
DOI: 10.2312/GFZ.b103-19089

Rare Earth Mixture	REO in g	REO in %	$CaCO_3$ in g	$\sum$ in g
	0.5097	50.97	0.4975	1.0054
	0.7049	70.49	0.2973	1.0022
	0.8073	80.73	0.2036	1.0010
Dysprosium	0.0017	0.17	1.0175	1.0192
	0.0068	0.68	0.9989	1.0057
	0.0125	1.25	0.9888	1.0013
	0.0268	2.68	0.9843	1.0111
	0.0550	5.50	0.9652	1.0202
	0.1137	11.37	0.9018	1.0155
	0.2080	20.80	0.7943	1.0023
	0.3003	30.03	0.7163	1.0166
	0.5225	52.25	0.5108	1.0333
	0.6999	69.99	0.3138	1.0137
	0.8045	80.45	0.2388	1.0433
	0.9568	95.68	0.049	1.0098
Holmium	0.0009	0.09	1.0029	1.0038
	0.0058	0.58	0.9945	1.0003
	0.0116	1.16	0.9938	1.0054
	0.0205	2.05	0.9831	1.0036
	0.0526	5.26	0.9487	1.0013
	0.1012	10.12	0.9082	1.0094
	0.1994	19.94	0.8051	1.0045
	0.2985	29.85	0.7024	1.0009
	0.5014	50.14	0.501	1.0024
	0.6994	69.94	0.3206	1.0200
	0.8032	80.32	0.1984	1.0016
	0.9491	94.91	0.0669	1.0160
Erbium	0.0014	0.14	1.0016	1.0030
	0.0051	0.51	0.9999	1.0050
	0.0127	1.27	0.9922	1.0049
	0.0223	2.23	0.9782	1.0005
	0.0505	5.05	0.9527	1.0032
	0.1008	10.08	0.9079	1.0087
	0.2014	20.14	0.8017	1.0031
	0.3036	30.36	0.7043	1.0079
	0.5003	50.03	0.5012	1.0015
	0.7130	71.30	0.2937	1.0067
	0.8091	80.91	0.2356	1.0447
	0.9647	96.47	0.0361	1.0008
Thulium	0.0021	0.21	1.0033	1.0054

STR 19/08. GFZ German Research Centre for Geosciences
DOI: 10.2312/GFZ.b103-19089

Rare Earth Mixture	REO in g	REO in %	$CaCO_3$ in g	$\sum$ in g
	0.0056	0.56	1.0343	1.0399
	0.0122	1.22	1.0558	1.0680
	0.0205	2.05	0.9917	1.0122
	0.0558	5.58	0.9623	1.0181
	0.1060	10.60	0.9455	1.0013
	0.2023	20.23	0.8587	1.0610
	0.3269	32.69	0.6821	1.0090
Ytterbium	0.0009	0.09	1.009	1.0093
	0.0050	0.50	0.9998	1.0048
	0.0102	1.02	0.9915	1.0017
	0.0212	2.12	0.9803	1.0015
	0.0544	5.44	0.9628	1.0172
	0.1031	10.31	0.902	1.0051
	0.2157	21.57	0.7895	1.0052
	0.3111	31.11	0.6962	1.0073
	0.4998	49.98	0.5097	1.0086
	0.7023	70.23	0.3163	1.0186
	0.8142	81.42	0.1858	1.0000
	0.9616	96.16	0.389	1.0005
Lutetium	0.0011	0.11	1.0149	1.0160
	0.0064	0.64	0.997	1.0034
	0.0110	1.10	0.9927	1.0037
	0.0228	2.28	0.9883	1.0111
	0.0517	5.17	1.0765	1.1282
	0.1048	10.48	0.9096	1.0144
	0.2077	20.77	0.8315	1.0392
	0.3054	30.54	0.695	1.0004
Yttrium	0.0010	0.10	0.9993	1.0003
	0.0065	0.65	0.9996	1.0061
	0.0103	1.03	0.991	1.0013
	0.0256	2.56	0.9851	1.0107
	0.0531	5.31	0.9643	1.0174
	0.1012	10.12	0.899	1.0002
	0.2097	20.97	0.8114	1.0211
	0.2992	29.92	0.7092	1.0084
	0.5015	50.15	0.5001	1.0016
	0.7192	71.92	0.2819	1.0002
	0.8114	81.14	0.2226	1.0340
	0.9595	95.95	0.0423	1.0018
Niobium	0.0017	0.17	1.0014	1.0031

STR 19/08. GFZ German Research Centre for Geosciences
DOI: 10.2312/GFZ.b103-19089

Rare Earth Mixture	REO in g	REO in %	$CaCO_3$ in g	$\sum$ in g
	0.0056	0.56	0.9975	1.0031
	0.0117	1.17	0.9912	1.0029
	0.0214	2.14	0.9881	1.0039
	0.0492	4.92	0.9534	1.0026
	0.1017	10.17	0.9084	1.0101
	0.1938	19.38	0.8116	1.0054
	0.2986	29.86	0.7049	1.0035
	0.5022	50.22	0.5018	1.0040
	0.7022	70.22	0.3001	1.0025
	0.8058	80.58	0.1963	1.0021
	0.9496	94.96	0.0527	1.0023
Tantalum	0.0017	0.17	1.006	1.0077
	0.0074	0.74	1.0028	1.0102
	0.0147	1.47	0.9984	1.0131
	0.0211	2.11	0.9819	1.0030
	0.0515	5.15	0.9771	1.0028
	0.1019	10.19	0.9003	1.0094
	0.2069	20.69	0.8177	1.0246
	0.3187	31.87	0.6822	1.0009
	0.5110	51.10	0.5082	1.0192
	0.7022	70.22	0.3004	1.0026
	0.8039	80.39	0.2201	1.0247
	0.9546	95.46	0.047	1.0016

STR 19/08. GFZ German Research Centre for Geosciences
DOI: 10.2312/GFZ.b103-19089

Appendix C - REO, Spectral Results and Absorption Depth, Plots

STR 19/08. GFZ German Research Centre for Geosciences
DOI: 10.2312/GFZ.b103-19089

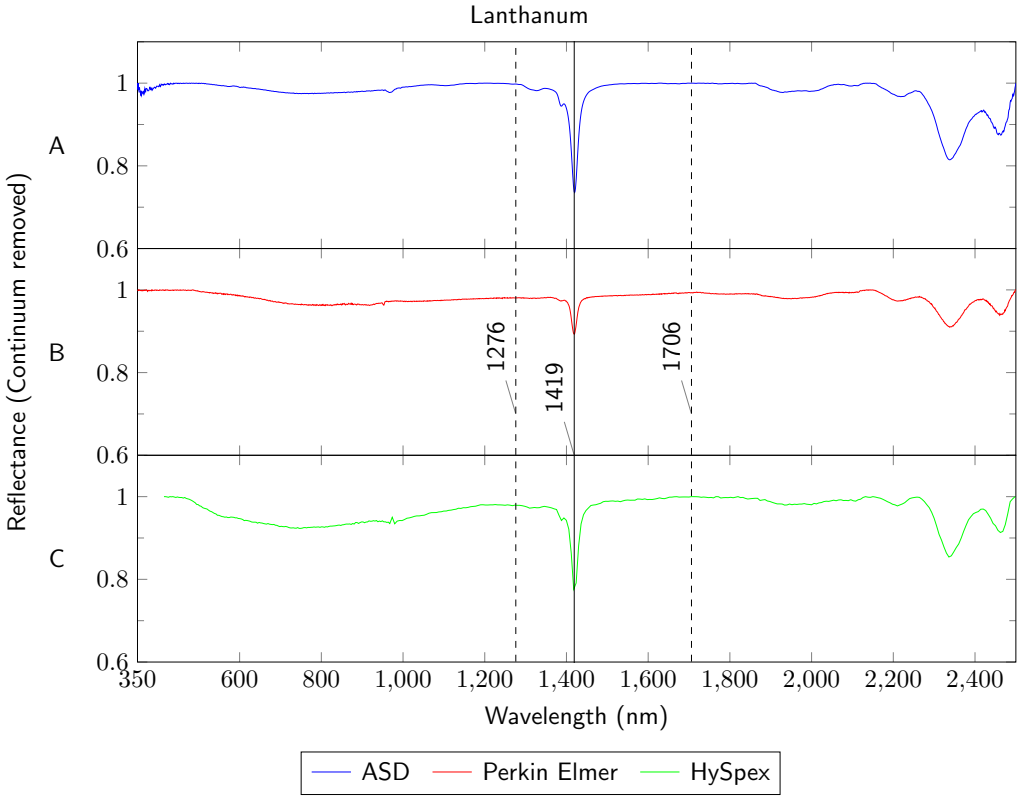

Figure C.1: Reflectance spectra for the REO lanthanum for the VNIR and SWIR region. The Figure shows the results from the measurements of the three spectrometer (***(A)*** *ASD Field Spec 3,* ***(B)*** *Perkin Elmer LAMBDA 950,* ***(C)*** *HySpex (VNIR-1600, SWIR-320m-e)*). The maxima (solid line) and shoulders (dashed line) are marked.

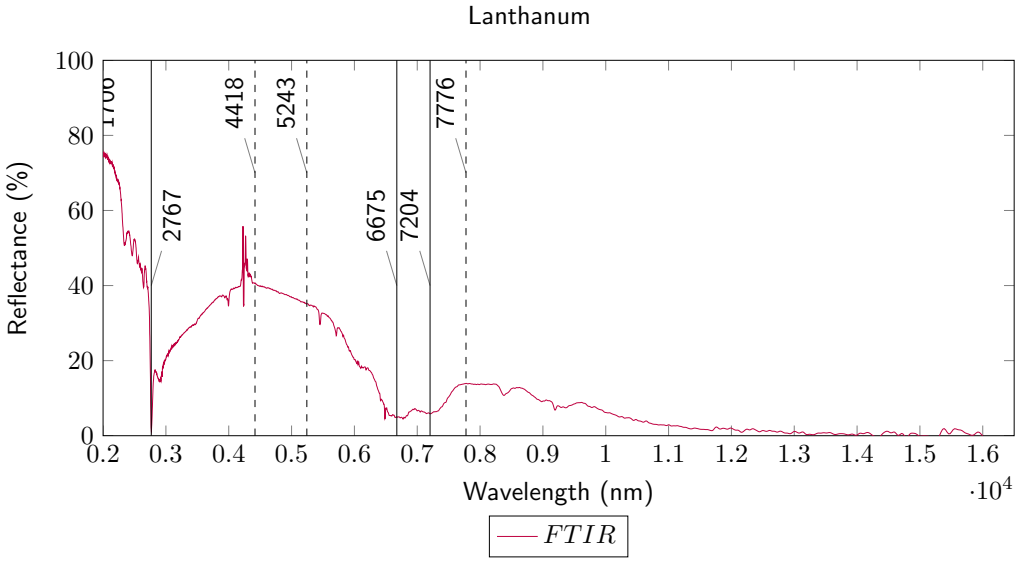

Figure C.2: Reflectance spectrum for the REO lanthanum for the TIR region. The Figure shows the results from the measurement with the *FTIR Spectrum GX*. The maxima (solid line) and shoulders (dashed line) are marked.

STR 19/08. GFZ German Research Centre for Geosciences
DOI: 10.2312/GFZ.b103-19089

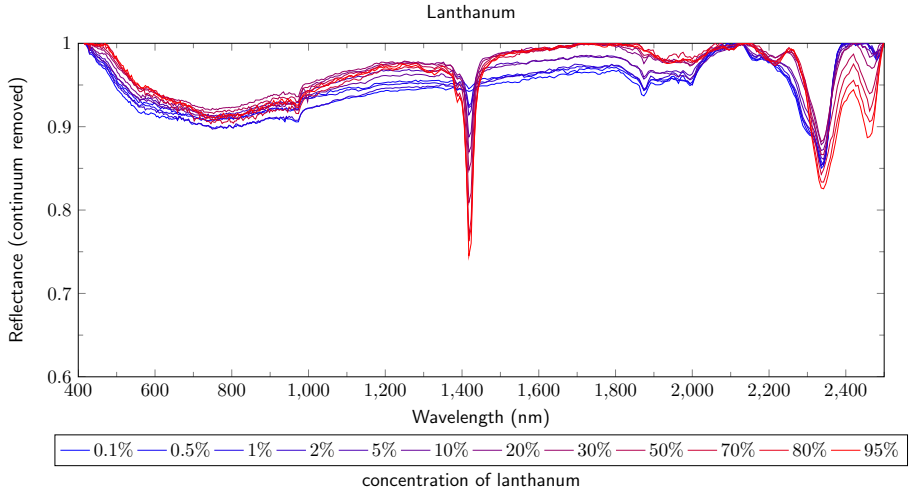

Figure C.3: Reflectance spectra for the REO lanthanum for the VNIR and SWIR region. The Figure shows the results from the measurement of the *HySpex (VNIR-1600, SWIR-320m-e)*. The spectra of all samples are colored from high (red) to low (blue) according to the concentration of lanthanum.

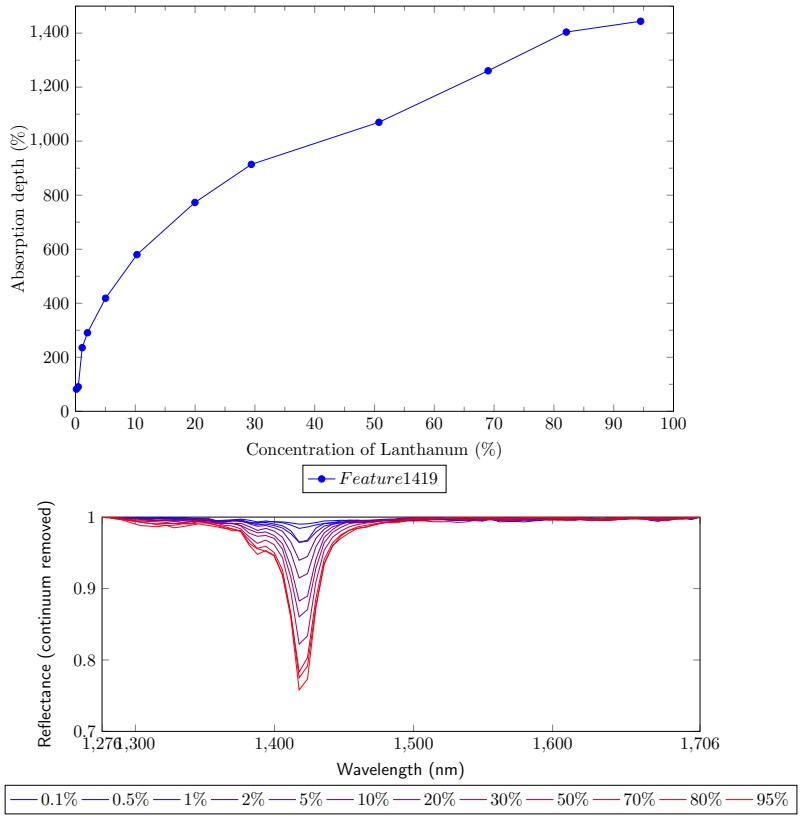

Figure C.4: The Figure **above** shows the correlation between the concentration of lanthanum and the absorption depth of the feature at 1419 nm. The results are from the measurement of the *HySpex (VNIR-1600, SWIR-320m-e)*. The Figure **below** shows the reflectance and depth of the absorption feature at 1914 nm.

STR 19/08. GFZ German Research Centre for Geosciences
DOI: 10.2312/GFZ.b103-19089

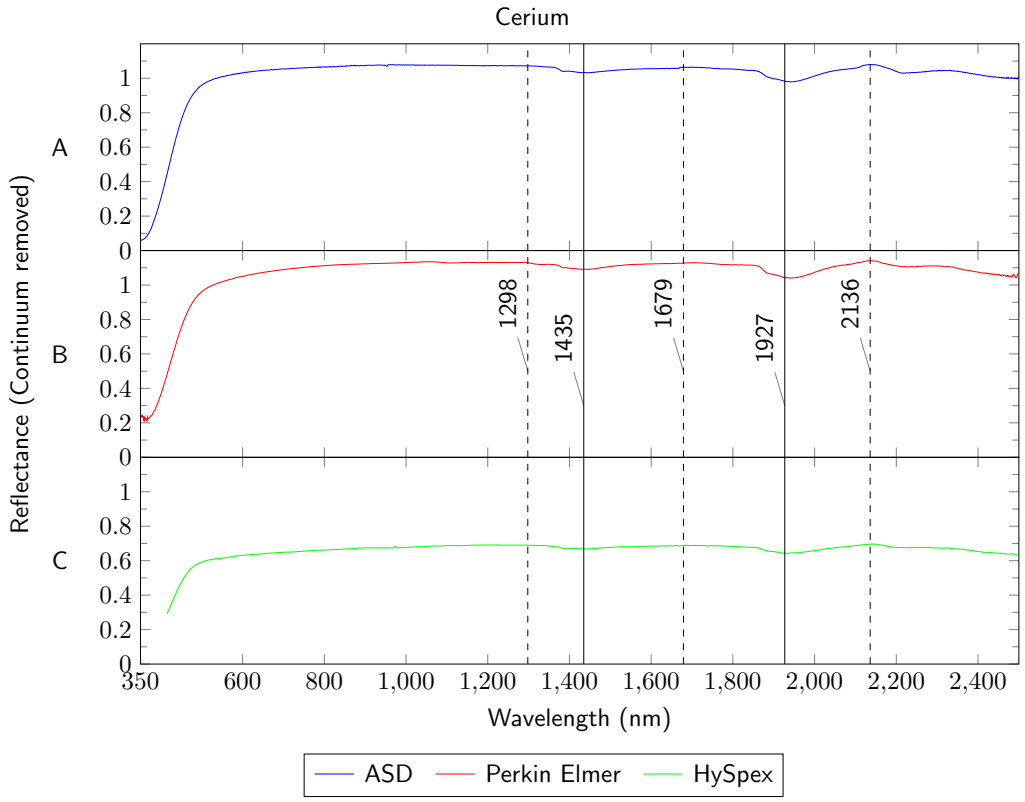

Figure C.5: Reflectance spectra for the REO cerium for the VNIR and SWIR region. The Figure shows the results from the measurements of the three spectrometer (***(A)*** *ASD Field Spec 3,* ***(B)*** *Perkin Elmer LAMBDA 950,* ***(C)*** *HySpex (VNIR-1600, SWIR-320m-e)*). The maxima (solid line) and shoulders (dashed line) are marked.

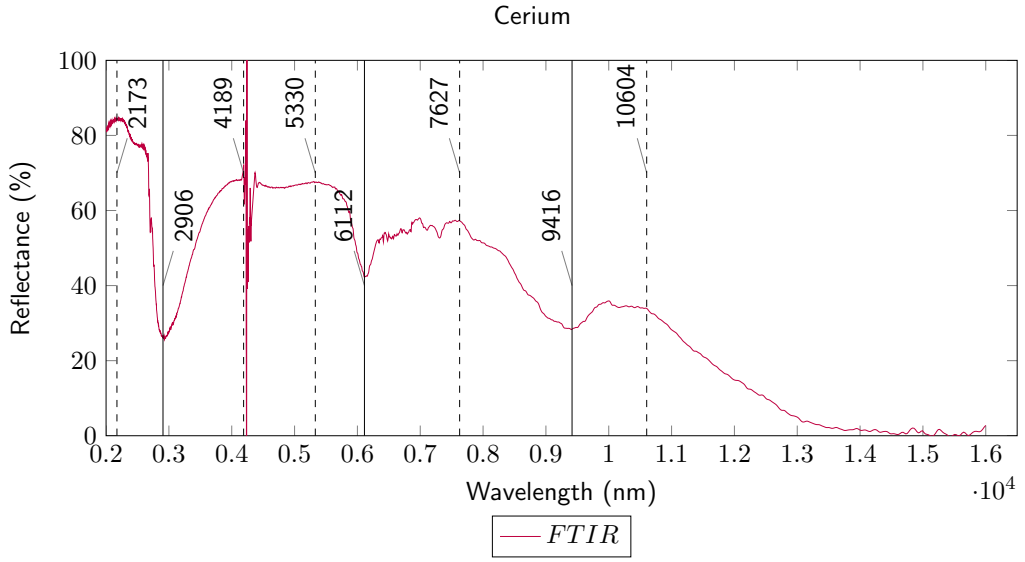

Figure C.6: Reflectance spectrum for the REO cerium for the TIR region. The Figure shows the results from the measurement with the *FTIR Spectrum GX*. The maxima (solid line) and shoulders (dashed line) are marked.

STR 19/08. GFZ German Research Centre for Geosciences
DOI: 10.2312/GFZ.b103-19089

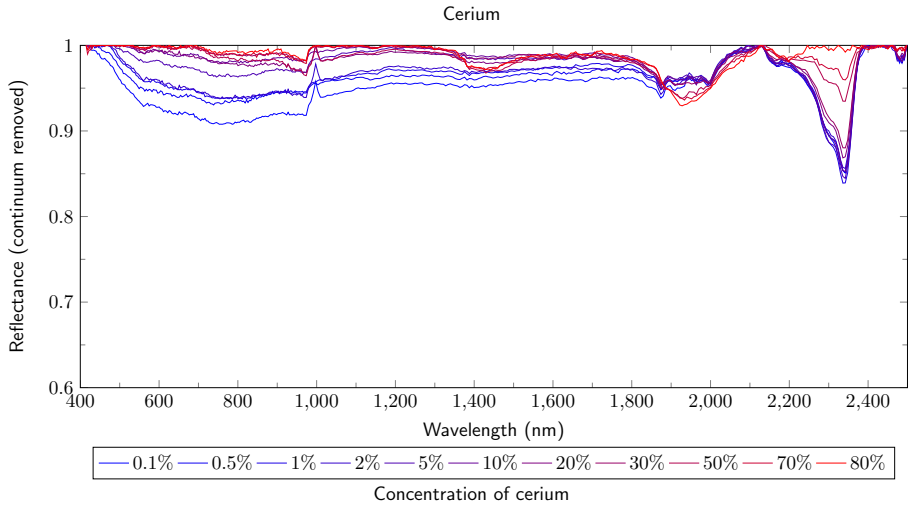

Figure C.7: Reflectance spectra for the REO cerium for the VNIR and SWIR region. The Figure shows the results from the measurement of the *HySpex (VNIR-1600, SWIR-320m-e)*. The spectra of all samples are colored from high (red) to low (blue) according to the concentration of cerium.

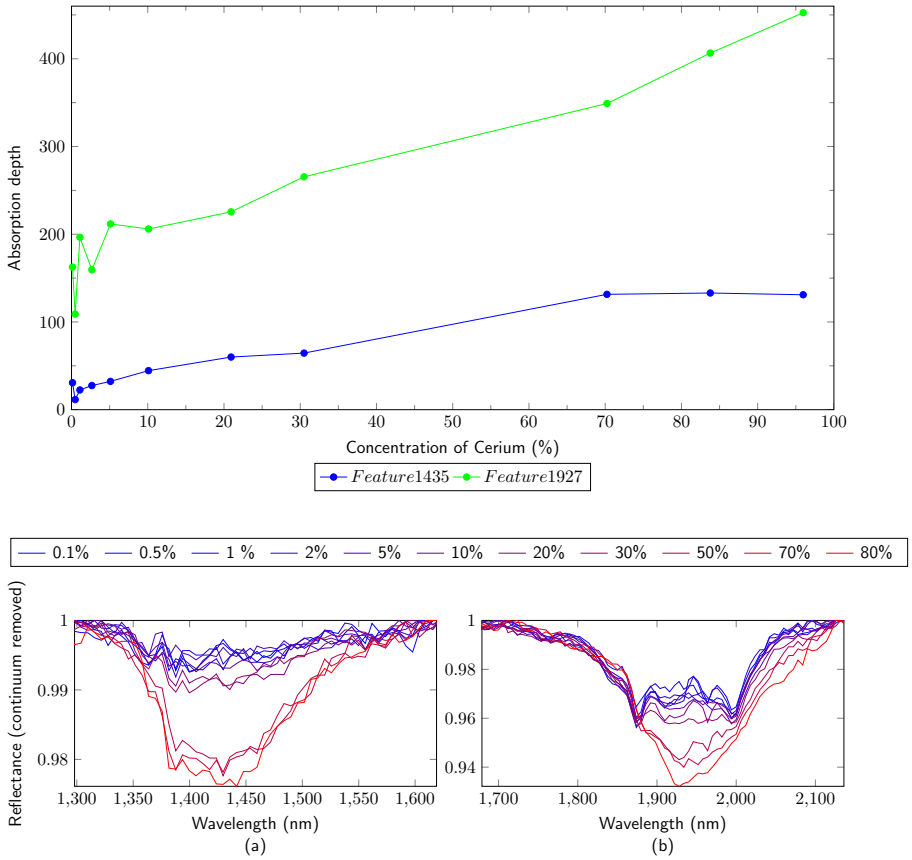

Figure C.8: The Figure **above** shows the correlation between the concentration of cerium and the absorption depth of the features at 1435 and 1927 nm. The results are from the measurement of the *HySpex (VNIR-1600, SWIR-320m-e)*. The Figure **(a)** shows the reflectance and depth of the absorption feature at 1435 nm. The Figure **(b)** shows the reflectance and depth of the absorption feature at 1927 nm.

STR 19/08. GFZ German Research Centre for Geosciences
DOI: 10.2312/GFZ.b103-19089

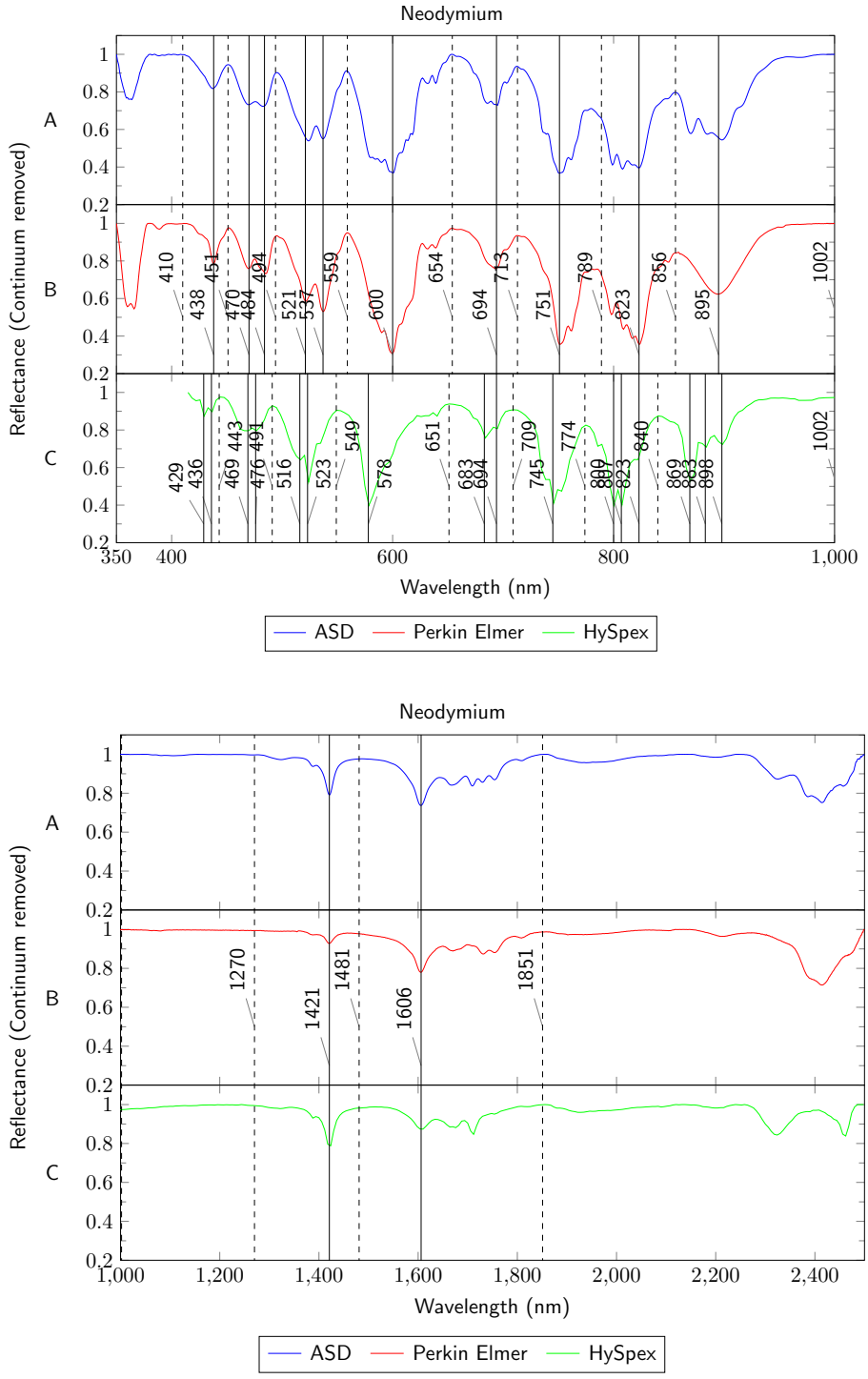

Figure C.9: Reflectance spectra for the REO neodymium for the VNIR and SWIR region. The Figure **above** shows the results from the measurements of the three spectrometer (***(A)*** *ASD Field Spec 3,* ***(B)*** *Perkin Elmer LAMBDA 950,* ***(C)*** *HySpex (VNIR-1600, SWIR-320m-e)*) in a wavelentgh region from 350 to 1000 nm. The Figure **below** shows the results from the measurements of the three spectrometer (***(A)*** *ASD Field Spec 3,* ***(B)*** *Perkin Elmer LAMBDA 950,* ***(C)*** *HySpex (VNIR-1600, SWIR-320m-e)*) in a wavelentgh region from 1000 to 2500 nm. The maxima (solid line) and shoulders (dashed line) are marked.

STR 19/08. GFZ German Research Centre for Geosciences
DOI: 10.2312/GFZ.b103-19089

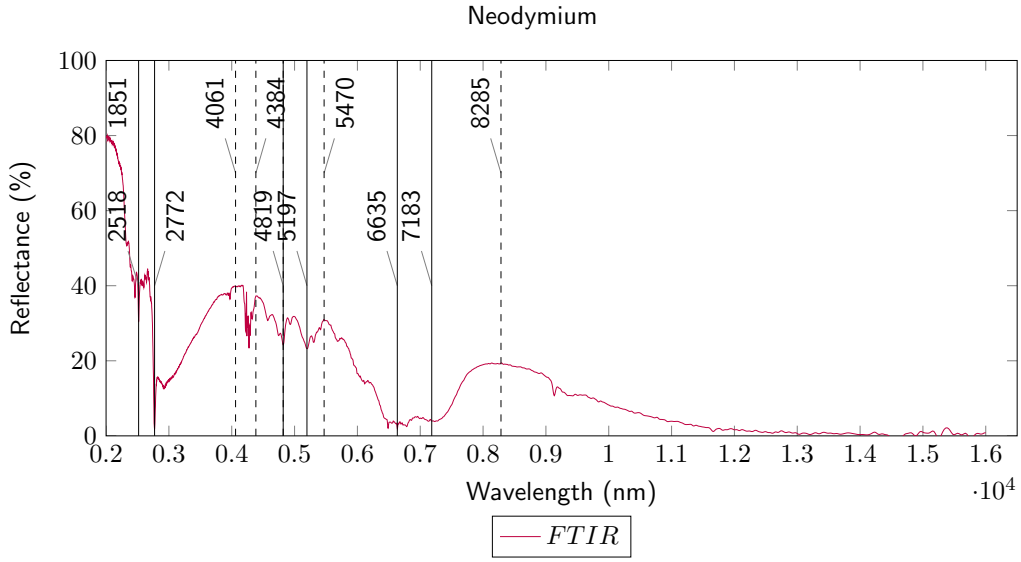

Figure C.10: Reflectance spectrum for the REO neodymium for the TIR region. The Figure shows the results from the measurement with the *FTIR Spectrum GX*. The maxima (solid line) and shoulders (dashed line) are marked.

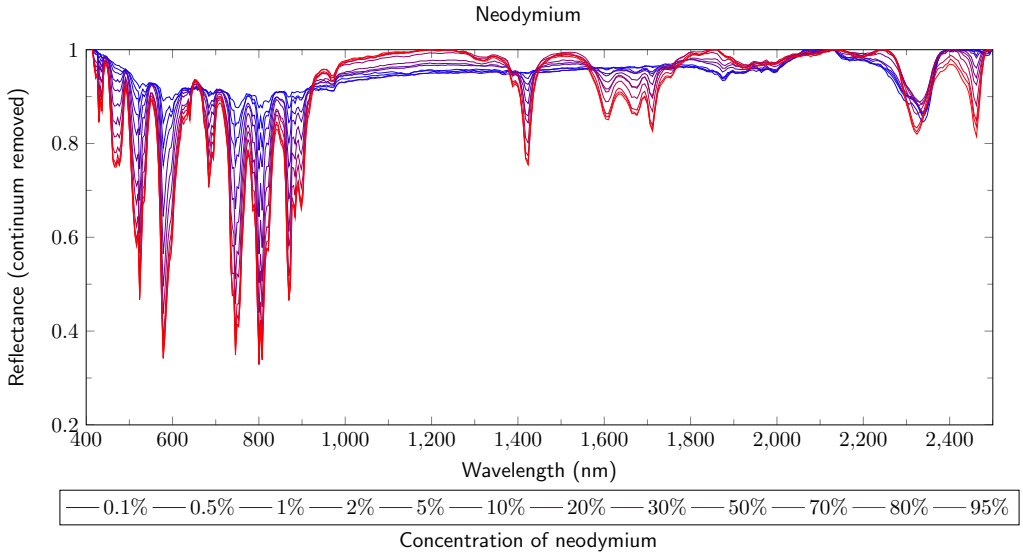

Figure C.11: Reflectance spectra for the REO neodymium for the VNIR and SWIR region. The Figure shows the results from the measurement of the *HySpex (VNIR-1600, SWIR-320m-e)*. The spectra of all samples are colored from high (red) to low (blue) according to the concentration of neodymium.

STR 19/08. GFZ German Research Centre for Geosciences
DOI: 10.2312/GFZ.b103-19089

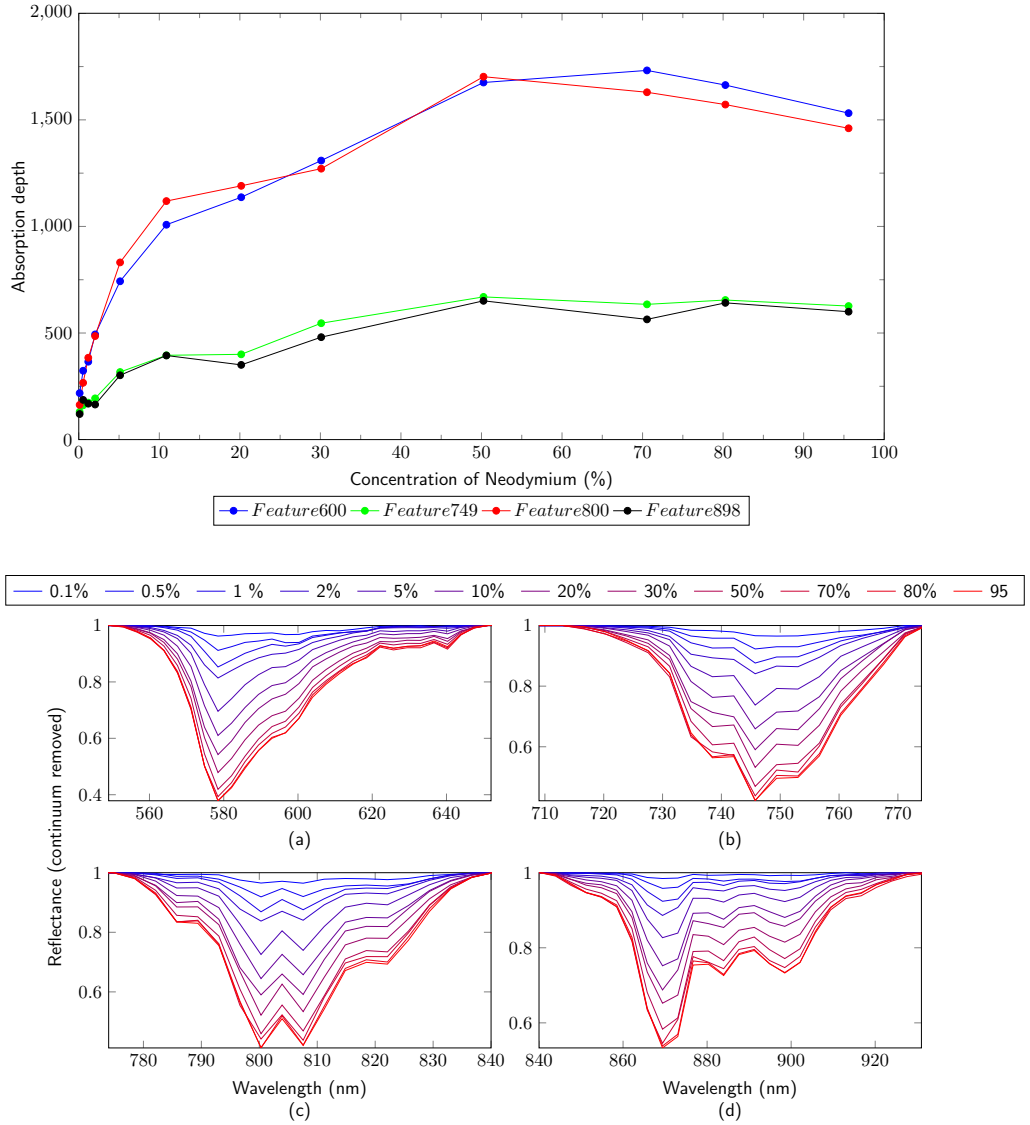

Figure C.12: The Figure **above** shows the correlation between the concentration of neodymium and the absorption depth of the features at 600, 749, 800 and 898 nm. The results are from the measurement of the *HySpex (VNIR-1600, SWIR-320m-e)*. The Figure **(a)** shows the reflectance and depth of the absorption feature at 600 nm. The Figure **(b)** shows the reflectance and depth of the absorption feature at 749 nm. The Figure **(c)** shows the reflectance and depth of the absorption feature at 800 nm. The Figure **(d)** shows the reflectance and depth of the absorption feature at 898 nm.

STR 19/08. GFZ German Research Centre for Geosciences
DOI: 10.2312/GFZ.b103-19089

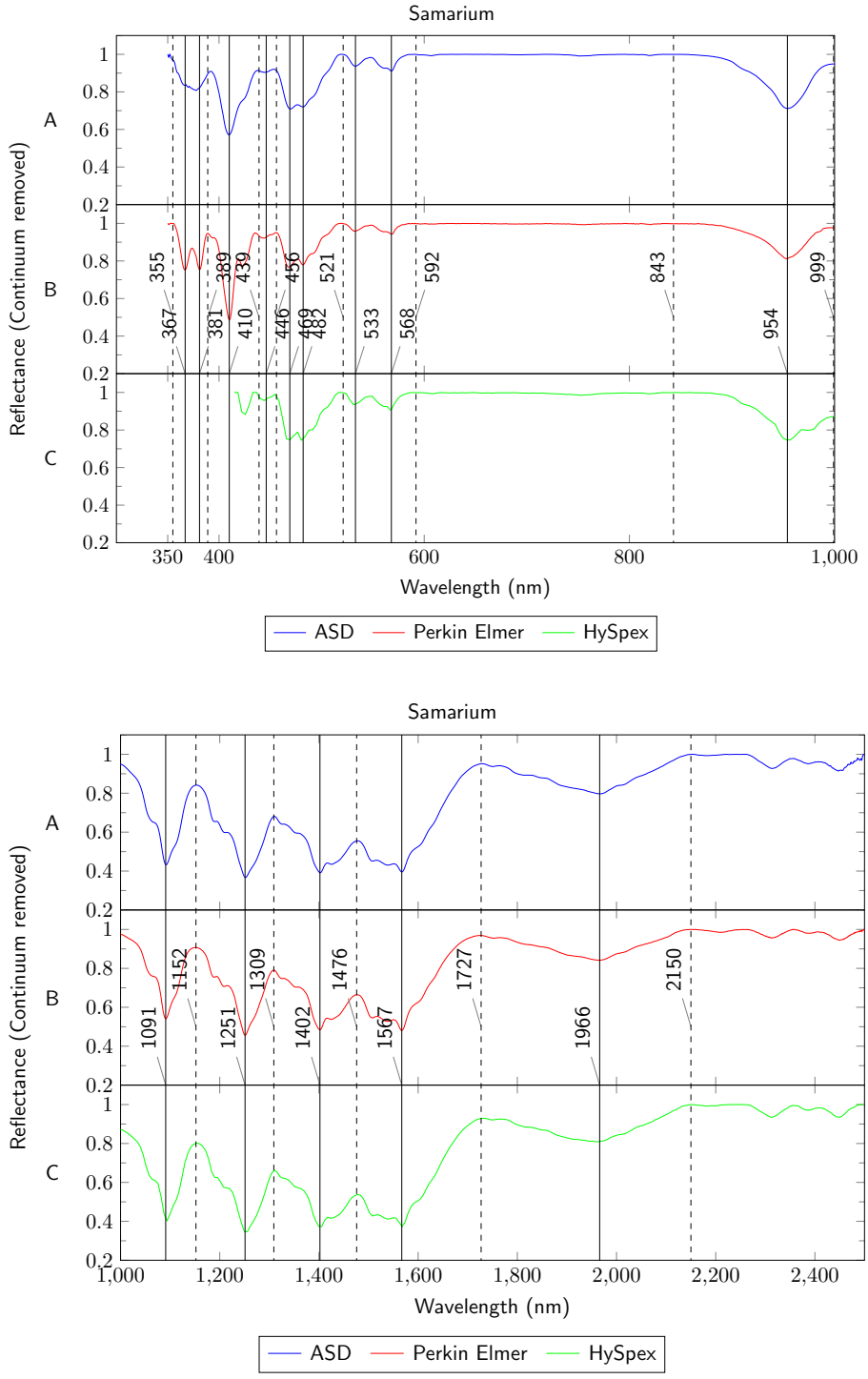

Figure C.13: Reflectance spectra for the REO samarium for the VNIR and SWIR region. The Figure **above** shows the results from the measurements of the three spectrometer (***(A)*** *ASD Field Spec 3,* ***(B)*** *Perkin Elmer LAMBDA 950,* ***(C)*** *HySpex (VNIR-1600, SWIR-320m-e)*) in a wavelentgh region from 350 to 1000 nm. The Figure **below** shows the results from the measurements of the three spectrometer (***(A)****ASD Field Spec 3,* ***(B)****Perkin Elmer LAMBDA 950,* ***(C)*** *HySpex (VNIR-1600, SWIR-320m-e)*) in a wavelentgh region from 1000 to 2500 nm. The maxima (solid line) and shoulders (dashed line) are marked.

STR 19/08. GFZ German Research Centre for Geosciences
DOI: 10.2312/GFZ.b103-19089

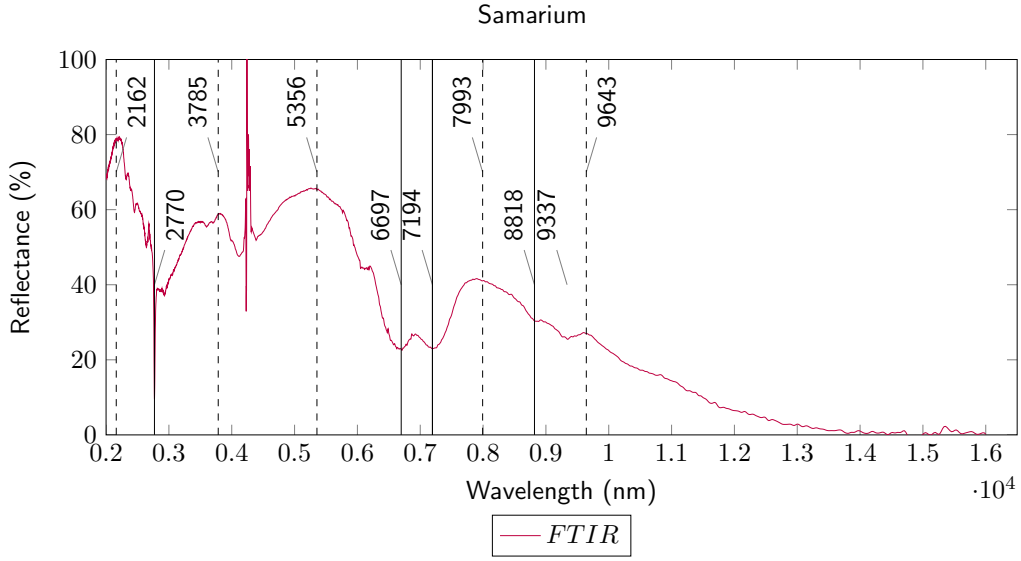

Figure C.14: Reflectance spectrum for the REO samarium for the TIR region. The Figure shows the results from the measurement with the *FTIR Spectrum GX*. The maxima (solid line) and shoulders (dashed line) are marked.

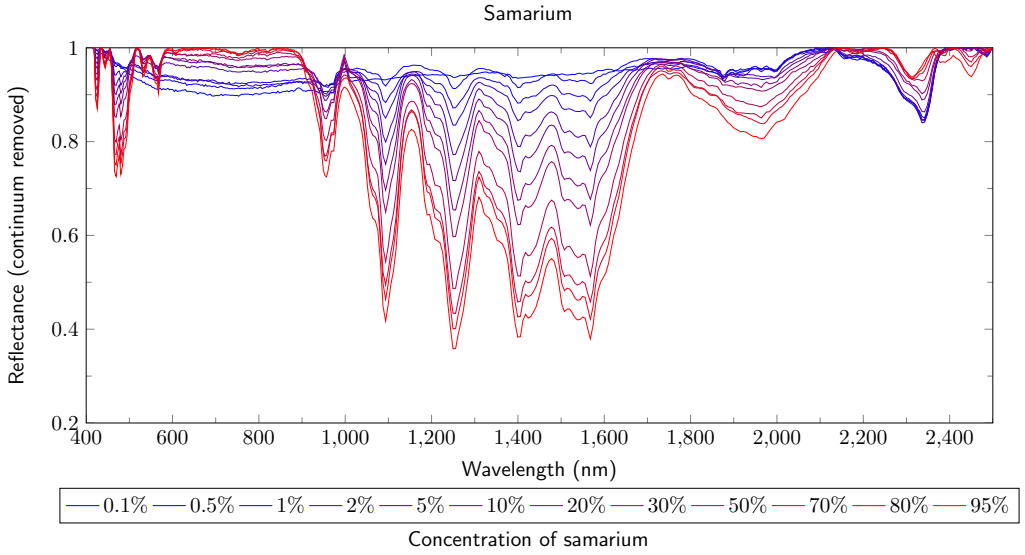

Figure C.15: Reflectance spectra for the REO samarium for the VNIR and SWIR region. The Figure shows the results from the measurement of the *HySpex (VNIR-1600, SWIR-320m-e)*. The spectra of all samples are colored from high (red) to low (blue) according to the concentration of samarium.

STR 19/08. GFZ German Research Centre for Geosciences
DOI: 10.2312/GFZ.b103-19089

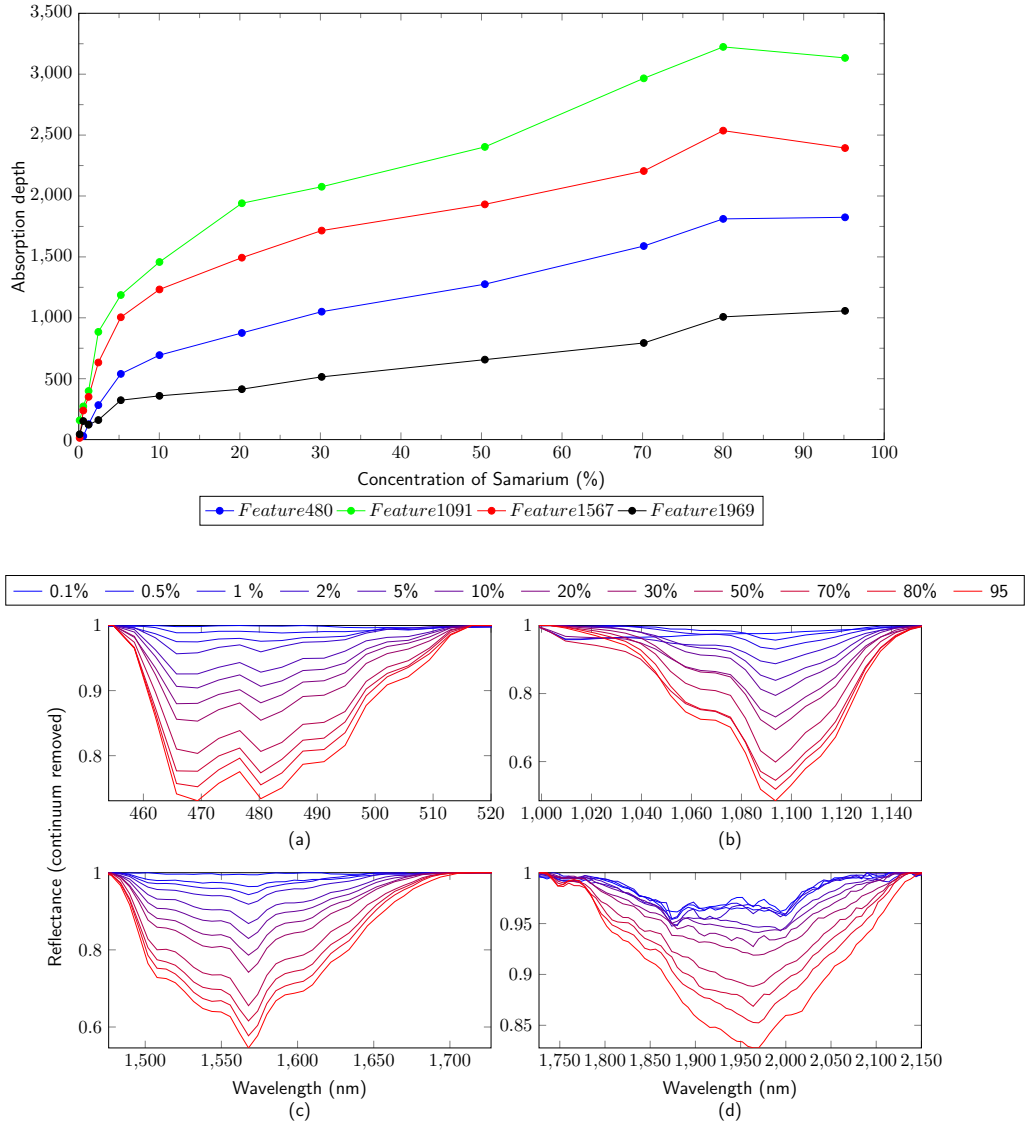

Figure C.16: The Figure **above** shows the correlation between the concentration of samarium and the absorption depth of the features at 480, 1091, 1567 and 1969 nm. The results are from the measurement of the *HySpex (VNIR-1600, SWIR-320m-e)*. The Figure **(a)** shows the reflectance and depth of the absorption feature at 480 nm. The Figure **(b)** shows the reflectance and depth of the absorption feature at 1091 nm. The Figure **(c)** shows the reflectance and depth of the absorption feature at 1567 nm. The Figure **(d)** shows the reflectance and depth of the absorption feature at 1969 nm.

STR 19/08. GFZ German Research Centre for Geosciences
DOI: 10.2312/GFZ.b103-19089

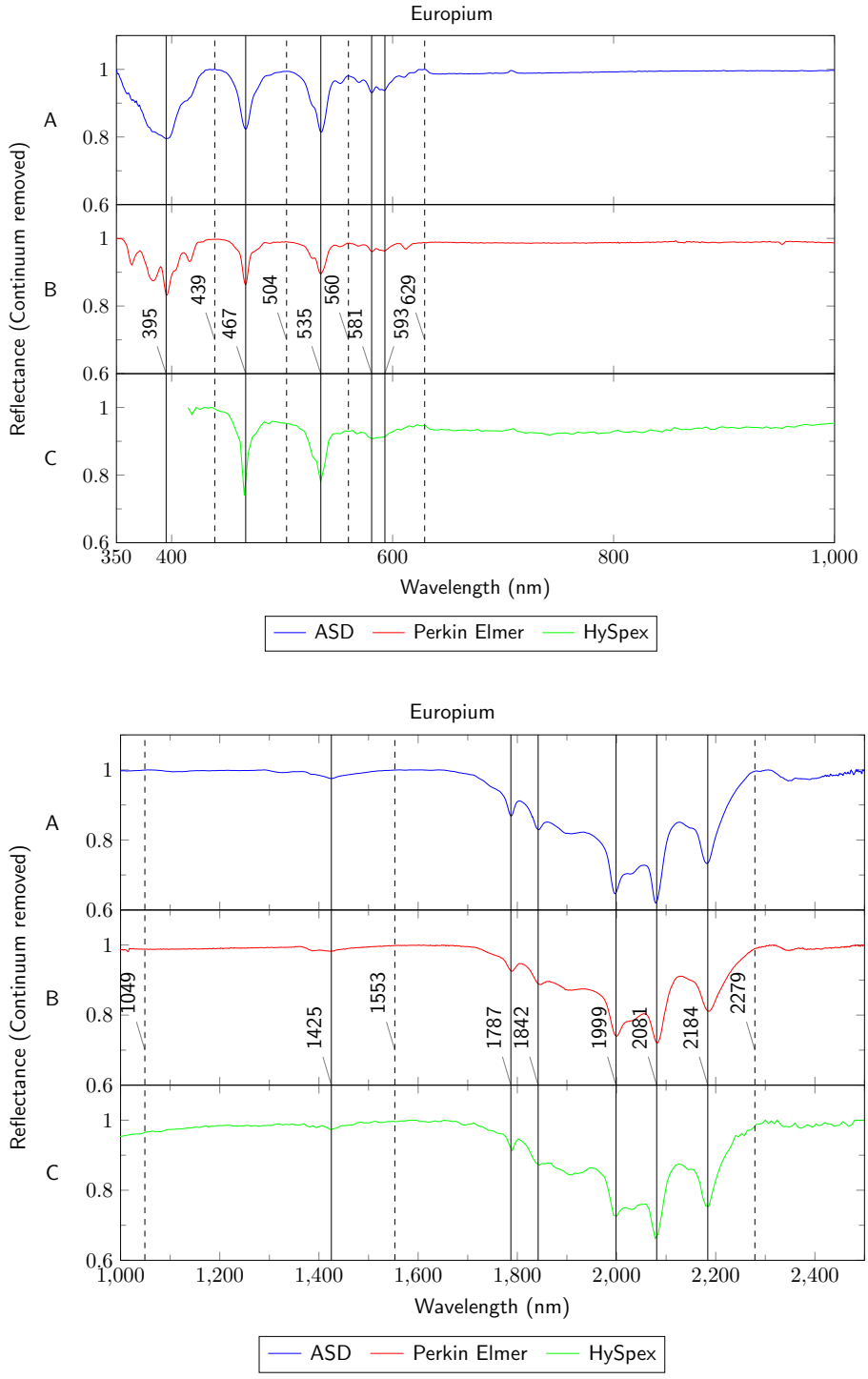

Figure C.17: Reflectance spectra for the REO europium for the VNIR and SWIR region. The Figure **above** shows the results from the measurements of the three spectrometer (***(A)*** *ASD Field Spec 3,* ***(B)*** *Perkin Elmer LAMBDA 950,* ***(C)*** *HySpex (VNIR-1600, SWIR-320m-e)*) in a wavelentgh region from 350 to 1000 nm. The Figure **below** shows the results from the measurements of the three spectrometer ((***(A)*** *ASD Field Spec 3,* ***(B)*** *Perkin Elmer LAMBDA 950,* ***(C)*** *HySpex (VNIR-1600, SWIR-320m-e)*) in a wavelentgh region from 1000 to 2500 nm. The maxima (solid line) and shoulders (dashed line) are marked.

STR 19/08. GFZ German Research Centre for Geosciences
DOI: 10.2312/GFZ.b103-19089

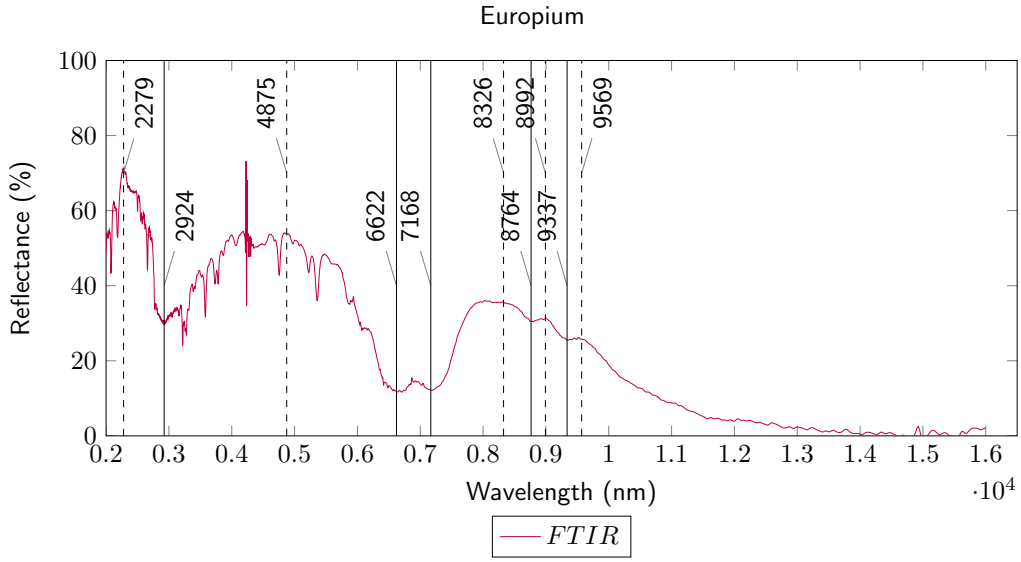

Figure C.18: Reflectance spectrum for the REO europium for the TIR region. The Figure shows the results from the measurement with the *FTIR Spectrum GX*. The maxima (solid line) and shoulders (dashed line) are marked.

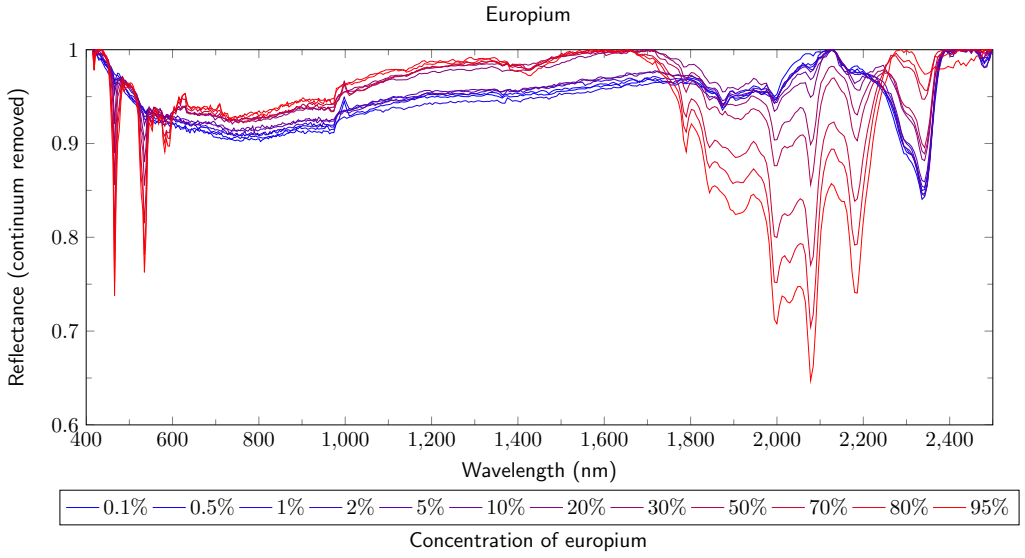

Figure C.19: Reflectance spectra for the REO europium for the VNIR and SWIR region. The Figure shows the results from the measurement of the *HySpex (VNIR-1600, SWIR-320m-e)*. The spectra of all samples are colored from high (red) to low (blue) according to the concentration of europium.

STR 19/08. GFZ German Research Centre for Geosciences
DOI: 10.2312/GFZ.b103-19089

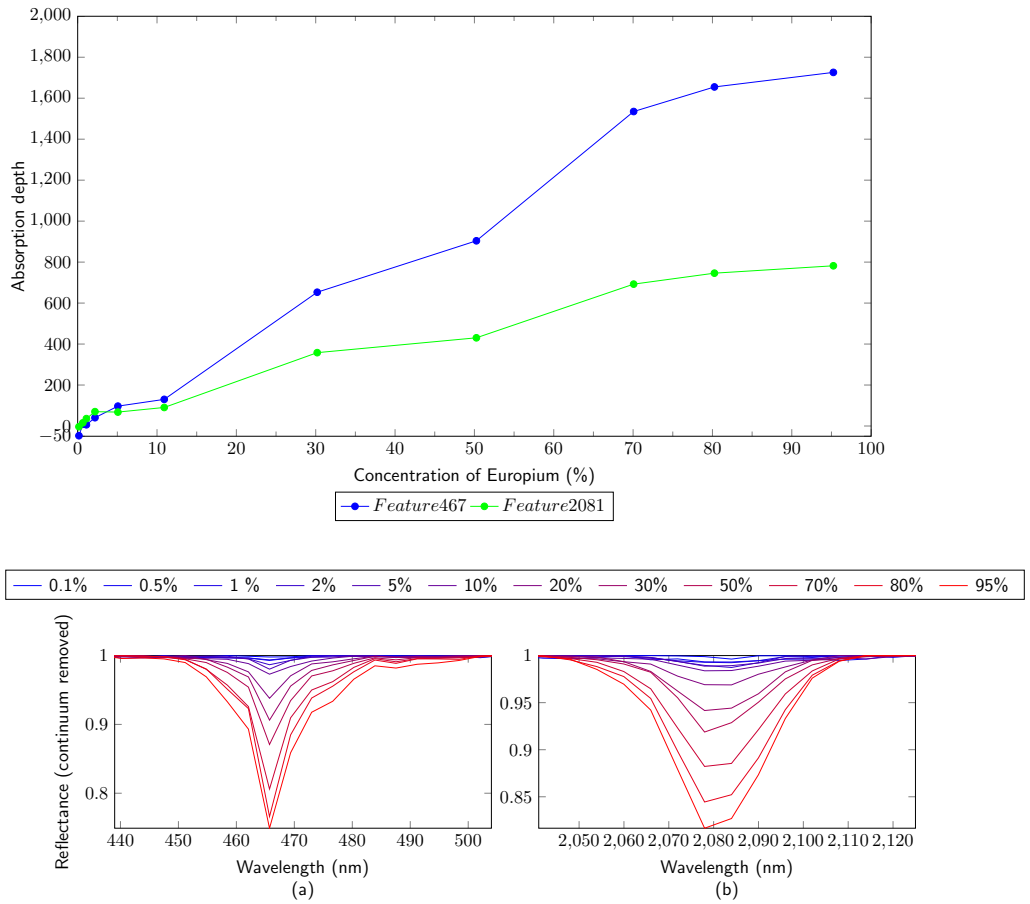

Figure C.20: The Figure **above** shows the correlation between the concentration of europium and the absorption depth of the features at 467 and 2081 nm. The results are from the measurement of the *HySpex (VNIR-1600, SWIR-320m-e)*. The Figure **(a)** shows the reflectance and depth of the absorption feature at 467 nm. The Figure **(b)** shows the reflectance and depth of the absorption feature at 2081 nm.

STR 19/08. GFZ German Research Centre for Geosciences
DOI: 10.2312/GFZ.b103-19089

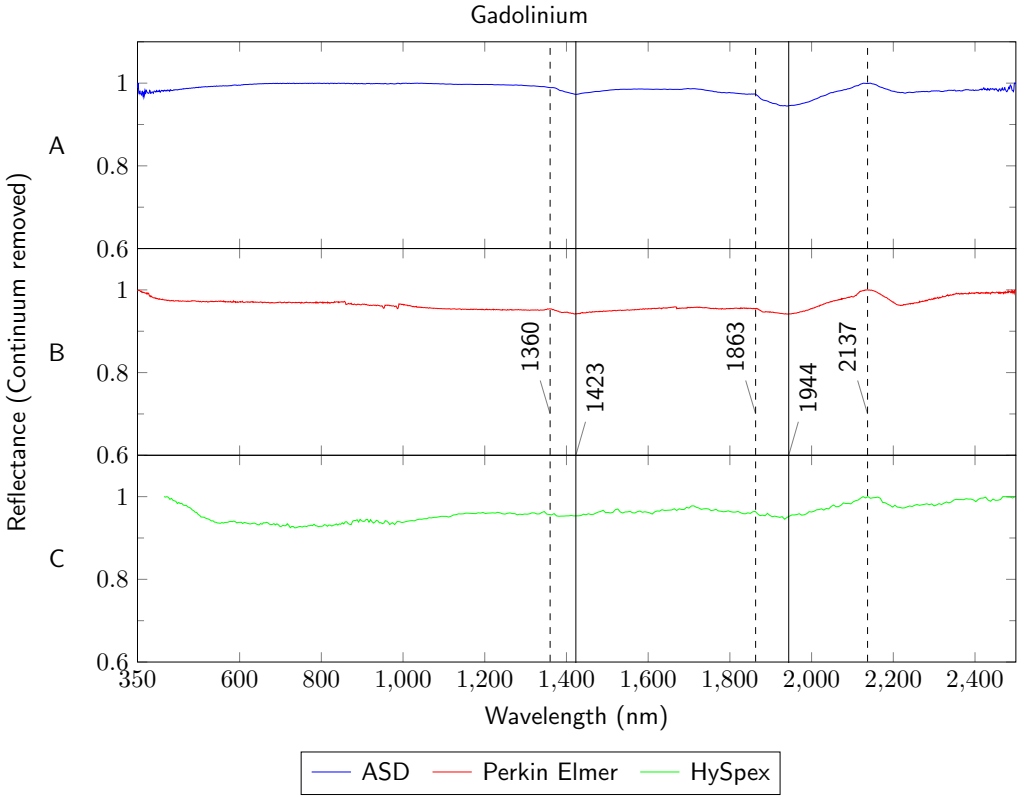

Figure C.21: Reflectance spectra for the REO gadolinium for the VNIR and SWIR region. The Figure shows the results from the measurements of the three spectrometer (***(A)*** *ASD Field Spec 3,* ***(B)*** *Perkin Elmer LAMBDA 950,* ***(C)*** *HySpex (VNIR-1600, SWIR-320m-e)*). The maxima (solid line) and shoulders (dashed line) are marked.

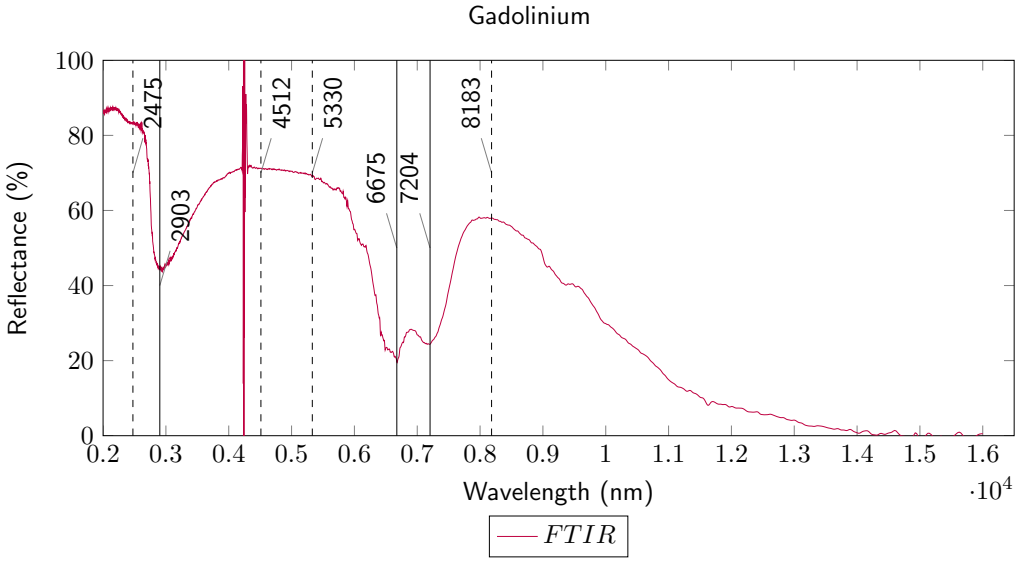

Figure C.22: Reflectance spectrum for the REO gadolinium for the TIR region. The Figure shows the results from the measurement with the *FTIR Spectrum GX*. The maxima (solid line) and shoulders (dashed line) are marked.

STR 19/08. GFZ German Research Centre for Geosciences
DOI: 10.2312/GFZ.b103-19089

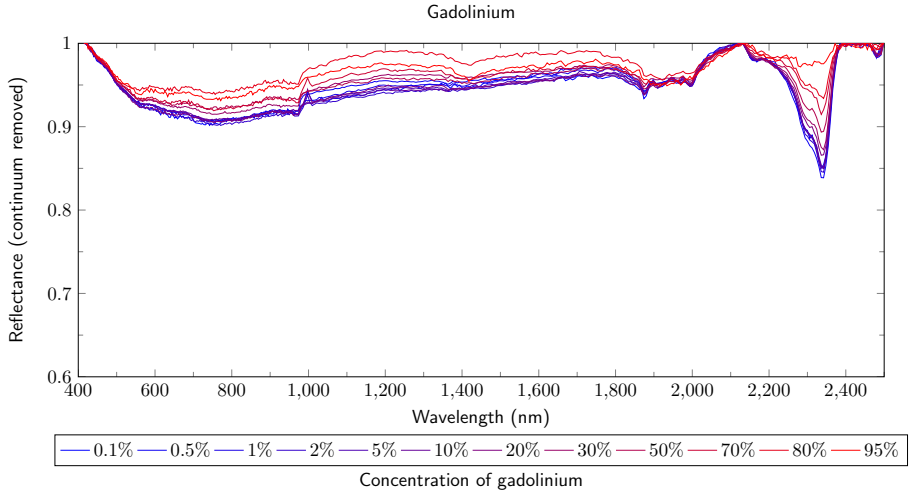

Figure C.23: Reflectance spectra for the REO gadolinium for the VNIR and SWIR region. The Figure shows the results from the measurement of the *HySpex (VNIR-1600, SWIR-320m-e)*. The spectra of all samples are colored from high (red) to low (blue) according to the concentration of gadolinium.

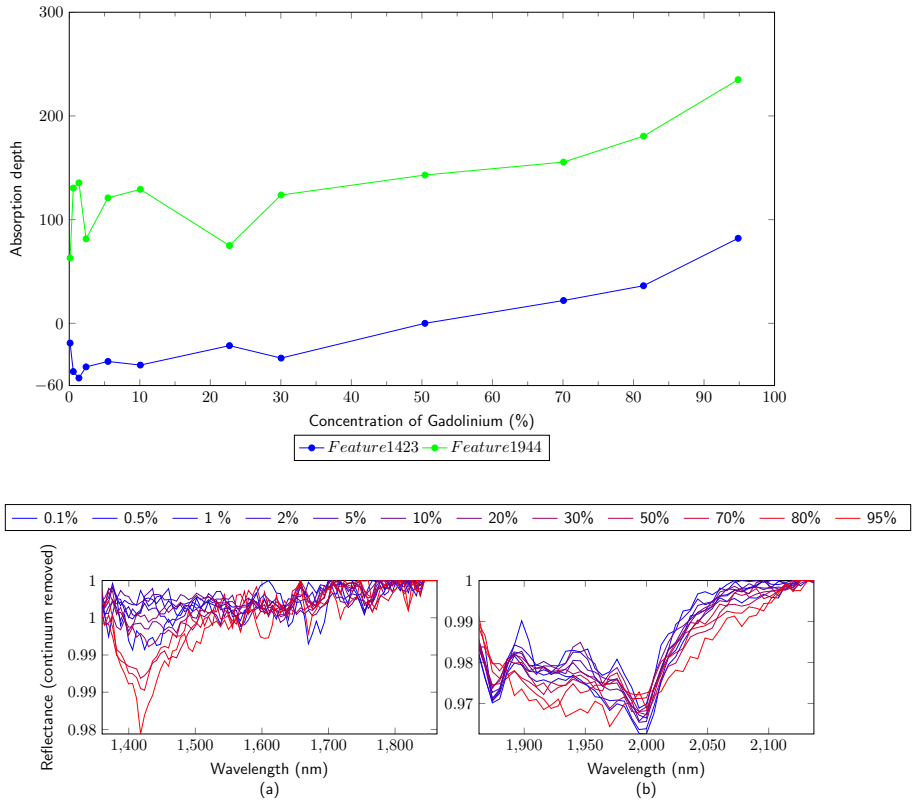

Figure C.24: The Figure **above** shows the correlation between the concentration of gadolinium and the absorption depth of the features at 1423 and 1944 nm. The results are from the measurement of the *HySpex (VNIR-1600, SWIR-320m-e)*. The Figure **(a)** shows the reflectance and depth of the absorption feature at 1324 nm. The Figure **(b)** shows the reflectance and depth of the absorption feature at 1944 nm.

STR 19/08. GFZ German Research Centre for Geosciences
DOI: 10.2312/GFZ.b103-19089

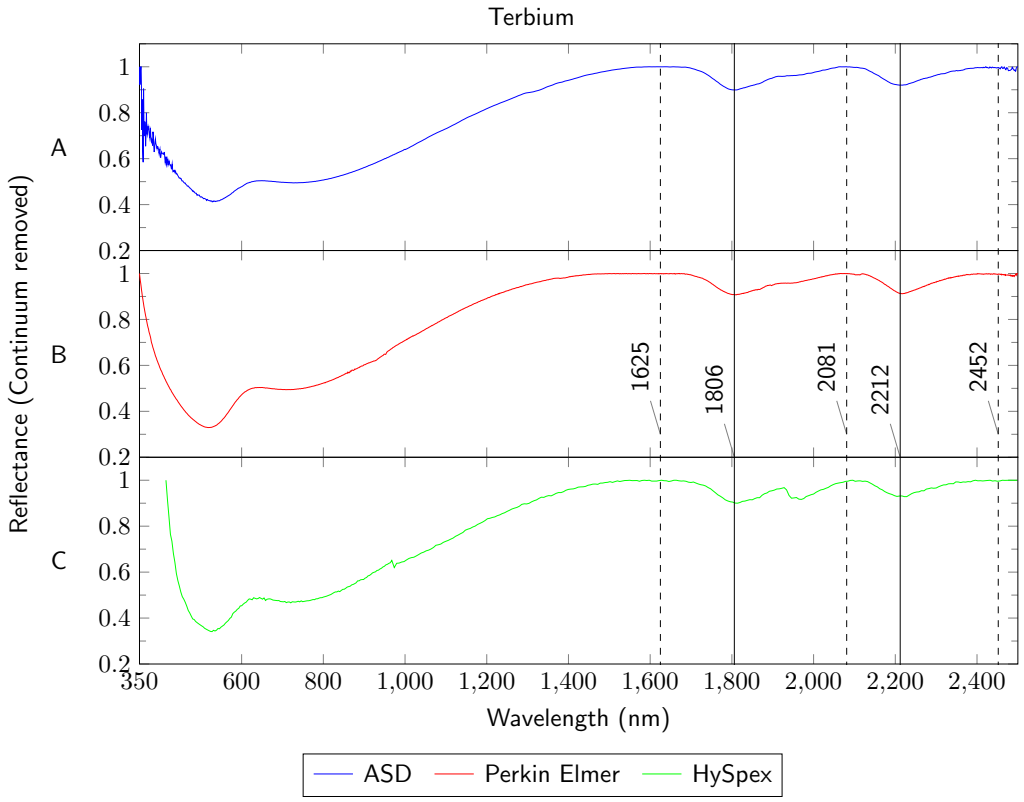

Figure C.25: Reflectance spectra for the REO terbium for the VNIR and SWIR region. The Figure shows the results from the measurements of the three spectrometer (***(A)*** *ASD Field Spec 3,* ***(B)*** *Perkin Elmer LAMBDA 950,* ***(C)*** *HySpex (VNIR-1600, SWIR-320m-e)*). The maxima (solid line) and shoulders (dashed line) are marked.

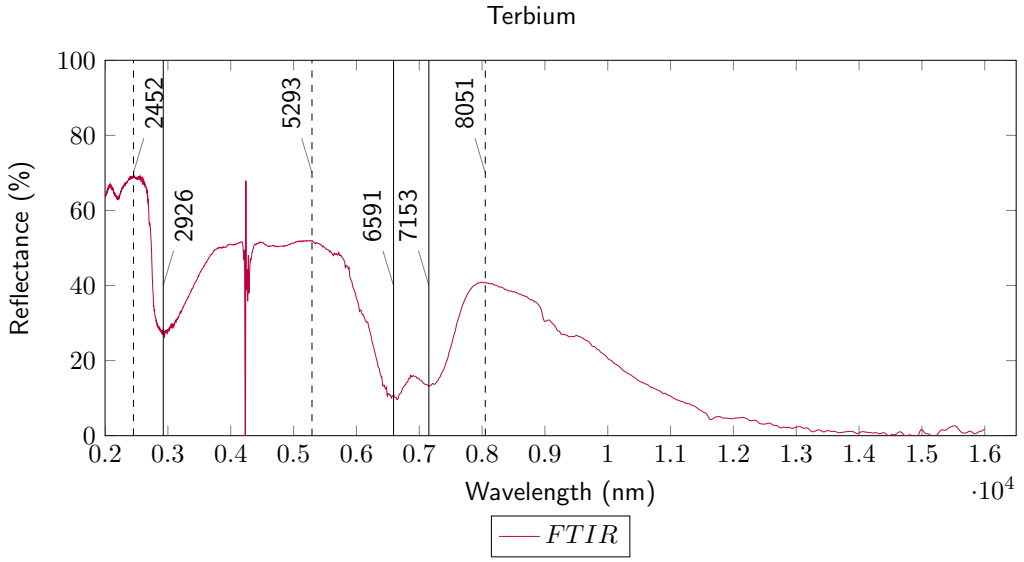

Figure C.26: Reflectance spectrum for the REO terbium for the TIR region. The Figure shows the results from the measurement with the *FTIR Spectrum GX*. The maxima (solid line) and shoulders (dashed line) are marked.

STR 19/08. GFZ German Research Centre for Geosciences
DOI: 10.2312/GFZ.b103-19089

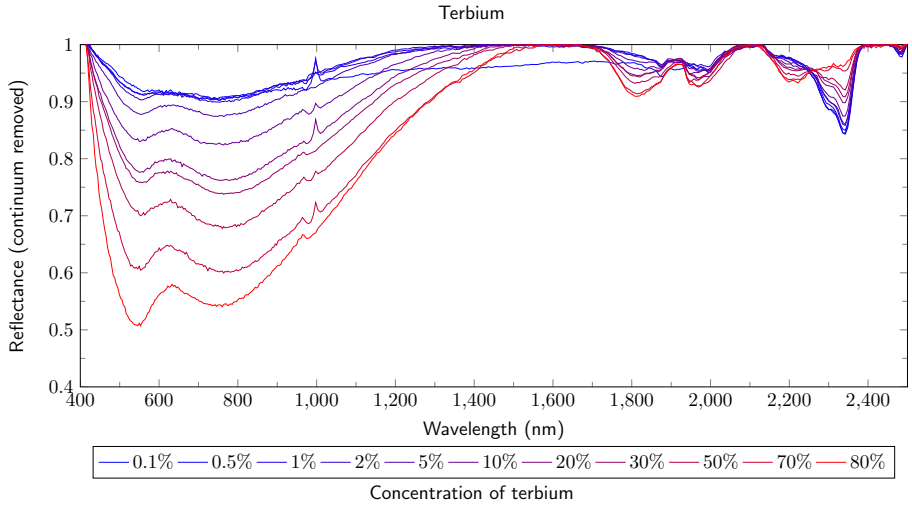

Figure C.27: Reflectance spectra for the REO terbium for the VNIR and SWIR region. The Figure shows the results from the measurement of the *HySpex (VNIR-1600, SWIR-320m-e)*. The spectra of all samples are colored from high (red) to low (blue) according to the concentration of terbium.

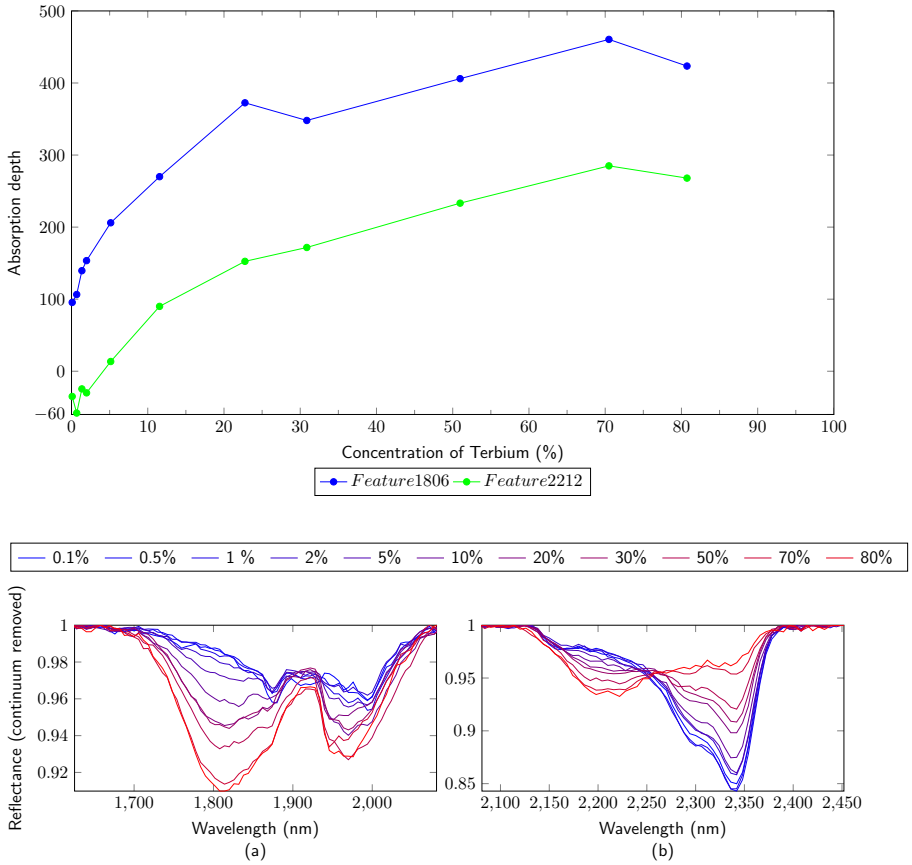

Figure C.28: The Figure **above** shows the correlation between the concentration of terbium and the absorption depth of the features at 1806 and 2212 nm. The results are from the measurement of the *HySpex (VNIR-1600, SWIR-320m-e)*. The Figure **(a)** shows the reflectance and depth of the absorption feature at 1806 nm. The Figure **(b)** shows the reflectance and depth of the absorption feature at 2212 nm.

STR 19/08. GFZ German Research Centre for Geosciences
DOI: 10.2312/GFZ.b103-19089

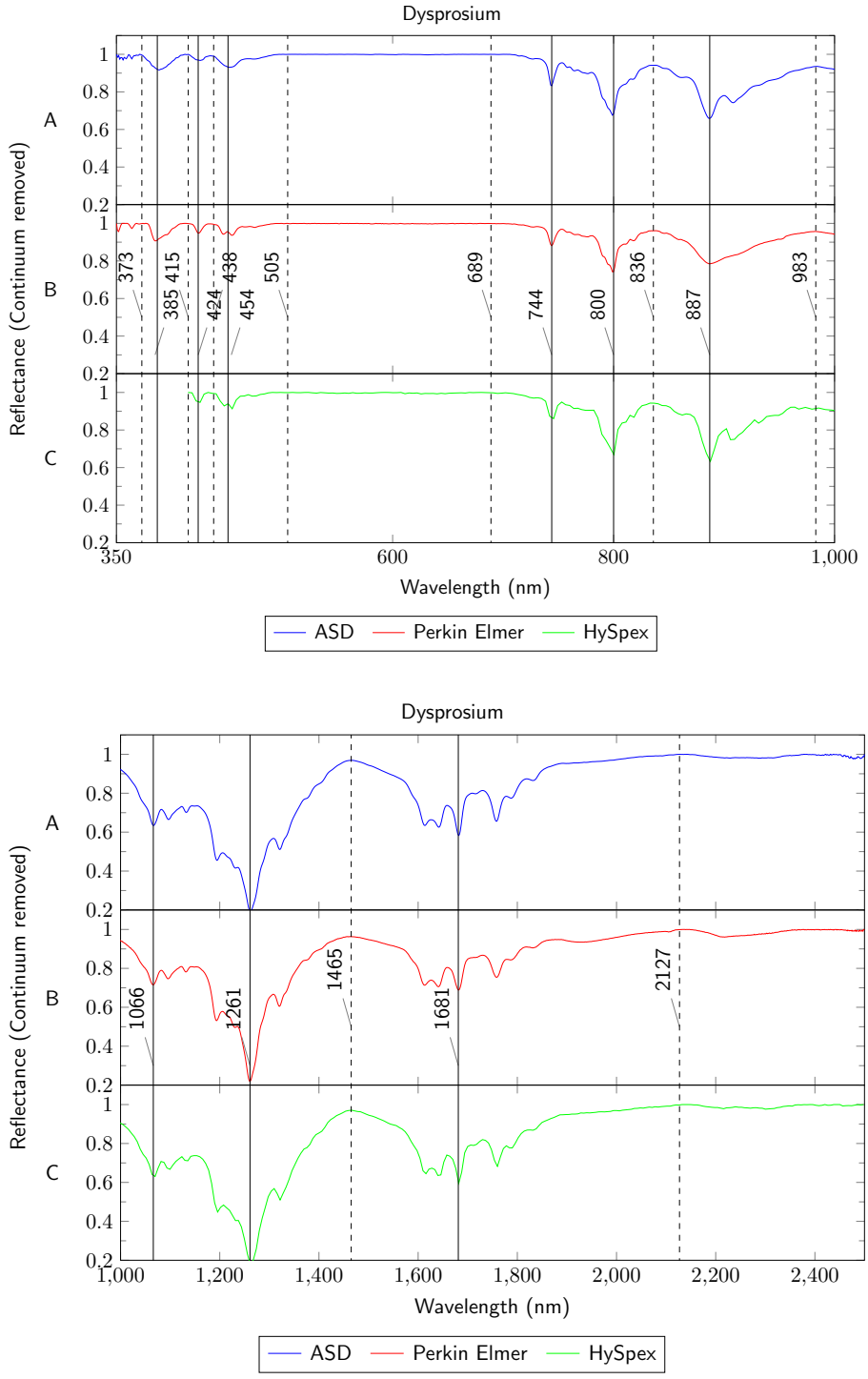

Figure C.29: Reflectance spectra for the REO dysprosium for the VNIR and SWIR region. The Figure **above** shows the results from the measurements of the three spectrometer (***(A)*** *ASD Field Spec 3,* ***(B)*** *Perkin Elmer LAMBDA 950,* ***(C)*** *HySpex (VNIR-1600, SWIR-320m-e)*) in a wavelentgh region from 350 to 1000 nm. The Figure **below** shows the results from the measurements of the three spectrometer (***(A)*** *ASD Field Spec 3,* ***(B)*** *Perkin Elmer LAMBDA 950,* ***(C)*** *HySpex (VNIR-1600, SWIR-320m-e)*) in a wavelentgh region from 1000 to 2500 nm. The maxima (solid line) and shoulders (dashed line) are marked.

STR 19/08. GFZ German Research Centre for Geosciences
DOI: 10.2312/GFZ.b103-19089

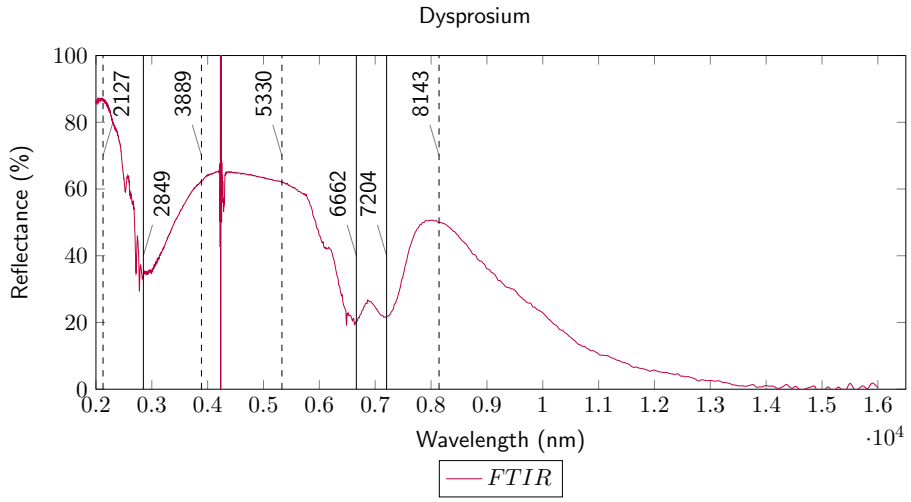

Figure C.30: Reflectance spectrum for the REO dysprosium for the TIR region. The Figure shows the results from the measurement with the *FTIR Spectrum GX*. The maxima (solid line) and shoulders (dashed line) are marked.

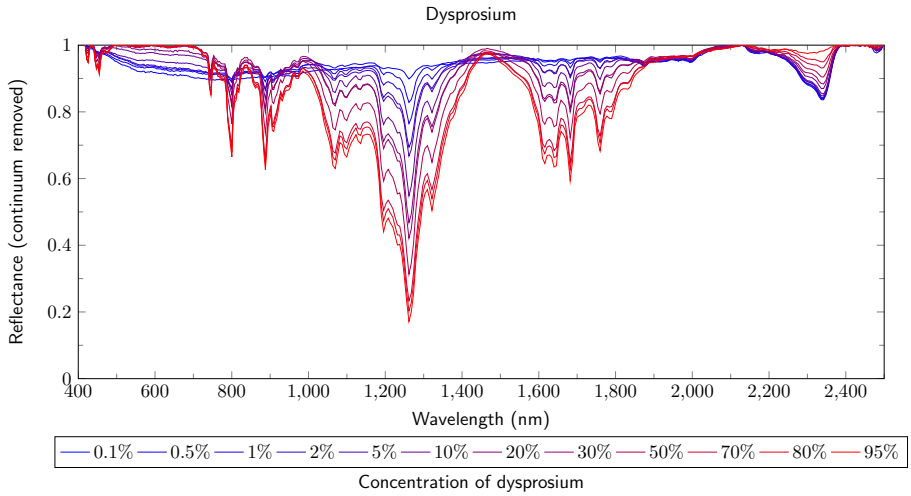

Figure C.31: Reflectance spectra for the REO dysprosium for the VNIR and SWIR region. The Figure shows the results from the measurement of the *HySpex (VNIR-1600, SWIR-320m-e)*. The spectra of all samples are colored from high (red) to low (blue) according to the concentration of dysprosium.

STR 19/08. GFZ German Research Centre for Geosciences
DOI: 10.2312/GFZ.b103-19089

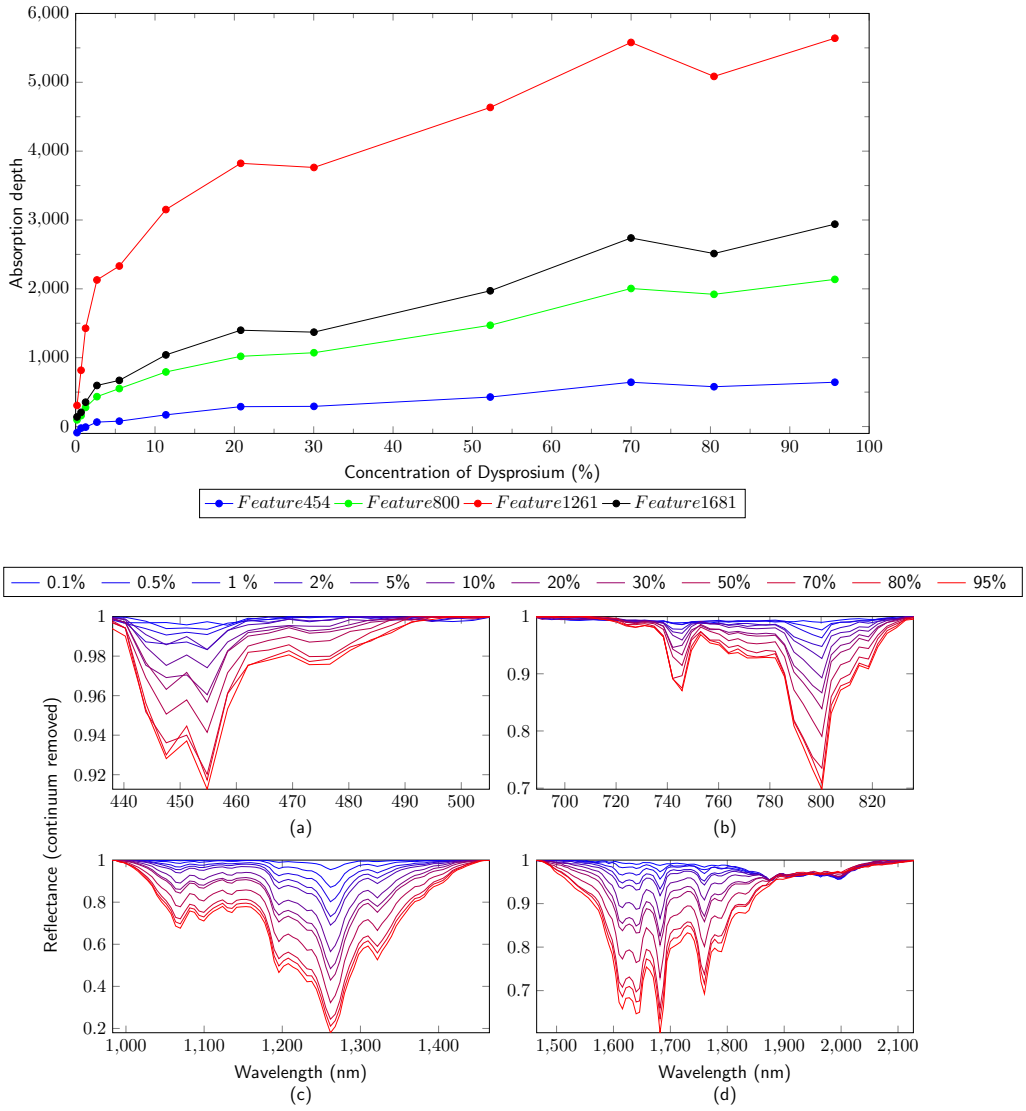

Figure C.32: The Figure **above** shows the correlation between the concentration of dysprosium and the absorption depth of the features at 454, 800, 1261 and 1681 nm. The results are from the measurement of the *HySpex (VNIR-1600, SWIR-320m-e)*. The Figure **(a)** shows the reflectance and depth of the absorption feature at 454 nm. The Figure **(b)** shows the reflectance and depth of the absorption feature at 800 nm. The Figure **(c)** shows the reflectance and depth of the absorption feature at 1261 nm. The Figure **(d)** shows the reflectance and depth of the absorption feature at 1681 nm.

STR 19/08. GFZ German Research Centre for Geosciences
DOI: 10.2312/GFZ.b103-19089

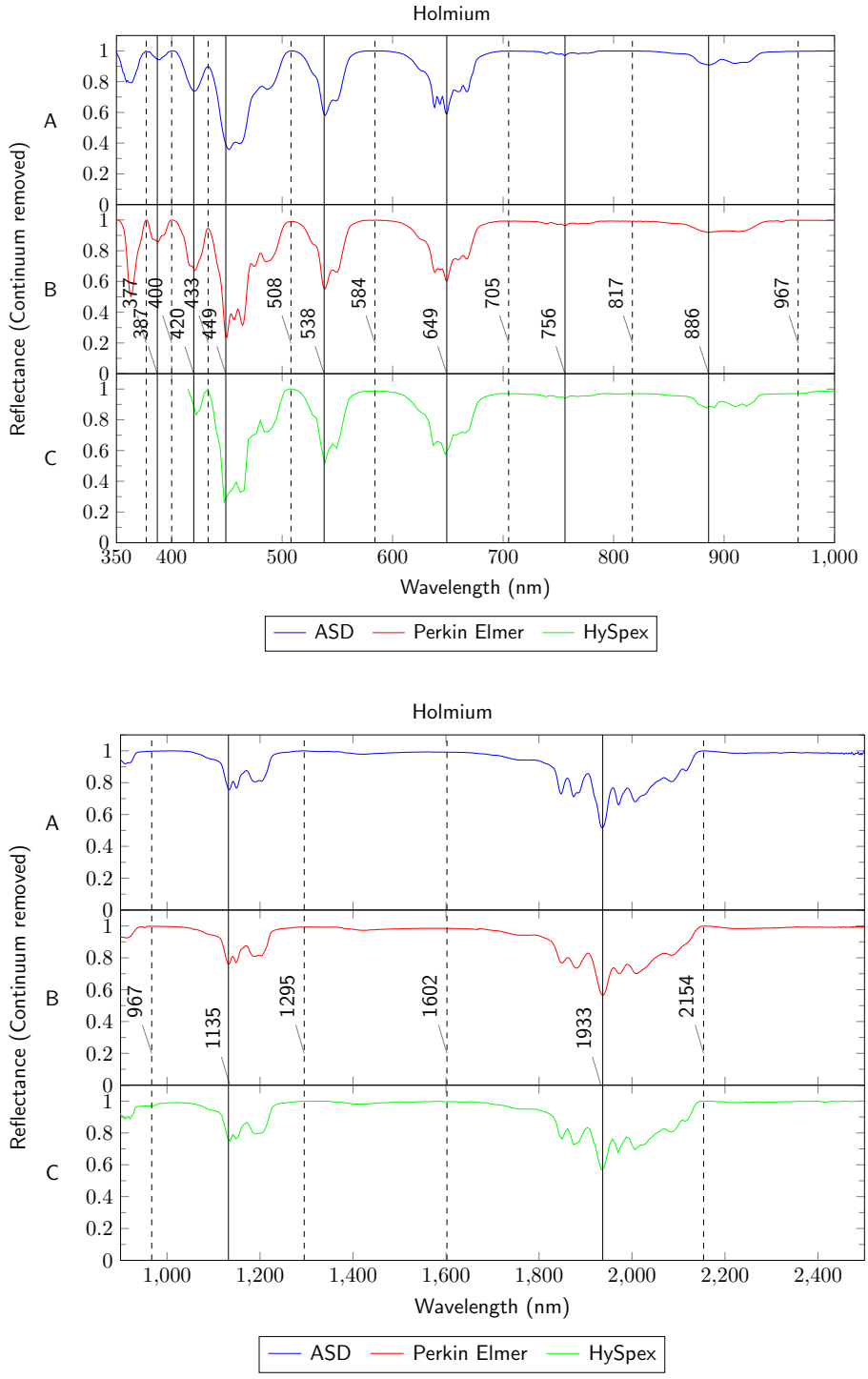

Figure C.33: Reflectance spectra for the REO holmium for the VNIR and SWIR region. The Figure **above** shows the results from the measurements of the three spectrometer (***(A)*** *ASD Field Spec 3,* ***(B)*** *Perkin Elmer LAMBDA 950,* ***(C)*** *HySpex (VNIR-1600, SWIR-320m-e)*) in a wavelentgh region from 350 to 1000 nm. The Figure **below** shows the results from the measurements of the three spectrometer (***(A)*** *ASD Field Spec 3,* ***(B)*** *Perkin Elmer LAMBDA 950,* ***(C)*** *HySpex (VNIR-1600, SWIR-320m-e)*) in a wavelentgh region from 900 to 2500 nm. The maxima (solid line) and shoulders (dashed line) are marked.

STR 19/08. GFZ German Research Centre for Geosciences
DOI: 10.2312/GFZ.b103-19089

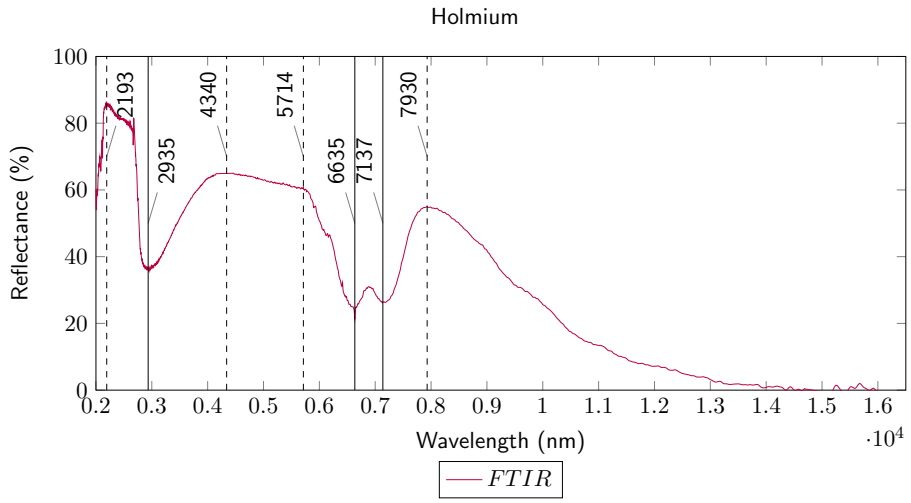

Figure C.34: Reflectance spectrum for the REO holmium for the TIR region. The Figure shows the results from the measurement with the *FTIR Spectrum GX*. The maxima (solid line) and shoulders (dashed line) are marked.

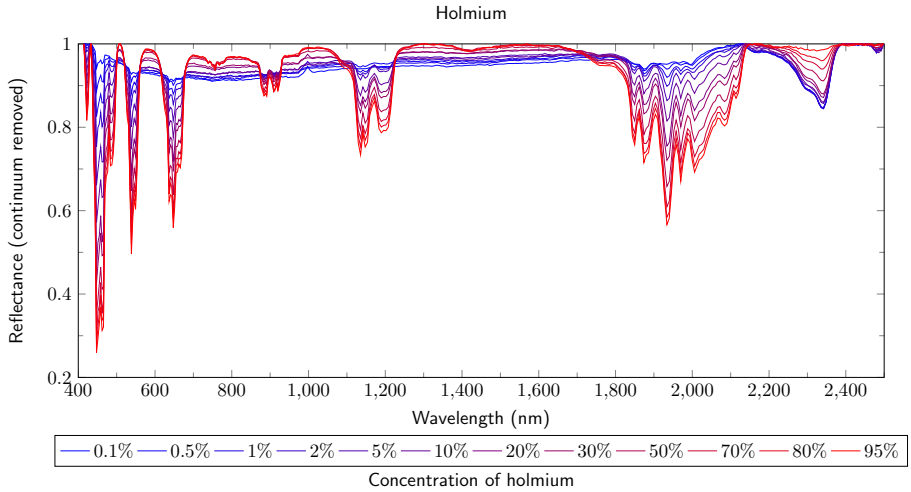

Figure C.35: Reflectance spectra for the REO holmium for the VNIR and SWIR region. The Figure shows the results from the measurement of the *HySpex (VNIR-1600, SWIR-320m-e)*. The spectra of all samples are colored from high (red) to low (blue) according to the concentration of holmium.

STR 19/08. GFZ German Research Centre for Geosciences
DOI: 10.2312/GFZ.b103-19089

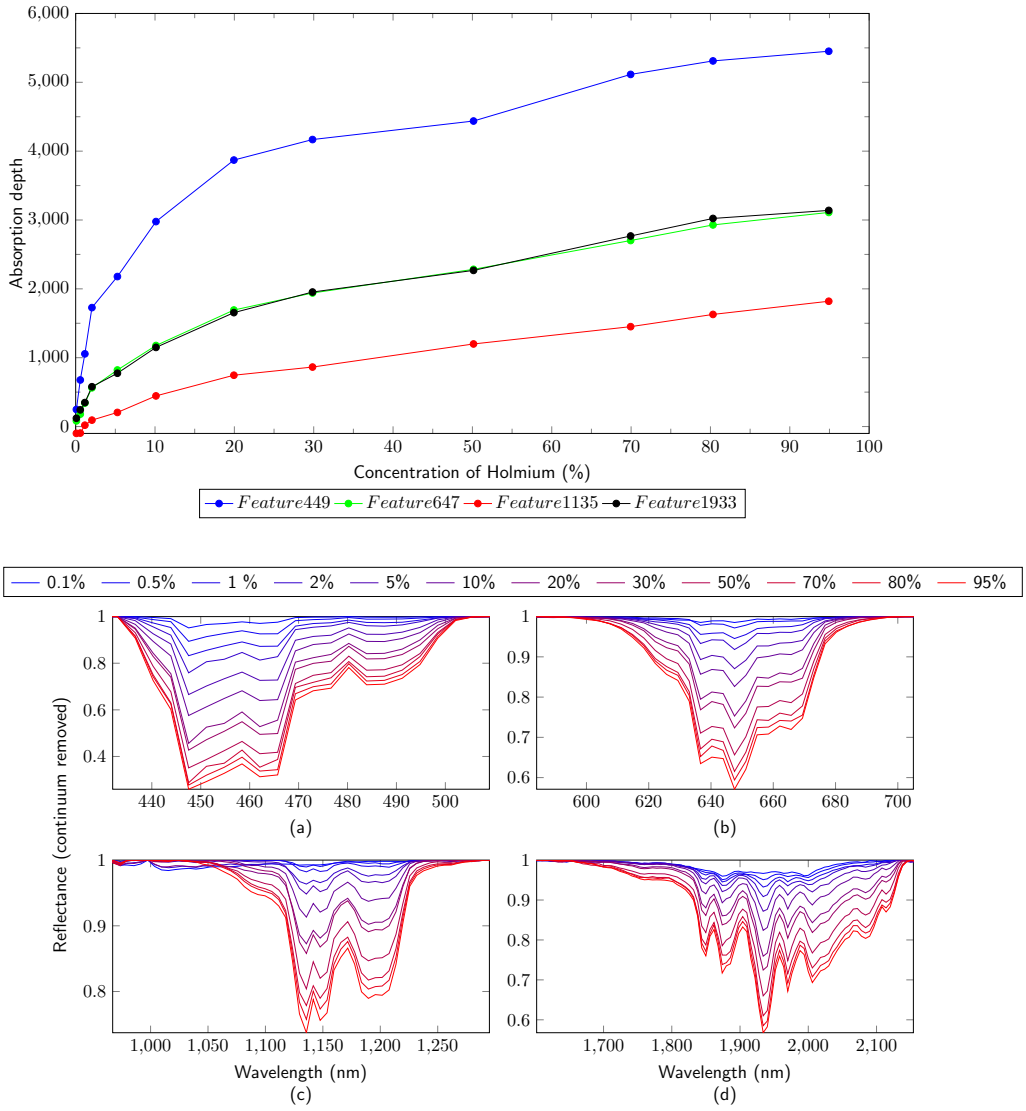

Figure C.36: The Figure **above** shows the correlation between the concentration of holmium and the absorption depth of the features at 449, 647, 1135 and 1933 nm. The results are from the measurement of the *HySpex (VNIR-1600, SWIR-320m-e)*. The Figure **(a)** shows the reflectance and depth of the absorption feature at 449 nm. The Figure **(b)** shows the reflectance and depth of the absorption feature at 647 nm. The Figure **(c)** shows the reflectance and depth of the absorption feature at 1135 nm. The Figure **(d)** shows the reflectance and depth of the absorption feature at 1933 nm.

STR 19/08. GFZ German Research Centre for Geosciences
DOI: 10.2312/GFZ.b103-19089

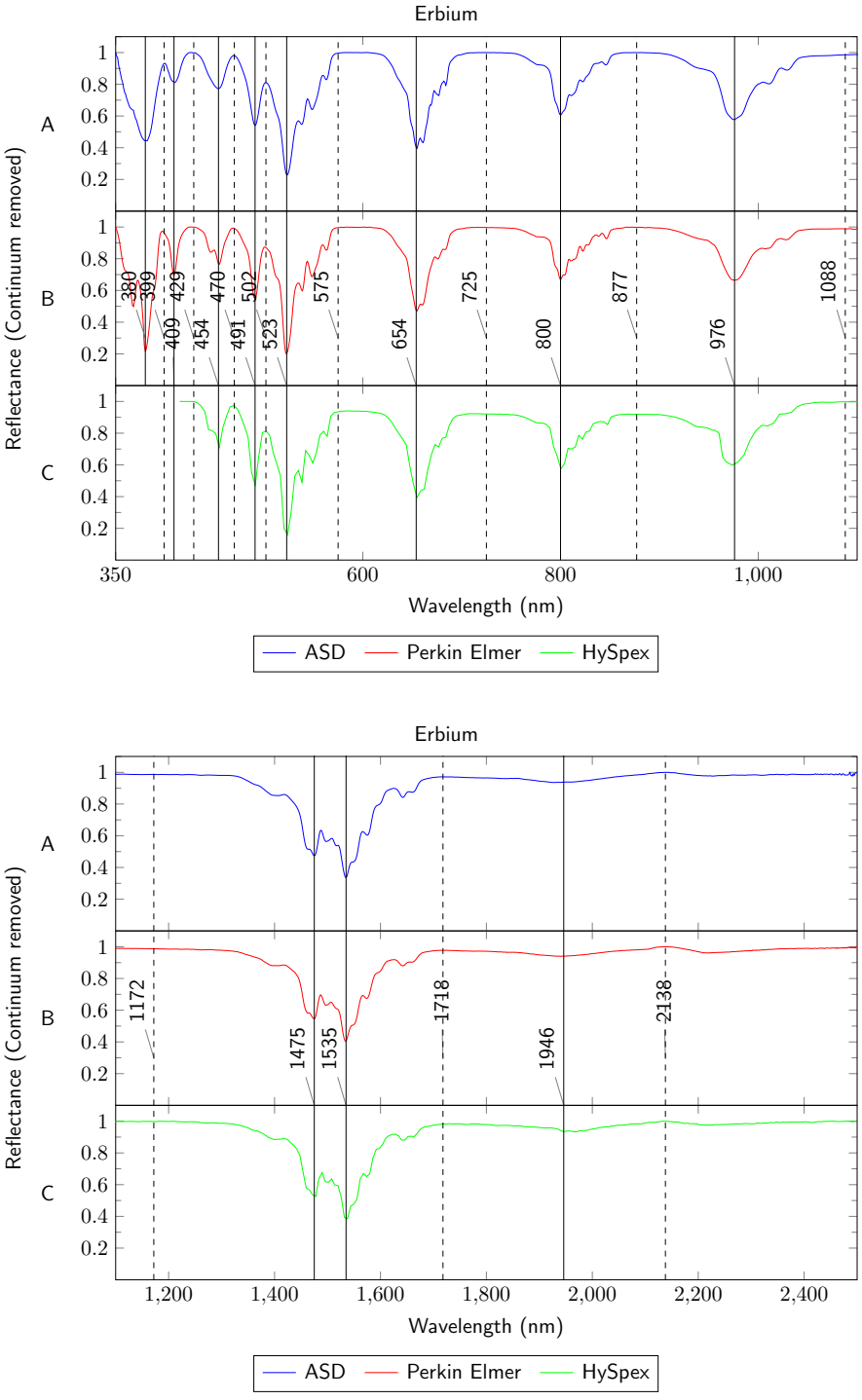

Figure C.37: Reflectance spectra for the REO erbium for the VNIR and SWIR region. The Figure **above** shows the results from the measurements of the three spectrometer (***(A)*** *ASD Field Spec 3,* ***(B)*** *Perkin Elmer LAMBDA 950,* ***(C)*** *HySpex (VNIR-1600, SWIR-320m-e)*) in a wavelentgh region from 350 to 1100 nm. The Figure **below** shows the results from the measurements of the three spectrometer (***(A)*** *ASD Field Spec 3,* ***(B)*** *Perkin Elmer LAMBDA 950,* ***(C)*** *HySpex (VNIR-1600, SWIR-320m-e)*) in a wavelentgh region from 1100 to 2500 nm. The maxima (solid line) and shoulders (dashed line) are marked.

STR 19/08. GFZ German Research Centre for Geosciences
DOI: 10.2312/GFZ.b103-19089

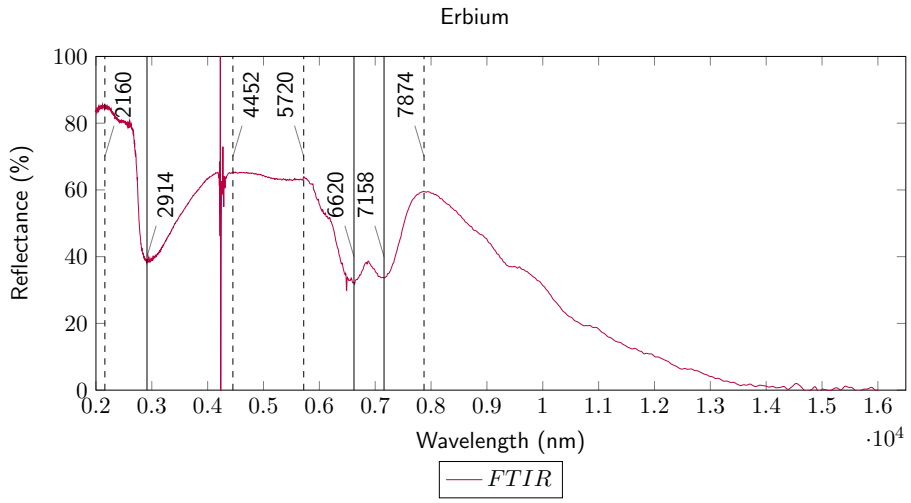

Figure C.38: Reflectance spectrum for the REO erbium for the TIR region. The Figure shows the results from the measurement with the *FTIR Spectrum GX*. The maxima (solid line) and shoulders (dashed line) are marked.

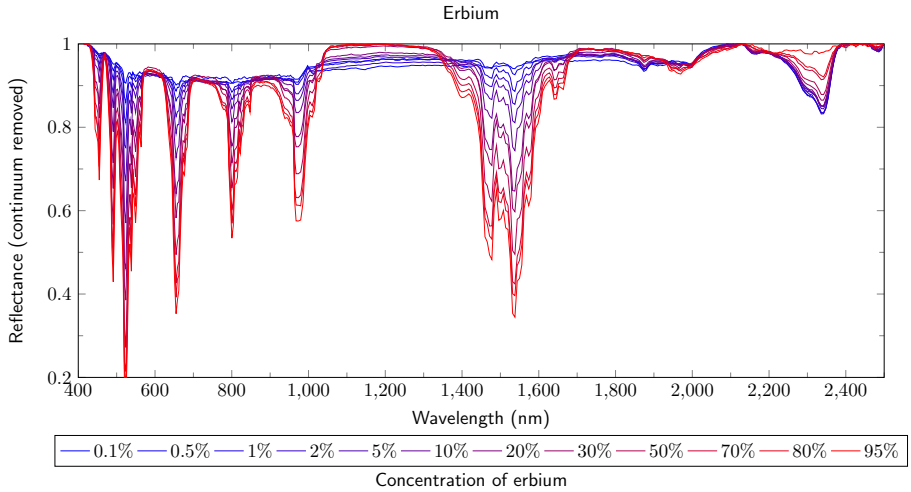

Figure C.39: Reflectance spectra for the REO erbium for the VNIR and SWIR region. The Figure shows the results from the measurement of the *HySpex (VNIR-1600, SWIR-320m-e)*. The spectra of all samples are colored from high (red) to low (blue) according to the concentration of erbium.

STR 19/08. GFZ German Research Centre for Geosciences
DOI: 10.2312/GFZ.b103-19089

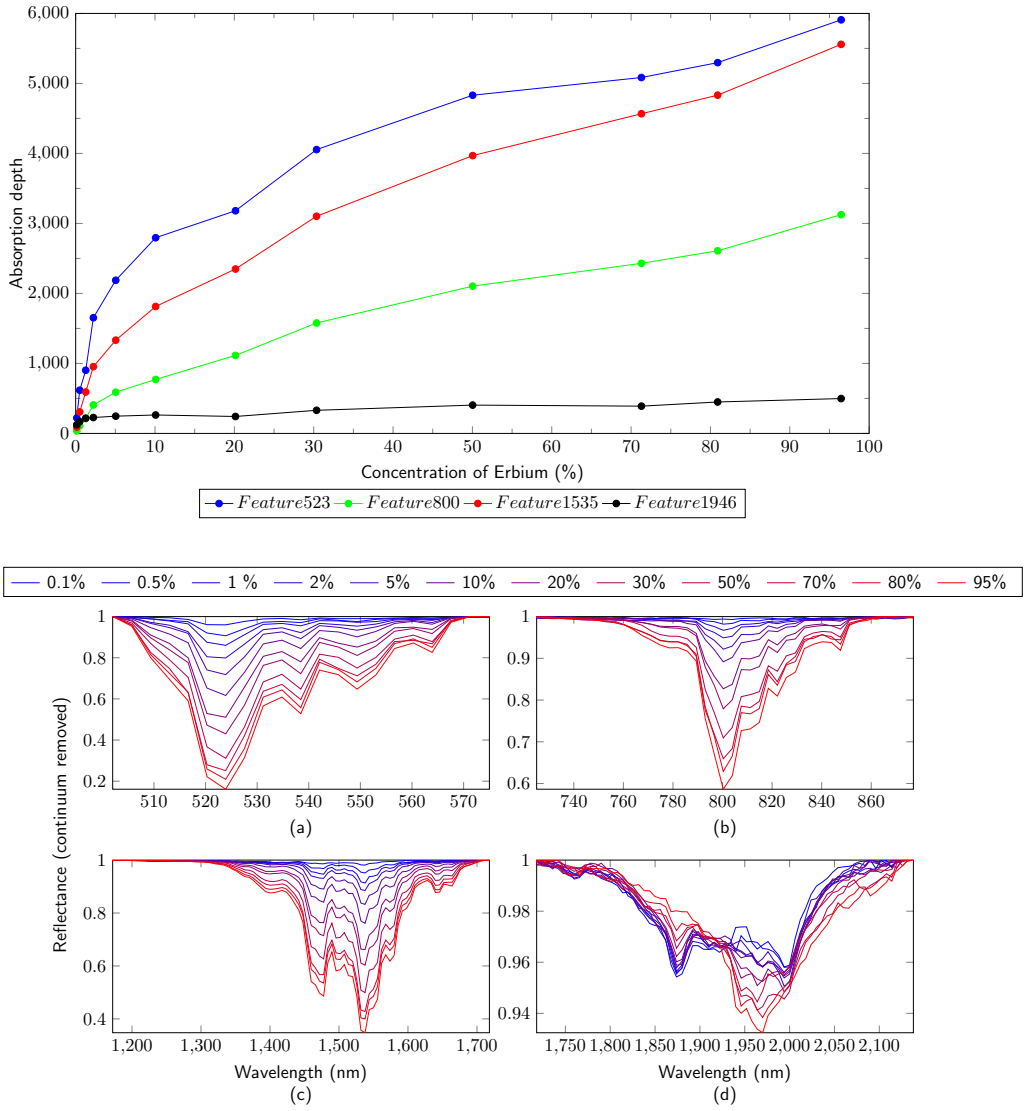

Figure C.40: The Figure **above** shows the correlation between the concentration of erbium and the absorption depth of the features at 523, 800, 1535 and 1946 nm. The results are from the measurement of the *HySpex (VNIR-1600, SWIR-320m-e)*. The Figure **(a)** shows the reflectance and depth of the absorption feature at 523 nm. The Figure **(b)** shows the reflectance and depth of the absorption feature at 800 nm. The Figure **(c)** shows the reflectance and depth of the absorption feature at 1535 nm. The Figure **(d)** shows the reflectance and depth of the absorption feature at 1946 nm.

STR 19/08. GFZ German Research Centre for Geosciences
DOI: 10.2312/GFZ.b103-19089

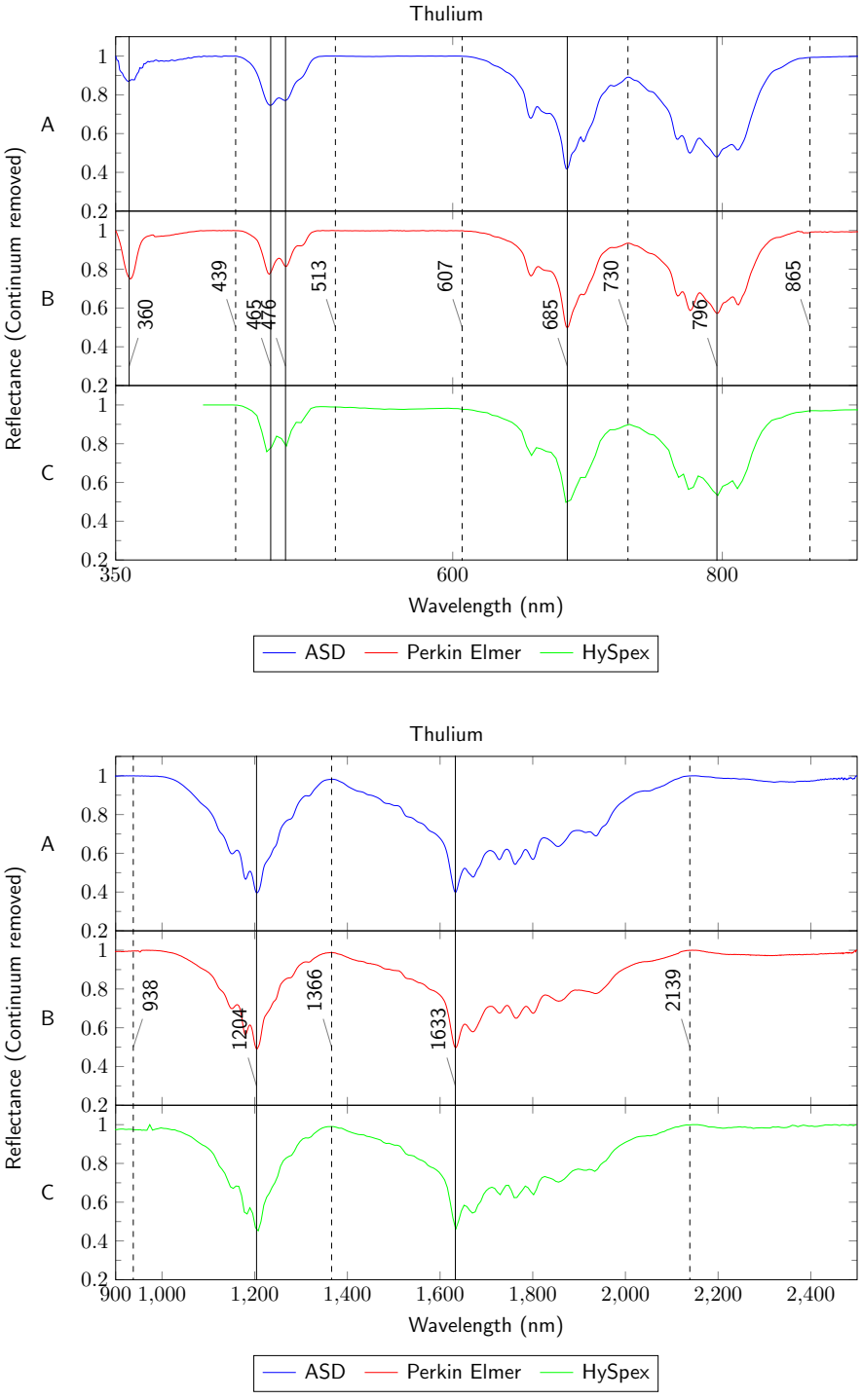

Figure C.41: Reflectance spectra for the REO thulium for the VNIR and SWIR region. The Figure **above** shows the results from the measurements of the three spectrometer (***(A)*** *ASD Field Spec 3,* ***(B)*** *Perkin Elmer LAMBDA 950,* ***(C)*** *HySpex (VNIR-1600, SWIR-320m-e)*) in a wavelentgh region from 350 to 900 nm. The Figure **below** shows the results from the measurements of the three spectrometer (***(A)*** *ASD Field Spec 3,* ***(B)*** *Perkin Elmer LAMBDA 950,* ***(C)*** *HySpex (VNIR-1600, SWIR-320m-e)*) in a wavelentgh region from 900 to 2500 nm. The maxima (solid line) and shoulders (dashed line) are marked.

STR 19/08. GFZ German Research Centre for Geosciences
DOI: 10.2312/GFZ.b103-19089

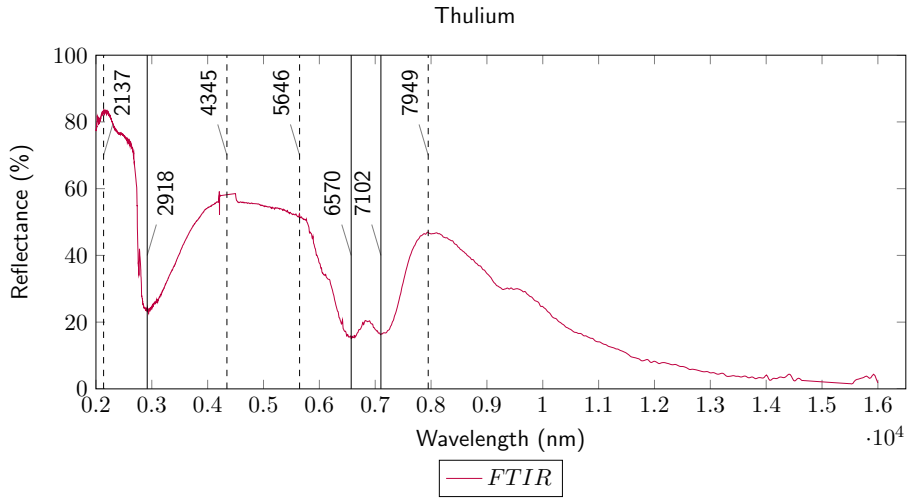

Figure C.42: Reflectance spectrum for the REO thulium for the TIR region. The Figure shows the results from the measurement with the *FTIR Spectrum GX*. The maxima (solid line) and shoulders (dashed line) are marked.

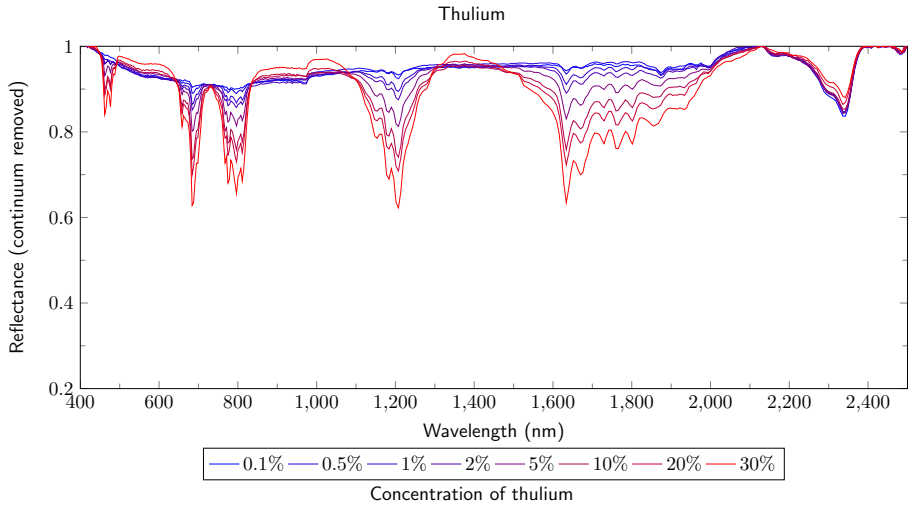

Figure C.43: Reflectance spectra for the REO thulium for the VNIR and SWIR region. The Figure shows the results from the measurement of the *HySpex (VNIR-1600, SWIR-320m-e)*. The spectra of all samples are colored from high (red) to low (blue) according to the concentration of thulium.

STR 19/08. GFZ German Research Centre for Geosciences
DOI: 10.2312/GFZ.b103-19089

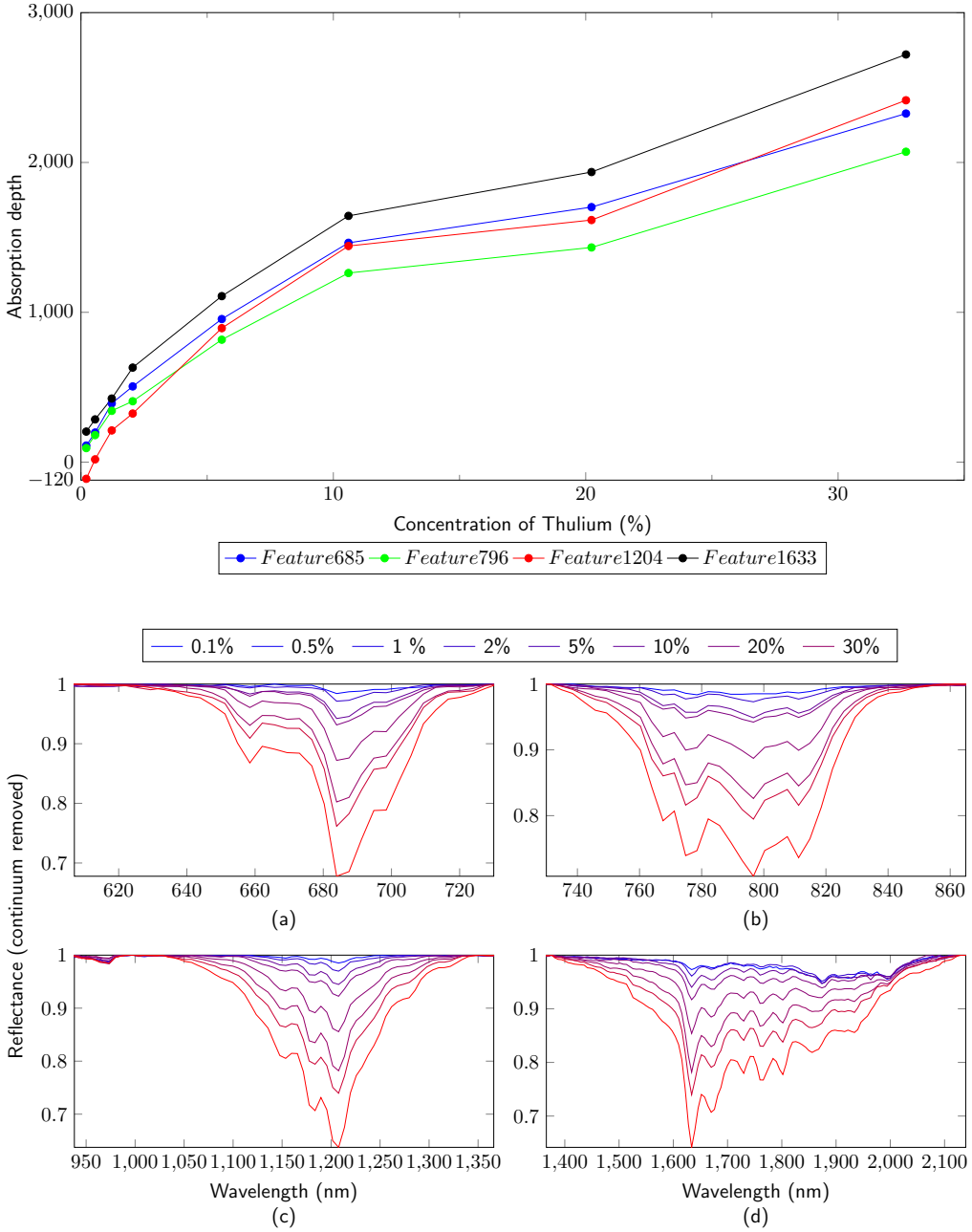

Figure C.44: The Figure **above** shows the correlation between the concentration of thulium and the absorption depth of the features at 685, 796, 1204 and 1633 nm. The results are from the measurement of the *HySpex (VNIR-1600, SWIR-320m-e)*. The Figure **(a)** shows the reflectance and depth of the absorption feature at 685 nm. The Figure **(b)** shows the reflectance and depth of the absorption feature at 796 nm. The Figure **(c)** shows the reflectance and depth of the absorption feature at 1204 nm. The Figure **(d)** shows the reflectance and depth of the absorption feature at 1633 nm.

STR 19/08. GFZ German Research Centre for Geosciences
DOI: 10.2312/GFZ.b103-19089

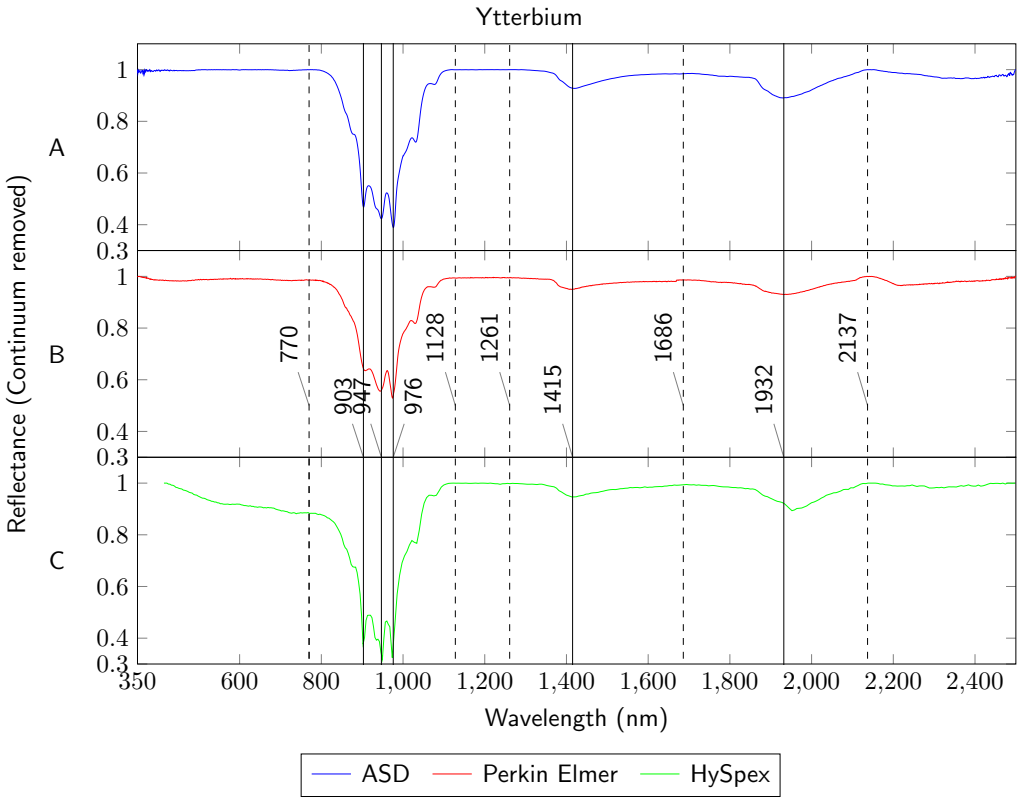

Figure C.45: Reflectance spectra for the REO ytterbium for the VNIR and SWIR region. The Figure shows the results from the measurements of the three spectrometer (***(A)*** *ASD Field Spec 3,* ***(B)*** *Perkin Elmer LAMBDA 950,* ***(C)*** *HySpex (VNIR-1600, SWIR-320m-e)*). The maxima (solid line) and shoulders (dashed line) are marked.

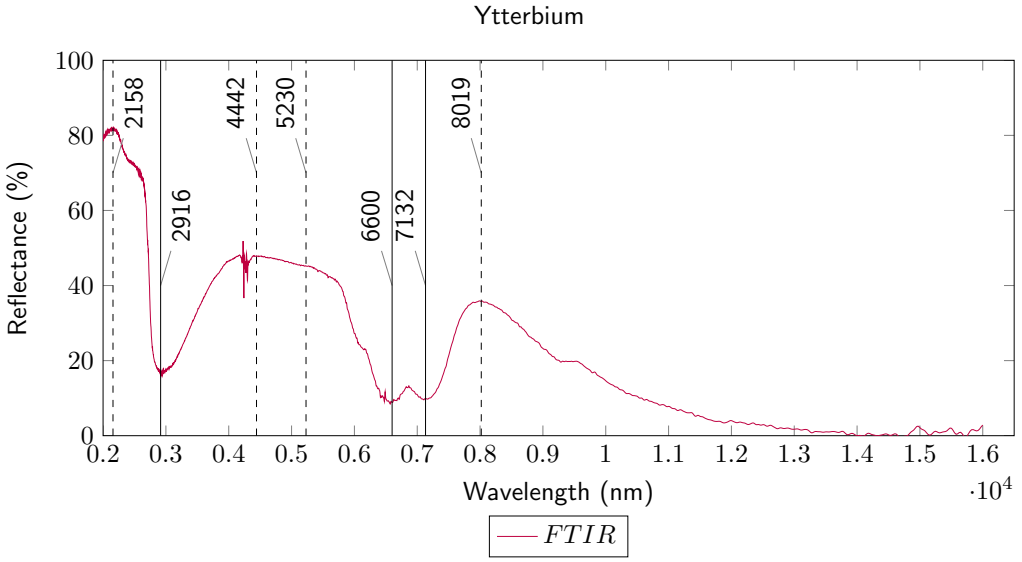

Figure C.46: Reflectance spectrum for the REO ytterbium for the TIR region. The Figure shows the results from the measurement with the *FTIR Spectrum GX*. The maxima (solid line) and shoulders (dashed line) are marked.

STR 19/08. GFZ German Research Centre for Geosciences
DOI: 10.2312/GFZ.b103-19089

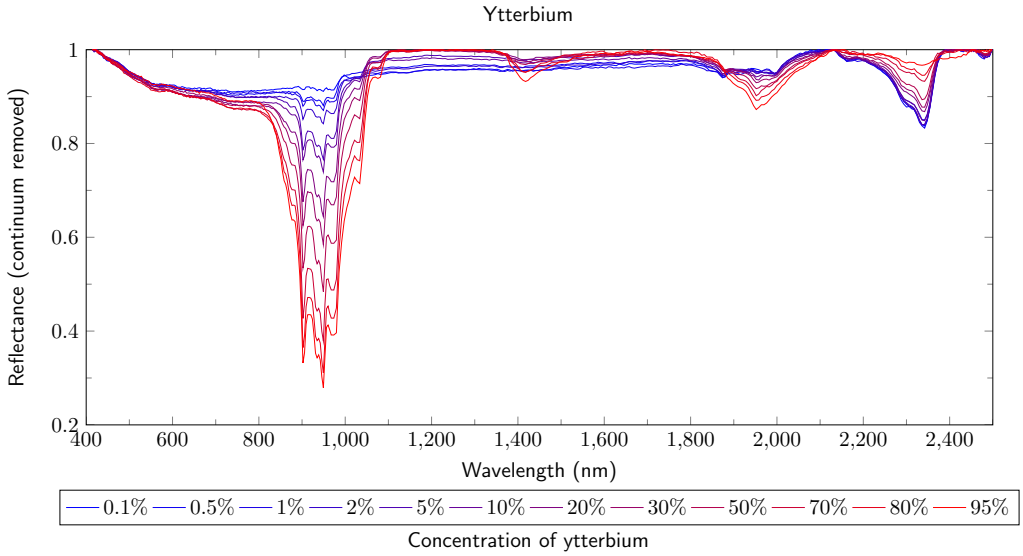

Figure C.47: Reflectance spectra for the REO ytterbium for the VNIR and SWIR region. The Figure shows the results from the measurement of the *HySpex (VNIR-1600, SWIR-320m-e)*. The spectra of all samples are colored from high (red) to low (blue) according to the concentration of ytterbium.

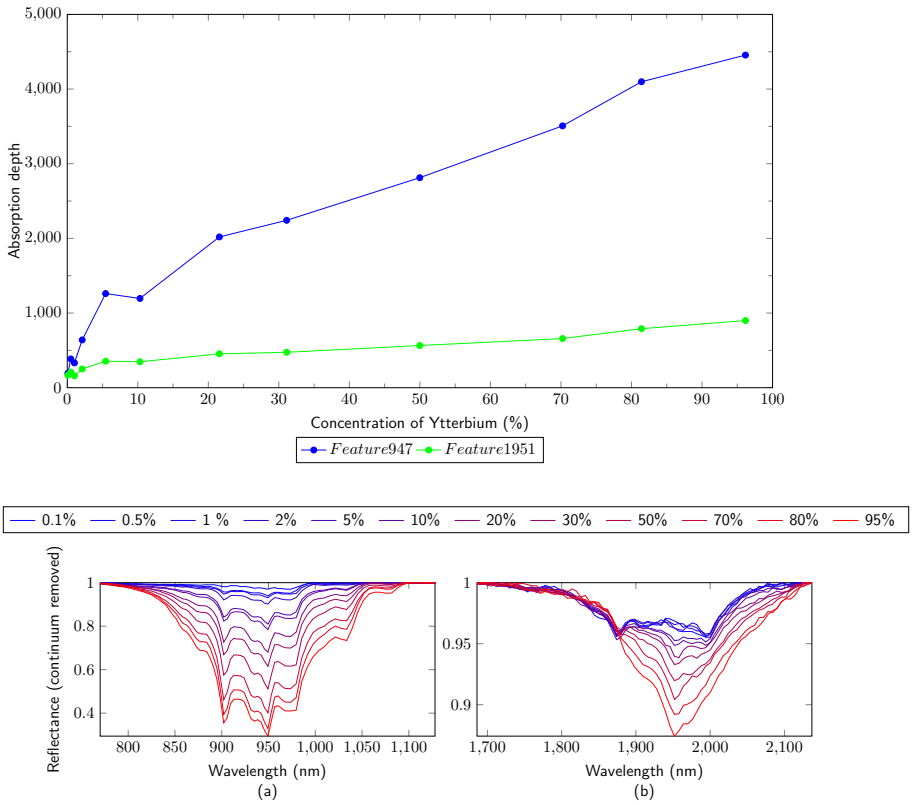

Figure C.48: The Figure **above** shows the correlation between the concentration of ytterbium and the absorption depth of the features at 947 and 1951 nm. The results are from the measurement of the *HySpex (VNIR-1600, SWIR-320m-e)*. The Figure **(a)** shows the reflectance and depth of the absorption feature at 947 nm. The Figure **(b)** shows the reflectance and depth of the absorption feature at 1951 nm.

STR 19/08. GFZ German Research Centre for Geosciences
DOI: 10.2312/GFZ.b103-19089

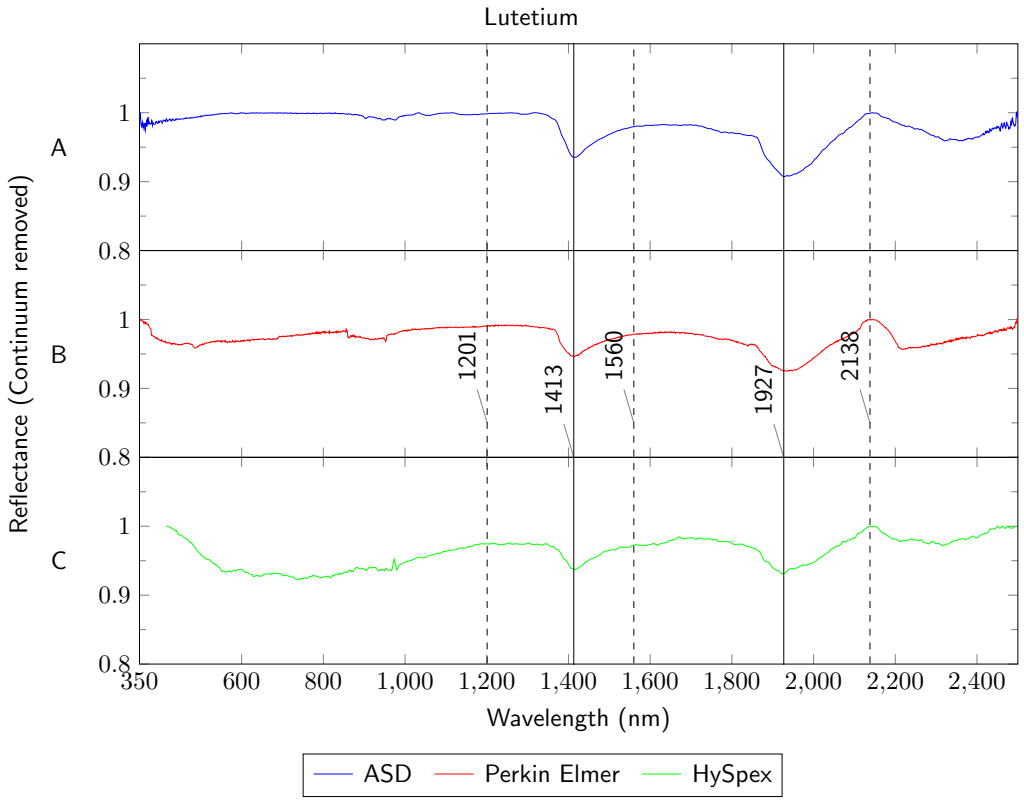

Figure C.49: Reflectance spectra for the REO lutetium for the VNIR and SWIR region. The Figure shows the results from the measurements of the three spectrometer (***(A)*** *ASD Field Spec 3,* ***(B)*** *Perkin Elmer LAMBDA 950,* ***(C)*** *HySpex (VNIR-1600, SWIR-320m-e)*). The maxima (solid line) and shoulders (dashed line) are marked.

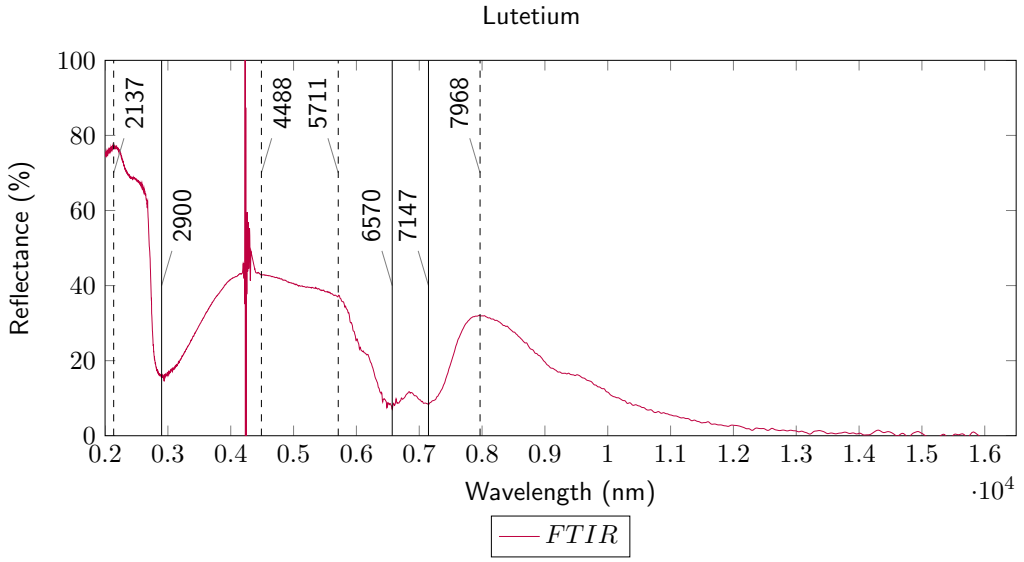

Figure C.50: Reflectance spectrum for the REO lutetium for the TIR region. The Figure shows the results from the measurement with the *FTIR Spectrum GX*. The maxima (solid line) and shoulders (dashed line) are marked.

STR 19/08. GFZ German Research Centre for Geosciences
DOI: 10.2312/GFZ.b103-19089

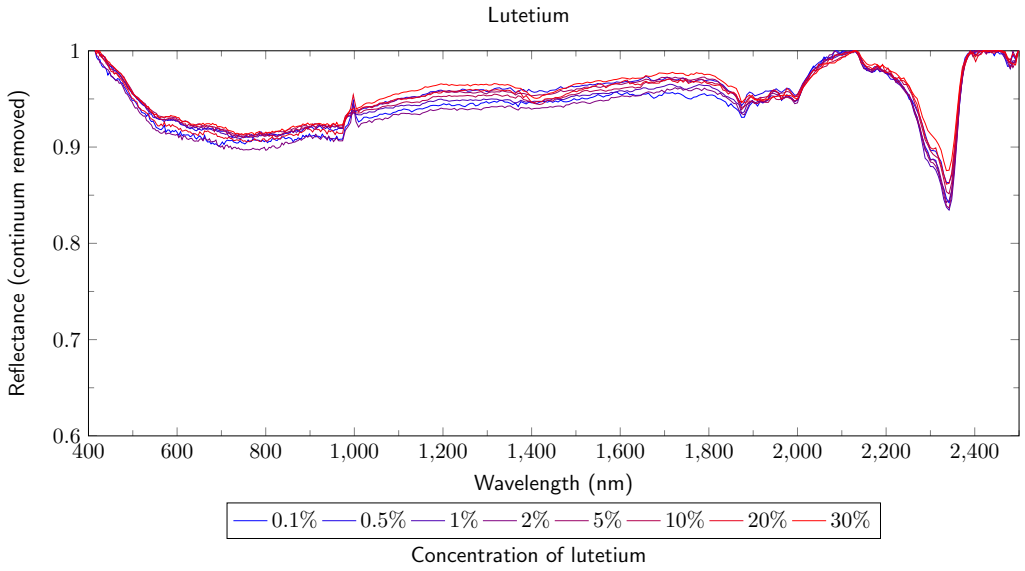

Figure C.51: Reflectance spectra for the REO lutetium for the VNIR and SWIR region. The Figure shows the results from the measurement of the *HySpex (VNIR-1600, SWIR-320m-e)*. The spectra of all samples are colored from high (red) to low (blue) according to the concentration of lutetium.

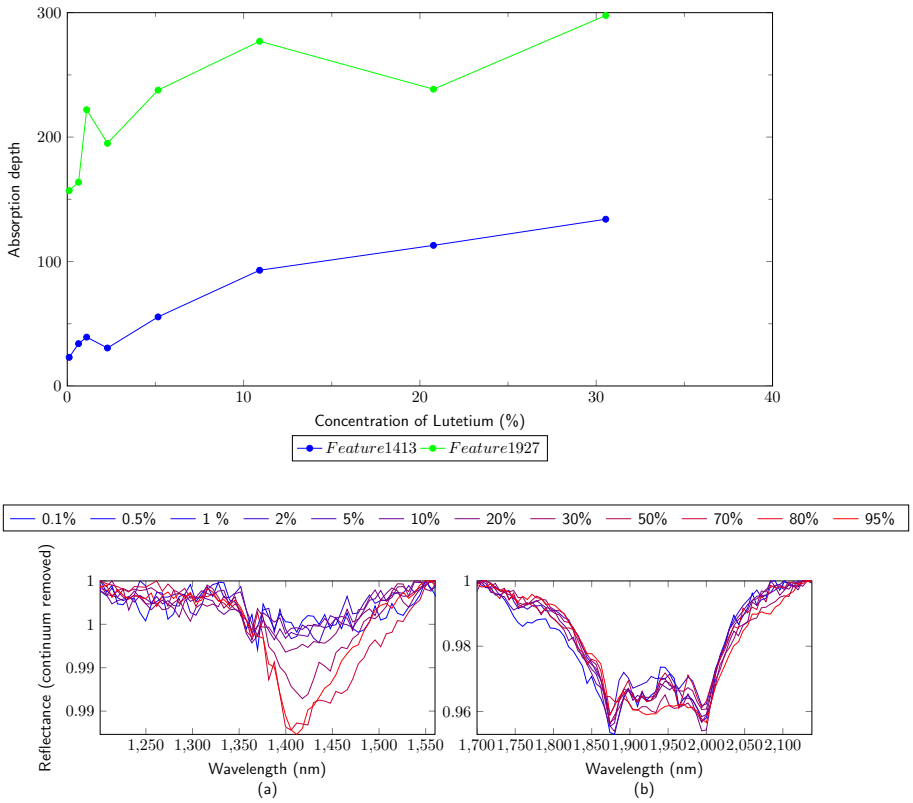

Figure C.52: The Figure **above** shows the correlation between the concentration of lutetium and the absorption depth of the features at 1413 and 1927 nm. The results are from the measurement of the *HySpex (VNIR-1600, SWIR-320m-e)*. The Figure **(a)** shows the reflectance and depth of the absorption feature at 1413 nm. The Figure **(b)** shows the reflectance and depth of the absorption feature at 1927 nm.

STR 19/08. GFZ German Research Centre for Geosciences
DOI: 10.2312/GFZ.b103-19089

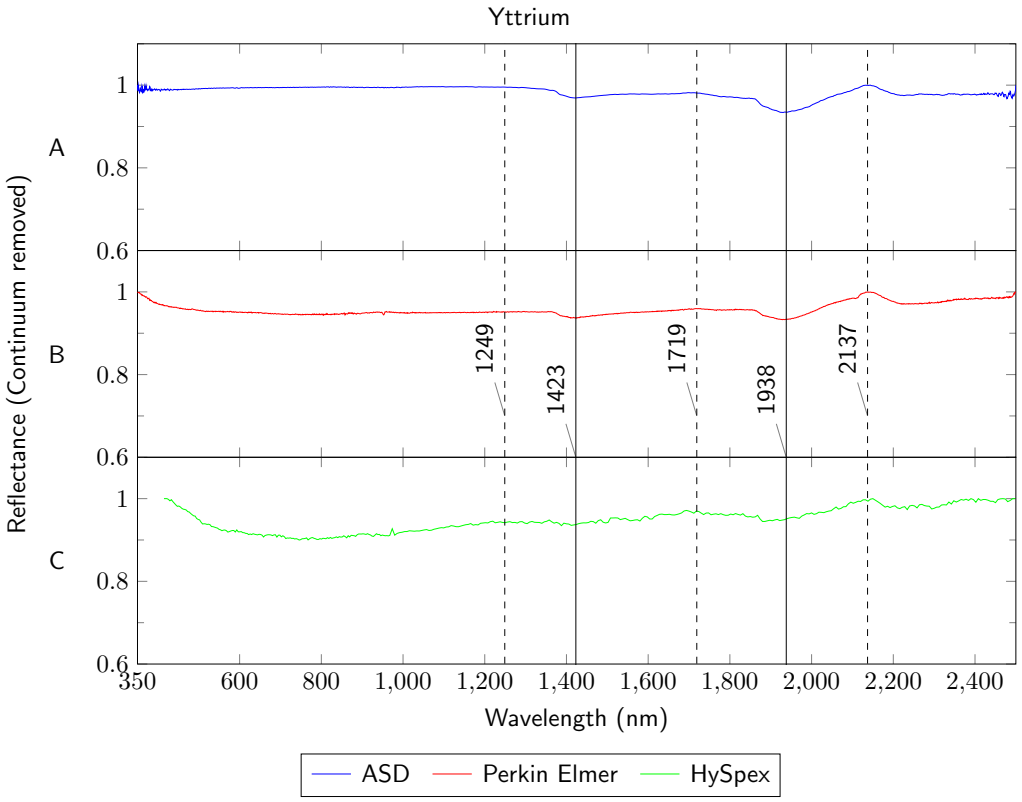

Figure C.53: Reflectance spectra for the REO yttrium for the VNIR and SWIR region. The Figure shows the results from the measurements of the three spectrometer (***(A)*** *ASD Field Spec 3,* ***(B)*** *Perkin Elmer LAMBDA 950,* ***(C)*** *HySpex (VNIR-1600, SWIR-320m-e)*). The maxima (solid line) and shoulders (dashed line) are marked.

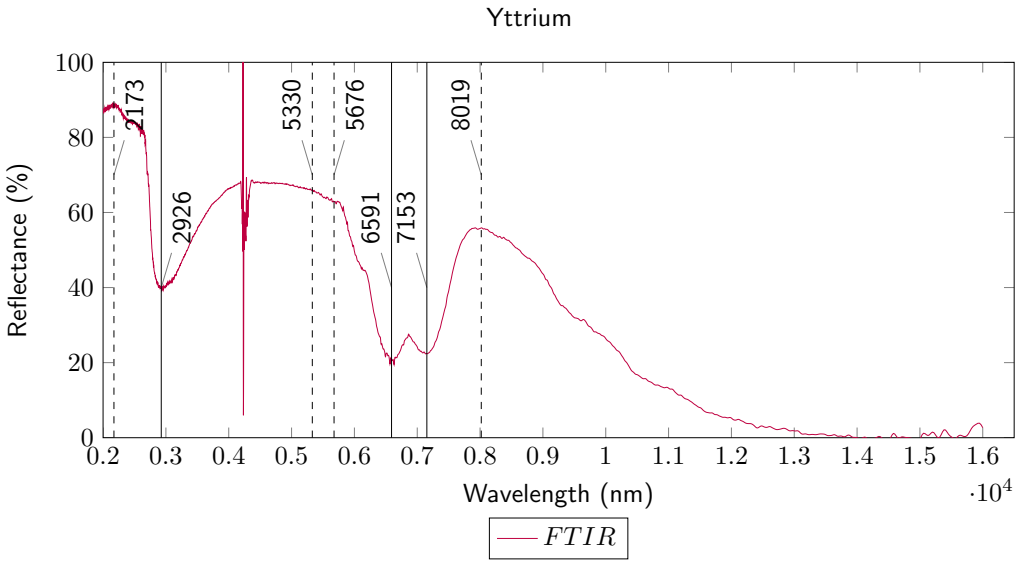

Figure C.54: Reflectance spectra for the REO yttrium for the TIR region. The Figure shows the results from the measurement with the *FTIR Spectrum GX*. The maxima (solid line) and shoulders (dashed line) are marked.

STR 19/08. GFZ German Research Centre for Geosciences
DOI: 10.2312/GFZ.b103-19089

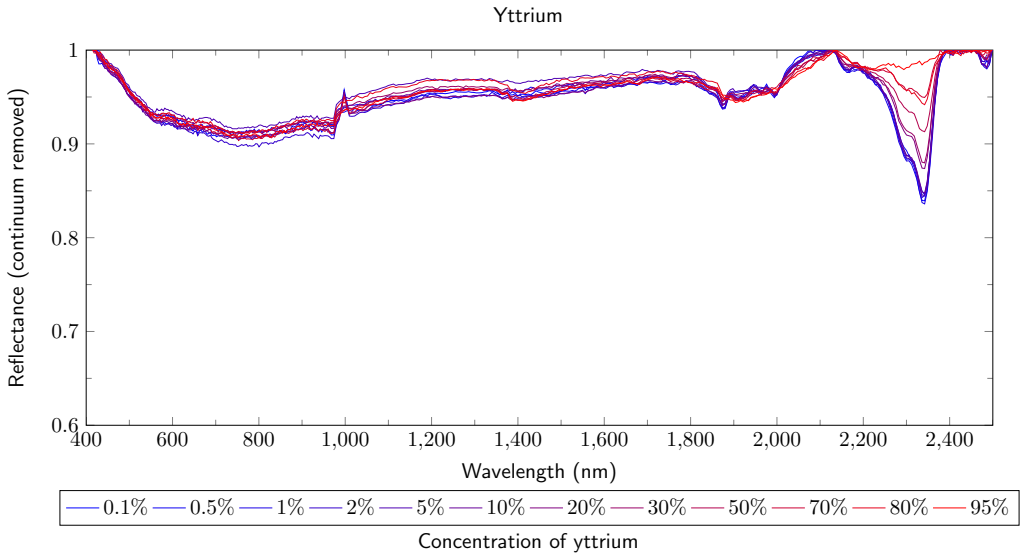

Figure C.55: Reflectance spectra for the REO yttrium for the VNIR and SWIR region. The Figure shows the results from the measurement of the *HySpex (VNIR-1600, SWIR-320m-e)*. The spectra of all samples are colored from high (red) to low (blue) according to the concentration of yttrium

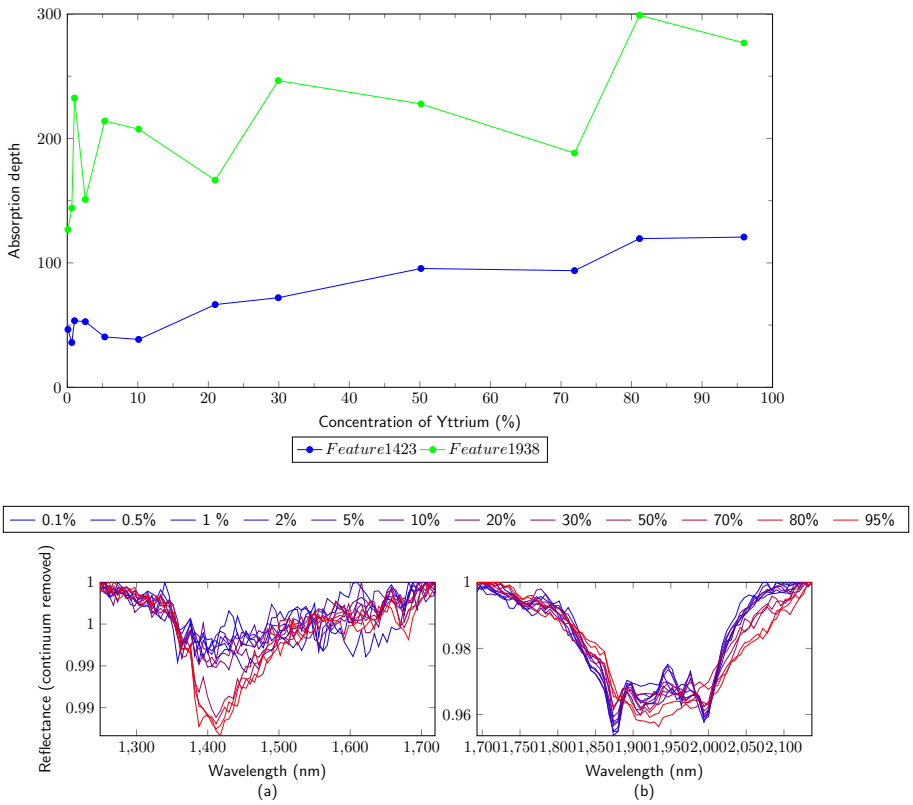

Figure C.56: The Figure **above** shows the correlation between the concentration of yttrium and the absorption depth of the features at 1423 and 1938 nm. The results are from the measurement of the *HySpex (VNIR-1600, SWIR-320m-e)*. The Figure **(a)** shows the reflectance and depth of the absorption feature at 1423 nm. The Figure **(b)** shows the reflectance and depth of the absorption feature at 1938 nm.

STR 19/08. GFZ German Research Centre for Geosciences
DOI: 10.2312/GFZ.b103-19089

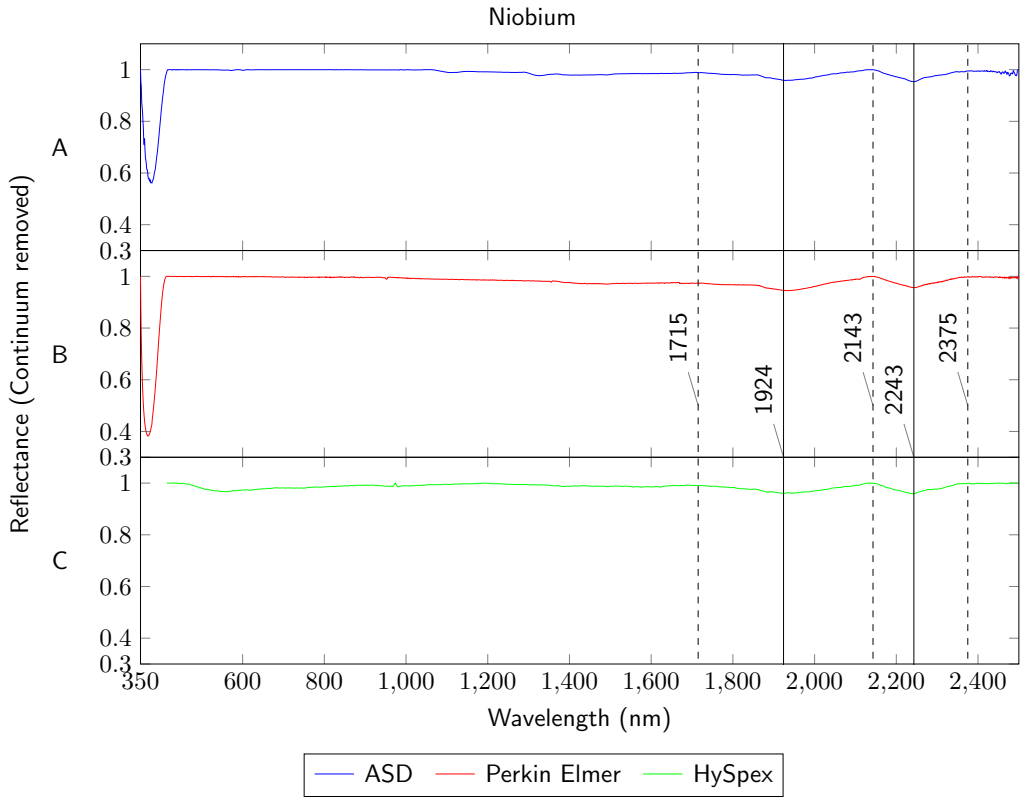

Figure C.57: Reflectance spectra for the REO niobium for the VNIR and SWIR region. The Figure shows the results from the measurements of the three spectrometer (***(A)*** *ASD Field Spec 3,* ***(B)*** *Perkin Elmer LAMBDA 950,* ***(C)*** *HySpex (VNIR-1600, SWIR-320m-e)*). The maxima (solid line) and shoulders (dashed line) are marked.

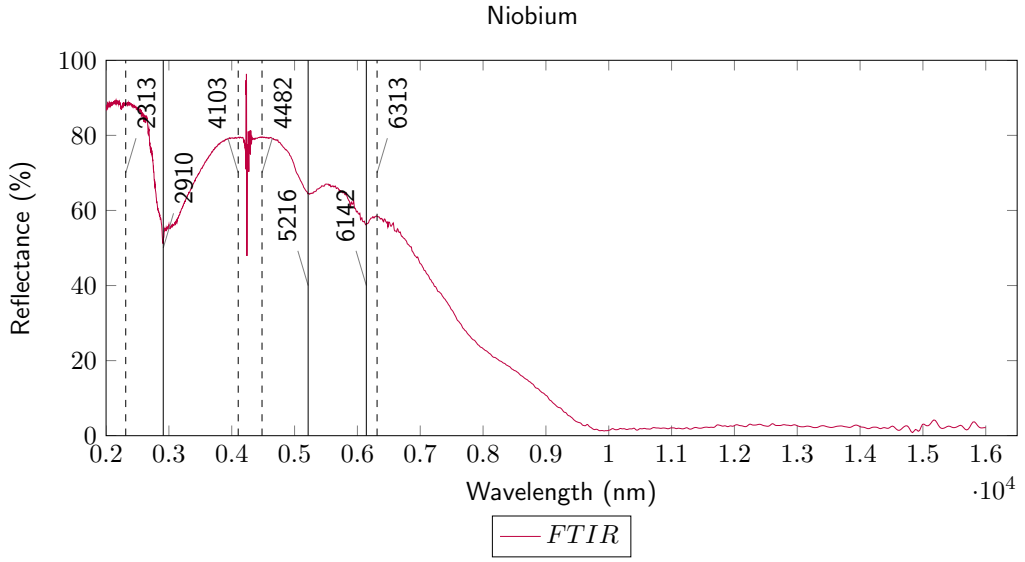

Figure C.58: Reflectance spectra for the REO niobium for the TIR region. The Figure shows the results from the measurement with the *FTIR Spectrum GX*. The maxima (solid line) and shoulders (dashed line) are marked.

STR 19/08. GFZ German Research Centre for Geosciences
DOI: 10.2312/GFZ.b103-19089

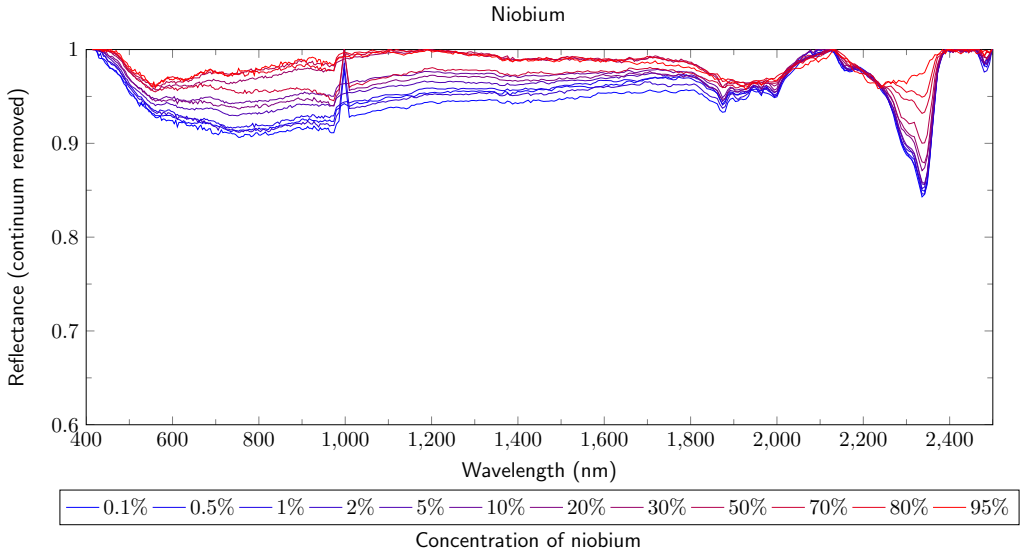

Figure C.59: Reflectance spectra for the REO niobium for the VNIR and SWIR region. The Figure shows the results from the measurement of the *HySpex (VNIR-1600, SWIR-320m-e)*. The spectra of all samples are colored from high (red) to low (blue) according to the concentration of niobium.

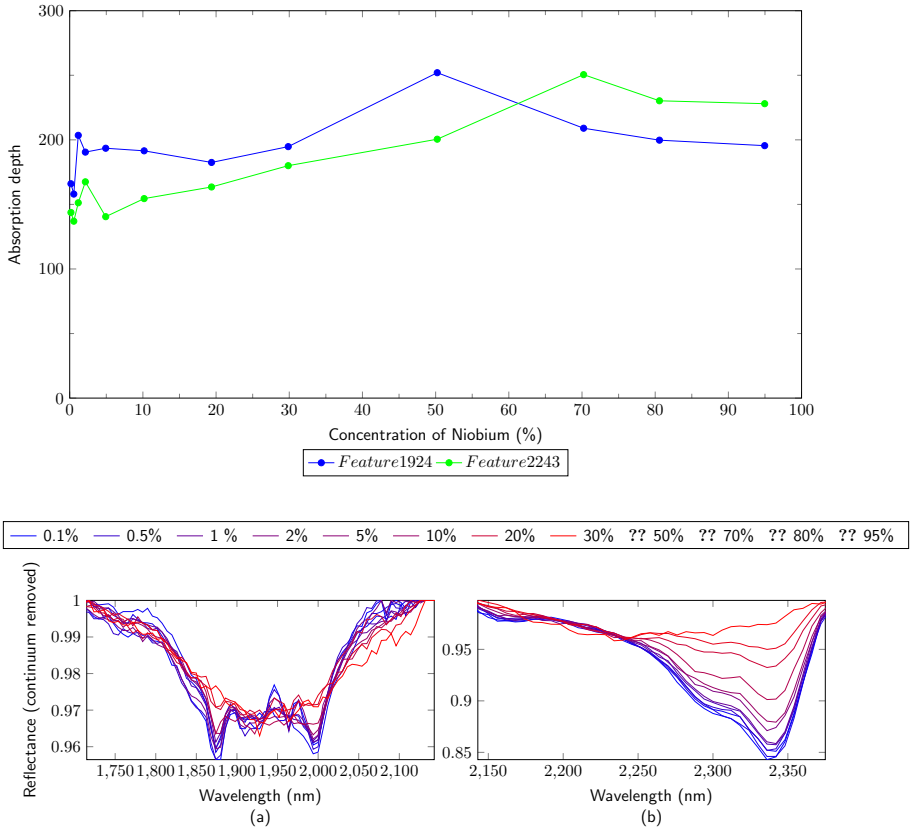

Figure C.60: The Figure **above** shows the correlation between the concentration of niobium and the absorption depth of the features at 1924 and 2243 nm. The results are from the measurement of the *HySpex (VNIR-1600, SWIR-320m-e)*. The Figure **(a)** shows the reflectance and depth of the absorption feature at 1924 nm. The Figure **(b)** shows the reflectance and depth of the absorption feature at 2243 nm.

STR 19/08. GFZ German Research Centre for Geosciences
DOI: 10.2312/GFZ.b103-19089

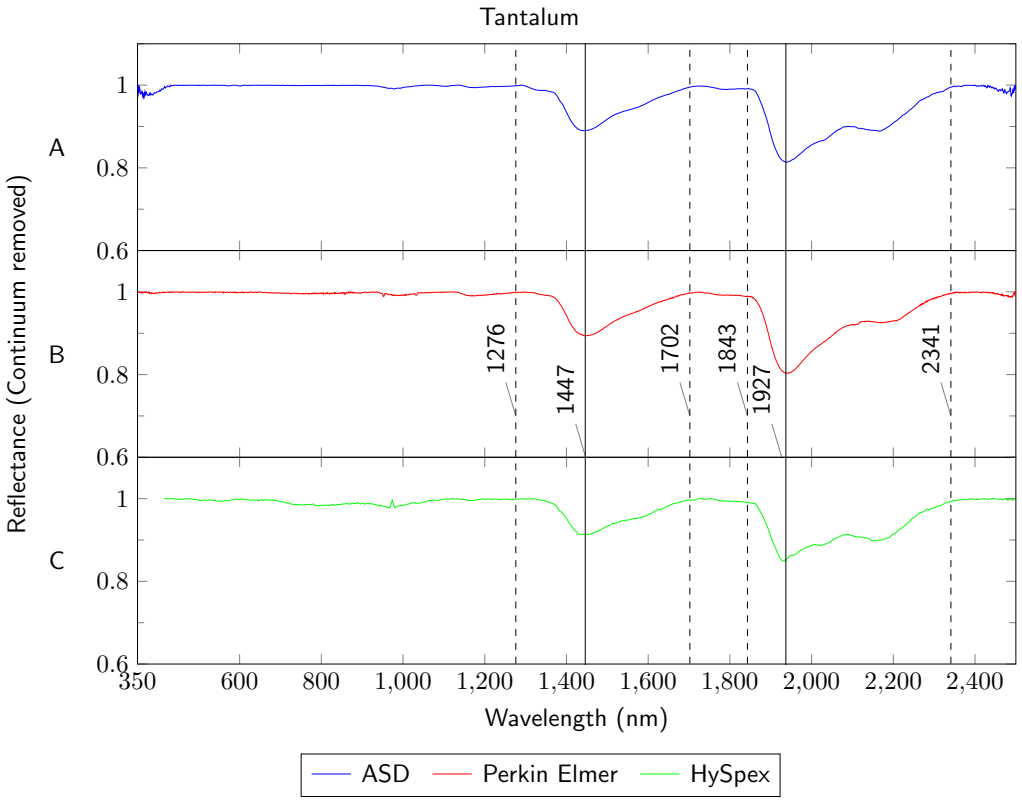

Figure C.61: Reflectance spectra for the REO tantalum for the VNIR and SWIR region. The Figure shows the results from the measurements of the three spectrometer (***(A)*** *ASD Field Spec 3,* ***(B)*** *Perkin Elmer LAMBDA 950,* ***(C)*** *HySpex (VNIR-1600, SWIR-320m-e)*). The maxima (solid line) and shoulders (dashed line) are marked.

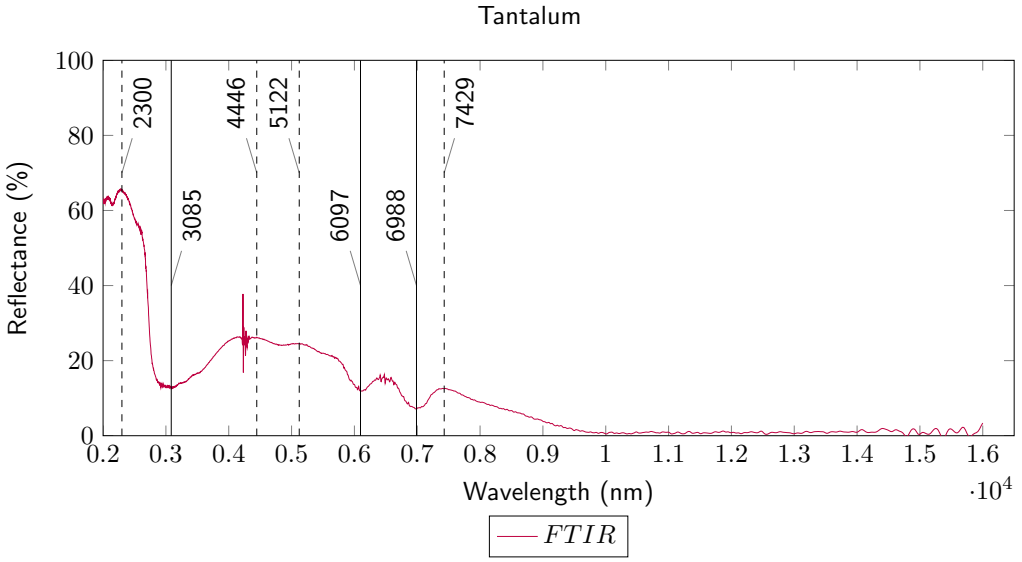

Figure C.62: Reflectance spectra for the REO tantalum for the TIR region. The Figure shows the results from the measurement with the *FTIR Spectrum GX*. The maxima (solid line) and shoulders (dashed line) are marked.

STR 19/08. GFZ German Research Centre for Geosciences
DOI: 10.2312/GFZ.b103-19089

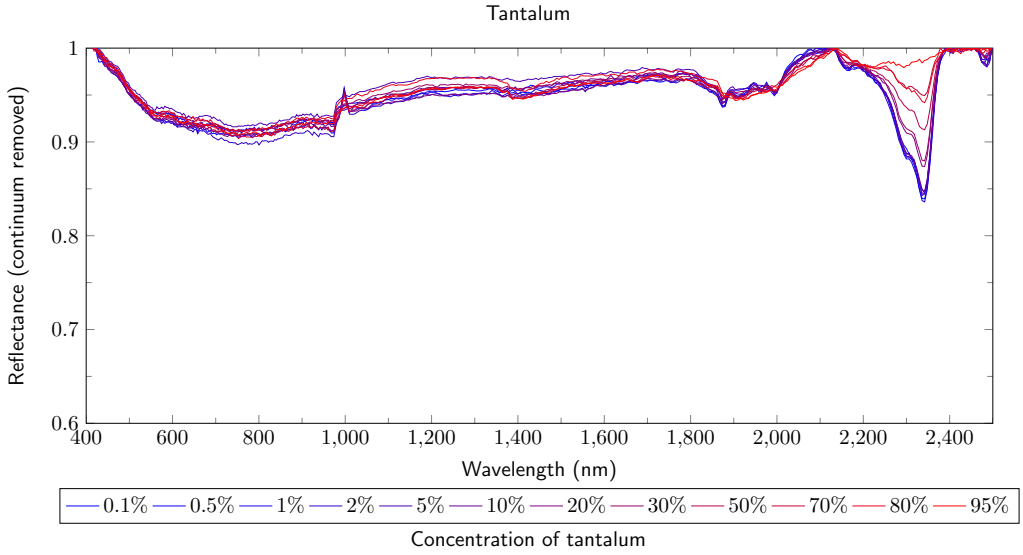

Figure C.63: Reflectance spectra for the REO tantalum for the VNIR and SWIR region. The Figure shows the results from the measurement of the *HySpex (VNIR-1600, SWIR-320m-e)*. The spectra of all samples are colored from high (red) to low (blue) according to the concentration of tantalum.

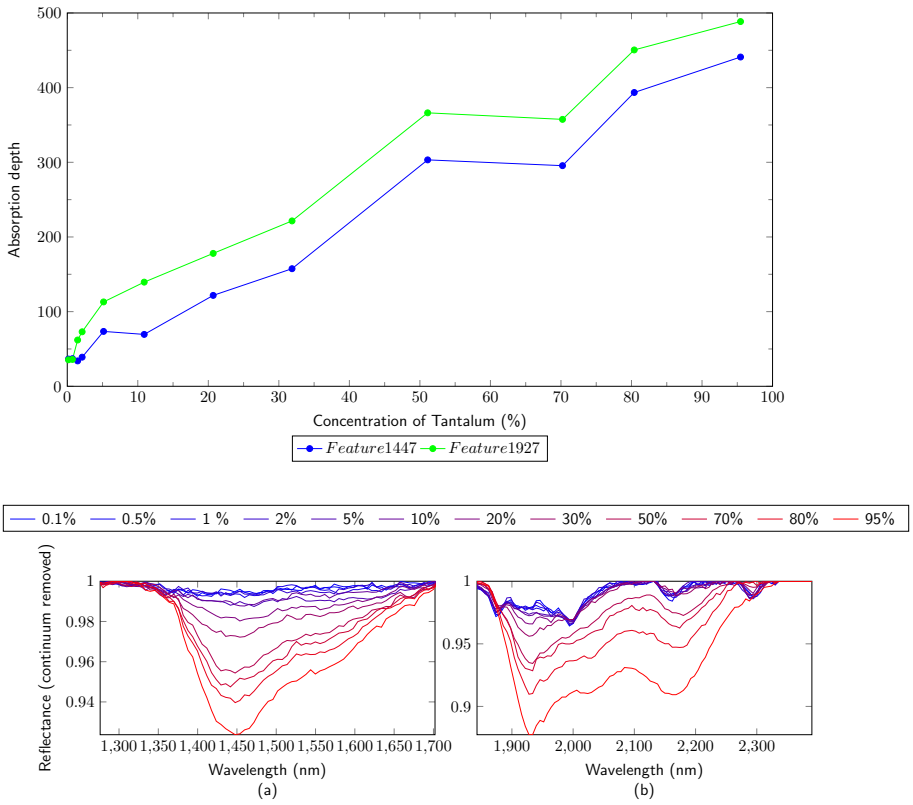

Figure C.64: The Figure **above** shows the correlation between the concentration of tantalum and the absorption depth of the features at 1447 and 1927 nm. The results are from the measurement of the *HySpex (VNIR-1600, SWIR-320m-e)*. The Figure **(a)** shows the reflectance and depth of the absorption feature at 1447 nm. The Figure **(b)** shows the reflectance and depth of the absorption feature at 1927 nm.

STR 19/08. GFZ German Research Centre for Geosciences
DOI: 10.2312/GFZ.b103-19089

Appendix D - REE Minerals - Spectral Results, Plots

STR 19/08. GFZ German Research Centre for Geosciences
DOI: 10.2312/GFZ.b103-19089

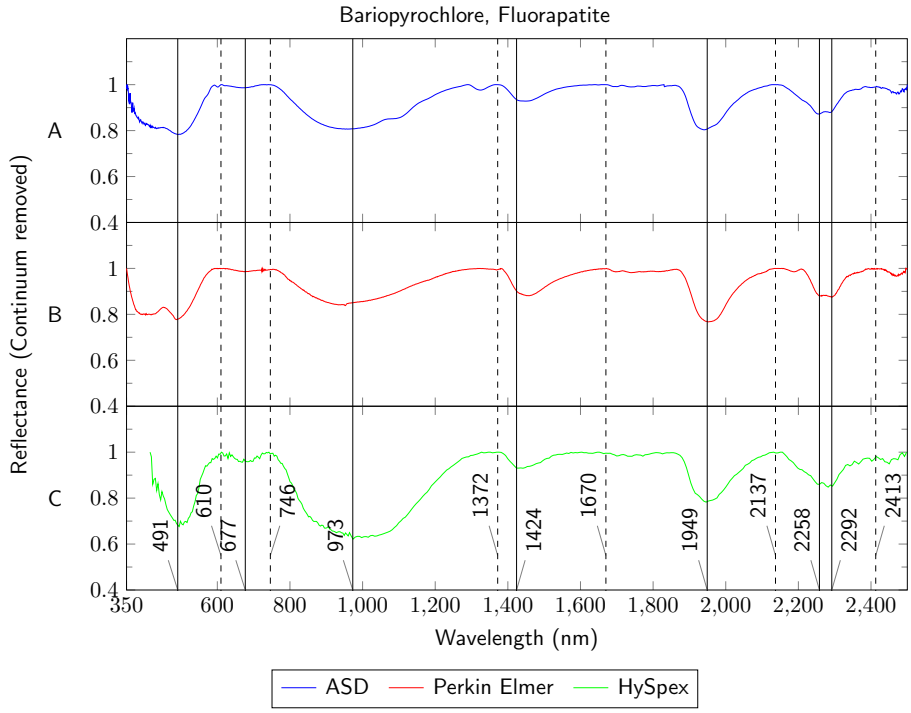

Figure D.65: Reflectance spectra for the rare earth mineral Bariopyrochlore, Fluorapatite for the VNIR and SWIR region. The Figure shows the results from the measurements of the three spectrometer (***(A)*** *ASD Field Spec 3,* ***(B)*** *Perkin Elmer LAMBDA 950,* ***(C)*** *HySpex (VNIR-1600, SWIR-320m-e)*). Spectra are stacked and absorption features as well as their maxima and shoulders are marked.

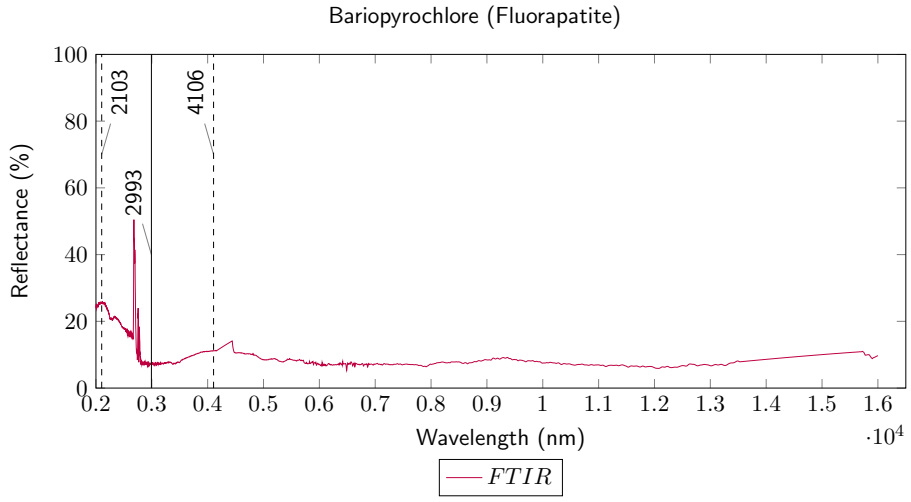

Figure D.66: Reflectance spectrum for the rare earth mineral Bariopyrochlore for the TIR region. The Figure shows the results from the measurement with the *FTIR Spectrum GX*. The maxima (solid line) and shoulders (dashed line) are marked.

STR 19/08. GFZ German Research Centre for Geosciences
DOI: 10.2312/GFZ.b103-19089

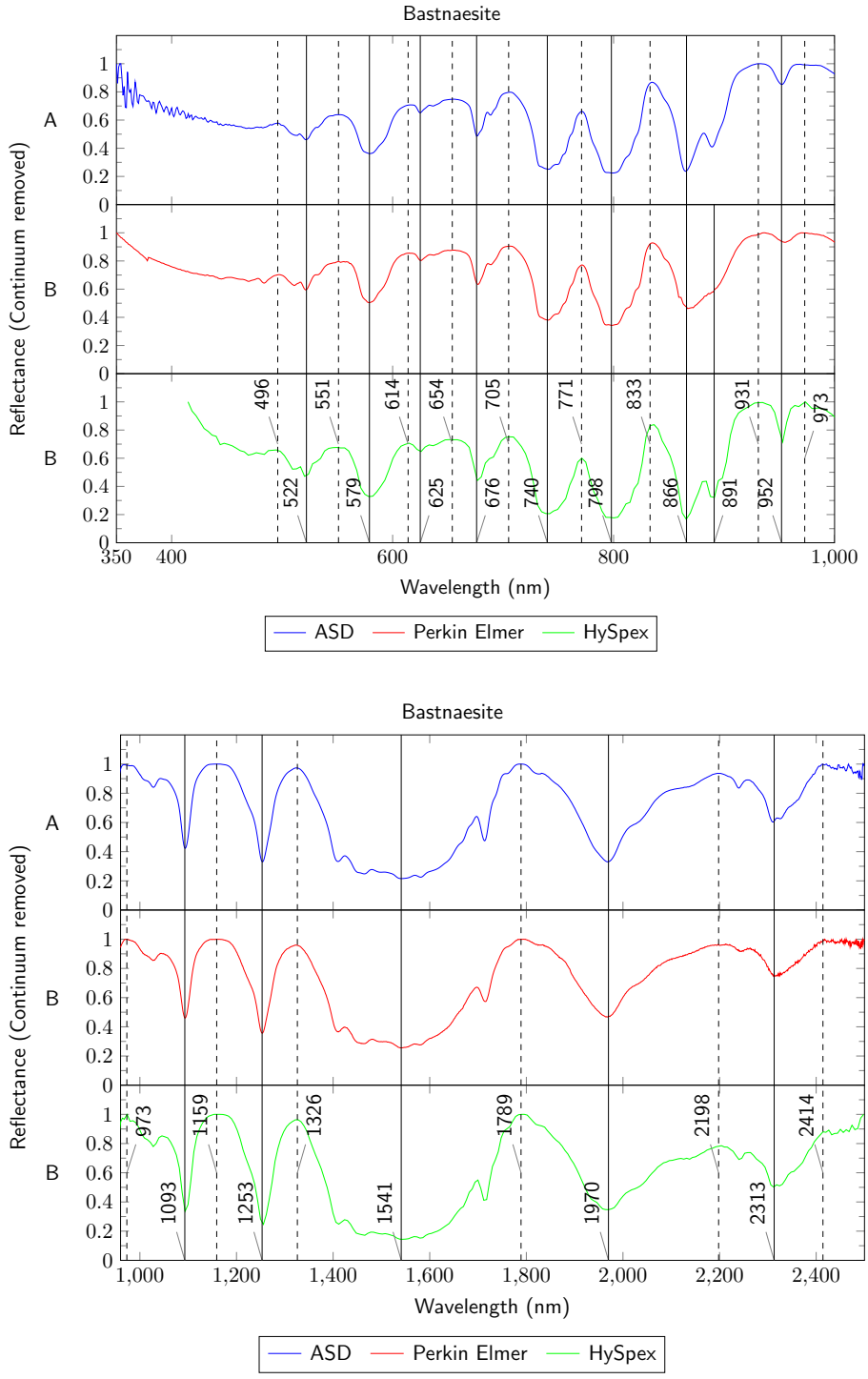

Figure D.67: Reflectance spectra for the rare earth mineral bastnaesite for the VNIR and SWIR region. The Figure **above** shows the results from the measurements of the three spectrometer (***(A)*** *ASD Field Spec 3,* ***(B)*** *Perkin Elmer LAMBDA 950,* ***(C)*** *HySpex (VNIR-1600, SWIR-320m-e)*) in a wavelentgh region from 350 to 1000 nm. The Figure **below** shows the results from the measurements of the three spectrometer (***(A)*** *ASD Field Spec 3,* ***(B)*** *Perkin Elmer LAMBDA 950,* ***(C)*** *HySpex (VNIR-1600, SWIR-320m-e)*) in a wavelentgh region from 960 to 2500 nm. The maxima (solid line) and shoulders (dashed line) are marked.

STR 19/08. GFZ German Research Centre for Geosciences
DOI: 10.2312/GFZ.b103-19089

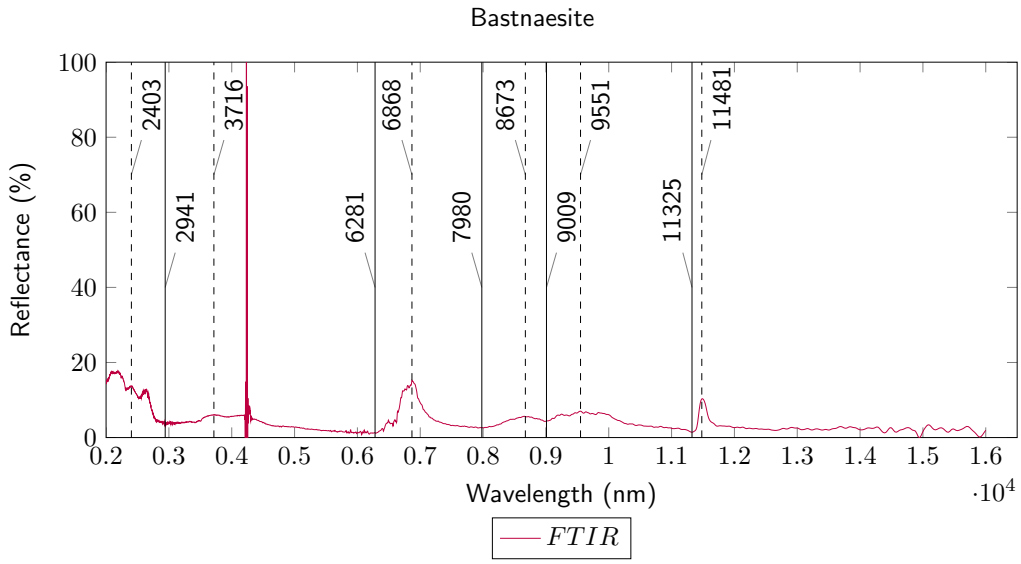

Figure D.68: Reflectance spectrum for the rare earth mineral bastnaesite for the TIR region. The Figure shows the results from the measurement with the *FTIR Spectrum GX*. The maxima (solid line) and shoulders (dashed line) are marked.

STR 19/08. GFZ German Research Centre for Geosciences
DOI: 10.2312/GFZ.b103-19089

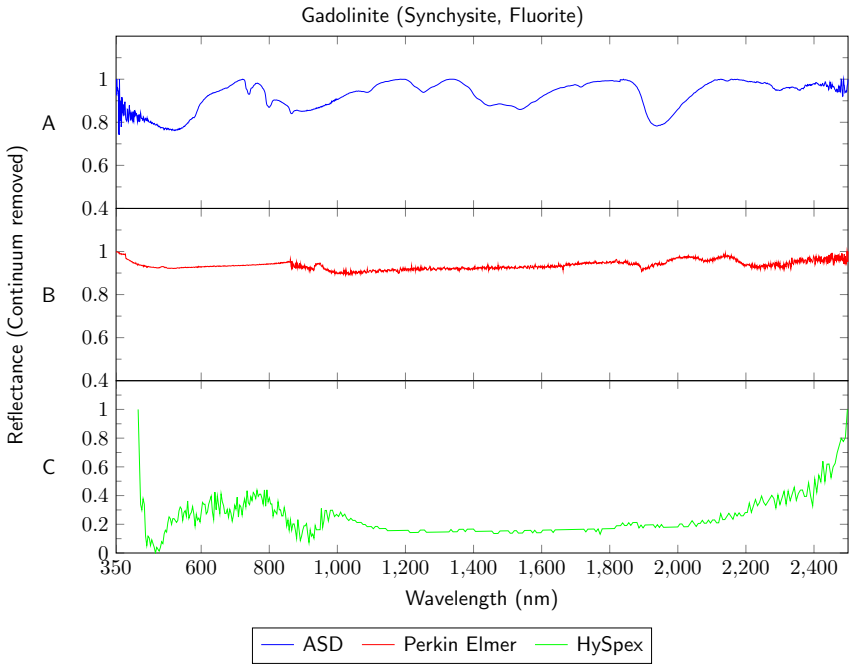

Figure D.69: Reflectance spectra for the rare earth mineral gadolinite for the VNIR and SWIR region. The Figure shows the results from the measurements of the three spectrometer (***(A)*** *ASD Field Spec 3,* ***(B)*** *Perkin Elmer LAMBDA 950,* ***(C)*** *HySpex (VNIR-1600, SWIR-320m-e)*). Spectra are stacked and absorption features as well as their maxima and shoulders are marked.

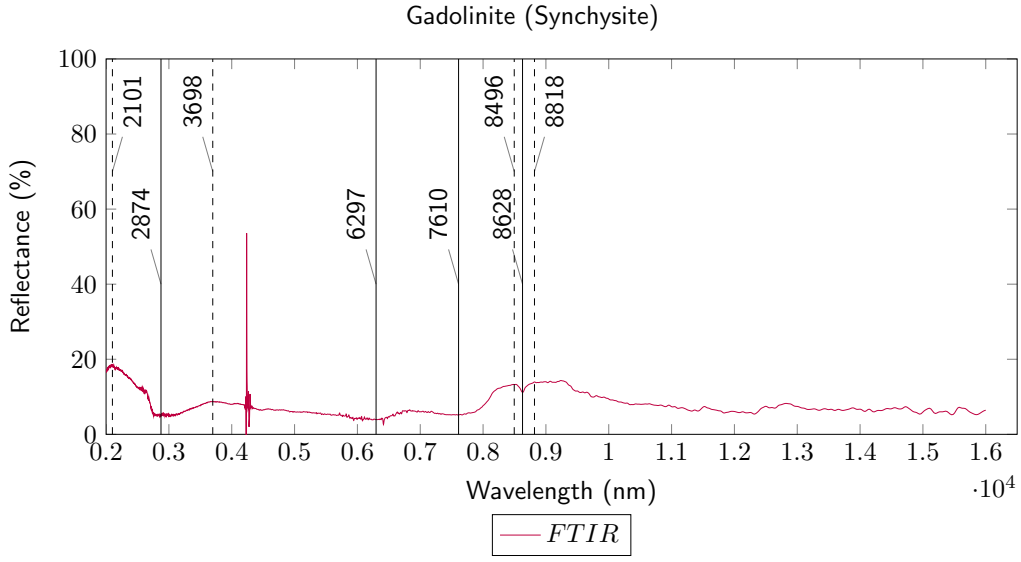

Figure D.70: Reflectance spectrum for the rare earth mineral gadolinite for the TIR region. The Figure shows the results from the measurement with the *FTIR Spectrum GX*. The maxima (solid line) and shoulders (dashed line) are marked.

STR 19/08. GFZ German Research Centre for Geosciences
DOI: 10.2312/GFZ.b103-19089

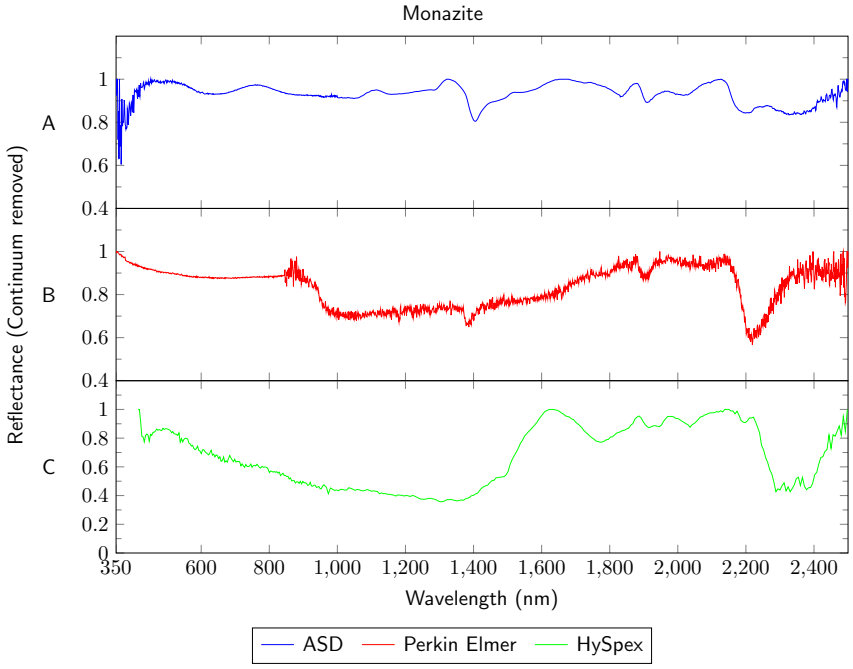

Figure D.71: Reflectance spectra for the rare earth mineral monazite for the VNIR and SWIR region. The Figure shows the results from the measurements of the three spectrometer (***(A)*** *ASD Field Spec 3,* ***(B)*** *Perkin Elmer LAMBDA 950,* ***(C)*** *HySpex (VNIR-1600, SWIR-320m-e)*). Spectra are stacked and absorption features as well as their maxima and shoulders are marked.

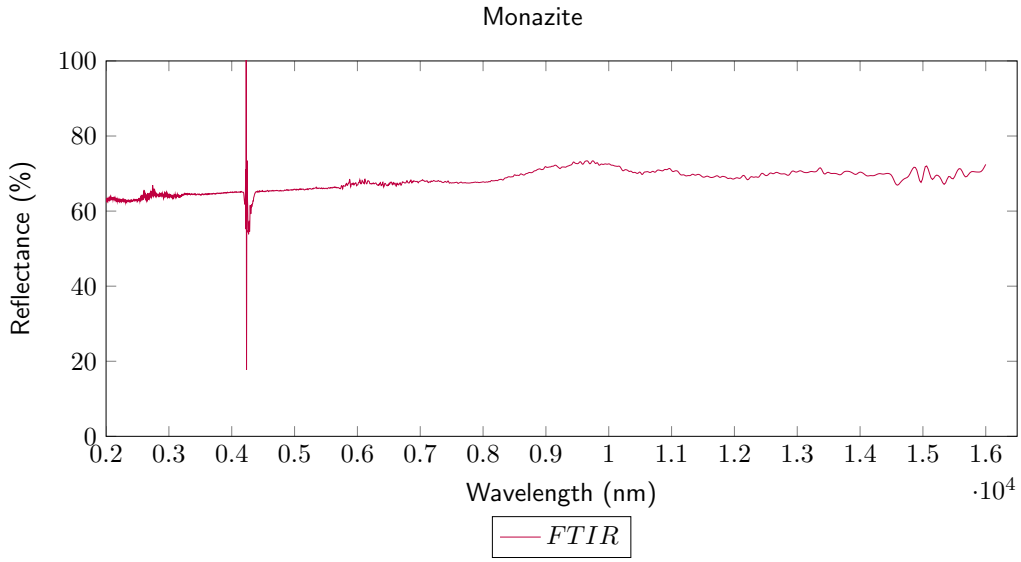

Figure D.72: Reflectance spectrum for the rare earth mineral monazite for the TIR region. The Figure shows the results from the measurement with the *FTIR Spectrum GX*. The maxima (solid line) and shoulders (dashed line) are marked.

STR 19/08. GFZ German Research Centre for Geosciences
DOI: 10.2312/GFZ.b103-19089

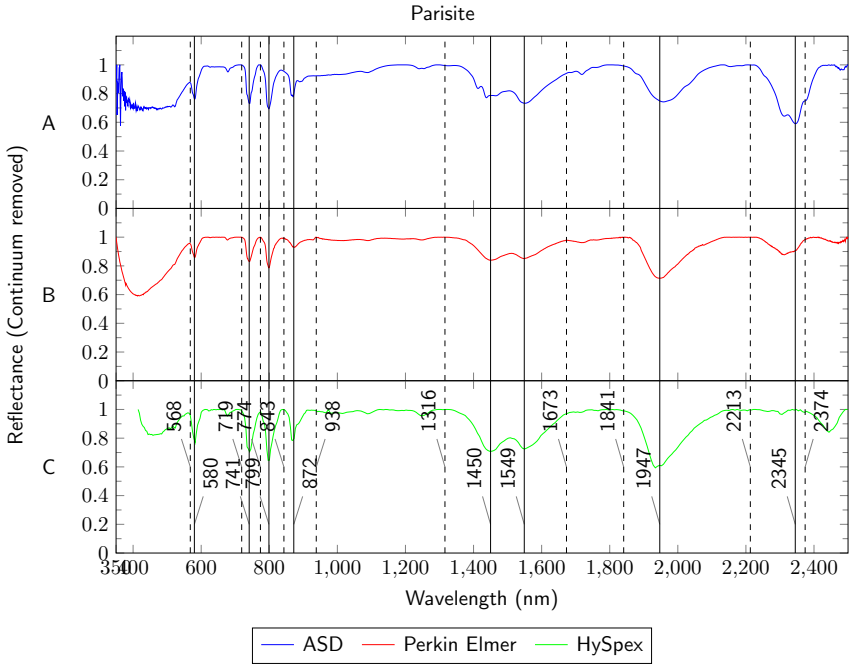

Figure D.73: Reflectance spectra for the rare earth mineral parisite for the VNIR and SWIR region. The Figure shows the results from the measurements of the three spectrometer (***(A)*** *ASD Field Spec 3,* ***(B)*** *Perkin Elmer LAMBDA 950,* ***(C)*** *HySpex (VNIR-1600, SWIR-320m-e)*). Spectra are stacked and absorption features as well as their maxima and shoulders are marked.

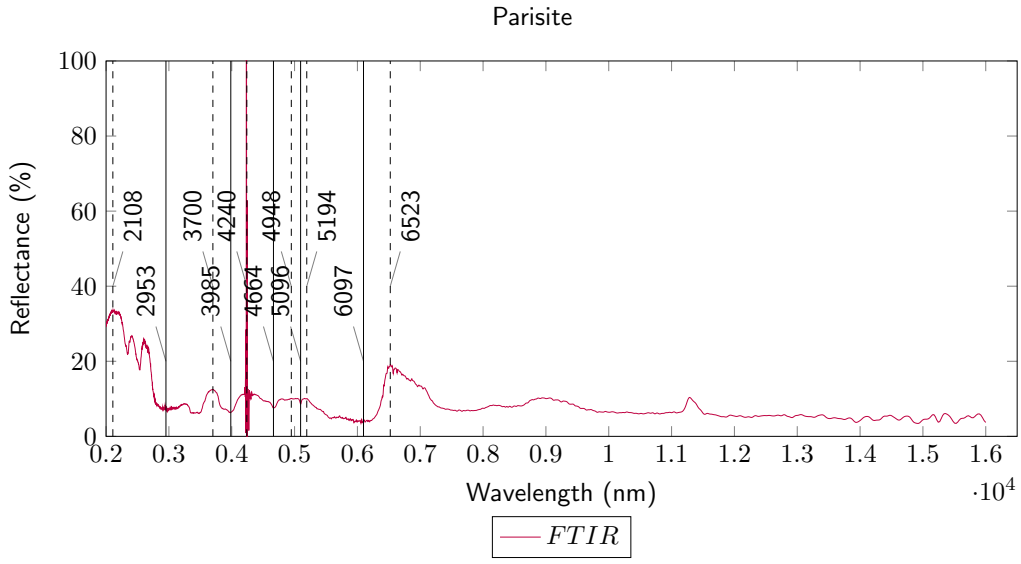

Figure D.74: Reflectance spectrum for the rare earth mineral parisite for the TIR region. The Figure shows the results from the measurement with the *FTIR Spectrum GX*. The maxima (solid line) and shoulders (dashed line) are marked.

STR 19/08. GFZ German Research Centre for Geosciences
DOI: 10.2312/GFZ.b103-19089

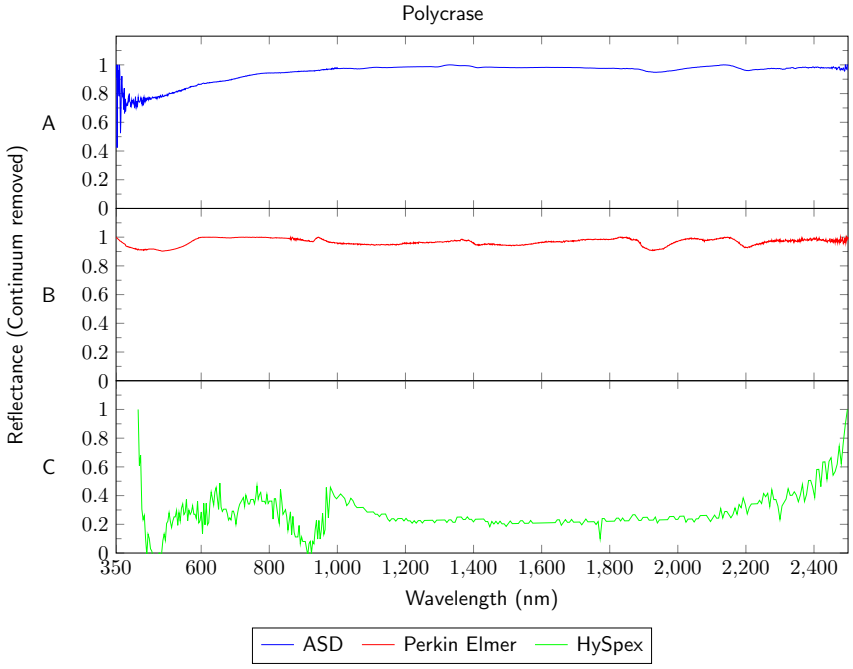

Figure D.75: Reflectance spectra for the rare earth mineral polycrase for the VNIR and SWIR region. The Figure shows the results from the measurements of the three spectrometer (***(A)*** *ASD Field Spec 3,* ***(B)*** *Perkin Elmer LAMBDA 950,* ***(C)*** *HySpex (VNIR-1600, SWIR-320m-e)*). Spectra are stacked and absorption features as well as their maxima and shoulders are marked.

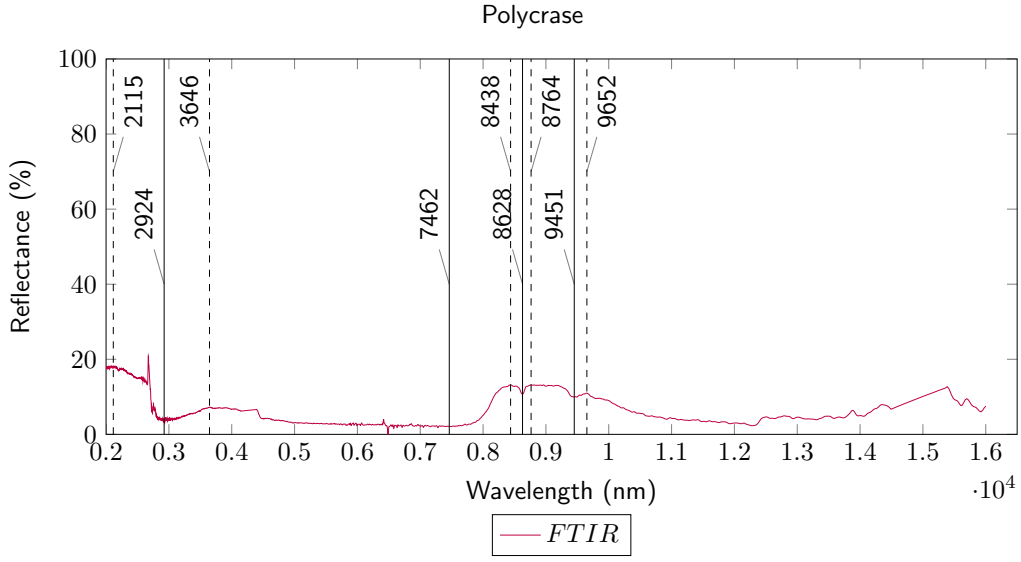

Figure D.76: Reflectance spectrum for the rare earth mineral polycrase for the TIR region. The Figure shows the results from the measurement with the *FTIR Spectrum GX*. The maxima (solid line) and shoulders (dashed line) are marked.

STR 19/08. GFZ German Research Centre for Geosciences
DOI: 10.2312/GFZ.b103-19089

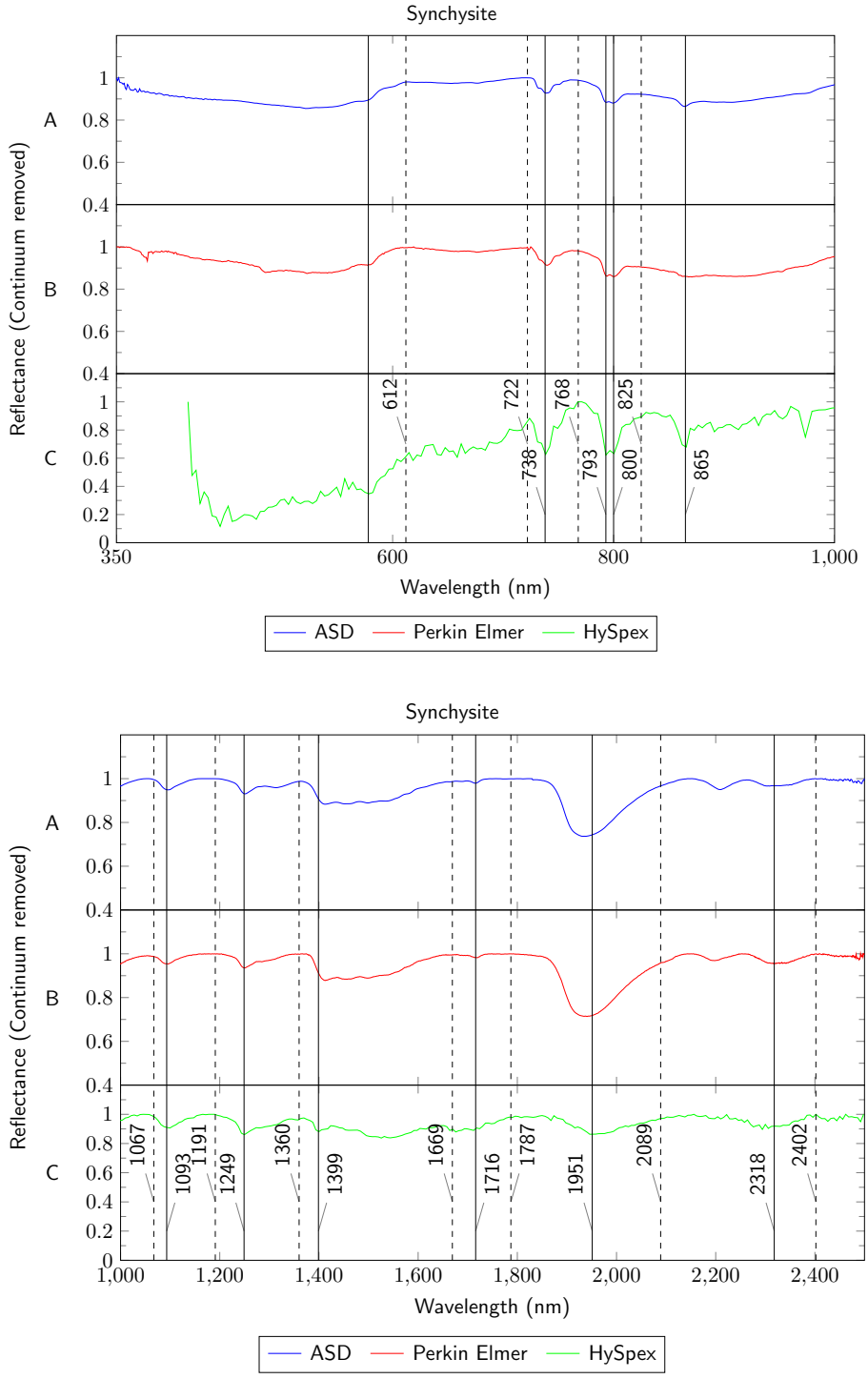

Figure D.77: Reflectance spectra for the rare earth mineral synchysite for the VNIR and SWIR region. The Figure **above** shows the results from the measurements of the three spectrometer (***(A)*** *ASD Field Spec 3,* ***(B)*** *Perkin Elmer LAMBDA 950,* ***(C)*** *HySpex (VNIR-1600, SWIR-320m-e)*) in a wavelentgh region from 350 to 1000 nm. The Figure **below** shows the results from the measurements of the three spectrometer (***(A)*** *ASD Field Spec 3,* ***(B)*** *Perkin Elmer LAMBDA 950,* ***(C)*** *HySpex (VNIR-1600, SWIR-320m-e)*) in a wavelentgh region from 1000 to 2500 nm. The maxima (solid line) and shoulders (dashed line) are marked.

STR 19/08. GFZ German Research Centre for Geosciences
DOI: 10.2312/GFZ.b103-19089

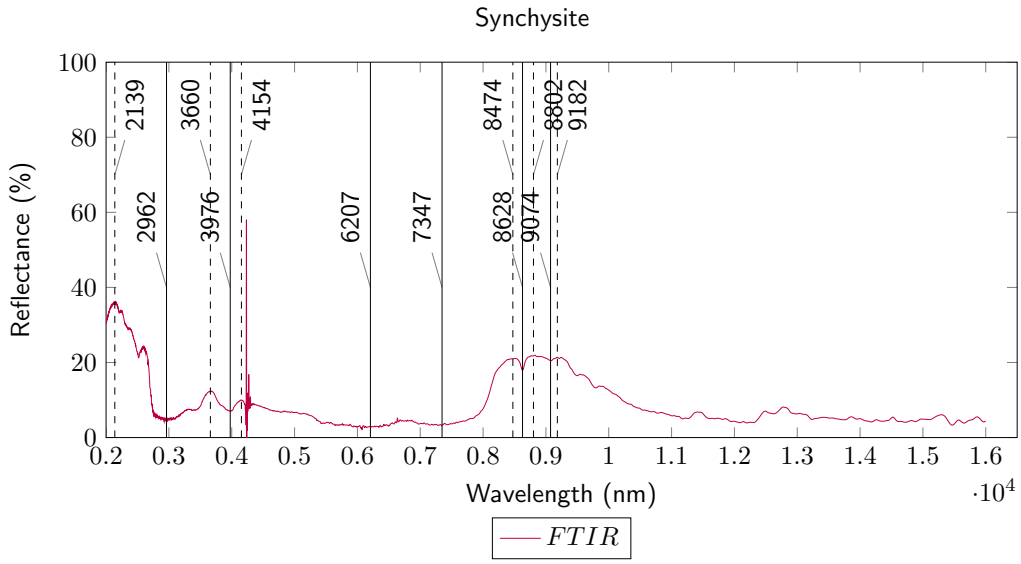

Figure D.78: Reflectance spectrum for the rare earth mineral synchysite for the TIR region. The Figure shows the results from the measurement with the *FTIR Spectrum GX*. The maxima (solid line) and shoulders (dashed line) are marked.

STR 19/08. GFZ German Research Centre for Geosciences
DOI: 10.2312/GFZ.b103-19089

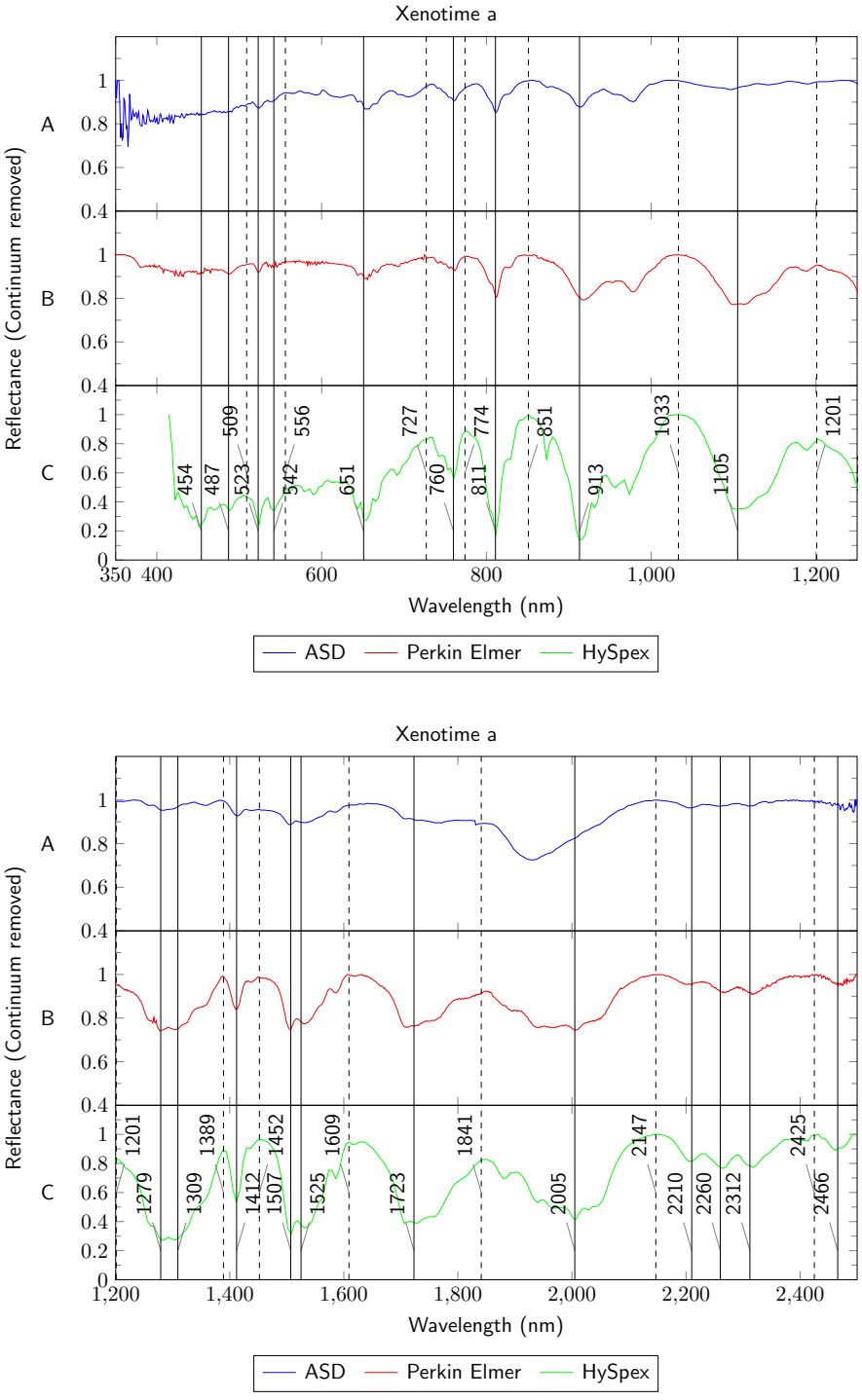

Figure D.79: Reflectance spectra for the rare earth mineral xenotime a for the VNIR and SWIR region. The Figure **above** shows the results from the measurements of the three spectrometer (***(A)*** *ASD Field Spec 3,* ***(B)*** *Perkin Elmer LAMBDA 950,* ***(C)*** *HySpex (VNIR-1600, SWIR-320m-e)*) in a wavelentgh region from 350 to 1200 nm. The Figure **below** shows the results from the measurements of the three spectrometer (***(A)*** *ASD Field Spec 3,* ***(B)*** *Perkin Elmer LAMBDA 950,* ***(C)*** *HySpex (VNIR-1600, SWIR-320m-e)*) in a wavelentgh region from 1200 to 2500 nm. The maxima (solid line) and shoulders (dashed line) are marked.

STR 19/08. GFZ German Research Centre for Geosciences
DOI: 10.2312/GFZ.b103-19089

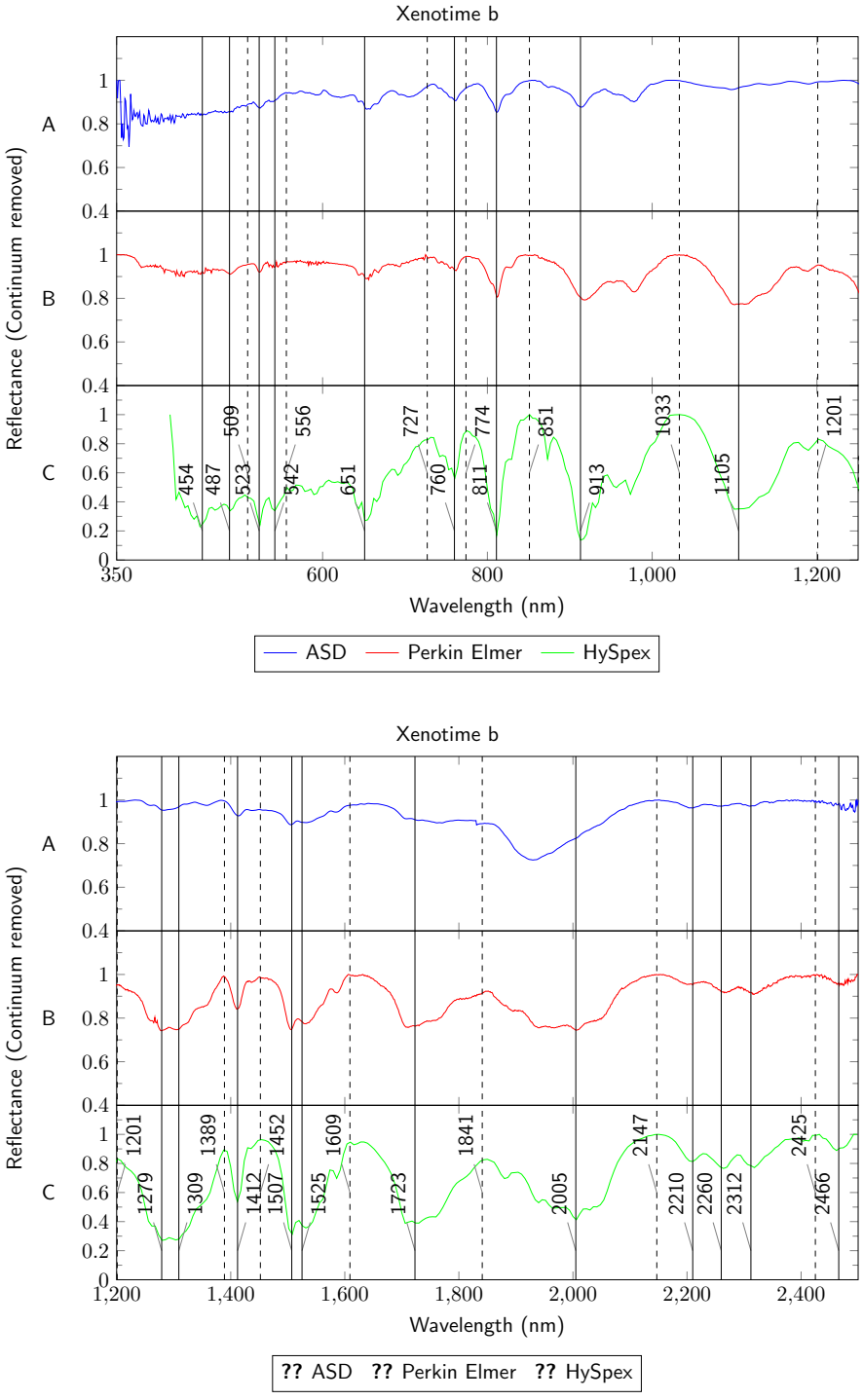

Figure D.80: Reflectance spectra for the rare earth mineral xenotime b for the VNIR and SWIR region. The Figure **above** shows the results from the measurements of the three spectrometer (***(A)*** *ASD Field Spec 3,* ***(B)*** *Perkin Elmer LAMBDA 950,* ***(C)*** *HySpex (VNIR-1600, SWIR-320m-e)*) in a wavelentgh region from 350 to 1200 nm. The Figure **below** shows the results from the measurements of the three spectrometer (***(A)*** *ASD Field Spec 3,* ***(B)*** *Perkin Elmer LAMBDA 950,* ***(C)*** *HySpex (VNIR-1600, SWIR-320m-e)*) in a wavelentgh region from 1200 to 2500 nm. The maxima (solid line) and shoulders (dashed line) are marked.

STR 19/08. GFZ German Research Centre for Geosciences
DOI: 10.2312/GFZ.b103-19089

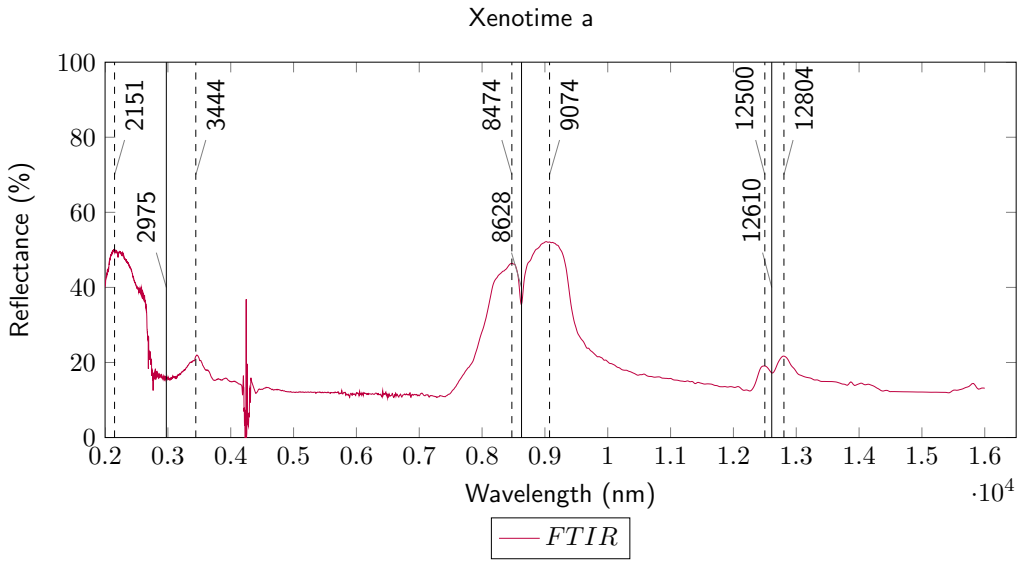

Figure D.81: Reflectance spectrum for the rare earth mineral xenotime a for the TIR region. The Figure shows the results from the measurement with the *FTIR Spectrum GX*. The maxima (solid line) and shoulders (dashed line) are marked.

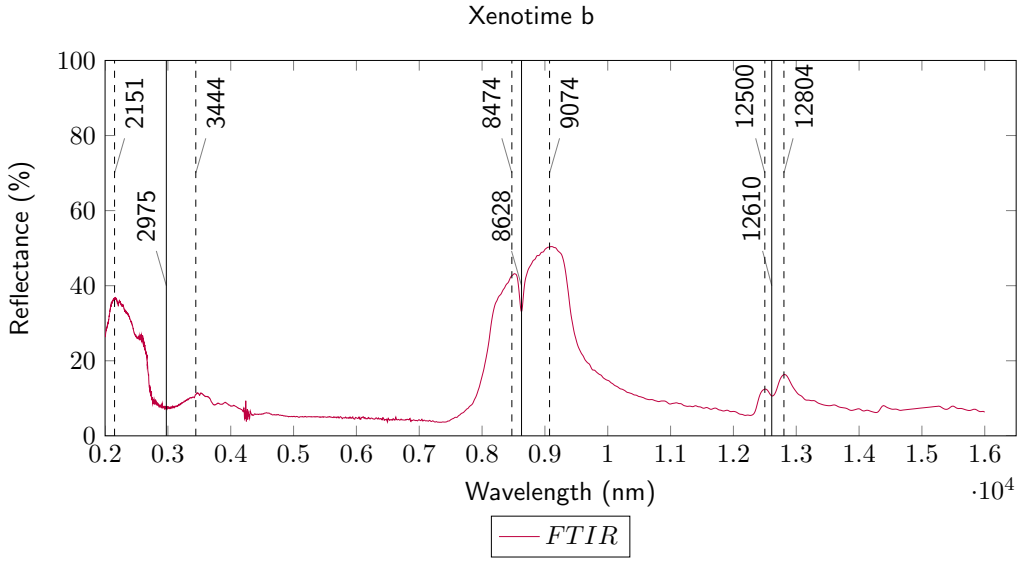

Figure D.82: Reflectance spectrum for the rare earth mineral xenotime b for the TIR region. The Figure shows the results from the measurement with the *FTIR Spectrum GX*. The maxima (solid line) and shoulders (dashed line) are marked.

STR 19/08. GFZ German Research Centre for Geosciences
DOI: 10.2312/GFZ.b103-19089

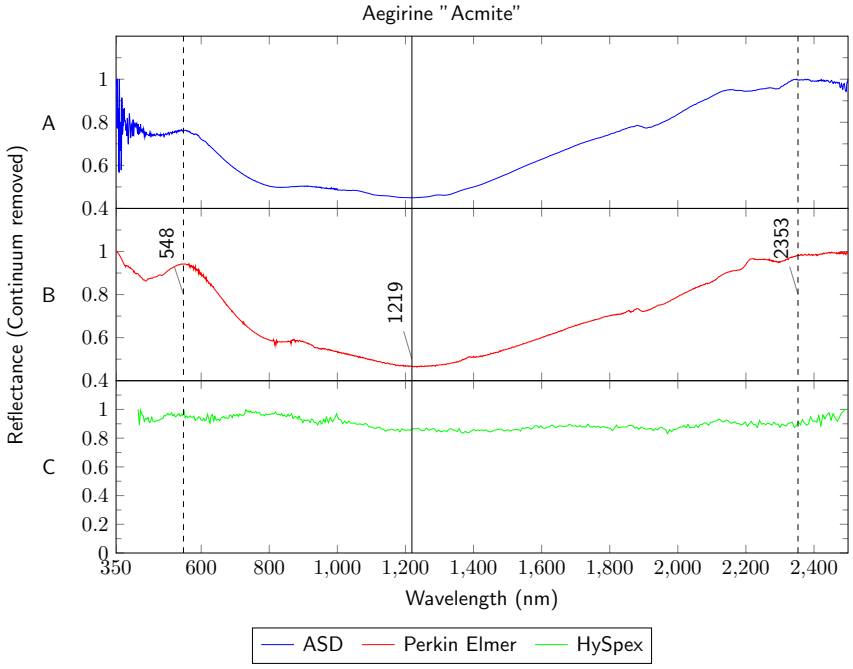

Figure D.83: Reflectance spectra for the rare earth mineral aegirine (acmite) for the VNIR and SWIR region. The Figure shows the results from the measurements of the three spectrometer (***(A)*** *ASD Field Spec 3,* ***(B)*** *Perkin Elmer LAMBDA 950,* ***(C)*** *HySpex (VNIR-1600, SWIR-320m-e)*). Spectra are stacked and absorption features as well as their maxima and shoulders are marked.

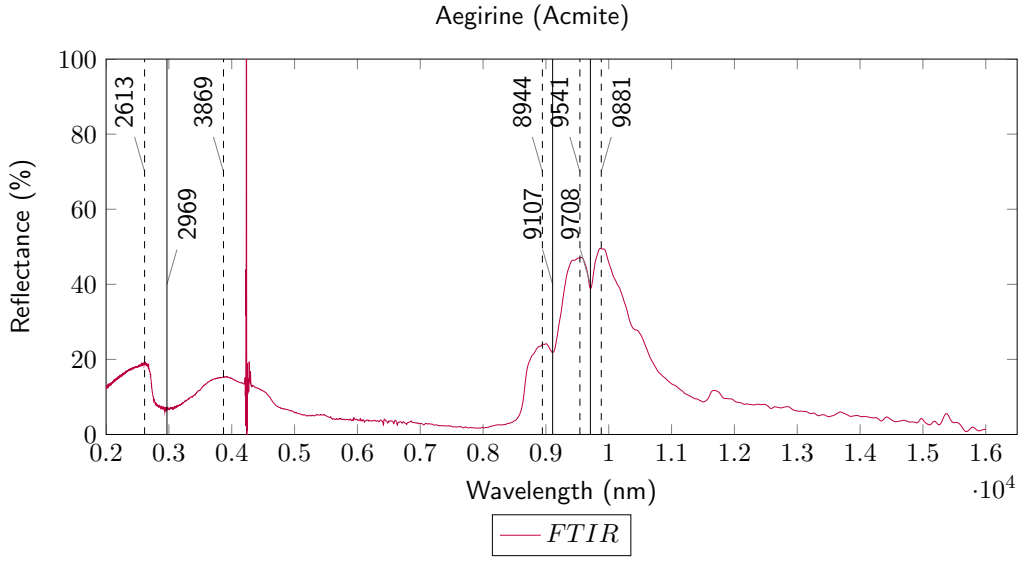

Figure D.84: Reflectance spectrum for the rare earth mineral aegirine for the TIR region. The Figure shows the results from the measurement with the *FTIR Spectrum GX*. The maxima (solid line) and shoulders (dashed line) are marked.

STR 19/08. GFZ German Research Centre for Geosciences
DOI: 10.2312/GFZ.b103-19089

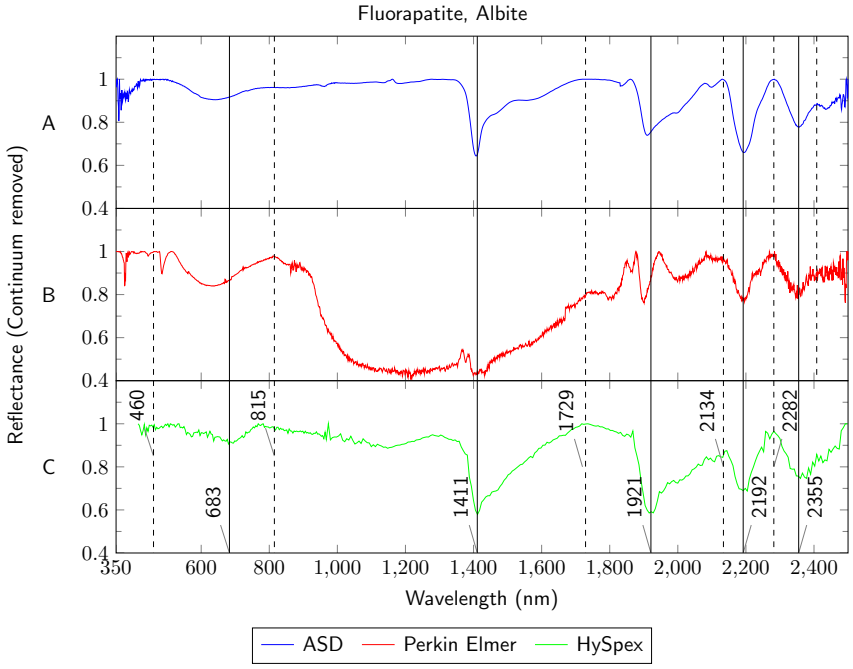

Figure D.85: Reflectance spectra for the rare earth mineral fluorapatite, albite for the VNIR and SWIR region. The Figure shows the results from the measurements of the three spectrometer (***(A)*** *ASD Field Spec 3,* ***(B)*** *Perkin Elmer LAMBDA 950,* ***(C)*** *HySpex (VNIR-1600, SWIR-320m-e)*). Spectra are stacked and absorption features as well as their maxima and shoulders are marked.

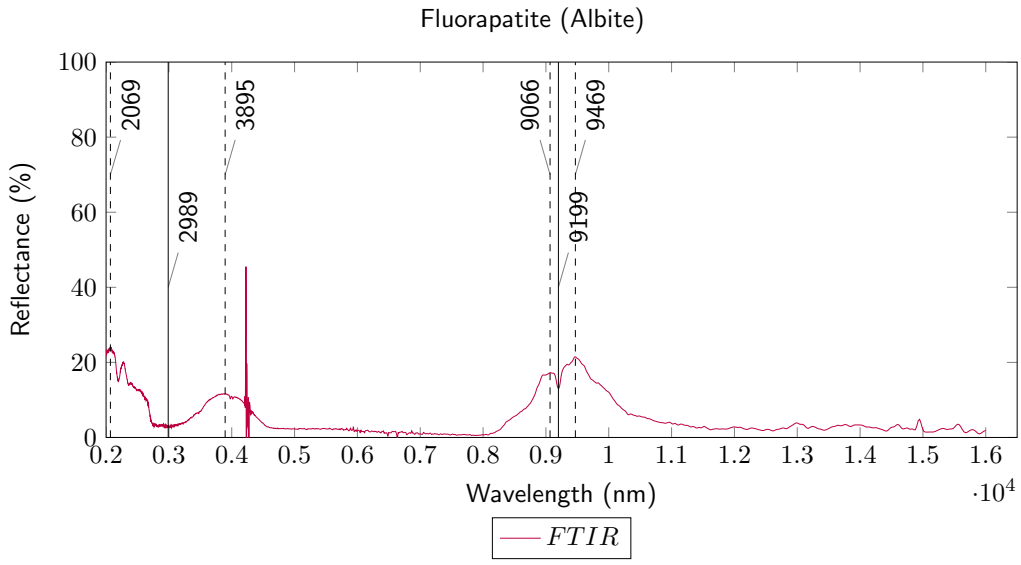

Figure D.86: Reflectance spectrum for the rare earth mineral fluorapatite for the TIR region. The Figure shows the results from the measurement with the *FTIR Spectrum GX*. The maxima (solid line) and shoulders (dashed line) are marked.

STR 19/08. GFZ German Research Centre for Geosciences
DOI: 10.2312/GFZ.b103-19089

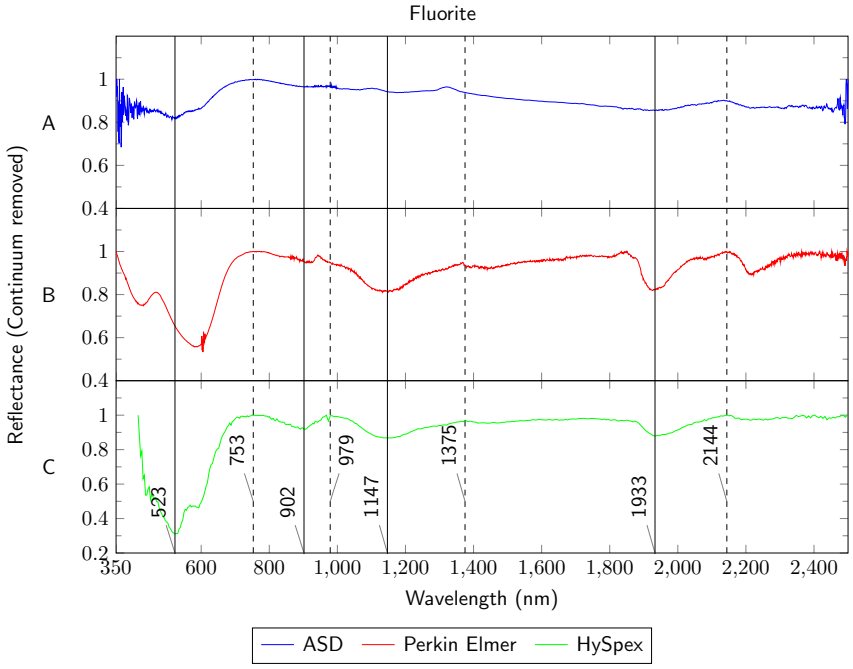

Figure D.87: Reflectance spectra for the rare earth mineral fluorite for the VNIR and SWIR region. The Figure shows the results from the measurements of the three spectrometer (***(A)*** *ASD Field Spec 3,* ***(B)*** *Perkin Elmer LAMBDA 950,* ***(C)*** *HySpex (VNIR-1600, SWIR-320m-e)*). Spectra are stacked and absorption features as well as their maxima and shoulders are marked.

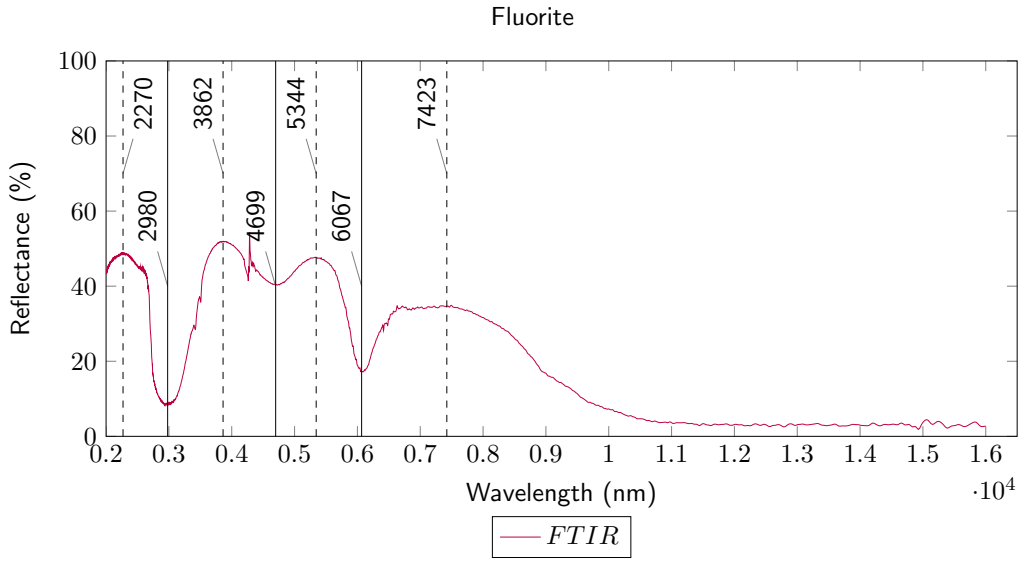

Figure D.88: Reflectance spectrum for the rare earth mineral fluorite for the TIR region. The Figure shows the results from the measurement with the *FTIR Spectrum GX*. The maxima (solid line) and shoulders (dashed line) are marked.

STR 19/08. GFZ German Research Centre for Geosciences
DOI: 10.2312/GFZ.b103-19089

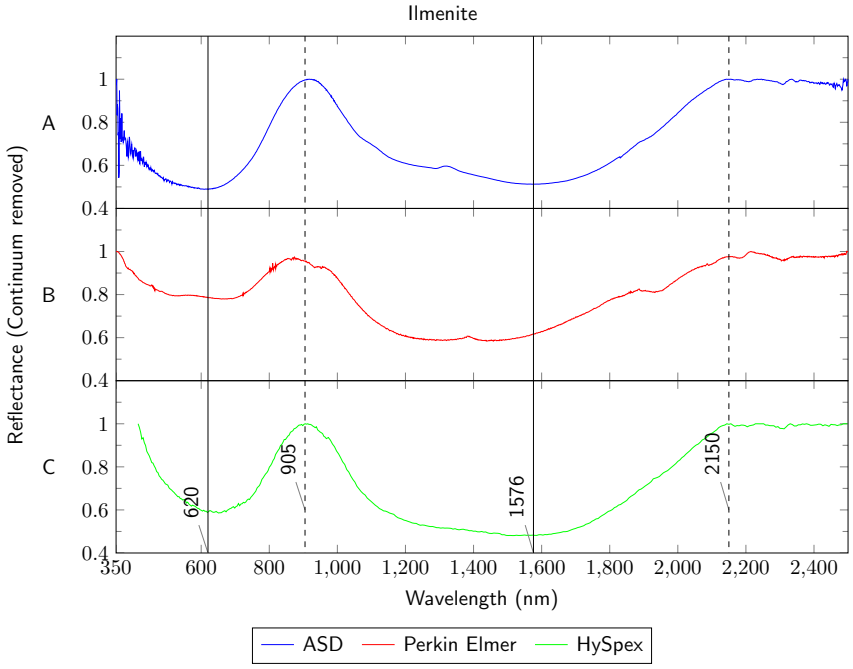

Figure D.89: Reflectance spectra for the rare earth mineral ilmenite for the VNIR and SWIR region. The Figure shows the results from the measurements of the three spectrometer (***(A)*** *ASD Field Spec 3,* ***(B)*** *Perkin Elmer LAMBDA 950,* ***(C)*** *HySpex (VNIR-1600, SWIR-320m-e)*). Spectra are stacked and absorption features as well as their maxima and shoulders are marked.

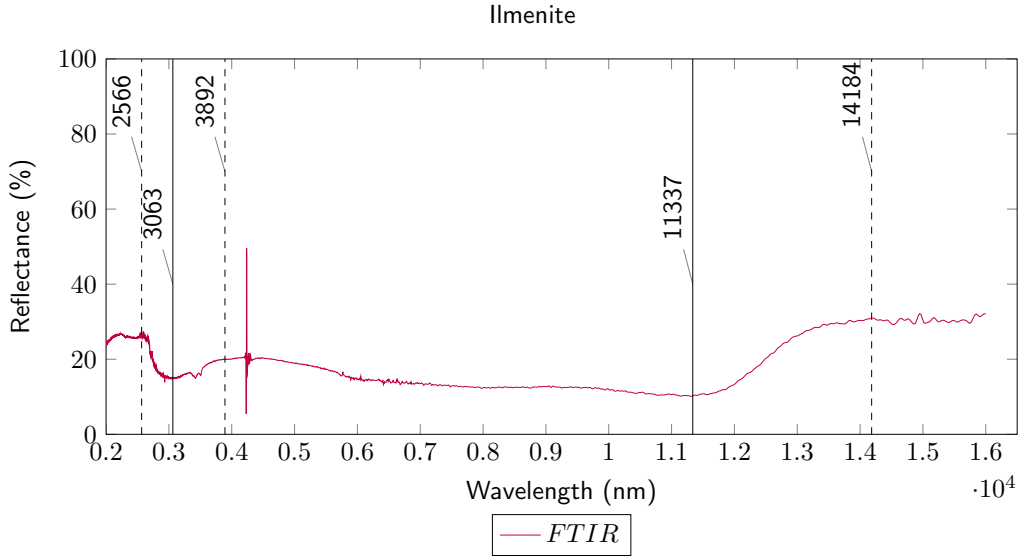

Figure D.90: Reflectance spectrum for the rare earth mineral ilmenite for the TIR region. The Figure shows the results from the measurement with the *FTIR Spectrum GX*. The maxima (solid line) and shoulders (dashed line) are marked.

STR 19/08. GFZ German Research Centre for Geosciences
DOI: 10.2312/GFZ.b103-19089

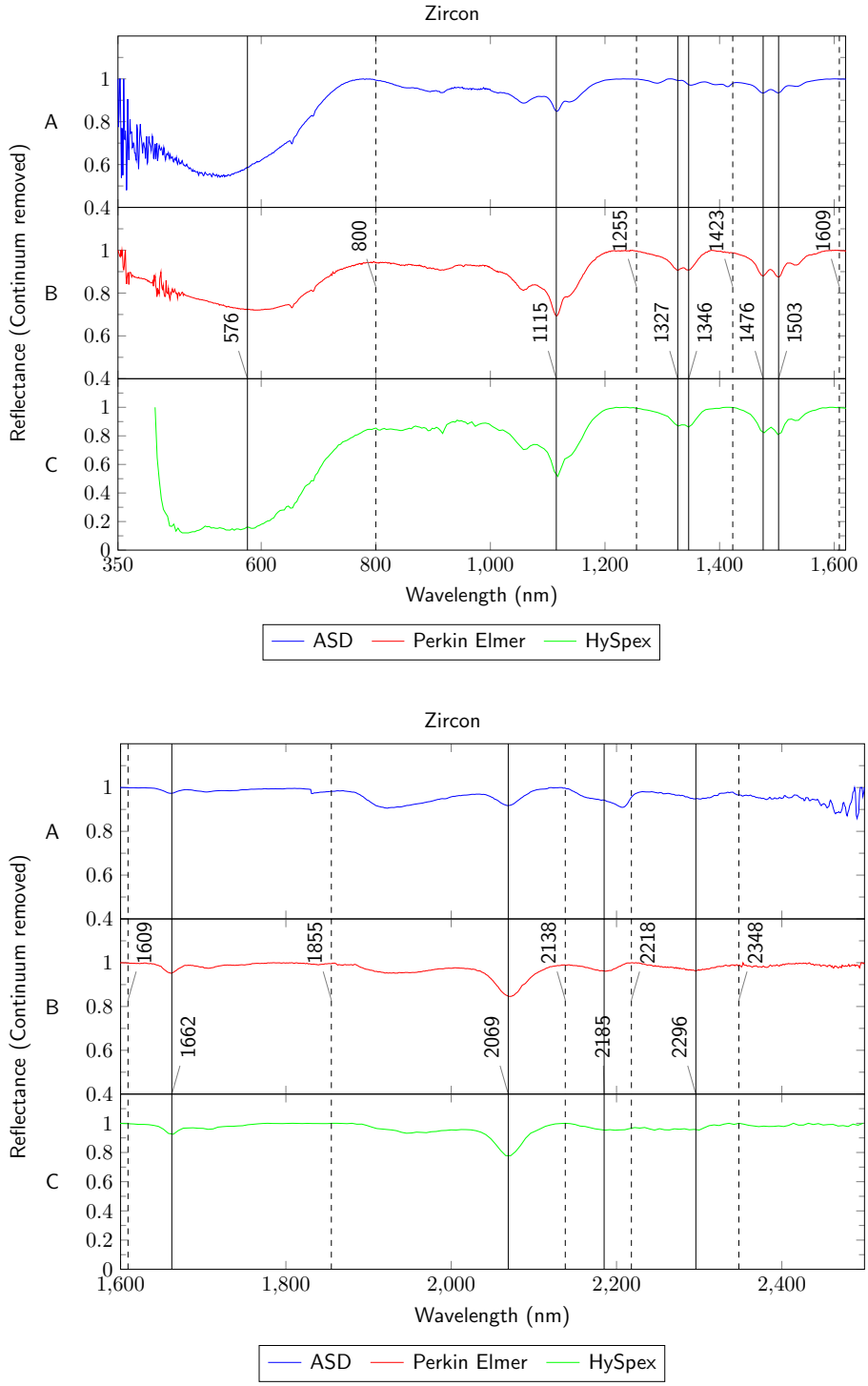

Figure D.91: Reflectance spectra for the rare earth mineral zircon for the VNIR and SWIR region. The Figure **above** shows the results from the measurements of the three spectrometer (***(A)*** *ASD Field Spec 3,* ***(B)*** *Perkin Elmer LAMBDA 950,* ***(C)*** *HySpex (VNIR-1600, SWIR-320m-e)*) in a wavelentgh region from 350 to 1620 nm. The Figure **below** shows the results from the measurements of the three spectrometer (***(A)*** *ASD Field Spec 3,* ***(B)*** *Perkin Elmer LAMBDA 950,* ***(C)*** *HySpex (VNIR-1600, SWIR-320m-e)*) in a wavelentgh region from 1620 to 2500 nm. The maxima (solid line) and shoulders (dashed line) are marked.

STR 19/08. GFZ German Research Centre for Geosciences
DOI: 10.2312/GFZ.b103-19089

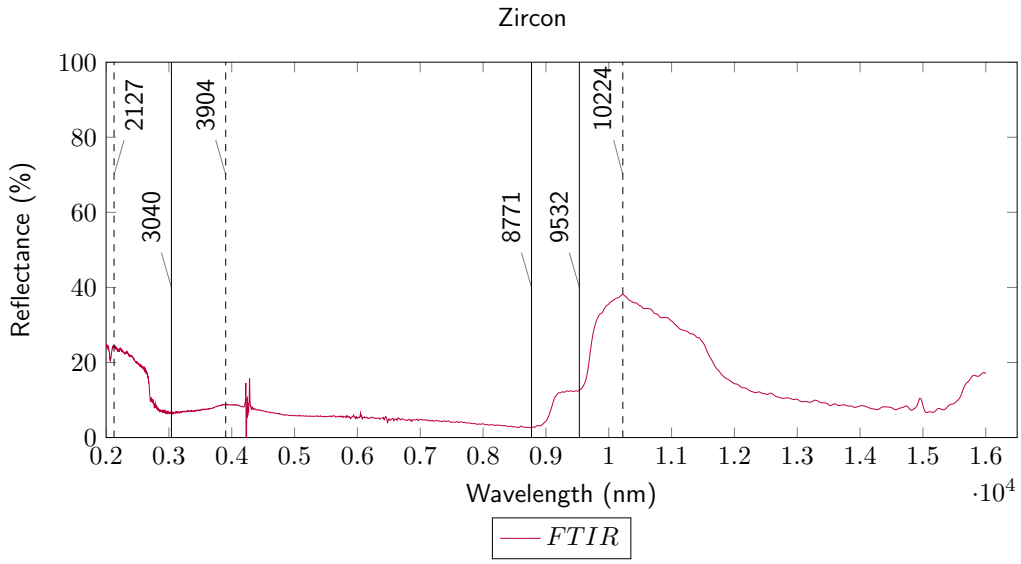

Figure D.92: Reflectance spectrum for the rare earth mineral zircon for the TIR region. The Figure shows the results from the measurement with the *FTIR Spectrum GX*. The maxima (solid line) and shoulders (dashed line) are marked.

STR 19/08. GFZ German Research Centre for Geosciences
DOI: 10.2312/GFZ.b103-19089

Appendix E - REE Minerals - XRF Results, Tables

Table E.1: The Table shows the results of the XRF measurements for the REE minerals bariopyrochlore, fluorapatite, bastnaesite, gadolinite and parisite.

Mineral	Bariopyrochlore,Fluorapatite	Bastnaesite	Gadolinite	Parisite
Duration	121.52	124.99	130.04	121.74
Units	Ppm	ppm	ppm	ppm
Nd	1287.38	41675.2	47251.46	16524.62
Nd Error	532.48	2435.04	1310.54	978.36
Pr	0	10339.05	10537.22	6130.12
Pr Error	N/A	907.36	389.94	506.83
Ce	2920.54	93976.44	72410.25	77382.27
Ce Error	311.75	3780.33	1554.6	2376.56
La	1605.83	44471.7	21159.56	54610.54
La Error	223.98	1728.5	472.57	1610.52
Ba	17998.67	462.27	94.29	20896.54
Ba Error	541.61	141.1	50.34	585.63
Sb	0	0	0	$<$ LOD
Sb Error	N/A	N/A	N/A	43.46
Sn	0	0	0	$<$ LOD
Sn Error	N/A	N/A	N/A	53.50
Cd	0	0	0	$<$ LOD
Cd Error	N/A	N/A	N/A	37.65
Pd	0	0	10.38	$<$ LOD
Pd Error	N/A	N/A	6.05	16.52
Ag	0	0	0	31.19
Ag Error	N/A	N/A	N/A	20.25
Bal	763237.13	768165.13	513584.06	461517.25
Bal Error	3565.35	6380	4841.69	8686.56
Mo	0	0	0	1318.90
Mo Error	N/A	N/A	N/A	62.14
Nb	60300.9	0	0	$<$ LOD
Nb Error	1315.99	N/A	N/A	93.63

STR 19/08. GFZ German Research Centre for Geosciences
DOI: 10.2312/GFZ.b103-19089

Mineral	Bariopyrochlore,Fluorapatite	Bastnaesite	Gadolinite	Parisite
Zr	588.71	333.76	0	< LOD
Zr Error	95.84	185.65	N/A	349.94
Y	113.57	6085.63	23357.12	2096.25
Y Error	15.26	177.02	342.72	67.57
Sr	385.07	496.46	213.28	30027.22
Sr Error	15.13	24.99	10.21	694.33
Rb	0	0	0	462.46
Rb Error	N/A	N/A	N/A	96.71
Bi	0	0	0	< LOD
Bi Error	N/A	N/A	N/A	3024.03
U	425.71	0	460.64	< LOD
U Error	29.28	N/A	23.77	84.37
Th	0	0	2048.51	12306.32
Th Error	N/A	N/A	834.92	1799.38
As	95.53	0	120.36	39229.51
As Error	41.38	N/A	50.28	935.91
W	0	0	0	< LOD
W Error	N/A	N/A	N/A	282.56
Re	0	0	0	< LOD
Re Error	N/A	N/A	N/A	540.01
Ta	0	0	0	4326.44
Ta Error	N/A	N/A	N/A	317.77
Hf	148.6	487.01	1649.11	2236.32
Hf Error	84.39	158.82	124.39	295.68
Ni	0	2225.97	8579.35	1592.59
Ni Error	N/A	526.39	345.05	302.12
Co	0	1362.45	6886.68	< LOD
Co Error	N/A	353.17	315.39	270.64
Fe	44869.63	5326.31	30740.28	5189.08
Fe Error	961.82	467.93	626.96	334.71
Mn	0	0	23857.36	< LOD
Mn Error	N/A	N/A	1236.99	1340.02
Cr	0	0	0	< LOD
Cr Error	N/A	N/A	N/A	10778.13
V	0	0	0	< LOD
V Error	N/A	N/A	N/A	19274.75
Ti	0	0	0	< LOD
Ti Error	N/A	N/A	N/A	32322.77
Ca	4971.37	2246.11	35649.96	152908.55
Ca Error	333.77	292.6	1320.06	5341.46

STR 19/08. GFZ German Research Centre for Geosciences
DOI: 10.2312/GFZ.b103-19089

Mineral	Bariopyrochlore,Fluorapatite	Bastnaesite	Gadolinite	Parisite
K	654.47	3135.05	392.1	1009.52
K Error	243.38	394.06	178.47	238.08
Cl	0	0	678	2958.83
Cl Error	N/A	N/A	51.78	132.52
S	2809.17	0	1661.58	44304.41
S Error	647.09	N/A	162.53	1561.28
P	0	7066.08	16094.78	4399.23
P Error	N/A	658.17	604.86	428.29
Si	96284.92	10229.21	149468.84	55042.40
Si Error	2770.4	1339.07	4180.68	2132.85
Al	0	0	15544.14	$<$ LOD
Al Error	N/A	N/A	1915.35	4280.59
Mg	0	0	17429.04	$<$ LOD
Mg Error	N/A	N/A	9227.02	34608.31

Table E.2: The Table shows the results of the XRF measurements for the REE minerals polycrase, synchysite, xenotime a and xenotime b.

Mineral	Polycrase	Synchysite	Xenoime a	Xenotime b
Duration	123.63	123.52	133.24	123.06
Units	ppm	ppm	ppm	ppm
Nd	397.06	5310.05	1090.92	419.78
Nd Error	108.75	186.27	157.05	163.57
Pr	146.73	1224.03	576.11	0
Pr Error	69.91	90.83	100.91	N/A
Ce	0	7223.98	209.56	0
Ce Error	N/A	148.57	89.78	N/A
La	0	2826.44	275.41	0
La Error	N/A	79.95	67.87	N/A
Ba	0	37.8	65.12	0
Ba Error	N/A	22	28.56	N/A
Sb	0	0	0	0
Sb Error	N/A	N/A	N/A	N/A
Sn	97.46	0	0	0
Sn Error	13.31	N/A	N/A	N/A
Cd	0	0	0	0
Cd Error	N/A	N/A	N/A	N/A
Pd	47.22	0	0	0

STR 19/08. GFZ German Research Centre for Geosciences
DOI: 10.2312/GFZ.b103-19089

Mineral	Polycrase	Synchysite	Xenoime a	Xenotime b
Pd Error	5.13	N/A	N/A	N/A
Ag	15.66	0	0	16.37
Ag Error	6.54	N/A	N/A	9.68
Bal	705860.19	577387.69	547866.19	497090.25
Bal Error	2563.04	2533.55	3098.96	4562.12
Mo	0	23.3	0	0
Mo Error	N/A	8.28	N/A	N/A
Nb	17703.58	324.74	0	0
Nb Error	275.24	20.92	N/A	N/A
Zr	531.78	39.58	0	0
Zr Error	173.21	20.39	N/A	N/A
Y	14913.33	11469.26	44863.73	67199.87
Y Error	239.8	117.95	586.69	1185.16
Sr	64.01	82.64	0	0
Sr Error	7.09	4.82	N/A	N/A
Rb	0	26.23	0	0
Rb Error	N/A	7.77	N/A	N/A
Bi	0	0	0	0
Bi Error	N/A	N/A	N/A	N/A
U	7068.32	13.21	0	0
U Error	127.95	5.97	N/A	N/A
Th	5503.5	0	0	0
Th Error	1234.76	N/A	N/A	N/A
As	932.99	0	463.49	4072.14
As Error	79.68	N/A	28.26	99.32
W	1872.14	145.71	757.12	1248.32
W Error	162.15	53.73	79.72	140.79
Re	444.59	155.63	381.09	418.15
Re Error	74.62	34.87	64.11	121.79
Ta	2597.32	71.89	0	0
Ta Error	212.77	46.46	N/A	N/A
Hf	1743.81	489.38	2524.98	3145.17
Hf Error	117.9	54.3	116.59	171.01
Ni	7151.46	2212.08	13937.07	16035.74
Ni Error	299.68	144.7	347.53	465.52
Co	3102.16	1005.01	11696.69	14766.94
Co Error	206.26	107.94	286.06	397.57
Fe	14214.57	4472.9	9879.12	12613.85
Fe Error	407.06	152.83	243.38	335.1
Mn	0	0	4207.4	7402.58

STR 19/08. GFZ German Research Centre for Geosciences
DOI: 10.2312/GFZ.b103-19089

Mineral	Polycrase	Synchysite	Xenoime a	Xenotime b
Mn Error	N/A	N/A	560.41	380.15
Cr	0	0	0	0
Cr Error	N/A	N/A	N/A	N/A
V	0	0	0	0
V Error	N/A	N/A	N/A	N/A
Ti	25056.61	0	0	0
Ti Error	3038.03	N/A	N/A	N/A
Ca	7909.08	86693.24	361.89	557.61
Ca Error	323.08	1281.67	77.43	107.84
K	4698.97	5786	0	0
K Error	227.17	203.12	N/A	N/A
Cl	462.41	371.04	555.7	0
Cl Error	31.74	34.53	29.5	N/A
S	1042.43	462.31	0	0
S Error	449.64	109.62	N/A	N/A
P	55943.05	12205.7	101415.52	127657.94
P Error	2615.02	348.84	1204.73	1806.86
Si	98128.99	220557.67	250510.16	226909.45
Si Error	2198.13	2463.68	2232.45	2523.27
Al	22350.58	59352.03	8357.95	10834.39
Al Error	1190.19	2203.86	903.47	1065.84
Mg	0	0	0	8923.29
Mg Error	N/A	N/A	N/A	5307.13

Table E.3: Table shows the results of the XRF measurements for the REE minerals aegirine, fluorapatite, fluorite, ilmenite and zircon.

Mineral	Aegirine, Acmite	Fluorapatite	Fluorite	Ilmenite	Zircon
Duration	171.23	124.13	124.61	122.64	135.99
Units	ppm	ppm	ppm	ppm	ppm
Nd	1416.93	932.17	1851.6	1283.89	0
Nd Error	169	128.11	143.42	148.17	N/A
Pr	807.44	564.44	1039.69	692.13	653.75
Pr Error	109.11	83.52	91.9	95.5	329.63
Ce	361.39	219.85	502.48	284.44	0
Ce Error	96.89	74.94	80.68	84.92	N/A
La	357.03	296.28	433.6	260.56	1086.01
La Error	72.88	56.75	60.55	63.67	277.64

STR 19/08. GFZ German Research Centre for Geosciences
DOI: 10.2312/GFZ.b103-19089

Mineral	Aegirine, Acmite	Fluorapatite	Fluorite	Ilmenite	Zircon
Ba	89.48	96.6	120.74	96.05	340.73
Ba Error	30.54	24.1	25.38	27.12	100.1
Sb	0	0	0	0	0
Sb Error	N/A	N/A	N/A	N/A	N/A
Sn	1073.52	27.38	0	0	0
Sn Error	34.07	13.02	N/A	N/A	N/A
Cd	0	0	0	0	0
Cd Error	N/A	N/A	N/A	N/A	N/A
Pd	0	0	0	0	0
Pd Error	N/A	N/A	N/A	N/A	N/A
Ag	0	0	0	0	0
Ag Error	N/A	N/A	N/A	N/A	N/A
Bal	515508.13	603891.25	410004.44	464517.38	337938.38
Bal Error	2127.85	2080.8	2688.49	3425.28	20967.98
Mo	0	0	0	14.76	0
Mo Error	N/A	N/A	N/A	8.97	N/A
Nb	239.16	0	0	2280.96	0
Nb Error	7.61	N/A	N/A	30.62	N/A
Zr	9083.92	0	0	375.15	527483.31
Zr Error	85.79	N/A	N/A	23.65	20553.65
Y	174.31	17.66	1141.72	6.66	447.57
Y Error	5.6	7.27	15.38	3.31	52.78
Sr	24.52	1277.09	73.19	10.74	0
Sr Error	2.31	15.69	3.33	2.08	N/A
Rb	0	1814.19	0	0	0
Rb Error	N/A	24.5	N/A	N/A	N/A
Bi	0	0	0	0	0
Bi Error	N/A	N/A	N/A	N/A	N/A
U	0	116.53	0	45.15	0
U Error	N/A	16.37	N/A	5.91	N/A
Th	0	343.21	0	0	0
Th Error	N/A	150.08	N/A	N/A	N/A
As	162.73	208.73	0	68.52	0
As Error	11.78	13.11	N/A	12.6	N/A
W	623.35	0	0	111.2	0
W Error	52.86	N/A	N/A	55.11	N/A
Re	0	88.04	0	0	0
Re Error	N/A	26.31	N/A	N/A	N/A
Ta	0	188.67	0	0	0
Ta Error	N/A	38.6	N/A	N/A	N/A

STR 19/08. GFZ German Research Centre for Geosciences
DOI: 10.2312/GFZ.b103-19089

Mineral	Aegirine, Acmite	Fluorapatite	Fluorite	Ilmenite	Zircon
Hf	995.93	0	60.38	109.05	0
Hf Error	57.75	N/A	31.61	45.59	N/A
Ni	246.07	0	382.65	0	0
Ni Error	90.93	N/A	94.47	N/A	N/A
Co	0	0	350.56	0	0
Co Error	N/A	N/A	60.41	N/A	N/A
Fe	202692.73	443.29	0	6583.05	0
Fe Error	1301.76	74.75	N/A	187.85	N/A
Mn	7847.25	0	1351.76	0	0
Mn Error	343.93	N/A	701.5	N/A	N/A
Cr	0	0	0	0	0
Cr Error	N/A	N/A	N/A	N/A	N/A
V	0	0	0	0	0
V Error	N/A	N/A	N/A	N/A	N/A
Ti	9874.38	0	3796.34	416458.47	0
Ti Error	3417.77	N/A	1263.01	17887.33	N/A
Ca	11926.02	127716.8	569416.38	1439.97	305.87
Ca Error	502.61	1184.83	3458.38	317.4	74.64
K	0	32918.78	0	800.11	0
K Error	N/A	417.97	N/A	236.91	N/A
Cl	385.16	0	0	384.75	128.48
Cl Error	33.19	N/A	N/A	56.53	34
S	0	690.79	0	621.6	2955.76
S Error	N/A	149.35	N/A	338.5	1472.22
P	5089.28	79523.7	0	3297.29	0
P Error	2640.45	788.8	N/A	422.85	N/A
Si	228012.66	104714.55	5211.43	10768.82	126036.2
Si Error	2754.57	1282.95	695.05	878.29	2049.88
Al	2730.55	43165.25	0	25517.55	0
Al Error	1048.5	2061.2	N/A	2938.16	N/A
Mg	0	0	0	63971.8	0
Mg Error	N/A	N/A	N/A	14604.85	N/A

STR 19/08. GFZ German Research Centre for Geosciences
DOI: 10.2312/GFZ.b103-19089

Appendix F - Approach, Spectra

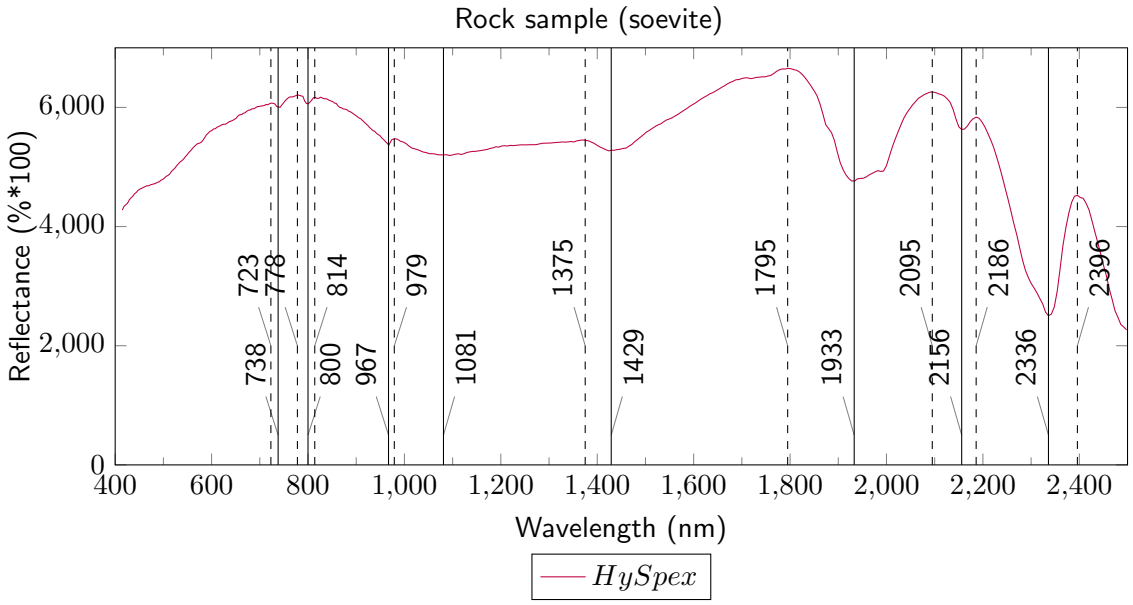

Figure F.93: Reflectance spectra for the rock sample (soevite) for the VNIR and SWIR region. The Figure shows the results from the measurement of the *HySpex (VNIR-1600, SWIR-320m-e)*. The absorption features as well as their maxima and shoulders are marked.

STR 19/08. GFZ German Research Centre for Geosciences
DOI: 10.2312/GFZ.b103-19089

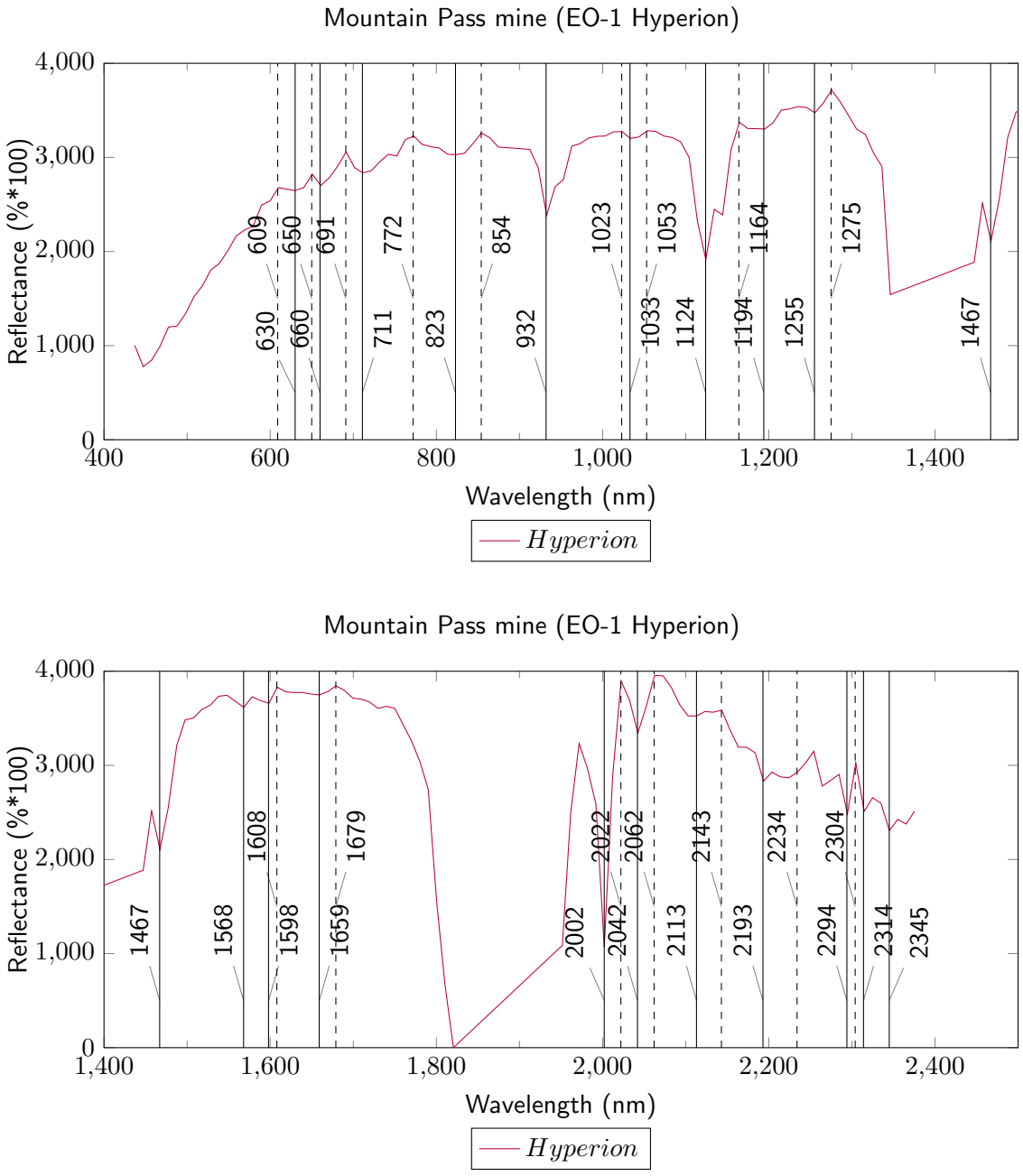

Figure F.94: Reflectance spectra (extracted by a ROI, covering the REE mine) for the Mountain Pass mine for the VNIR and SWIR region. The Figure **above** shows the results from the sensor EO-1 Hyperion in a wavelentgh region from 400 to 1500 nm. The Figure **below** shows the results from the sensor EO-1 Hyperion in a wavelentgh region from 1400 to 2500 nm. The maxima (solid line) and shoulders (dashed line) are marked.

STR 19/08. GFZ German Research Centre for Geosciences
DOI: 10.2312/GFZ.b103-19089

Eigenständigkeitserklärung

Hiermit versichere ich, dass ich die vorliegende Masterarbeit selbstständig und nur unter Verwendung der angegebenen Quellen und Hilfsmittel verfasst habe. Die Arbeit wurde bisher in gleicher oder ähnlicher Form keiner anderen Prüfungsbehörde vorgelegt.

Declaration of independent work

I hereby declare that this master's thesis is the product of my own independent work. All content and ideas drawn directly or indirectly from external sources are indicated as such. The thesis has not been submitted to any other examining body and has not been published.

Ort (Place), Datum (Date)	Unterschrift (Signature)

ISSN 2190-7110